

IntechOpen

# Sorption in 2020s

*Edited by George Kyzas and Nikolaos Lazaridis*





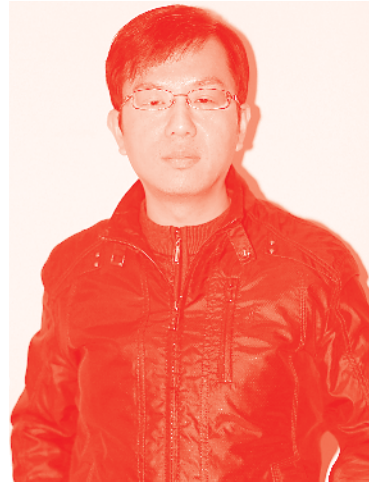
---

# Sorption in 2020s

*Edited by George Kyzas  
and Nikolaos Lazaridis*

Published in London, United Kingdom

---



## IntechOpen





*Supporting open minds since 2005*



Sorption in 2020s

<http://dx.doi.org/10.5772/intechopen.77842>

Edited by George Kyzas and Nikolaos Lazaridis

#### Contributors

Xiaogang Yang, Xiani Huang, Guang Li, Collins Ezeh, Chenggong Sun, Colin Snape, Ndubisi Aviara, Aman Sharma, Anna Derylo-Marczewska, Malgorzata Seczkowska, Magdalena Blachnio, Jacques Romain Njimou, Emmanuel Njungab, Fridolin Kouatchie Njeutcha, André Talla, Nkeng George Elambo, Yıldırım İsmail Tosun, Samuel Asoaming, André Lajeunesse, Alexandre Camiré, Bruno Chabot

#### © The Editor(s) and the Author(s) 2020

The rights of the editor(s) and the author(s) have been asserted in accordance with the Copyright, Designs and Patents Act 1988. All rights to the book as a whole are reserved by INTECHOPEN LIMITED. The book as a whole (compilation) cannot be reproduced, distributed or used for commercial or non-commercial purposes without INTECHOPEN LIMITED's written permission. Enquiries concerning the use of the book should be directed to INTECHOPEN LIMITED rights and permissions department ([permissions@intechopen.com](mailto:permissions@intechopen.com)).

Violations are liable to prosecution under the governing Copyright Law.



Individual chapters of this publication are distributed under the terms of the Creative Commons Attribution 3.0 Unported License which permits commercial use, distribution and reproduction of the individual chapters, provided the original author(s) and source publication are appropriately acknowledged. If so indicated, certain images may not be included under the Creative Commons license. In such cases users will need to obtain permission from the license holder to reproduce the material. More details and guidelines concerning content reuse and adaptation can be found at <http://www.intechopen.com/copyright-policy.html>.

#### Notice

Statements and opinions expressed in the chapters are these of the individual contributors and not necessarily those of the editors or publisher. No responsibility is accepted for the accuracy of information contained in the published chapters. The publisher assumes no responsibility for any damage or injury to persons or property arising out of the use of any materials, instructions, methods or ideas contained in the book.

First published in London, United Kingdom, 2020 by IntechOpen

IntechOpen is the global imprint of INTECHOPEN LIMITED, registered in England and Wales, registration number: 11086078, 7th floor, 10 Lower Thames Street, London, EC3R 6AF, United Kingdom

Printed in Croatia

British Library Cataloguing-in-Publication Data

A catalogue record for this book is available from the British Library

Additional hard and PDF copies can be obtained from [orders@intechopen.com](mailto:orders@intechopen.com)

Sorption in 2020s

Edited by George Kyzas and Nikolaos Lazaridis

p. cm.

Print ISBN 978-1-83880-113-7

Online ISBN 978-1-83880-114-4

eBook (PDF) ISBN 978-1-78985-565-4

# We are IntechOpen, the world's leading publisher of Open Access books Built by scientists, for scientists

4,700+

Open access books available

120,000+

International authors and editors

135M+

Downloads

151

Countries delivered to

Our authors are among the  
Top 1%

most cited scientists

12.2%

Contributors from top 500 universities



WEB OF SCIENCE™

Selection of our books indexed in the Book Citation Index  
in Web of Science™ Core Collection (BKCI)

Interested in publishing with us?  
Contact [book.department@intechopen.com](mailto:book.department@intechopen.com)

Numbers displayed above are based on latest data collected.  
For more information visit [www.intechopen.com](http://www.intechopen.com)







# Meet the editors



Dr George Z. Kyzas is an Associate Professor in the Department of Chemistry at the International Hellenic University (IHU). He was born in Drama (Greece) and studied Chemistry in the Department of Chemistry at the Aristotle University of Thessaloniki (AUTH). He obtained his BSc, MSc, and PhD from the Department of Chemistry (AUTH) specializing in Chemical Technology and Materials Science. He then worked as a PostDoc

Researcher in the Department of Chemistry (AUTH) on many research projects, while at the same time he was an Adjunct Assistant Professor at Eastern Macedonia and Thrace Institute of Technology (Greece). He was then officially assigned as Associate Professor in the Department of Chemistry (International Hellenic University), being the Head of the Department. His research interests include the synthesis of various nanomaterials (inorganic, aluminates, polymers, graphenes, agro-food residues, etc.) for the treatment of wastewaters (dyes, heavy metals, pharmaceuticals, phenols, oil-spills, etc.). His scientific work has been published in more than 110 papers in international journals with a high impact factor (IF, ave 4.3). He has published 8 books, 36 chapters in scientific books, and 1 patent. He has also acted 7 times as Guest Editor for special issues of journals and has more than 80 presentation in international conferences. His work is widely recognized with over 5,000 citations based on Scopus database (h-index 42). He has been awarded with scholarships from the Research Committee of the Aristotle University of Thessaloniki (2009, 2013), the State Scholarship Foundation (2013), and the Stavros Niarchos Foundation (2016). He has also participated in about 20 research projects as a researcher. He is a reviewer in more than 200 scientific journals and participates as an assessor in Greek and European research projects.



Prof. Nikolaos K. Lazaridis was born in Thessaloniki (Greece) and obtained his BSc (1979) and PhD (1991) degrees from the Aristotle University of Thessaloniki (Greece), where today he is Professor of the Laboratory of General & Inorganic Chemical Technology of School of Chemistry. He teaches transport phenomena and has vast industrial experience. He has authored numerous scientific articles, mainly on wastewater treatment.

His scientific work has been published in more than 90 papers in international journals with a high impact factor. His work is widely recognized with over 4,500 citations based on Scopus database (h-index 40). He has also participated in about 20 research projects as a researcher. He is a reviewer in many scientific journals.



# Contents

<b>Preface</b>	<b>XIII</b>
<b>Chapter 1</b> Influence of Pesticide Properties on Adsorption Capacity and Rate on Activated Carbon from Aqueous Solution <i>by Magdalena Blachnio, Anna Derylo-Marczewska and Malgorzata Seczkowska</i>	<b>1</b>
<b>Chapter 2</b> Sorption Capacities of a Lignin-Based Electrospun Nanofibrous Material for Pharmaceutical Residues Remediation in Water <i>by Alexandre Camiré, Bruno Chabot and André Lajeunesse</i>	<b>25</b>
<b>Chapter 3</b> Processes and Factors Affecting Phosphorus Sorption in Soils <i>by Samuel Kwesi Asomaning</i>	<b>45</b>
<b>Chapter 4</b> Microwave Radiated Sorption-Hazardous Emission Control by Popped Borax and Salted Pumice for Coal Combustion in Thermal Power Plants <i>by Yildirim İsmail Tosun</i>	<b>61</b>
<b>Chapter 5</b> Treatment of Agro-Food Wastewaters and Valuable Compounds Recovery by Column Sorption Runs <i>by Jacques Romain Njimou, Fridolin Kouatchie Njeutcha, Emmanuel Njungab, André Talla and Nkeng George Elambo</i>	<b>81</b>
<b>Chapter 6</b> Glyphosate Resistance of <i>Chloris virgata</i> Weed in Australia and Glyphosate Mobility Are Connected Problems <i>by Aman D. Sharma</i>	<b>105</b>
<b>Chapter 7</b> Hybrid Two-step Preparation of Nanosized MgAl Layered Double Hydroxides for CO <sub>2</sub> Adsorption <i>by Xiani Huang, Xiaogang Yang, Guang Li, Collins I. Ezech, Chenggong Sun and Collins Snape</i>	<b>123</b>

## **Chapter 8**

Moisture Sorption Isotherms and Isotherm Model Performance  
Evaluation for Food and Agricultural Products

*by Ndubisi A. Aviara*

**143**

# Preface

Sorption is a physical and chemical process by which one substance becomes attached to another. Specific cases of sorption are treated as: (i) Absorption – “the incorporation of a substance in one state into another of a different state” (e.g., liquids being absorbed by a solid or gases being absorbed by a liquid); (ii) Adsorption – the physical adherence or bonding of ions and molecules onto the surface of another phase (e.g., reagents adsorbed to a solid catalyst surface); (iii) Ion exchange – an exchange of ions between two electrolytes or between an electrolyte solution and a complex. At the beginning of the 21st century, separation processes presented a comprehensive application of the major operations performed by various industries, such as chemical, food, environmental, and biotechnology. Sorption, one of the preferred separation processes because of its effectiveness at different interfaces, has caught the attention of many scientists. This book is aimed at presenting a general knowledge of sorption and a number of applications, as well as recognizing its functions and paramount importance in chemical and biochemical plants, including environmental treatment. This book will be a reference book for those who are interested in sorption techniques from various industries. The above information clearly indicates that the “world” of sorption has various sections. Therefore, the target audience of this book is vast. Specialists, researchers, and professors from more than 20 countries have published their research in this book. We are grateful to all of the authors who have contributed their tremendous expertise to this book. We wish to acknowledge the outstanding support from Mr Gordan Tot, Publishing Process Manager, IntechOpen Science Croatia who collaborated tirelessly in crafting this book.

The future of sorption is indeed bright!

**George Z. Kyzas (MSc, PhD)**

Associate Professor,  
Department of Chemistry, International Hellenic University,  
Kavala, Greece

**Nikolaos K. Lazaridis (MSc, PhD)**

Professor,  
Department of Chemistry, Aristotle University of Thessaloniki,  
Thessaloniki, Greece



# Dedication

*My parental Professor N. Lazaridis, who gave me the opportunity to follow the world of Academia and Research.*





# Influence of Pesticide Properties on Adsorption Capacity and Rate on Activated Carbon from Aqueous Solution

*Magdalena Blachnio, Anna Derylo-Marczewska  
and Malgorzata Seczkowska*

## Abstract

The adsorbate structural properties such as the type, number, and position of substituents on benzene ring of organic compound, as well as a length and arrangement of hydrocarbon chain in a space, exert a significant influence on the adsorption process. The measurements of adsorption equilibria and kinetics of several pesticides belonging to the group of halogenated phenoxyacids differentiated in terms of structural and physicochemical properties were studied in order to characterize the adsorption mechanism and correlate it with the pollutant properties. Regarding a complexity of investigations (capacity and rate) comprising 21 structurally closely related active substances showing the carcinogenic activity on living organisms and relatively long half-life time in the environment, the proposed intensive studies on the removal of pollutants by adsorption process are very important in cognitive and practical terms.

**Keywords:** pesticide adsorption, activated carbon, adsorption equilibrium, adsorption kinetics

## 1. Introduction

The improvement of effectiveness of pollutant removal from water and sewage using activated carbons has been a subject of numerous studies. The influence of adsorbate, adsorbent, solution properties, and experiment conditions on adsorption process has been analyzed.

Noteworthy is the impact of adsorbate properties on adsorption process such as solubility, molecule dimension, ability to dissociation, and physicochemical properties. Hydrophobicity which can be expressed by solubility is the main driving force of adsorption process of organics from aqueous solutions on activated carbons. The lower solubility of a pollutant is the highest adsorption on hydrophobic carbon is observed. Additionally, analyzing adsorption of pollutants from aqueous solutions on microporous materials, it is necessary to take into account molecule dimension due to a possible sieve effect. Moreover, the influence of functional groups on adsorbate aromatic ring on the differentiation of adsorptive affinity of organic compounds to activated carbon should be also regarded.

The influence of adsorbate substituents on adsorption mechanism is similar to that of surface groups of adsorbent. Depending on their nature, they can attract or repel electrons and affect the dispersive interactions between adsorbate aromatic ring and graphene layers of activated carbon. The adsorbate functional groups that are electron donors activate the aromatic ring by moving electrons toward it, and thereby they enhance the interactions between adsorbate molecule and  $\pi$  electrons of adsorbent graphene planes. On the other hand, the deactivating groups as electron acceptors reduce the electron density of aromatic ring; thus, interactions of adsorbate-adsorbent surface are weakened [1–7].

The research on effect of adsorbate properties on adsorption process is an extension of the studies already published in the paper [8]. The pesticides belonging to a group of chloride phenoxyacid derivatives were used as adsorbates in view of their common usage in agriculture and hence a high probability of infiltration to surface and underground waters. Their presence in water affects its quality, worsens its properties, and in some cases makes it unsuitable to consume. These pesticides show a carcinogenic activity on living organisms and a relatively long half-life time in the environment; therefore, the intensive study on their removal by adsorption process is very important for practical applications. The experimental studies include measurements of the adsorption isotherms and concentration rate profiles as well as their interpretation on the basis of the generalized Langmuir (GL) equation for equilibrium data and diffusion models (intraparticle diffusion model (IDM) and pore diffusion model (PDM)) and multi-exponential (m-exp) equation for kinetic data. Based on the obtained results, the correlations between adsorbate structure, its properties, and adsorption uptake and rate were analyzed. The evaluation of the theoretical equilibrium and kinetic equations and models based on a fitting quality and consistency with adsorption mechanism was also made.

## 2. Experimental

### 2.1 Materials and methods

The selected adsorbates comprise 21 compounds which are structurally differentiated with regard to the number, position, and type of the functional groups and length and spatial arrangement of the hydrocarbon part in a molecule. Not all of these substances are used as pesticides because of their low biological activity. However, due to complexity of the research issues, it seems to be reasonable to include them as a subject of the investigation.

**Table 1** presents the physicochemical properties of the adsorbates collected on the basis of literature data or calculations using computer programs generally available. All the substances are analytical reagent grade purity. The chemical names and abbreviations of them are as follows: 4-chlorophenoxyacetic acid (4-CPA); 2,4-dichlorophenoxyacetic acid (2,4-D); 2,4,5-trichlorophenoxyacetic acid (2,4,5-CPA); 2,4,6-trichlorophenoxyacetic acid (2,4,6-CPA); 4-chloro-3-methylphenoxyacetic acid (4-CMPA); 4-chloro-2-methylphenoxyacetic acid (MCPA); 2,4-dibromophenoxypropionic acid (2,4-BrPA); 2,4,6-tribromophenoxypropionic acid (2,4,6-BrPA); 2-(3-chlorophenoxy)propionic acid (3-CPP); 3-(4-chlorophenoxy)propionic acid (4-CP); 2-(4-chlorophenoxy)propionic acid (4-CPP); 2-(2,4-dichlorophenoxy)propionic acid (2,4-CPP); 2-(2,5-dichlorophenoxy)propionic acid (2,5-CPP); 2-(3,4-dichlorophenoxy)propionic acid (3,4-CPP); 2-(2,4,5-trichlorophenoxy)propionic acid (2,4,5-CPP); 2-(4-chloro-2-methylphenoxy)propionic

Common name	pK <sub>a</sub> [9]	Solubility g/dm <sup>3</sup> 20–25°C	K <sub>ow</sub> /log D [9]		K <sub>ow</sub> /log P	D <sub>min</sub> /Å [9]	D <sub>max</sub> /Å [9]
			pH = 1.81	pH = 10.38			
4-CPA	3.14	0.848 [10]	1.88	−1.63	1.85 [11]	4.33	9.38
2,4-D	2.80	0.682 [10]	2.46	−1.03	2.37 [11]	4.88	9.49
2,4,5-CPA	2.56	0.268 [10]	3.04	−0.42	2.89 [11]	6.22	8.88
2,4,6-CPA	2.57	0.247 [10]	3.04	−0.42	2.89 [11]	5.42	8.84
4-CMPA	3.36	0.650 [12]	2.40	−1.12		5.42	8.96
MCPA	3.36	0.825 [10]	2.40	−1.12	3.25 [13]	5.47	9.52
2,4-BrPA	1.96	0.059 [14]	2.60	−0.70		5.03	9
2,4,6-BrPA	1.50	0.015 [15]	3.12	0.07		5.71	9
3-CPP	3.27	1.200 [16]	2.45	−1.06		5	7.79
4-CP	3.70	0.770 [12]	2.13	−1.39		4.33	9.87
4-CPP	3.27	1.475 [10]	2.45	−1.06		5.22	8.65
2,4-CPP	2.95	0.829 [10]	3.04	−0.46		5.59	9.03
2,5-CPP	2.95	0.181 [14]	3.04	−0.46		5.62	8.63
3,4-CPP	2.94	0.130 [12]	3.04	−0.46		5.5	8.76
2,4,5-CPP	2.70	0.140 [10]	3.62	0.15	3.80 [13]	5.62	9
MCPP	3.47	0.895 [10]	2.97	−0.55	3.13 [13]	5.86	8.64
4-CMPP	3.46	0.690 [15]	2.97	−0.55		5.86	7
CFA	3.37	0.582 [17]	2.89	−0.63	2.84 [13]	4.42	9.14
4-CPB	3.42	0.315 [14]	2.98	−0.54		5.22	9.7
MCPB	3.59	0.048 [10]	3.50	−0.03	3.28 [18]	6.36	9.65
4-CMPB	3.59	0.17 [12]	3.50	−0.03		5.86	9.28

**Table 1.** *Physicochemical properties of the studied pesticides, where pK<sub>a</sub> is the value based on partial charge distribution in a molecule, log D is the octanol-water coefficient at a given pH, log P is the partition coefficient of a compound between octanol and water, and D<sub>min</sub> and D<sub>max</sub> are measures between the most distant molecule atoms.*

acid (MCPP); 2-(4-chloro-3-methylphenoxy)propionic acid (4-CMPP); 2-(4-chlorophenoxy)-2-methylpropionic acid (CFA); 2-(4-chlorophenoxy)butanoic acid (4-CPB); 4-(4-chloro-2-methylphenoxy)butanoic acid (MCPB); and 2-(4-chloro-2-methylphenoxy)butanoic acid (4-CMPB).

The microporous activated carbon F300 was used as adsorbent ( $S_{BET} = 762 \text{ m}^2/\text{g}$ ,  $V_t = 0.46 \text{ cm}^3/\text{g}$ ,  $V_{mic} = 0.28 \text{ cm}^3/\text{g}$ ;  $pH_{pzc} \sim 9.8$ ). The characteristics of adsorbent are given in the paper [8]. The methodology of equilibrium and kinetic measurements is also described in the paper [8].

### 3. Results and discussion

#### 3.1 Adsorption equilibria

##### 3.1.1 Effect of type and number of adsorbate substituents

Substituents on benzene ring of aromatics have a great influence on adsorption process on activated carbon. It is not directly related to their interaction with an adsorbent but mainly with changes in molecular properties of adsorbed compound [19–23]. The crucial factors are the nature of the substituents, number, and their mutual position on benzene ring. In the study the adsorption process of compounds with substituents with electron-acceptor ( $\text{—Cl}$ ,  $\text{—Br}$ ) and electron-donor properties ( $\text{—CH}_3$ ) was analyzed. It is well known that substituents affect acid-base properties (pKa), water solubility, hydrophobicity ( $K_{ow}$ ), dipole moment, molecular weight, and spatial dimension in space of an organic compound. In turn, these properties affect a mechanism and a range of adsorption process. Nevertheless, solubility in water and hydrophobicity of substance most often play a superior role in adsorption process.

As pKa values of the studied pesticides are within the range of 1.50–3.70, thus, the buffers of pH = 1.81 or 10.38 were used to prepare the experimental solutions. Thus, the compounds in solutions were nearly undissociated and completely dissociated, respectively. In the case of the compounds of very low solubility, the studies at alkaline pH conditions were carried out. For the systems for which the adsorption process was carried out in acidic solutions, the isotherms both in the standard linear  $a = f(c_{eq})$  and reduced coordinates  $a = f(c_{eq}/c_s)$  are presented. The second form of presentation allows to study the affinity of a given type of compound to the activated carbon surface without the effect of solubility. In all the pictures, the experimental points and the theoretical isotherms using the generalized Langmuir equation are presented.

In **Figures 1** and **2** the comparison of the adsorption isotherms of chlorophenoxyacetic and chlorophenoxypropionic acid derivatives with a different type and number of substituents on aromatic ring on activated carbon F300 at pH = 1.81 is shown. In the case of phenoxyacetic pesticides, relatively small changes in capacities are observed which can be arranged as follows: 2,4-D  $\sim$  4-CPA > MCPA. The

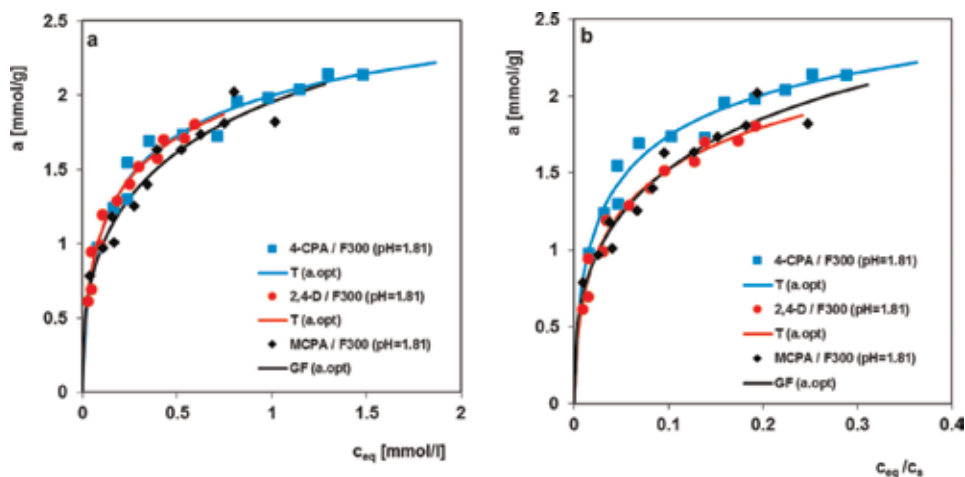


**Figure 1.** The 2,4-D; MCPA; and 4-CPA adsorption isotherms on F300, pH = 1.81 in linear (a) and reduced coordinate system (b).

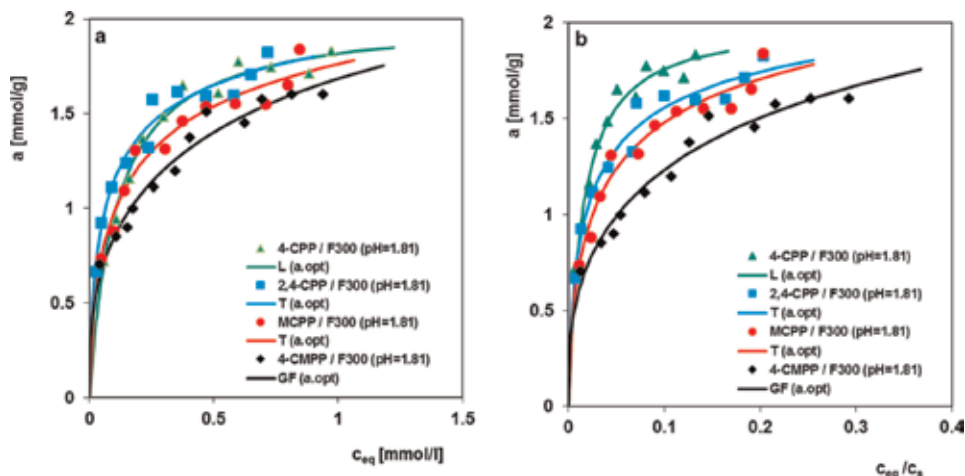


**Figure 2.**  
The 4-CPP; 2,4-CPP; MCPP; and 4-CMPP adsorption isotherms on F300, pH = 1.81 in linear (a) and reduced coordinate system (b).

differences in the course of adsorption isotherms for the phenoxypropionic pesticides are greater. Taking into account their affinity to the carbon F300, it looks as follows: 2,4-CPP  $\sim$  4-CPP > MCPP > 4-CMPP.

The solubility values were collected from literature, and partition coefficients between octane and water ( $K_{ow}$ ) were calculated using the Marvin 5.6.0.3 computer program taking into account conditions of adsorption process. For 2,4-D, 4-CPA, and MCPA, the solubilities are equal to 0.682, 0.957, and 0.825 g/dm<sup>3</sup> while log D 2.46, 1.88, and 2.40, respectively. For the phenoxypropionic derivatives, 2,4-CPP, 4-CPP, MCPP, and 4-CMPP, the solubilities are 0.829, 1.475, 0.895, and 0.69 g/dm<sup>3</sup>, while the values characterizing hydrophobicity are 3.04, 2.45, 2.97, and 2.97, respectively. As one can see, there is no correlation between solubility/hydrophobicity and the adsorption affinity for the most systems. Analyzing the adsorption isotherms reduced by the solubility parameter, it can be concluded that only in the case of 2,4-D and MCPA, the differences in adsorption result from solubility/hydrophobicity. For other systems, solubility/hydrophobicity is not the only factor determining the effectiveness of adsorption process, and other factors should be considered.

The mechanism of adsorption process is mainly based on the dispersion or donor-acceptor interactions (pH = 1.81, thus both adsorbates and functional groups on active carbon surface are undissociated) and the local repelling electrostatic interactions between positively charged sites on adsorbent surface (as a result of attraction and localization of graphene plane electrons by oxygen functional groups) and a local positive charge in adsorbate molecule (as a result of electron-acceptor properties of chlorine on benzene ring). Generally, the more substituents in a molecule, the greater the local charge and stronger the local electrostatic interactions.

Another aspect concerns a spatial structure of compounds, as the ones with substituents in a para-position have better access to adsorbent micropores. In particular, this applies for halogenophenoxyacetic acids, where the hydrocarbon part is not branched, like in  $\beta$ -halogenophenoxypropionic acids. Therefore, the capacities for 4-CPA and 2,4-D, as well as for 4-CPP and 2,4-CPP, are similar, although comparing the solubility and log D values, one could assume a different situation. A simple explanation is a symmetrical structure of 4-CPA, which means that its molecular volume is smaller than for 2,4-D which enables a better access and

greater packing density in the adsorptive space. In a group of phenoxypropionic acid derivatives, the 4-CPP and 2,4-CPP adsorptions are higher than for MCPA and 4-CMPP. The molecules of all these compounds have at least one  $\text{—Cl}$  group causing a weak deactivation of aromatic ring in the ortho- and para-position and strong deactivation in the meta-position. Consequently, the electron density of benzene ring is decreased, and the interactions of adsorbate-carbon surface are weakened. Moreover, MCPA and 4-CMPP molecules have additional  $\text{—CH}_3$  group that activates weakly aromatic ring in the ortho- and para-position, resulting in the electrons shift toward the ring. Thus, the interactions of adsorbate ring electrons with  $\pi$  electrons of adsorbent graphene planes are increased. The total effect is a result of at least partial compensation of two types of the functional groups. Therefore, the structural properties of these compounds do not explain clearly the differentiation of their adsorption affinities to activated carbon. An essential factor may be the influence of a position of the electron-acceptor group relative to the electron-donor group on the interactions of adsorbate-adsorbent as well as the steric effect.

In **Figure 3**, the comparison of the adsorption isotherms of chloro- and bromophenoxyacetic derivatives from solutions at  $\text{pH} = 10.38$  is presented. The adsorption decreases in the series: 2,4,6-BrPA > 2,4-BrPA > 2,4,6-CPA  $\sim$  2,4-D > 4-CPA > MCPA. At alkaline conditions the electrostatic interactions are predominant in adsorption mechanism due to dissociated forms of both the adsorbate and the adsorbent functional groups. The repulsive forces between the pesticide anions and negatively charged adsorbent groups appear. However, a halogen with the electron-withdrawing properties on benzene ring decreases the total electron charge of the aromatic ring and shows a local positive charge. The obtained effect results in the creation of local attractive interactions which decrease the electrostatic repulsion between adsorbate and adsorbent. If a degree of halogen substitution increases, the strength of interactions increases, and it leads to stronger adsorption on active carbon. This explanation is true if substituents in a molecule are of the same type, e.g., bromine or chlorine. Comparing the adsorption affinities in the systems with different substituents, it can be observed that the compounds containing bromine show a stronger affinity for the adsorbent surface compared to compounds with chlorine, regardless of a number of substituents in molecule. In the case of MCPA containing a methyl group with electron-donor properties, the weakest adsorption is observed. Increase of the electron density within aromatic ring raises the

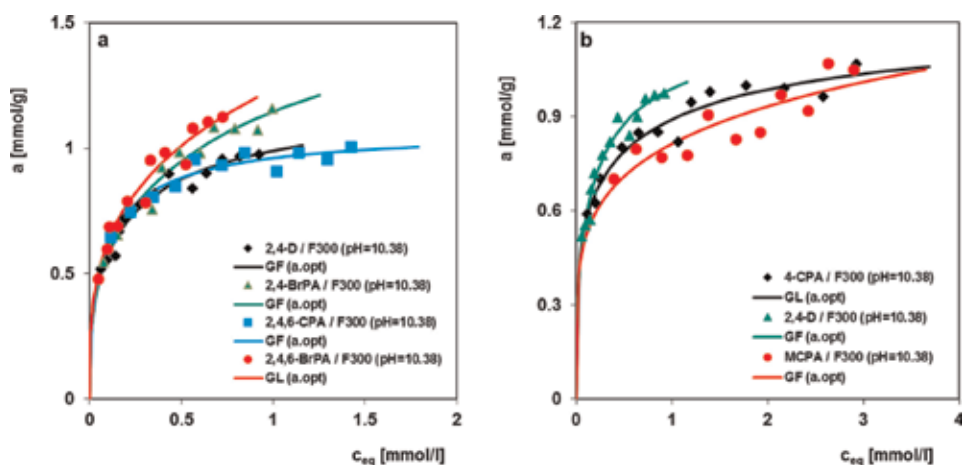


**Figure 3.** The 2,4-D; 2,4-BrPA; 2,4,6-CPA; and 2,4,6-BrPA adsorption isotherms on F300,  $\text{pH} = 10.38$  (a). The 4-CPA; 2,4-D; and MCPA adsorption isotherms on F300,  $\text{pH} = 10.38$  (b).

electrostatic repulsion with the negatively charged surface of the activated carbon. A similar effect is observed in the case of phenoxypropionic acid derivatives with a different halogen substituent in the para-position at acidic pH.

In **Figure 4a** a comparison of the adsorption isotherms for 2,4-D, 2,4,5-CPA, and 2,4,6-CPA, i.e., the compounds with a differentiated number and position of chlorine atoms on benzene ring, is presented. Similar adsorption is observed for 2,4-D and 2,4,6-CPA, whereas for 2,4,5-CPA the process is significantly greater. 2,4-D shows the weakest hydrophobic properties; its molecule contains two chlorine atoms. The other two compounds 2,4,5-CPA and 2,4,6-CPA are characterized by the similar log D values, but they contain three chlorine atoms. Therefore, the differences in adsorption affinity to adsorbent should be attributed to the steric effect. In the group of chlorophenoxypropionic acids differentiated in terms of a number of substituents in a molecule, the adsorbate affinity to the adsorbent active sites increases in the order 2,4,5-CPP > 2,4-CPP > 2,5-CPP > 4-CPP (**Figure 4b**). The octanol/water partition coefficient values (log D) for these compounds at pH = 10.38 are 0.15, -0.46, -0.46, and -1.06, respectively. 2,5-CPP is weakly removed at a given pH than its isomeric form 2,4-CPP although its hydrophobicity should promote the adsorption process. Probably an arrangement of the substituents in 2,5-CPP leads to difficulties in diffusion of the adsorbate molecules into small pores of adsorbent that consequently decreases adsorption.

The comparison of the 4-CMPA and 4-CPA (pH = 10.38) adsorption isotherms (**Figure 5**) shows that removal of the methyl group weakens the adsorption affinity. Similar behavior occurs for their phenoxypropionic and phenoxybutanoic homologs, for which the adsorption of 4-CMPP > 4-CPP and 4-CMPB > 4-CPB (**Figures 6 and 7**). The observed trend fully coincides with the hydrophobicity of pesticides. For the series of 4-CMPA and 4-CPA, log D is -1.12 and -1.63, respectively; for 4-CMPP and 4-CPP, log D is equal to -0.55 and -1.06, respectively, while for 4-CMPB and 4-CPB, this parameter is -0.03 and -0.54, respectively.

### 3.1.2 Effect of substituent position on aromatic ring

The adsorption affinity of organics depends on a number and type of substituents, as well as on their position on the benzene ring. This is related to the occurrence of the steric and inductive effects of adsorbate. The courses of adsorption

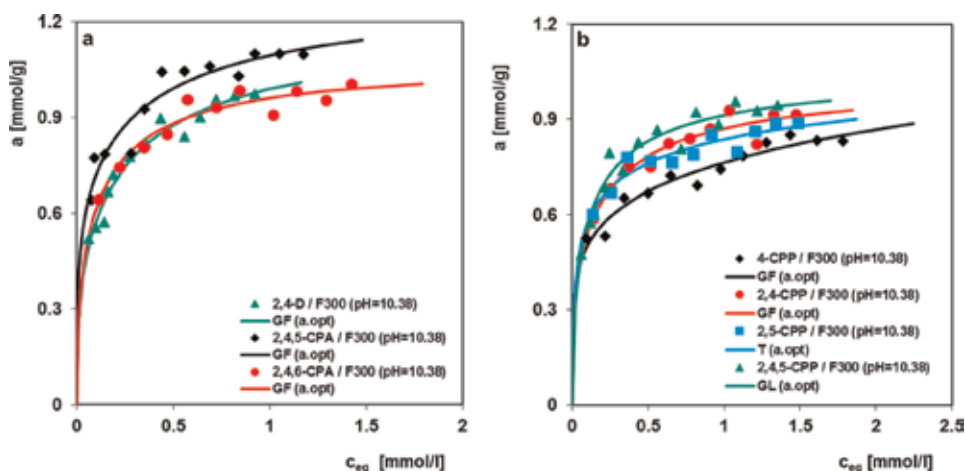


**Figure 4.** The 2,4-D; 2,4,5-CPA; and 2,4,6-CPA adsorption isotherms on F300, pH = 10.38 (a). The 4-CPP; 2,4-CPP; 2,5-CPP; and 2,4,5-CPP adsorption isotherms on F300, pH = 10.38 (b).

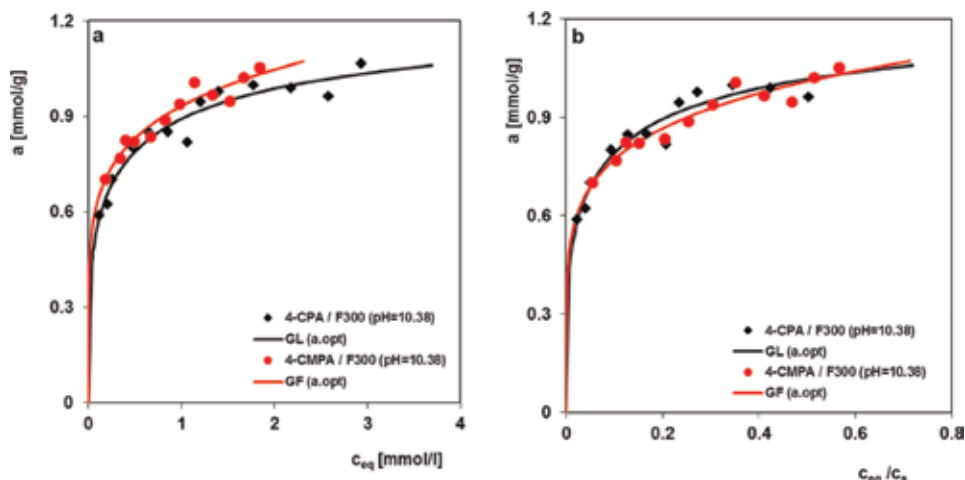


**Figure 5.** The 4-CPA and 4-CMPA adsorption isotherms on F300,  $pH = 10.38$  in linear (a) and reduced coordinate system (b).

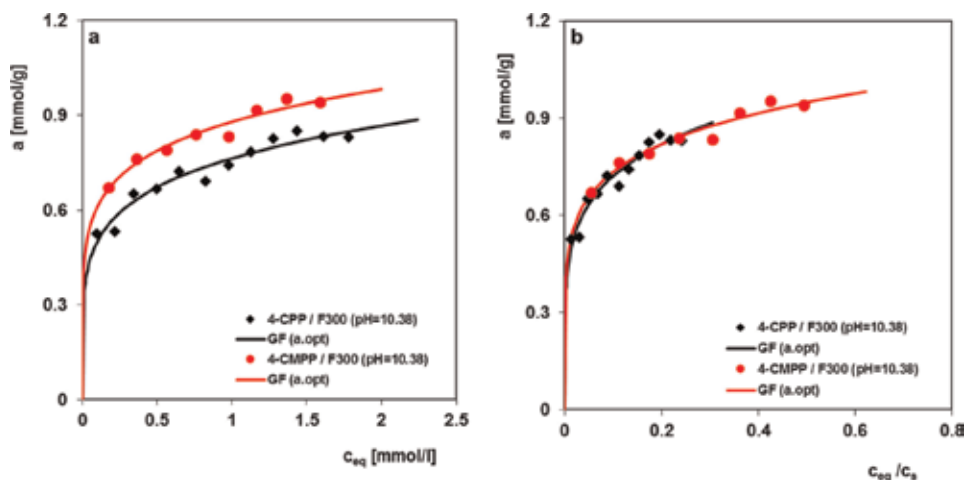


**Figure 6.** The 4-CPP and 4-CMPP adsorption isotherms on F300,  $pH = 10.38$  in linear (a) and reduced coordinate system (b).

isotherms measured at alkaline pH for 2,4,5-CPA and 2,4,6-CPA (**Figure 8**) and 2,4-CPP and 2,5-CPP (**Figure 9a**) indicate that the less symmetric distribution of electron charge density in benzene ring is, the stronger adsorption affinity is observed. Therefore, higher affinities for 2,4,5-CPA and 2,4-CPP than for 2,4,6-CPA and 2,5-CPP are found. Analyzing the solubility of these substances, one can say that this parameter is not a main factor controlling the adsorption process.

As results from **Figure 9b** at basic conditions for the isomers of dichlorophenoxypropionic acid, their affinity to the activated carbon increases as follows: 3,4-CPP > 2,4-CPP > 2,5-CPP. The strongly adsorbed compound is characterized by two adjacent chlorine atoms with electron-acceptor properties, causing the overlap of local positive charges in the benzene ring. The negatively charged oxygen groups on the carbon surface interact electrostatically with the positive local charge of the pesticide rings, intensifying the adsorption process. The interactions of other compounds with F300 are disturbed by the steric effect due to the position of



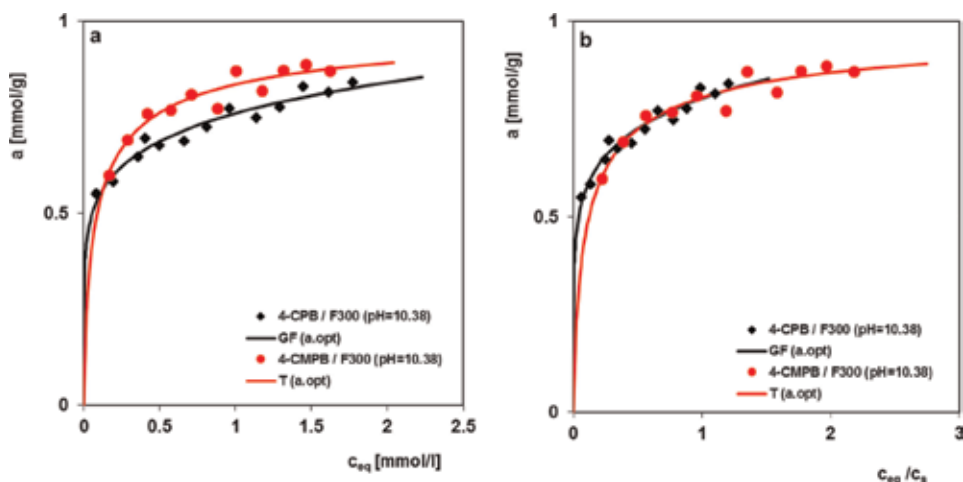


**Figure 7.**  
The 4-CPB and 4-CMPB adsorption isotherms on F300, pH = 10.38 in linear (a) and reduced coordinate system (b).

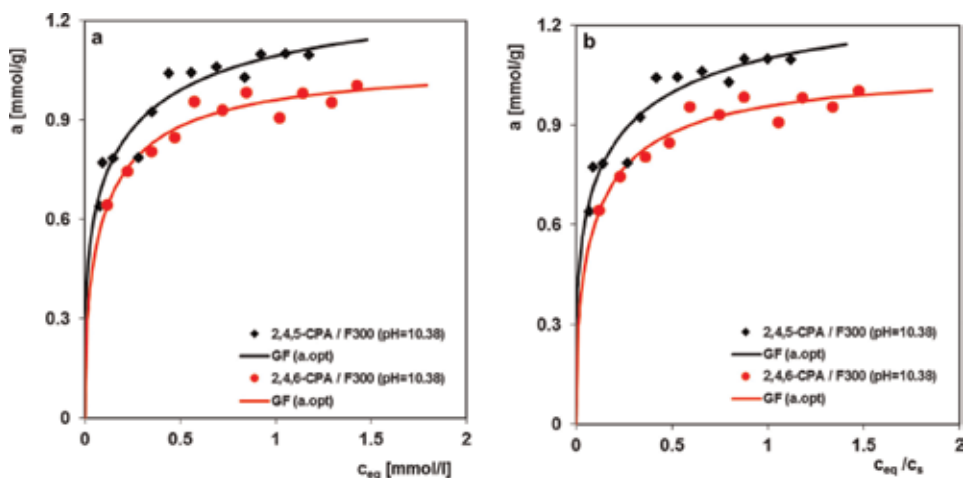


**Figure 8.**  
The 2,4,5-CPA and 2,4,6-CPA adsorption isotherms on F300, pH = 10.38 in linear (a) and reduced coordinate system (b).

substituent at the second carbon in the ring and in the case of 2,5-CPP additionally due to a symmetrical distribution of the  $\sigma^+$  charge. This explains the differentiation in adsorption of these compounds.

The comparison of the isotherms for 4-CMPP and MCPB at alkaline pH (**Figure 10a**) gives information that a shift of methyl group position on aromatic ring from ortho- to meta-position does not affect adsorption process. The same situation is observed for their homologs from the phenoxybutanoic group; the adsorption affinity of both compounds to activated carbon is similar (**Figure 10b**).

### 3.1.3 Effect of structure of hydrocarbon chain in adsorbate molecule

To analyze the impact of hydrocarbon chain structure on the adsorption process, the systems with chlorogenic phenoxyacetic derivatives and their homologs—phenoxypropionic and phenoxybutanoic derivatives—were studied. The graphs are grouped with regard to hydrocarbon chain structure, while the aromatic part of

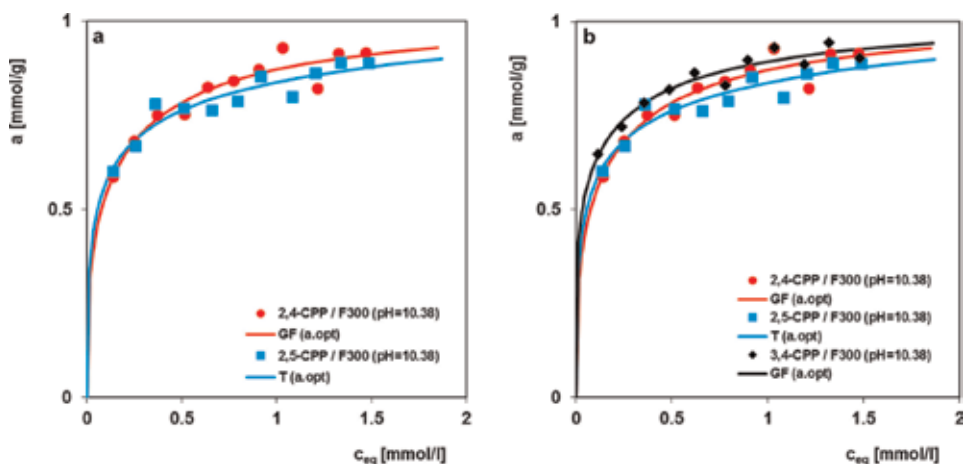


**Figure 9.** The 2,4-CPP and 2,5-CPP adsorption isotherms on F300,  $pH = 10.38$  (a). The 2,4-CPP; 2,5-CPP; and 3,4-CPP adsorption isotherms on F300,  $pH = 10.38$  (b).

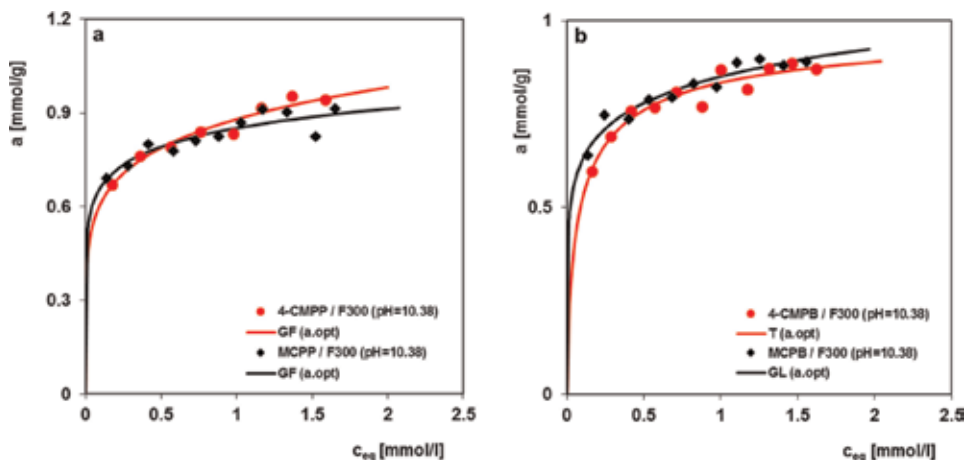


**Figure 10.** The 4-CMPP and MCPB adsorption isotherms on F300,  $pH = 10.38$  (a). The 4-CMPB and MCPB adsorption isotherms on F300,  $pH = 10.38$  (b).

molecules is the same. In the case of adsorption processes carried out at  $pH = 10.38$ , the adsorption affinities of the studied compounds are as follows: 2,4,5-CPA > 2,4,5-CPP (**Figure 11a**), 2,4-D > 2,4-CPP (**Figure 11b**), MCPB ~ MCPB (**Figure 12a**), 4-CMPA > 4-CMPP > 4-CMPB (**Figure 12b**), and 4-CPA > 4-CP > 4-CPP ~ 4-CPB > CFA (**Figure 13**). For the systems for which it was possible to measure the adsorption process at  $pH = 1.81$ , the adsorption affinities of pesticides are 2,4-D ~ 2,4-CPP (**Figure 14**), MCPA > MCPB (**Figure 15**), and 4-CPA > 4-CPP > CFA (**Figure 16**).

Analyzing the coefficient  $K_{o/w}$  values, one can say that the adsorption mechanism is more dependent on physicochemical properties of the adsorbates related with their spatial structure of hydrocarbon part rather than on the total hydrophobicity. For example, in the case of pesticides with decreasing adsorptive affinity to activated carbon, 4-CPA, 4-CPP, and CFA at  $pH = 1.81$ ,  $\log D$  is  $-1.12 < -0.55 < -0.03$ . Relatively smaller influence of the hydrophobicity of these compounds on their adsorption process is confirmed in most cases by the adsorption isotherm course in the reduced coordinates. The above hypothesis is focused on two factors

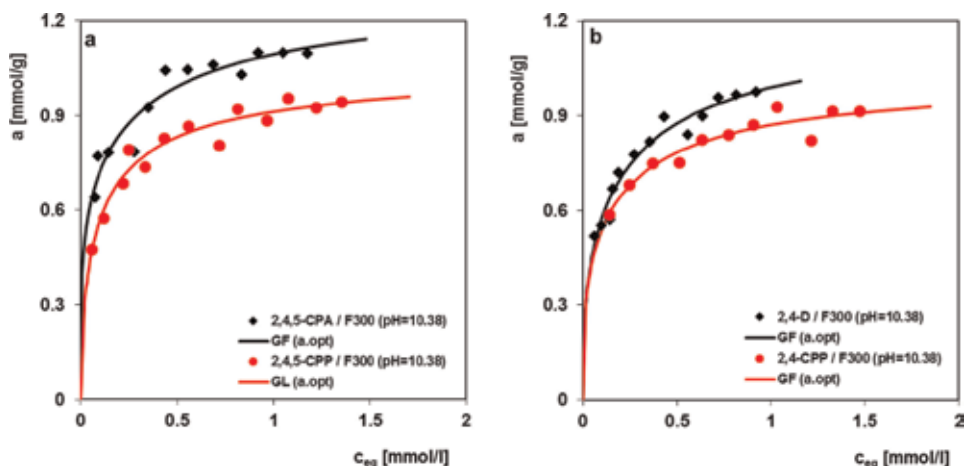


**Figure 11.** The 2,4,5 CPA and 2,4,5-CPP adsorption isotherms on F300, pH = 10.38 (a). The 2,4-D and 2,4-CPP adsorption isotherms on F300, pH = 10.38 (b).

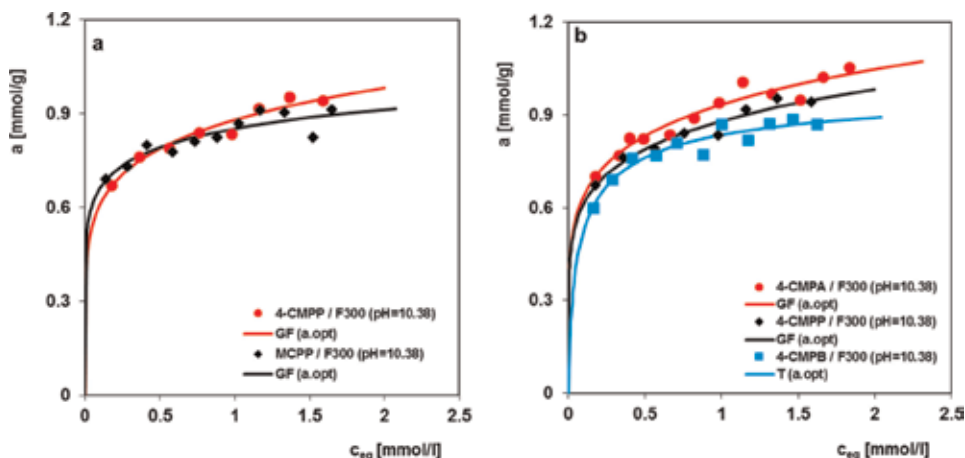


**Figure 12.** The MCPP and MCPB adsorption isotherms on F300, pH = 10.38 (a). The 4-CMPA; 4-CMPP; and 4-CMPB adsorption isotherms on F300, pH = 10.38 (b).

related with a hydrocarbon chain structure of halogen phenoxyacetic derivatives: a number of carbons forming a hydrocarbon chain and arrangement of carbons in a chain. Considerations on adsorption of the pesticides with different number of aliphatic carbon atoms are concerned on phenoxyacetic, phenoxypropionic, and phenoxybutanoic derivatives. In the case of phenoxypropionic and phenoxybutanoic derivatives, the hydrocarbon parts form branched chains. Merely 4-CP has an unbranched chain. 4-CP and its phenoxyacetic homolog 4-CPA were used to compare the adsorption affinity of adsorbates with unbranched hydrocarbon chain (**Figure 13a**). The other compounds which form the homologous series were used to analyze the adsorption of molecules with different number of carbons in a branched aliphatic chain. On the basis of adsorption isotherms of the abovementioned pesticides, one can conclude that a number of carbon atoms in unbranched hydrocarbon chain do not affect the adsorbate affinity to the activated carbon surface. The increase of a number of carbon atoms in branched hydrocarbon chain for the most homologous series results in a decrease in adsorption or occasionally does not affect it at all. These

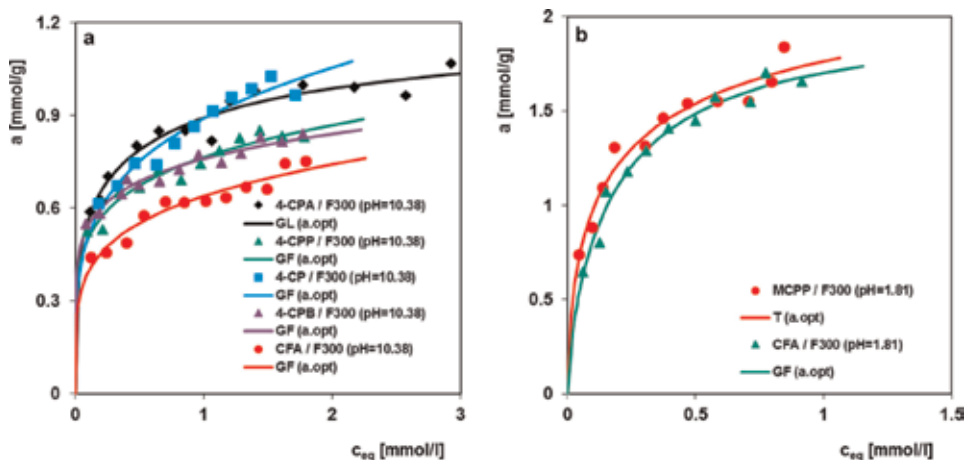


**Figure 13.** The 4-CPA; 4-CPP; 4-CP; 4-CPB; and CFA adsorption isotherms on F300, pH = 10.38 (a). The MCPP and CFA adsorption isotherms on F300, pH = 1.81 (b).

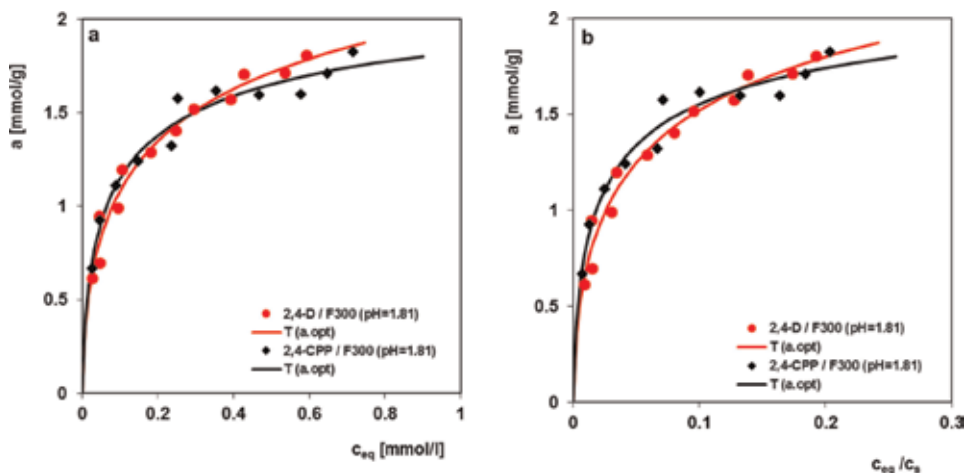


**Figure 14.** The 2,4-D and 2,4-CPP adsorption isotherms on F300, pH = 1.81 in linear (a) and reduced coordinate system (b).

observations apply to the adsorption systems studied at acidic and basic conditions. According to the Lundelius principle, the more developed structure of compounds from the same homologous series, the greater adsorption should occur [16]. The lack of compliance of the obtained results with the Lundelius principle indicates that there are also other factors. The adsorbent is characterized by a microporous structure with the highest contribution of pores with a diameter of 4.5–9 Å. Minimal diameter of the compounds calculated using the Marvin Space 5.6.0.3 program is in the range of 4.33–6.36 Å, while their maximal diameter is in the range of 7–9.87 Å. Thus, smaller adsorbent micropores may have been inaccessible especially for the homologs with the highest molecular sizes. CFA and 4-CPB are hydrocarbon chain isomers (**Figure 13a**), and they differ in an order of the respective aliphatic carbon atoms. This in turn is related with the differences in spatial structure of the molecules. Adsorption capacity for 4-CPB is higher than for CFA, which results from stronger adsorption of the substance with less branched aliphatic part. The comparison of the 4-CP and 4-CPP adsorption (**Figure 13**) confirms the thesis that

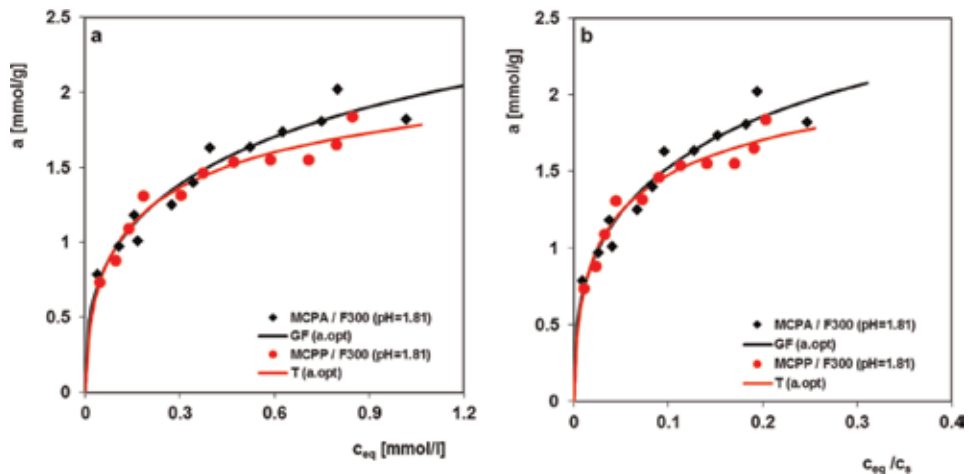


**Figure 15.**  
 The MCPA and MCPP adsorption isotherms on F300, pH = 1.81 in linear (a) and reduced coordinate system (b).

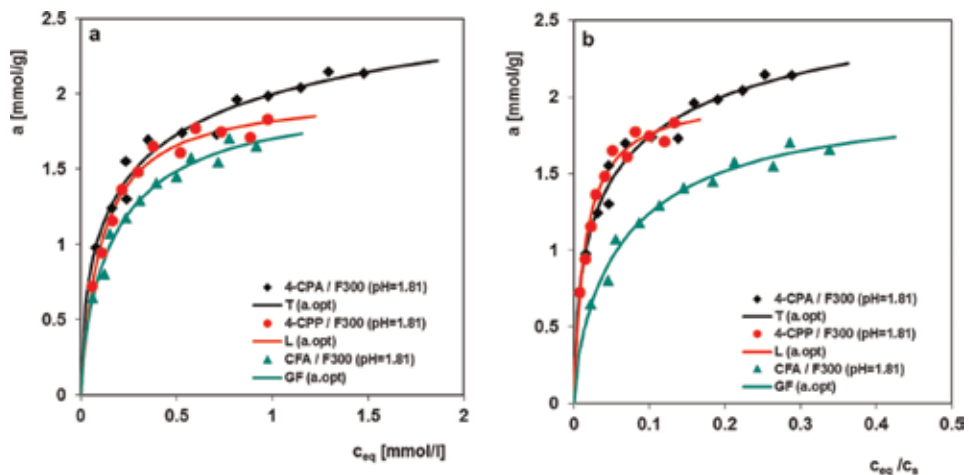


**Figure 16.**  
 The 4-CPA, 4-CPP, and CFA adsorption isotherms on F300, pH = 1.81 in linear (a) and reduced coordinate system (b).

hydrocarbon part linearity enables better adsorption. Linearity of the compound structure is related with poorer solubility compared to its branched isomer. Therefore, stronger adsorption of 4-CP compared to 4-CPP is mainly due to their solubility differentiation as evidenced by the overlapping isotherms in the reduced coordinates. Among the pesticides there are also structural isomers differentiated with regard to both phenolic and hydrocarbon part. This applies to CFA and MCPP for which the CFA adsorption is weaker (**Figure 13b**). The isopropyl group as the side branch of hydrocarbon chain has decisive influence on limiting the adsorbate-adsorbent interactions.

### 3.2 Analysis of experimental isotherms by means of the GL isotherm

All the studied experimental systems were analyzed by the generalized Langmuir isotherm equation (GL) [24–26] that for the specific values of heterogeneity parameters are reduced to four equations: Langmuir (L,  $m = n = 1$ ), Langmuir-

Freundlich (LF,  $0 < m = n \leq 1$ ), generalized Freundlich (GF,  $0 < m \leq 1, n = 1$ ), and Tóth isotherm (T,  $m = 1, 0 < n \leq 1$ ). These isotherms were obtained from the global integral equation assuming that the Langmuir isotherm is a local one. In the optimization procedure, a method of the minimal sum of square deviations of adsorption values was used assuming the limitation of adsorption capacity ( $a_m \leq 20$  mmol/g) and the equilibrium constant  $K$  ( $K \leq 10^5$  l/mmol). **Table 2** presents the parameters of this equation, the correlation coefficients  $R^2$ , and standard deviations  $SD(a)$ .

The parameters for two systems correspond to the simple L isotherm equation which is characteristic for energetically homogeneous system. For the other

System, pH (type of isotherm)	$a_m$	$m$	$n$	$\log K$	$R^2$	$SD(a)$
4-CPA/F300, pH 1.81 (T)	3.34	1	0.40	1.59	0.957	0.087
4-CPA/F300, pH 10.38 (GL)	1.25	0.25	0.78	-0.35	0.940	0.043
2,4-D/F300, pH 1.81 (T)	3.69	1	0.35	1.81	0.968	0.079
2,4-D/F300, pH 10.38 (GF)	1.19	0.35	1	0.14	0.960	0.035
2,4,5-CPA/F300, pH 10.38 (GF)	1.29	0.25	1	0.01	0.907	0.054
2,4,6-CPA/F300, pH 10.38 (GF)	1.07	0.38	1	0.46	0.923	0.036
4-CMPA/F300, pH 10.38 (GF)	15.11	0.17	1	-7.25	0.936	0.030
MCPA/F300, pH 1.81 (GF)	3.09	0.34	1	-0.45	0.937	0.110
MCPA/F300, pH 10.38 (GF)	20	0.20	1	-7.04	0.766	0.064
2,4-BrPA/F300, pH 10.38 (GF)	1.83	0.33	1	-0.49	0.957	0.046
2,4,6-BrPA/F300, pH 10.38 (GL)	20	0.32	0.29	-3.71	0.949	0.056
3-CPP/F300, pH 1.81 (L)	1.92	1	1	0.93	0.948	0.082
4-CP/F300, pH 10.38 (GF)	20	0.24	1	-5.53	0.955	0.033
4-CPP/F300, pH 1.81 (L)	2.02	1	1	0.96	0.977	0.058
4-CPP/F300, pH 10.38 (GF)	20	0.18	1	-7.73	0.939	0.031
2,4-CPP/F300, pH 1.81 (T)	2.41	1	0.48	1.79	0.96	0.081
2,4-CPP/F300, pH 10.38 (GF)	1.02	0.32	1	0.181	0.916	0.035
2,5-CPP/F300, pH 10.38 (T)	1.32	1	0.29	2.94	0.896	0.032
3,4-CPP/F300, pH 10.38 (GF)	1.03	0.22	1	0.05	0.937	0.026
2,4,5-CPP/F300, pH 10.38 (GL)	1.07	0.56	0.75	0.83	0.942	0.041
MCPP/F300, pH 1.81 (T)	2.83	1	0.40	1.67	0.951	0.083
MCPP/F300, pH 10.38 (GF)	1.12	0.11	1	-1	0.822	0.034
4-CMPP/F300, pH 1.81 (GF)	2.60	0.34	1	-0.41	0.961	0.070
4-CMPP/F300, pH 10.38 (GF)	12.90	0.16	1	-7.35	0.949	0.026
CFA/F300, pH 1.81 (GF)	2.02	0.66	1	0.53	0.995	0.061
CFA/F300, pH 10.38 (GF)	20	0.21	1	-7.03	0.928	0.030
4-CPB/F300, pH 10.38 (GF)	10.42	0.15	1	-7.81	0.952	0.022
MCPB/F300, pH 10.38 (GL)	4.65	0.45	0.08	5	0.934	0.025
4-CMPB/F300, pH 10.38 (T)	1.02	1	0.59	1.54	0.923	0.027

**Table 2.**

*Values of parameters of the generalized Langmuir equation characterizing the experimental systems.*

systems, satisfying optimization using the T and GF equations or the general form of the GL isotherm was obtained. The GL equation corresponds to the quasi-Gaussian function of adsorption energy distribution; the heterogeneity parameters characterize the extension of this function toward the higher ( $m < 1$ ) and lower ( $n < 1$ ) adsorption energies (if  $m \neq n$ , the energy distribution is asymmetrical,  $m$  the smaller and  $n$  the greater heterogeneity). The Tóth equation is represented by the asymmetrical quasi-Gaussian function of the adsorption energy that is extended toward low energies, whereas the GF isotherm corresponds to the exponential function with the characteristic minimal energy. The applied equations show slightly different behavior in the area of low and high adsorption. For low concentrations, only the T isotherm reduces itself to the Henry's equation, while the other isotherms to the classic Freundlich equation. In the range of high concentrations, all the equations show typical Langmuir behavior; however, the GF equation reaches the maximum adsorption most quickly. For many experimental systems, in limited ranges of concentration and adsorption, various types of isotherms may exhibit similar behavior; hence, they can describe the same data well. Unequivocal selection of the model can be made on the basis of precise experimental data in a wide range of concentrations and adsorptions (required range depends on the system heterogeneity). In the case of experimental systems, the choice of theoretical adsorption isotherm should be considered as approximate one because it is based on the standard deviation values obtained in the optimization procedure within a limited measurement range and with relatively large scattering of experimental points (adsorbent inhomogeneity).

Analyzing the heterogeneity parameters which characterize the experimental systems, one can conclude that in most cases they achieve values much lower than one. It indicates a significant impact of the energetic heterogeneity. Attention should be paid to high values of the adsorption capacity for several experimental systems. In the case of experimental isotherms with a narrow range of relative adsorption  $\theta$ , the adsorption optimization method by using the adsorption capacity limit (20 mmol/g—reaching this value or even a lower value of 10 mmol/l indicates that the determined capacity is unrealistic; consequently the value of the constant  $K$  is not also reliable) leads to the achievement of minimal  $SD$  for high values of the parameter  $a_m$ . The best results for the generalized Freundlich isotherm were obtained due to the specific features of this equation. **Figure 17** presents the results of model calculations for dependence of the isotherm slope in logarithmic coordinates ( $\varphi = \ln a / \ln \theta$ ) as a function of the surface coverage  $\theta$  for the GL and GF equations. For the GL equation, it can be described [25, 26] as

$$\varphi = \frac{d \ln a}{d \ln c_{eq}} = \frac{m}{1 + (Kc)^n} = m \left( 1 - \theta^{n/m} \right) \quad (1)$$

Analyzing the calculated curves, one can observe the different nature of the GF equation in relation to the other isotherms being special cases of the GL isotherm. For the LF equation ( $m = n = 0.5$ ), the slope  $\varphi$  is always a linear function of the relative adsorption (**Figure 17a**); for other types of GL isotherm, a shift of the slope always takes place at lower values of the coverage than for GF. The GF equation shows the weakest initial slope of the dependence  $\varphi$  on the coverage. Additionally, the stability ranges of slope  $\varphi$  strongly depend on a value of the heterogeneity parameter  $m$ ; for the systems with high heterogeneity ( $m = 0.2$ ), this area clearly increases (**Figure 17b**). In particular, for  $m = 0.2$  the slope remains almost constant—a decrease of 5% occurs until relative adsorption of 0.55 is achieved, while for  $\theta < 0.4$  a shift of the slope does not exceed 1%.

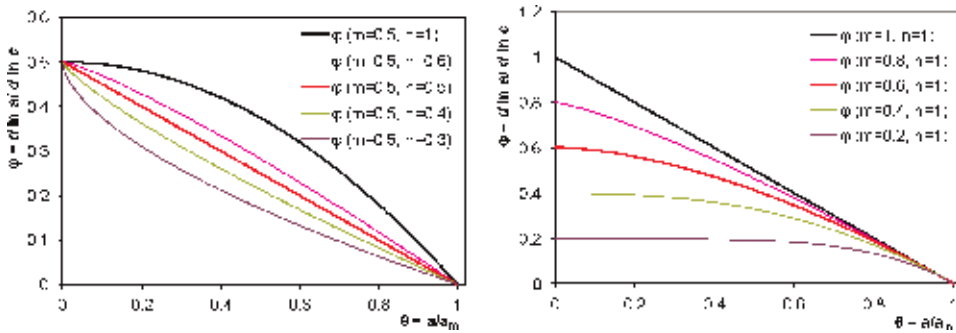


**Figure 17.** Model dependencies of the adsorption isotherm slope in logarithmic coordinates,  $\varphi = \ln a / \ln \theta$ , as a function of surface coverage  $\theta$  for the GL (left side) and GF (right side) equations for various values of the heterogeneity parameters  $m$  and  $n$ .

The above observations are confirmed by the results of model calculations presented in **Figure 18** as the dependences of relative slope  $\varphi / \varphi_{\theta=0}$  as a function of surface coverage  $\theta$  for the GL type equation and the dependences of surface coverage  $\theta$  corresponding to the specific relative slope  $\varphi$ . A distinguish type of variability of these dependences for the GF equation is observed in comparison to the other GL isotherms. It means that in the case of GF isotherm a widest range of the steady slope  $\varphi$  corresponding de facto the Freundlich isotherm is followed by a rapid change of isotherm character into a typical isotherm with the adsorption *plateau*. Many of the experimental systems exhibit typical behavior for the Freundlich isotherm—despite existence of the adsorption limitations (due to the limited pore volume). This behavior perfectly explains the above analysis. Other factors affecting such behavior comprise a multilayered nature of some isotherms and intermolecular interactions in the surface phase (it can lead to the increase of the linearity range  $\varphi$ —especially for the LF or Tóth isotherms) [26].

Referring to a general problem of accuracy of the determination of adsorption isotherm parameters, it should be emphasized that a key problem is to determine the adsorption capacity  $a_m$  that for every optimization is in fact the extrapolated value and as a result the most susceptible to error. Simultaneously, the error in  $a_m$  determination is transferred to other parameters. For the experimental data in a range of low adsorption, it is possible to achieve a relatively high accuracy of determination of the heterogeneity parameter  $m$  and the aggregated value (corresponding to an adsorption coefficient in the Freundlich equation),  $\ln k_F \approx m$

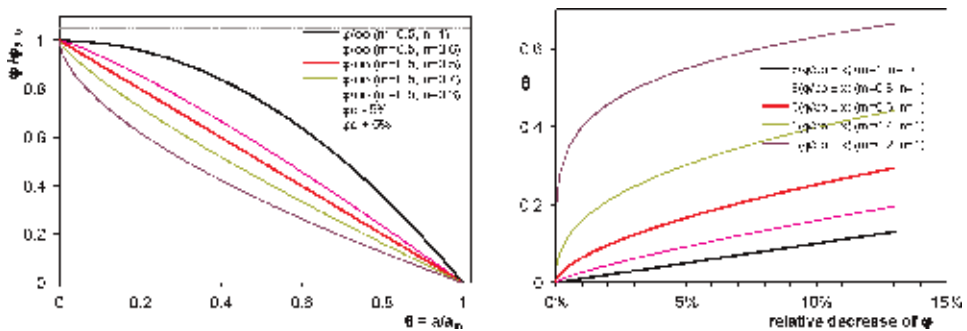


**Figure 18.** Model dependences of relative slope  $\varphi / \varphi_{\theta=0}$  as a function of surface coverage  $\theta$  for the GL equation at various values of heterogeneity parameters  $m$  and  $n$  (left side, the deviations  $\varphi \pm 5\%$  are marked) and model dependences of the surface coverage  $\theta$  corresponding to relative shift of slope  $\varphi$  for the GF equation (right side).



$\ln K + \ln a_m$ . Unfortunately, the accuracy of determination of the adsorption equilibrium constant  $\ln K$  depends not only on  $\ln a_m$  but also on a value of  $m$  (error of  $a_m$  determination increases for small  $m$  because  $\ln K = [(m \ln K + \ln a_m) - \ln a_m]/m$ ). When the adsorption data can be described well by the Freundlich isotherm (no systematic deviations from linearity in the logarithmic coordinates), this means that there are not points in the experimental data from which a reliable value  $a_m$  could be calculated. It would be possible only if the experimental isotherm shows a change of the slope in the logarithmic coordinates. On the other hand, a greater accuracy of the determination of the adsorption capacity  $a_m$  and heterogeneity parameter  $n$  can be obtained mainly for the data in a range of high adsorption.

It should be stated that a fully reliable optimization of the theoretical model can be obtained if the experimental data are distributed evenly in a range of both low and high concentration/adsorption regions. It is important that the range of relative adsorption is symmetrical in relation to  $\theta = 0.5$  (e.g., from the point of view of isotherm parameter analysis, the range  $\theta = 0.1-0.9$  is much better than  $0.01-0.1$  or  $0.9-0.99$ ). Unfortunately, the measurements in both ranges are burdened with a relatively large experimental errors—for low concentrations a problem is related to the apparatus quality (e.g., the signal noises), and for high ones, the main barrier is a necessity of dilution preparation (or necessity of changing the measurement method) and slight changes in solution concentration due to adsorption near to a saturation point of the surface phase with the adsorbate.

### 3.3 Adsorption kinetics

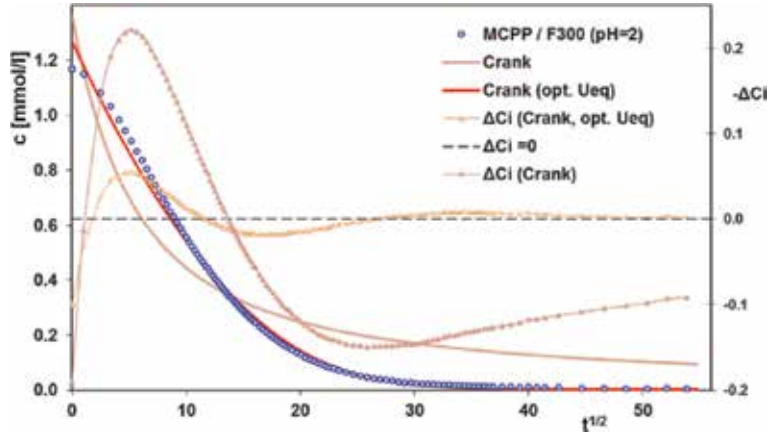
In order to investigate an effect of the adsorbate properties on adsorption rate, the measurements of adsorption kinetics for selected systems were conducted. As the activated carbon is characterized by high porosity, it seemed reasonable to include diffusion effects in a kinetic description. The Crank model (intraparticle diffusion model) in a standard form as well as in a simplified one is a fundamental model of intraparticle diffusion process. The full IDM model takes into account the changes of adsorbate concentration during adsorption process and a spherical shape of adsorbent particles with a radius  $r$  [27]:

$$F = 1 - 6 \cdot (1 - u_{eq}) \sum_{n=1}^{\infty} \frac{\exp(-p_n^2 \cdot \frac{D_t}{r^2})}{9 \cdot u_{eq} + (1 - u_{eq})^2 \cdot p_n^2}, \tan p_n = \frac{3p_n}{\left[3 + \left(\frac{1}{u_{eq}} - 1\right)p_n^2\right]} \quad (2)$$

where  $u_{eq}$  is the relative adsorbate uptake at equilibrium,  $F$  is the adsorption progress,  $p_n$  is the non-zero roots of  $\tan p_n$  function,  $D$  is the effective diffusion coefficient, and  $r$  is the adsorbent particle radius.

However, for the analyzed experimental kinetics, the full IDM equation describes the data very poorly (the curves and points are marked as “Crank” in **Figure 19**). The Crank model analysis for MCPP/F300 at pH = 2 was chosen and presented as representative for all experimental systems; the quality of optimization of all of them was very similar. If effective concentration of the adsorbate in a surface layer is different than in a volume phase, it can be assumed that  $u_{eq}$  is also a fitting parameter. If concentration during adsorption process remains almost constant,  $u_{eq}$  is close to 0, and then one gets a simplified form of the Crank model [8, 28–30]:

$$F = 1 - \frac{6}{\pi^2} \sum_{n=1}^{\infty} \frac{1}{n^2} \exp\left(\frac{-\pi^2 n^2 D t}{r^2}\right) \quad (3)$$


**Figure 19.**

The comparison of the optimization using the Crank model (Crank) and the optimization neglecting a relation of a parameter  $u_{eq}$  of the Crank model with concentration change during adsorption process (Crank, opt.  $U_{eq}$ ) for the MCPP adsorption data on F300 at pH = 2. The figure shows deviations for both optimizations (triangles).

As one can see, the adsorption data can be described quite satisfactorily by using the simplified form of Crank model. It should be assumed that as a result of the rapid initial adsorption stage, the outer part of the granules becomes an adsorbate reservoir providing constant conditions for adsorbate penetration inside the granules. The standard deviation of concentration for the simplified Crank model decreased 3–5 times compared to the full IDM model. In turn, the obtained values of parameter  $D/r^2$  of the order  $10^{-3}$ – $10^{-5}$  are acceptable, while those determined on the basis of the full model IDM were unsatisfactory. Nevertheless, nonlinearity of experimental data in the initial range in  $c \sim t^{1/2}$  coordinates (linearity is the fundamental assumption of all variants of the Crank model) proves that this model is not suitable for the description of the adsorption process for the studied systems

In practice, a somewhat better choice was the McKay model (pore diffusion model) [31]. It additionally takes into account a resistance during adsorbate transfer through adsorbent surface layer and assumes that the adsorbate evenly penetrates the granules, and a clear boundary between an area in which adsorption equilibrium is established, and the one without adsorbate is formed:

$$\frac{dF}{d\tau_s} = \frac{3(1 - u_{eq} \cdot F) \cdot (1 - F)^{\frac{1}{3}}}{1 - B \cdot (1 - F)^{\frac{1}{3}}} = \frac{3x[1 - u_{eq}(1 - x^3)]}{1 - Bx} \quad (4)$$

$$\tau_s u_{eq} = \frac{1}{6} \left\{ \left( 2B - \frac{1}{X} \right) \cdot \ln \left[ \frac{x^3 + X^3}{1 + X^3} \right] + \frac{3}{X} \ln \left[ \frac{x + X}{1 + X} \right] \right\} + \frac{1}{X \cdot \sqrt{3}} \cdot \left\{ \arctan \left( \frac{2 - X}{X \cdot \sqrt{3}} \right) - \arctan \left( \frac{2 \cdot x - X}{X \cdot \sqrt{3}} \right) \right\} \quad (5)$$

Here,  $x=(1-F)^{\frac{1}{3}}$  is an auxiliary variable;  $X=\left(\frac{1}{1-u_{eq}}\right)^{\frac{1}{3}}$  is the parameter; and  $B = 1 - B_i$ ,  $B_i$  is the Biot number, where  $B_i = K_f r / D_p$ ,  $K_f$  is the external mass transfer coefficient,  $D_p$ , is the effective pore diffusion coefficient, and  $\tau_s$  is the dimensionless model time, where  $\tau_s = c_0 / (\rho_t a_{eq}) \cdot (D_p / r^2) \cdot t$  and  $\rho_t$  is the particle density.

As shown in **Figure 20**, the McKay model describes quite well the kinetics of experimental systems in the initial range, and it does not exhibit the same feature as the IDM model. The initial part of curve is a characteristic for typical adsorption

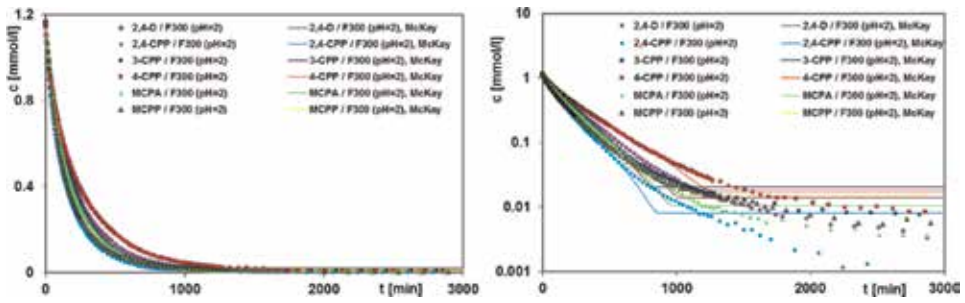


**Figure 20.** Comparison of the optimization procedure using the McKay model to the adsorption pesticides data on F300 at  $pH = 2$ .

systems. However, in the subsequent stage of experiment, one can see significant discrepancies between the model and data, because this model predicts that the system comes to equilibrium after a finite time (curve bend corresponds to reaching the equilibrium state). It is reflected in the increase of the standard deviations with time, inversely to the IDM model. It should be added that obtaining an acceptable optimization using the McKay model was associated with treating a parameter  $u_{eq}$  (total adsorbate loss from solution) as the optimized parameter regardless of equilibrium concentration, the same assumption as for the simplified Crank model.

Very good results in the analysis of the kinetic data were obtained for the multi-exponential equation (**Figure 21**). This equation describes kinetics as an independent parallel series of first-order processes or approximation of follow-up processes [8, 32–34]. Generally, the multi-exponential equation characterizes well enough the experimental systems with a heterogenous pore structure or a complex pore system with differentiated pore distribution. A mathematical form of the multi-exponential equation is as follows:

$$F = 1 - \sum_{i=1}^n f_i \exp(-k_i t), \quad \sum_{i=1}^n f_i = 1 \quad (6)$$

where  $n$  is the number of exponential terms and the coefficient  $f_i$  ( $i = 1, 2, \dots, n$ ) is the fraction of adsorbed equilibrium amount corresponding to the adsorption process characterized by the rate coefficient  $k_i$ .

Both the experimental and optimized concentration profiles for the studied systems are presented in two coordinate systems: the relative concentration  $(c/c_0) \sim$  time ( $t$ ) and relative concentration  $(c/c_0) \sim$  square root of time ( $t^{1/2}$ ). The latter form of presentation allows precisely to depict the fit quality in a broad range of measured concentrations.

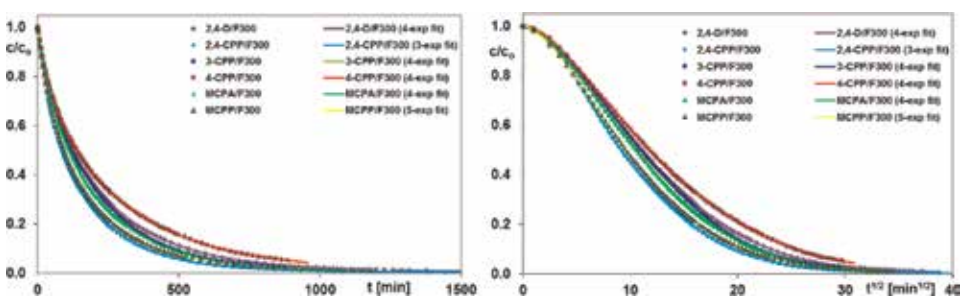


**Figure 21.** Comparison of the optimization using the multi-exponential equation to the experimental data in the coordinates: relative concentration  $c/c_0 \sim$  time and  $c/c_0 \sim$  time<sup>1/2</sup>.

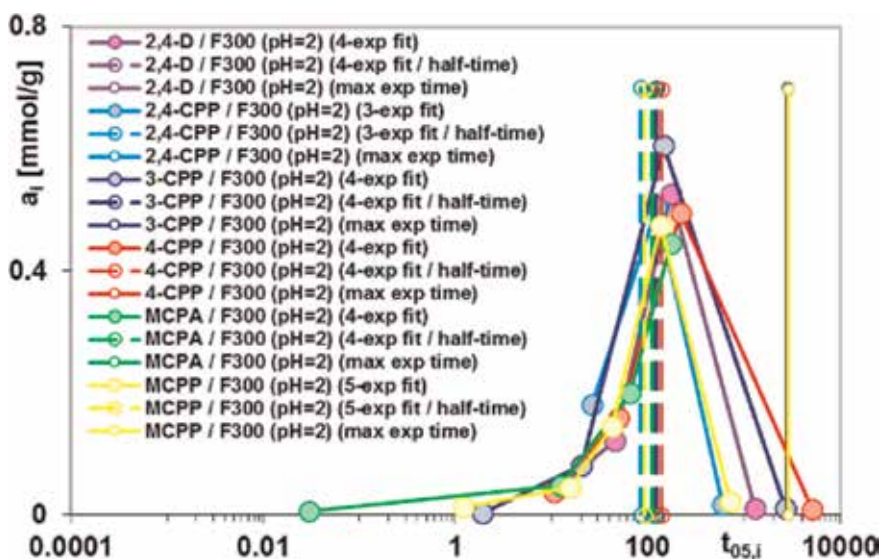


**Figure 22.** Distributions of adsorbed amounts versus adsorption half-times determined from the multi-exponential equation.

Analyzing the values of adsorption half-time and time needed to reach a nearby equilibrium state, one can state that the kinetics of studied pesticides on a given type of carbon material is relatively slow as a result of the micropore predominant contribution in the adsorbent structure. The kinetic curves for the selected adsorbates can be set from the fastest to the slowest ones in order: 2,4-CPP > MCPP > MCPA > 3-CPP > 2,4-D > 4-CPP. The differences are not very significant, but it is clearly noticeable that adsorption of compounds with hydrocarbon chain of propionic acid is faster compared to their homologs of acetic acid, i.e., 2,4-CPP > 2,4-D and MCPP > MCPA. This is undoubtedly a result of the increase of the hydrophobic interactions between the adsorbate and activated carbon surface ( $\text{pH}_{\text{pzc}} \sim 9.8$ ). These interactions along with dispersive ones are the main mechanism of adsorption process in aqueous systems at fixed  $\text{pH} = 2$ . One can say that in the case of these pairs of compounds, differences in a length of the hydrocarbon chain (a molecule dimension as well) do not affect differentiation of the diffusion rate in the microporous structure of activated carbon. Completely reverse trend in the adsorption capacity for these compounds determined on the basis of equilibrium isotherms was observed. The shorter hydrocarbon chain of adsorbate, the greater adsorption capacity for a given compound due to possibility of greater packing in the adsorbent structure.

Additionally a comparison of the adsorption kinetics for the studied systems is presented as spectrum of  $m$ -exp optimized parameters in the coordinate system: the adsorbed amounts  $a_i$  versus the adsorption half-times  $t_{05,i}$ , for respective exponential terms (Figure 22). The spectra are similar in shape and consist of 3–5 terms depending on differentiation in the rate of particular stages of the adsorption process. The faster the kinetics, the greater the adsorbed amounts  $a_i$  for the lower adsorption half-times  $t_{05,i}$  and larger corresponding rate coefficients.

## **Author details**

Magdalena Blachnio, Anna Derylo-Marczewska\* and Malgorzata Seczkowska  
Faculty of Chemistry, Maria Curie-Sklodowska University, Lublin, Poland

\*Address all correspondence to: [annad@hektor.umcs.lublin.pl](mailto:annad@hektor.umcs.lublin.pl)

## **IntechOpen**

---

© 2019 The Author(s). Licensee IntechOpen. This chapter is distributed under the terms of the Creative Commons Attribution License (<http://creativecommons.org/licenses/by/3.0>), which permits unrestricted use, distribution, and reproduction in any medium, provided the original work is properly cited. 

## References

- [1] El-Sonbati AZ, El-Bindary AA, Mohamed KS, Al-Sarawy AA, Farid MA. Removal of hazardous azocoumarin dye from aqueous solutions using activated carbon prepared from rice straw. *Desalination and Water Treatment*. 2016;**57**:19391-19401
- [2] Radovic LR, Moreno-Castilla C, Rivera-Utrilla J. Carbon materials as adsorbents in aqueous solutions. In: Radovic LR, editor. *Chemistry and Physics of Carbon*. New York: Marcel Dekker; 2000. pp. 227-405
- [3] Urita C, Urita K, Araki T, Yoshida M, Moriguchi I. New insights into the heat of adsorption of water, acetonitrile, and n-hexane in porous carbon with oxygen functional groups. *Journal of Colloid and Interface Science*. 2019;**552**:412-417
- [4] Derylo-Marczewska A, Swiatkowski A, Biniak S, Walczyk M. Effect of properties of chemically modified activated carbon and aromatic adsorbate molecule on adsorption from liquid phase. *Colloids and Surfaces A: Physicochemical and Engineering Aspects*. 2008;**327**:1-8
- [5] Basrur D, Ishwara Bhat J. An investigation on the characterization of activated carbon from areca leaves and their adsorption nature towards different dyes. *Global Nest Journal*. 2019;**21**:124-130
- [6] Belo CR, Cansado IPDP, Mourão PAM. Synthetic polymers blend used in the production of high activated carbon for pesticides removal from liquid phase. *Environmental Technology*. 2017;**38**:285-296
- [7] Ruzhen X, Yan J, Yao C, Wenju J. The importance of surface functional groups in the adsorption of copper onto walnut shell derived activated carbon. *Water Science and Technology*. 2017; **76**(11):3022-3034
- [8] Derylo-Marczewska A, Blachnio M, Marczewski AW, Seczkowska M, Tarasiuk B. Phenoxyacid pesticide adsorption on activated carbon—Equilibrium and kinetics. *Chemosphere*. 2019;**214**:349-360
- [9] Marvin 14.8.25.0 Suite Program (Copyright© 1998–2014 ChemAxon Ltd.)
- [10] Yalkowsky SH, He Y. *Handbook of Aqueous Solubility Data*. 1st ed. USA: CRC Press Library of Congress; 2003
- [11] Türker L. AM1 treatment of some phenoxyacetic acid herbicides. *Turkish Journal of Biology*. 2000;**24**:291-298
- [12] Yildirim EH. *Surface Chemistry of Solid and Liquid Interfaces*. 1st ed. Oxford: Blackwell Publishing; 1988
- [13] Birnbaum LS. The role of structure in the disposition of halogenated aromatic xenobiotics. *Environmental Health Perspectives*. 1985;**61**:11-20
- [14] Dawson RMC, Elliot DC, Elliot WH, Jones KM. *Data for Biochemical Research*. 1st ed. Oxford: Oxford Science Publications; 1986
- [15] Bandosz TJ. *Activated Carbon Surfaces in Environmental Remediation*. 1st ed. New York: Elsevier Publishing; 2006
- [16] Hornsby G, Wauchope RD, Herner DA. *Pesticide Properties in the Environment*. 1st ed. USA: Springer; 1995
- [17] Dordio AV, Teimão J, Ramalho I, Carvalho AJP, Estêvão Candeias AJ. Selection of a support matrix for the removal of some phenoxyacetic

compounds in constructed wetlands systems. *Science of the Total Environment*. 2007;**380**:237-246

[18] Hu JY, Aizawa T, Ookubo Y, Morita T, Magara Y. Adsorptive characteristics of ionogenic aromatic pesticides in water on powdered activated carbon. *Water Research*. 1998; **32**:2593-2600

[19] Dąbrowski A, Podkościelny P, Hubicki Z, Barczak M. Adsorption of phenolic compounds by activated carbon—A critical review. *Chemosphere*. 2005;**58**:1049-1070

[20] Wang W, Gong Q, Chen Z, Wang WD, Huang Q, Song S, et al. Adsorption and competition investigation of phenolic compounds on the solid-liquid interface of three-dimensional foam-like graphene oxide. *Chemical Engineering Journal*. 2019;**378**: 122085

[21] Garba ZN, Zhou W, Lawan I, Xiao W, Zhang M, Wang L, et al. An overview of chlorophenols as contaminants and their removal from wastewater by adsorption: A review. *Journal of Environmental Management*. 2019;**241**:59-75

[22] Abdul Ameer AM. Removal of mixture of phenolic compounds from aqueous solution by tire car adsorption. *IOP Conference Series: Materials Science and Engineering*. 2019;**518**: 11820-11834

[23] Mu'azu ND, Jarrah N, Zubair M, Alagha O. Removal of phenolic compounds from water using sewage sludge-based activated carbon adsorption: A review. *International Journal of Environmental Research and Public Health*. 2017;**14**:1094-1127

[24] Marczewski AW, Jaroniec M. A new isotherm equation for single-solute adsorption from dilute solutions on

energetically heterogeneous solids. *Chemical Monthly*. 1983;**114**:711-715

[25] Jaroniec M, Marczewski AW. Physical adsorption on energetically heterogeneous solids. I. Generalized Langmuir equation and its energy distribution. *Chemical Monthly*. 1984; **115**:997-1012

[26] Jaroniec M, Marczewski AW. Physical adsorption on energetically heterogeneous solids. II. Theoretical extension of a generalized Langmuir equation and its application for analysing adsorption data. *Chemical Monthly*. 1984;**115**:1013-1038

[27] Crank J. *Mathematics of Diffusion*. 2nd ed. London: Oxford University Press; 1975

[28] Marczewski AW. Analysis of kinetic Langmuir model. Part I: Integrated kinetic Langmuir equation (IKL): A new complete analytical solution of the Langmuir rate equation. *Langmuir*. 2010;**26**:15229-15238

[29] Marczewski AW, Derylo-Marczewska A, Słota A. Adsorption and desorption kinetics of benzene derivatives on mesoporous carbons. *Adsorption*. 2013;**19**(2-4):391-406

[30] Blachnio M, Budnyak TM, Derylo-Marczewska A, Marczewski AW, Tertykh VA. Chitosan-silica hybrid composites for removal of sulfonated azo dyes from aqueous solutions. *Langmuir*. 2018;**34**:2258-2273

[31] McKay G, El Geundi M, Nassar MM. Pore diffusion during the adsorption of dyes onto bagasse pith. *Process Safety and Environment Protection*. 1996; **74**(4):277-288

[32] Derylo-Marczewska A, Blachnio M, Buczek B, Swiatkowski A. Adsorption of chlorophenoxy pesticides on activated carbon with gradually removed external

particle layers. *Chemical Engineering Journal*. 2017;**308**:408-418

[33] Derylo-Marczewska A, Blachnio M, Marczewski AW, Swiatkowski A, Tarasiuk B. Adsorption of selected herbicides from aqueous solutions on activated carbon. *Journal of Thermal Analysis and Calorimetry*. 2010;**101**: 785-794

[34] Marczewski AW, Seczkowska M, Derylo-Marczewska A, Blachnio M. Adsorption equilibrium and kinetics of selected phenoxyacid pesticides on activated carbon—effect of temperature. *Adsorption*. 2016;**22**(4): 777-790



# Sorption Capacities of a Lignin-Based Electrospun Nanofibrous Material for Pharmaceutical Residues Remediation in Water

*Alexandre Camiré, Bruno Chabot and André Lajeunesse*

## Abstract

The threat of pharmaceutical residues in natural waters is a pressing concern in both developed and underdeveloped countries. Originating mostly from municipal and farms effluents, pharmaceuticals, poorly eliminated by traditional wastewater treatments enter the environment through sewage treatment plants discharges. Their adsorption on ecological adsorptive materials such as lignin may represent an interesting remediation solution. The present study sets out the sorption capacities and properties of a newly developed lignin-based nanofibrous material for typical pharmaceutical residues (fluoxetine, venlafaxine, ibuprofen, and carbamazepine) found in surface waters. This green biomaterial showed, in addition to its high recovery yield, excellent reusability through desorption (more than 90% recovered). As an example, adsorption levels reached 78 mg/g for adsorption of fluoxetine compared to 5–10, 49 and 75–80 for unfunctionalized silica, zeolites and ion-exchange resins respectively. The innovative approach reported therein perfectly meets the concept of circular economy sought in modern societies.

**Keywords:** adsorption-desorption cycles, electrospinning, lignin, pharmaceutical residues, kinetics, isotherms, wastewater

## 1. Introduction

As water scarcity becomes even more present in underdeveloped countries, developed states have to face a different challenge: water pollution from emerging contaminants [1]. Pollutants such as pharmaceutical residues come in a variety of forms and origins causing great issues [2, 3]. Many measures are established to reduce such contamination mostly in the form of water treatments and legislation [1]. However, great limitations are associated with the traditional techniques used in wastewater treatment plants. Most of them are due to either their cost or their low removal efficiency on emerging contaminants [4, 5]. For instance, degradation processes such as ozonation or chlorination were proven efficient for the degradation of organic molecules [6, 7]. However, these techniques have high operational costs and often cause dangerous degradation by-products that would follow the water flow and end up in rivers and lakes [8].

A specific technique distinguishes itself from the others; sorption. Such a treatment has the advantage of capturing contaminants with lower operational costs and without generating any dangerous by-products [5]. The most exploited sorbent is activated carbon (AC) which has high adsorption capacity and low specificity [5, 9]. Its efficiency comes from its high surface area on which contaminants can be adsorbed through interaction forces such as van der Waals [5]. It is often used for water purification through commercially available filters. Activated carbon can be made from various biological residues giving value to waste [9–11]. However, the synthesis of ACs necessitates the carbonization of the material itself and an activation step which can be costly and not environmentally friendly [5].

Another option is the production of adsorbents from highly available natural polymers. Therefore, the product would be green, inexpensive and biocompatible. As many biosorbents are still being studied throughout the world, their potential is not fully exploited, and low attention is given to polymers such as lignin. Lignin, the second most abundant biopolymer after cellulose, is a naturally occurring polymer composing wood at 20–40% [12, 13]. Giving resistance and rigidity to the cell walls of plants, this biopolymer is water insoluble and resistant to organic solvents [12]. Lignin is also a highly variable biopolymer which is composed of its three main monomers (coniferyl alcohol, sinapyl alcohol and p-coumaryl alcohol) in a random pattern [13]. Its composition is further randomized by the addition of functional groups (mainly sulfate and carboxyl groups) during its extraction phase [13]. Even though it is variable, all lignins contain phenols, aliphatic alcohols and ethers [14]. Right now, lignin is mostly used to produce energy in the pulp and paper industry (where it is mainly extracted) and regenerate chemical reagents [15]. Although it is not its main use, lignin has already been used as an adsorbent for heavy metals or even dyes [16–19]. However, to our best knowledge, lignin has never been tested for pharmaceutical residues removal at trace levels. Therefore, the development of this lignin-based electrospun nanofibrous materials open up new opportunities for reducing inputs of pharmaceuticals into the environment.

To be able to achieve a satisfying adsorption capacity for trace contaminants and compete with AC, it is necessary to increase the surface area of the material. A simple way is the transformation of the polymer into nanofibres through electrospinning. This technique exploits the stretching of polymers exposed to a high voltage under defined experimental conditions [20, 21]. In electrospinning, a polymer is dissolved and introduced into a syringe (see **Figure 1**). Voltage is applied between the needle of the syringe and a collector plate. As a drop is formed at the tip of the needle, its surface tension will be disrupted by the electrical field and cause a Taylor cone and the formation of the fibres [22, 23]. Typically, fibres as thin as the nanometres scale are obtainable through this method [20, 24]. Because of its

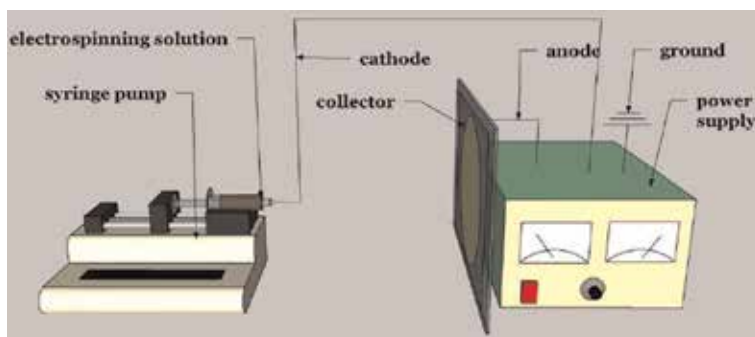


**Figure 1.**  
*Typical electrospinning setup.*

limited known uses, the electrospinning of lignin is not popular even if its electrospinnability with a co-polymer is known [23–25]. Hence, the material and the application are unprecedented.

In this study, electrospun lignin nanofibres will be exploited for the adsorption of pharmaceutical residues in water. Precisely, fluoxetine and venlafaxine (antidepressant), carbamazepine (anticonvulsant) and ibuprofen (anti-inflammatory) will be tested for adsorption on developed nanofibres. The material's adsorption will be characterized by kinetic and isotherm studies. Its capacity to be reusable will also be determined by using various desorption environments.

## 2. Methodology

### 2.1 Chemicals and equipment

Alkali lignin (AL) low sulfur (28,000 Da, CAS 8064-05-1) and poly (vinyl alcohol) (PVA) 98–99% hydrolysis (31,000–50,000 Da, CAS 9002-89-5) were provided by Sigma-Aldrich (St-Louis, MO, USA). Sodium hydroxide pellets (NaOH) 98% (CAS 1310-73-2) and methanol HPLC grade (CAS-67-51-1) were provided by Alfa Aesar (Ward Hill, MA, USA). Hydrochloric acid (CAS 7647-01-0), acetonitrile HPLC grade (CAS 75-05-8), sodium citrate dihydrate (CAS 6132-04-3), sodium chloride (CAS 7647-14-5) and o-phosphoric acid HPLC grade 85% v/v (CAS 7664-38-2) were purchased from Fisher Scientific (Fair Lawn, NJ, USA). Fluoxetine hydrochloride (FLX) (CAS 56296-78-7), venlafaxine hydrochloride (VEN) (CAS 99300-78-4), carbamazepine (CAR) (CAS 298-46-4) and ibuprofen (IBU) (CAS 15687-27-1) were provided by Sigma-Aldrich (Oakville, ON, Canada). Citric acid anhydrous (CAS 77-92-9) was provided by Jungbunzlauer (Bale, Swiss). Commercial adsorbents used for comparison were Amberlyst<sup>®</sup> 15 (CAS 39389-20-3), Dowex<sup>®</sup> Marathon<sup>®</sup> C (CAS 69011-20-7), SiliaFlash<sup>®</sup> F60 40–60 µm particle size, fumed silica (CAS 112945-52-5) and Valfor<sup>®</sup> 100 sodium aluminosilicate zeolite respectively from Alfa Aesar (Ward Hill, MA, USA), Sigma-Aldrich (St-Louis, MO, USA), Silicycle (Quebec City, QC, Canada), and The PQ Corporation (Valley Forge, PA, USA).

The electrospinning setup was composed of a syringe pump (Kd scientific) and a power supply (Gamma High Voltage Research). Two laboratory ovens (Fisher Scientific Isotemp Oven and ThermoScientific HERATharm oven) were used for conservation and stabilization of the membranes. An orbital shaker (Lab Line model 3520) and an environmental orbital shaker incubator (Lab Line model 3528) were used for adsorption tests. Nanofibres were characterized using a Hitachi SUI510 scanning electron microscope (SEM). A Shimadzu Prominence I-series high performance liquid chromatograph (HPLC) coupled with a diode array detector (DAD) with a reverse phase column XB-C18, 100 Å, 150 × 3 mm, 2.6 µm particle size (Phenomenex, Kinetex<sup>®</sup>) was used to analyze contaminated water samples.

### 2.2 Electrospinning solution preparation

The electrospinning solutions were prepared as reported in Camire et al. [26]. Briefly, solution of AL and PVA 15% wt were prepared by dissolving AL in NaOH 1 M and PVA in water heated to 80°C for 60 min. After the dissolution, both solutions were mixed in a mass ratio of 1:1. This solution was stirred for an hour and settled at room temperature for another hour. The AL:PVA solution was then used directly for electrospinning or kept at 4°C in a refrigerator for a maximum of

1 month. Before use, the refrigerated solution was brought to room temperature in a hot water bath for an hour.

### **2.3 Electrospinning**

The previous prepared solution was injected in a 5 mL syringe with a 20-gauge needle for electrospinning. The syringe was set to the syringe pump and voltage was applied between the needle and the collector. The collector was a non-stick cookie sheet giving good electrospinning, reusability and easy recovery of the nanofibres. The electrospinning parameters were based on results obtained previously [26]. The conditions were a flow rate of 0.1 mL/h with an applied DC voltage of 15 kV. The collector was placed 20 cm away from the tip of the needle. The temperature was kept at 22°C and relative humidity maintained between 10 and 40%. A razor blade was used to recover the nanofibrous mat from the collector. All experiments were conducted in a customized electrospinning box. The electrospun nanofibre mat was then kept overnight in a laboratory oven at 80°C for drying and stabilization purposes.

### **2.4 Nanofibre stabilization**

Due to electrospun nanofibres' high solubility in water, AL:PVA nanofibres mats were stabilized using two consecutive techniques. Both techniques are based on previous works [26]. The first method used the glass transition temperature of polymers to raise their crystallinity and hence their water resistance. Therefore, nanofibres were heated in a laboratory oven at 160°C for 3 h. Next, the membranes were immersed in a 0.5 M sodium citrate buffer pH 4.5 for a period of 3 h. This process aims to protonate AL's phenol groups which were previously deprotonated during the preparation of the electrospinning solution in a method similar to the extraction methods of black liquor [15]. During this step, the morphology of the membrane changes drastically due to the dissolution of a part of the PVA. The dissolution causes a rise in the concentration of AL (the membranes become browner) and cross-linking of the nanofibres. After exposure to the buffer, the membranes were washed several times with purified water, stretched and dried on a metallic surface. Finally, the nanofibrous mats were recovered using a razor blade.

### **2.5 Adsorption tests**

In this section, three types of tests were performed: adsorption of a single contaminant on AL:PVA membranes as well as commercial adsorbents, and adsorption of multiple contaminants on AL:PVA membranes. All adsorption tests were conducted in batches by adding a defined amount of adsorbent to a stirred solution containing a specific concentration of contaminants. All tested solutions were composed of purified water with 5% of methanol and contaminants adjusted at the targeted concentration. The organic solvent's purpose was to ensure that pharmaceuticals were solubilized in water. Separate 2500 ppm standard solutions of FLX, VEN, CAR and IBU were prepared by dissolving the corresponding stock solutions in methanol. Those solutions were then diluted for adsorption tests. Before, during and after the adsorption test, aliquots of 500 µL of the contaminated water were sampled, diluted with 500 µL of mobile phase, vortexed and injected in HPLC-DAD to determine the concentration of contaminants in solution. For tests using one contaminant on AL:PVA membranes, 50 ppm FLX solution was used as a model contaminated water. For tests with commercial adsorbents, adjustments were made to compensate for the size difference between adsorbents. Therefore, solutions of 250 ppm FLX in 10 mL were prepared to keep the same contaminant to

adsorbent mass ratio. For tests with multiple contaminants, 12.5 ppm of FLX, IBU, CAR and VEN were added to water to simulate contaminated water.

The adsorption tests were initialized by the addition of 25 mg of adsorbent (nanofibres or commercial adsorbent) to the solution. The tests were conducted over a period of 150 min to ensure that equilibrium was reached. Using a calibration curve and the area under the peaks on the chromatograms, the remaining concentration of the solution was calculated. From this value, the adsorption capacity at time  $t$  ( $Q_t$ ) was calculated using the following equation:

$$Q_t = \frac{(C_0 - C_t)}{m} \times V \quad (1)$$

where  $C_t$  is the concentration of the contaminant (ppm) at time  $t$  (min),  $C_0$  is the initial concentration of contaminants (ppm),  $V$  is the volume of the solution (L), and  $m$  is the mass of adsorbents (g).

For samples containing one contaminant, samples injected in HPLC-DAD were eluted using a mobile phase composed of acetonitrile and a 0.1% solution of phosphoric acid (60:40% v/v ratio). The flow rate was adjusted at 0.45 mL/min for 3.75 min with a detection at 230 nm. For samples containing more than one contaminant, the mobile phase was composed of acetonitrile and 0.1% phosphoric acid with a ratio of 40:60% v/v. The flow rate was adjusted to 0.5 mL/min for a period of 20 min with a detection still at 230 nm. In all cases, 10  $\mu$ L of the samples were injected using an autosampler. For all contaminants, a 10-point (0.5–100 ppm) calibration curve was established to determine the concentration. All tests were performed in triplicate.

## 2.6 Kinetic studies

Kinetic curves were obtained by sampling at intervals during the adsorption process. Samples were collected at 0, 5, 10, 15, 20, 30, 40, 50, 60, 75, 90, 120 and 150 min after the addition of the adsorbent. The equilibrium time of 150 min was determined by an initial kinetic test. The same sampling and injection processes as traditional adsorption tests were conducted for kinetic studies. By calculating the adsorption capacity through time, it is possible to obtain a kinetic curve which can be compared to adsorption kinetic models. Adsorption kinetic models give crucial information on the adsorption parameters and the limiting processes occurring during the adsorption. Typically, three steps occur during the adsorption: transfer of the adsorbate to the external surface of the adsorbent, internal diffusion of the adsorbate to active sites and sorption reaction with the adsorbent [27, 28]. In this study, three models were compared: pseudo-first order, pseudo-second order and Elovich. In all cases, the kinetic constants were calculated using Matlab's curve fitting app. To determine the best fitting model, determination coefficients and root of mean square errors (RMSE) were compared. The pseudo-first order model is represented by Eq. (2):

$$Q_t = Q_e(1 - e^{-k_1 t}) \quad (2)$$

In Eq. (2),  $Q_e$  corresponds to the adsorption capacity at equilibrium (mg/g),  $Q_t$  the adsorption capacity (mg/g) at time  $t$  (min) and  $k_1$  the pseudo-first order kinetic adsorption constant ( $\text{min}^{-1}$ ) [10, 29]. The pseudo-second order model is represented by Eq. (3):

$$Q_t = \frac{k_2 Q_e^2 t}{1 + k_2 Q_e t} \quad (3)$$

where  $k_2$  is associated to the pseudo-second order kinetic adsorption constant ( $\text{mg g}^{-1} \text{min}^{-1}$ ) [10, 29]. The Elovich model is represented by Eq. (4):

$$Q_t = \frac{\ln(\alpha\beta) + \ln t}{\beta} \quad (4)$$

where  $\alpha$  is the initial adsorption rate constant ( $\text{mg g}^{-1} \text{min}^{-1}$ ) and  $\beta$  is the initial desorption rate constant ( $\text{g mg}^{-1}$ ) [10, 29].

## 2.7 Isotherms

The adsorption isotherms were performed for AL:PVA membranes to obtain information on the adsorption sites and the type of reaction occurring. For these tests, 50 ppm solutions of FLX were prepared as typical adsorption tests. Samples were collected at 0 and 180 min (equilibrium). From those samples, the concentration ( $C_e$ ) and adsorption capacity ( $Q_e$ ) at equilibrium were calculated. Isotherms are obtained by varying the mass of adsorbents (resulting in a varying adsorption capacity and concentration at equilibrium) at fixed temperatures. For our tests, adsorbent masses of 5, 10, 15, 20, 25, 30 and 35 mg were tested and temperatures of 25, 40 and 60°C were compared. The curves obtained by plotting the  $C_e$  versus  $Q_e$  are then compared to isotherm models (Freundlich, Langmuir, Sips, Redlich-Peterson) to gain important information. **Table 1** shows the different equations for the models studied.

Here,  $Q_e$  is the adsorption capacity at equilibrium ( $\text{mg/g}$ ),  $C_e$  is the concentration in solution at equilibrium (ppm),  $k_F$  is the Freundlich isotherm constant ( $\text{mg/g} [\text{L/mg}]^{1/n}$ ),  $n$  is the heterogeneity factor (dimensionless),  $Q_{max}$  is the maximum adsorption capacity ( $\text{mg/g}$ ),  $k_L$  is the Langmuir isotherm constant ( $\text{L/mg}$ ),  $k_S$  is the Sips isotherm constant ( $[\text{L/mg}]^{1/n}$ ),  $k_R$  is the Redlich-Peterson isotherm constant ( $\text{L/g}$ ),  $a_R$  being the Redlich-Peterson isotherm constant ( $[\text{L/g}]^{b_R}$ ) and  $b_R$  is the Redlich-Peterson model exponent (dimensionless).

## 2.8 Thermodynamic study

The thermodynamic parameters (enthalpy, entropy and Gibbs's free energy) are calculated through a thermodynamic study. These parameters are obtained by using the  $C_e$  and  $Q_e$  recovered from isotherms adsorption tests and the Van't Hoff and 2nd thermodynamic law equations. The Van't Hoff equation corresponds to:

$$\ln \frac{Q_e}{C_e} * 1000 \frac{\text{g}}{\text{L}} = \frac{\Delta S^\circ}{R} - \frac{\Delta H^\circ}{RT} \quad (5)$$

Models	Non-linear equation	Equation
Freundlich	$Q_e = k_F C_e^{1/n}$	(5)
Langmuir	$Q_e = \frac{Q_{max} k_L C_e}{1 + k_L C_e}$	(6)
Sips	$Q_e = \frac{Q_{max} k_S C_e^{1/n}}{1 + k_S C_e^{1/n}}$	(7)
Redlich-Peterson	$Q_e = \frac{k_R C_e}{1 + a_R C_e^{b_R}}$	(8)

**Table 1.**  
Isotherm models non-linear equations [10, 30].

where  $\Delta S^\circ$  is the standard entropy ( $\text{J mol}^{-1} \text{K}^{-1}$ ) and  $\Delta H^\circ$  is the standard enthalpy ( $\text{J mol}^{-1}$ ) [31]. The second thermodynamic law equation corresponds to:

$$\Delta G^\circ = \Delta H^\circ - T\Delta S^\circ \quad (6)$$

where  $\Delta G^\circ$  is the standard Gibbs's free energy ( $\text{J mol}^{-1}$ ) [31]. These values will give information on the amount of thermal energy produced, the energy of the bonds, the spontaneity of the reaction and the favourability of an adsorption reaction.

## 2.9 Desorption tests

The capacity of an adsorbent to be desorbed is also an important characteristic value since it can have a significant contribution on economics and life cycle assessment of the process. Therefore, the reusability of the AL:PVA membranes was evaluated by desorption. For this purpose, multiple conditions were tested to recover the contaminant safely. Hence, the nanofibres were exposed to solutions of methanol (to create an environment in which the contaminant is highly soluble), purified water (to verify the risk of desorption due to equilibrium), heated solutions (might be able to revert the sorption reaction), salts (ion exchange and/or competition) and combined techniques (except heated methanol solutions). In all cases, the membranes were immersed in 50 mL of solution for 4 h. For temperature effect, solutions were heated to 60°C to verify desorption. The salt used for desorption was sodium chloride since it is a simple and non-toxic substance, largely found in typical wastewater. Concentrations of sodium chloride of 1, 2 and 3 M were tested. Initial and final samples were injected in HPLC-DAD to determine the concentration of FLX recovered. The desorption solution showing the best desorption efficiency was used for repeated adsorption/desorption cycles to evaluate the reusability. Between each test, the membranes were recovered and dried in a vacuum desiccator to prevent humidity from interfering with the measured masses. For membranes exposed to salts, these were washed several times with purified water to dissolve salts, and then dried in a vacuum desiccator.

## 3. Results and discussion

### 3.1 Electrospinning and nanofibre stabilization

Mixed solutions of AL and PVA were prepared for the production of membranes for adsorption tests. Using the specified electrospinning parameters, it was possible to obtain steady nanofibre formation for periods of a few hours to produce thin nanofibrous mats. Those were thermally stabilized giving the nanofibres a brownish colour and more rigidity. Their immersion in a sodium citrate buffer finalized the stabilization process to provide fibres stability at various pHs enabling their use for adsorption. As shown in **Figure 2**, the stabilization process had a slight impact on the visual aspects of the membranes. However, the impact is more obvious when seen by scanning electron microscopy. **Figure 2b** shows that nanofibres of  $183 \pm 5$  nm in diameter were obtained by the electrospinning with a low number of beads or defects. This size does not technically correspond to nanofibres (0–100 nm), but the adsorption properties shall be akin to real nanofibres considering the small difference. **Figure 2d** shows the nanofibres after a thermal process. This image shows a similar nanofibrous aspect with small variations of the nanofibre diameter ( $156 \pm 5$  nm). However, nanofibres seem to be closer to each other with slight cross-linking giving it

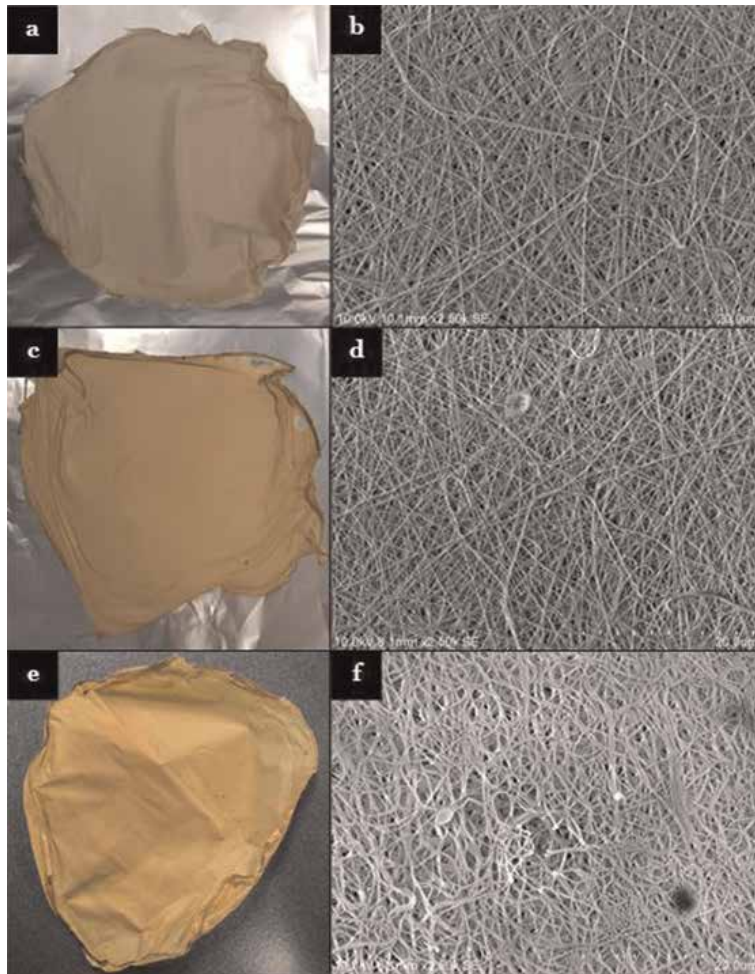


**Figure 2.** Images of AL:PVA nanofibres after electrospinning (a), after thermal treatment (c) and after final chemical treatment (e) and corresponding MEB images at  $2500\times$  (b, d and f, respectively).

rigidity. With the chemical stabilization (**Figure 2f**), the cross-linking is obvious due to swelling and fusing of nanofibres ( $188 \pm 10$  nm). However, it should be emphasized that this kind of treatment often causes the loss of porosity of the material. In fact, without the thermal process, the acid treatment causes the nanofibres to completely fuse together lowering the porosity of the material [26, 32].

Interestingly, humidity had a real impact on the different steps of electrospinning. In fact, at low humidity (e.g., 10%), it was possible to electrospin, but the efficiency was lower. This might be due to the fast evaporation of the solvent during electrospinning which caused the drop of polymers at the tip of the needle to dry before electrospinning or the electrospinning jet to break before reaching the collector surface. The recovery of nanofibres was also more difficult due to higher adherence to the metal plates. At higher humidity (between 30 and 40%), the electrospinning resulted in a larger nanofibre mat surface area on the collector, which was easily peeled off, almost without the use of a razor blade. The advantages of the higher humidity also appeared during the stabilization step. Indeed, a higher humidity reduced the drying speed of the membranes, but also reduced their stickiness to the collector plate. It is therefore important to control the humidity within a certain range to achieve good nanofibre mat formation and easy processability.



### 3.2 General adsorption

The adsorption tests were first conducted for FLX since it has the most potential for adsorption. Therefore, 25mg of AL:PVA nanofibres were used to adsorb 50 ppm of FLX in a 50 mL solution. The test lasted 150 min with a sample collected at the beginning and at the end. **Table 2** shows the results obtained for this adsorption test. For comparison purposes of the adsorption, the same test was also carried out using commercial adsorbents. However, considering the smaller size of the commercial adsorbent, adjustments were necessary to conduct adsorption tests without any bias. Hence, the volume of the solution was reduced to 10 mL and the concentration was risen to 250 ppm to keep the same mass of FLX (2.5 mg solution) for the same mass of adsorbents. Therefore, the maximum adsorption capacity obtainable for each test was 100 mg/g. The summary of these results is available in **Table 2**.

As expected, unfunctionalized silica adsorbents (Siliaflash<sup>®</sup> and fumed silica) had low adsorption potential for FLX. This is due to the lack of functional groups for adsorption and/or ionic charges. Due to its ion-exchange properties, Valfor<sup>®</sup> had a better adsorption propensity than silica. However, considering the exchange mechanism (exchange with a sodium ion from the adsorbent) and the size of the FLX molecules, it is possible that the adsorption was limited by the number of available sites and competition between FLX molecules. This type of sorbent might be more appropriate for metal ions [33]. Both ion-exchange resins had good adsorption capacities. Both being cation exchange resins and strongly acidic, they possessed functional groups (sulfate) appropriate for the adsorption of ionic molecules such as alkaline pharmaceutical residues. It is therefore encouraging that a biosorbent made of lignin can yield similar or better adsorption capacities than commercial sorbents.

For a potential application in wastewater treatments, it is important to evaluate its capacity to adsorb multiple and various contaminants at the same time. Hence, the adsorption capacities of the developed nanofibres were compared with four contaminants, fluoxetine (antidepressant), venlafaxine (antidepressant), carbamazepine (anticonvulsant) and ibuprofen (anti-inflammatory). The adsorption was evaluated separately and simultaneously to detect possible competitions between contaminants (see **Table 3**).

The contaminants having the most affinity for the membranes were in the decreasing order FLX, VEN, CAR and IBU. IBU and CAR had a low affinity for the nanofibres with almost no adsorption in simultaneous adsorption. This follows the logical assumption that could be made from the structures of the molecules and their chemical properties. For instance, both FLX and VEN are alkaline pharmaceuticals that are easily protonated at a neutral pH. However, fluoxetine has more aromatic rings and possesses Fluor promoting hydrogen bonding and  $\pi$ -stacking. For CAR and IBU, the molecules are respectively neutral and anionic at pH 7 which

Adsorbent	Adsorption capacity (mg/g)
AL:PVA nanofibres	78.24 ± 1.35
Amberlyst <sup>®</sup> 15	80.96 ± 0.35
Dowex <sup>®</sup> Marathon <sup>®</sup> C	77.03 ± 0.94
Valfor <sup>®</sup> 100	49.00 ± 4.39
Fumed silica	8.54 ± 0.62
Siliaflash <sup>®</sup> F60	4.25 ± 0.35

**Table 2.**  
*Adsorption capacity comparison of AL:PVA membranes with commercially available adsorbents.*

Contaminant	Simultaneous adsorption capacity* (mg/g)	Individual adsorption capacity** (mg/g)
Fluoxetine (FLX)	22.85 ± 0.28	78.24 ± 1.35
Venlafaxine (VEN)	11.05 ± 1.02	49.76 ± 2.80
Carbamazepine (CAR)	1.02 ± 0.02	8.04 ± 0.01
Ibuprofen (IBU)	0.62 ± 0.39	5.00 ± 0.46

\*Initial concentration of 12.5 ppm.  
\*\*Initial concentration of 50 ppm.

**Table 3.**  
Affinity comparison of the AL:PVA nanofibres for various pharmaceutical contaminants.

completely prevent any ionic bonding between lignin's phenols and cationic groups from pharmaceuticals. AL is also a weak acid which would hardly make any ionic bonds with an acidic compound such as IBU.

### 3.3 Kinetic studies

Kinetic studies give interesting data about the reaction order, type and time necessary to reach equilibrium. For this purpose, kinetic curves were plotted by observing the adsorption capacity at multiple times for FLX alone and for the simultaneous adsorption of contaminants. First, adsorption capacity for fluoxetine was measured at 0, 5, 10, 15, 20, 30, 40, 50, 60, 75, 90, 120 and 150 min to obtain a kinetic curve. Using Matlab<sup>®</sup>, the kinetic models' parameters were calculated using non-linear regression analysis. These results are shown in **Table 4**. From **Figure 3**, it is possible to observe the different kinetic curves corresponding to pseudo-first and pseudo-second order and Elovich kinetic models as well as the experimental values. From **Figure 3** and **Table 4**, it is clear that the pseudo-first order best fitted the experimental data. The pseudo-first order indicates that the adsorption occurs in one step. Good correlation with this model also shows that the reaction is regulated by the time necessary for the reaction and not by the diffusion in the nanofibrous

Kinetic model	Parameter	Value
Pseudo-first order	$R^2$	0.9989
	RMSE	0.7117
	$K_1$ (min <sup>-1</sup> )	0.086
	$Q_e$ (mg/g)	63.98
Pseudo-second order	$R^2$	0.9790
	RMSE	3.046
	$K_2$ (g/mg/min)	0.0017
	$Q_e$ (mg/g)	71.14
Elovich	$R^2$	0.9229
	RMSE	5.832
	$\alpha$ (mg/g min)	33.37
	$\beta$ (g/mg)	0.08453

**Table 4.**  
Kinetic parameters for pseudo-first order, pseudo-second order and Elovich models.

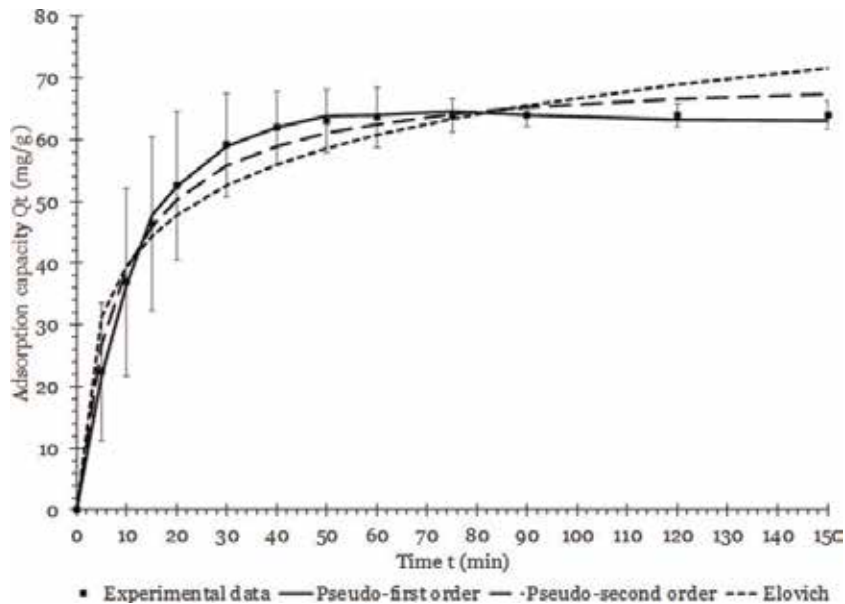


**Figure 3.**  
*Kinetic curve for the adsorption of FLX on AL:PVA nanofibres.*

material. However, the literature shows that no assumptions can be made from the kinetic model to determine the adsorption mechanism (physisorption or chemisorption for instance) [28]. Still, considering the chemical structure of lignin, physisorption is more logical. For physisorption, the main possible interaction forces are van der Waals,  $\pi$ -stacking, hydrogen bonds, hydrophobicity, steric and polarity interactions [10].

More information can also be obtained from **Figure 3**. For instance, following the observation of the graph, it is possible to conclude that equilibrium is obtained within 1 h and that most of the adsorption occurs in the first 20 min. Such a fast adsorption could allow multiple applications to the adsorbent in addition to the retention of contaminants in wastewater. Also, due to the sampling, the total amount of contaminant available is lower which causes a lower adsorption capacity during kinetics. During the test, it was also possible to follow the adsorption process by monitoring of the pH becoming more acid as the alkaline FLX was removed from the solution.

A kinetic experiment was also conducted with simultaneous contaminants. The kinetic curve for each contaminant is presented in **Figure 4**. For FLX, the curve was almost identical to the individual curve which suggests that no significant competition occurred for FLX. For VEN, the adsorption was significantly longer with equilibrium at 90 min. Its final adsorption capacity, however, remained similar by roughly adsorbing half of the initial concentration. For IBU and CAR, the adsorption was fast (equilibrium within 5 min) and their adsorption capacity was low. Their low adsorption capacities show that AL:PVA membranes might be ineffective for such contaminants except for really low quantities. Coupling AL:PVA nanofibres with other adsorbents could be an alternative to adsorb a wider pharmaceutical contaminants spectrum. For instance, recent studies on chitosan and poly (ethylene oxide) showed good adsorption capacities for IBU in water [32].

### 3.4 Isotherm studies

The goal of the experiment is to understand the behaviour of adsorption sites while specific changes are made. By monitoring the variation of concentration and

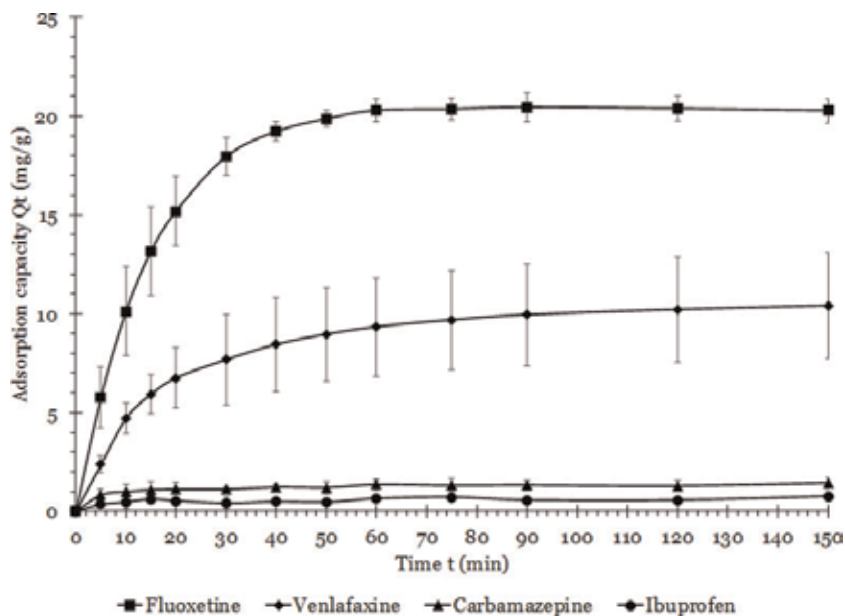


**Figure 4.**  
Kinetic curve for simultaneous adsorption of FLX, VEN, CAR and IBU.

adsorption capacity at equilibrium while varying the mass of adsorbents, it is possible to obtain an isotherm curve which can be compared to isotherm models. The Freundlich, Langmuir, Sips (or Langmuir-Freundlich) and Redlich-Peterson models were compared to the data. The isotherm constants and statistical analysis of the fitting at various temperatures are presented in **Table 5**.

Results show that, for all temperatures, the Sips model best fitted the experimental data with the highest  $R^2$  and RMSE coefficients. This model indicates that a contaminant will link to multiple adsorption sites simultaneously. Also, this model can also be reduced to both Freundlich and Langmuir isotherms depending on the concentration of contaminants (low concentration and high concentration respectively) [10, 27, 30]. Considering that in real remediation conditions the concentrations are lower, it would be appropriate to predict the adsorption to be closer to a Freundlich isotherm. In the Freundlich model, the adsorption occurs in multi-layers with heterogeneous sites adsorbing a single molecule [10]. In the Langmuir model, however, the adsorption is in monolayers on homogeneous sites [10]. In these types of models, the pH, the temperature and the concentration remain the dominating factors affecting adsorption. This is further observed when the temperature increased and the adsorption capacity accordingly got lower. However, the isotherm models had much lower correlation as the temperature went up.

### 3.5 Thermodynamic studies

Thermodynamic parameters give interesting information on energy transfers during adsorption. Using the experimental data obtained from fluoxetine's isotherms and Eqs. (9) and (10), standard enthalpy, standard entropy, standard Gibbs's free energy were calculated. For enthalpy, a value of  $-7987$  J/mol or  $-7.99$  kJ/mol was obtained which indicates that the adsorption reaction is exothermic. This means that no heat is necessary for efficient adsorption and that supplying heat would be unfavourable for adsorption in this case. Also, this value falls into the energy

Isotherm	Parameter	25°C	40°C	60°C
Freundlich	$R^2$	0.9655	0.9510	0.8486
	RMSE	4.716	6.200	6.113
	$k_F$	11.22	2.298	8.093
	$N$	0.6441	1.131	0.6326
Langmuir	$R^2$	0.9783	0.9374	0.8242
	RMSE	3.746	7.006	5.893
	$Q_{max}$	249.2	3.242e+4	175.3
	$k_L$	0.02292	1.083e-4	0.02223
Sips	$R^2$	0.9899	0.9510	0.8877
	RMSE	2.859	6.933	6.079
	$Q_{max}$	140.3	9.285e+4	82.32
	$k_S$	0.05902	8.513e-5	0.06166
	$N$	1.83	1.132	3.277
Redlich-Peterson	$R^2$	0.9855	0.9510	0.8669
	RMSE	3.423	6.933	6.620
	$k_R$	4.499	117.5	2.983
	$a_R$	3.122e-4	50.23	1.523e-4
	$b_R$	2.021	-0.135	2.183

**Table 5.**  
 Isotherm parameters for various isotherm models at 25, 40 and 60°C.

range normally associated with hydrogen bonds (4–50 kJ/mol) and  $\pi$ -stacking (8–12 kJ/mol) [34, 35]. For entropy, a value of 42.01 J/mol.k was obtained. A positive value indicates that there is a gain in entropy and that the reaction is favourable. For  $\Delta G^\circ$  (at 25°C), a value of -20.51 kJ/mol was calculated which shows that the reaction is spontaneous. Moreover, values close to -20 kJ indicate that physisorption is prevalent [31].

Hence, the adsorption seems to be an appropriate method for water remediation against pharmaceutical contaminants since it consumes low to no energy. Its exothermic nature is also advantageous in cold climate countries like Canada since heating costs would be higher. In addition, it is possible to use the information obtained through thermodynamic to develop a desorption method for nanofibres. For this reason, the use of heated solutions for desorption will be investigated in the next section.

### 3.6 Desorption and reusability study

One of the benefits of sorption is the possibility of desorption. In this way, multiple adsorption and desorption cycles are possible, and the material is reusable. For these reasons, various desorption solutions were tested on AL:PVA nanofibres for the recovery of FLX. This step's purpose also was obtaining a simpler matrix in which the contaminants can easily be recovered (dried form) or disposed safely. The solutions used had to be either non-toxic or easily evaporated and reused. The effect of temperature was also investigated for a simple desorption method. Results obtained for each tested desorption method are presented in **Table 6**. As shown in this table, the use of an organic solvent such as methanol has the disadvantage of causing

Desorption solution	Fluoxetine recovered (%)	Qualitative result
100% methanol	89	High mass loss
50% methanol	36	Slight mass loss
100% water	1	None
100% water 60°C	30	None
1M NaCl 25°C	52	None
1M NaCl 60°C	92	None
2M NaCl 60°C	76	None
3M NaCl 60°C	19	None

**Table 6.**

*Impact of various desorption solutions on desorption of fluoxetine and AL:PVA nanofibres.*

degradation of the membranes in addition to the desorption. Even, it is possible that the desorption detected is due to the degradation of nanofibres. Therefore, pure methanol and 50% methanol solution were discarded. Using pure water, almost no desorption occurred which means that the strength of the bond is sufficiently strong to prevent a new equilibrium. When pure water is heated, however, FLX can be desorbed to some extent (30%) which follows the assumptions made in thermodynamic study. Then, sodium chloride was tested for the desorption of FLX. First, 1 M NaCl solution was tested at room temperature which indicated that salts were effective to recover the pharmaceutical contaminant. Afterwards, the same desorption was tested at 60°C. With this method, more than 90% of the fluoxetine could be recovered without affecting the membrane's integrity. The concentration of salt was also varied to verify if a higher concentration would give a better desorption. Instead, higher salt concentrations reduced desorption capacity. Considering the difference in size of FLX compared to NaCl, this might be due to the saturation of the solution in which the fluoxetine cannot be dissolved.

To attest the reusability of the membranes, the best desorption method (1M NaCl solution heated to 60°C) was tested for three adsorption/desorption cycles (see **Figure 5**). In this process, the membranes were dried and weighed before each adsorption or desorption tests to observe possible mass loss.

To simplify comparison, **Figure 5** shows the mass of FLX instead of the adsorption capacity. First, it is interesting to observe that the amount desorbed is increasing with desorption cycles. This can be due to a higher number of FLX molecules on the membranes on the second and third cycle (the amount not desorbed on the previous cycles plus the amount adsorbed on the current cycle). Moreover, the adsorption capacity of the membranes was not affected by the desorption as shown by the small rise in mass adsorbed on the third cycle. The small weight gain could have been caused by a slight rise in porosity of the material due to stretching during adsorption and desorption tests. During this test, no significant mass losses were measured through the 3 cycles. Since the membranes are not degrading and do not lose adsorption capacity after the third cycle, it would be logical to assume that the synthesized membranes could still be used for even more cycles.

### 3.7 Applications and perspectives

The potential of AL:PVA nanofibres was clearly demonstrated through our study. This promising new technology can be exploited in many fields that require adsorption. For instance, the main application dedicated in this study is the adsorption of pharmaceutical contaminants in wastewater. In such application, the

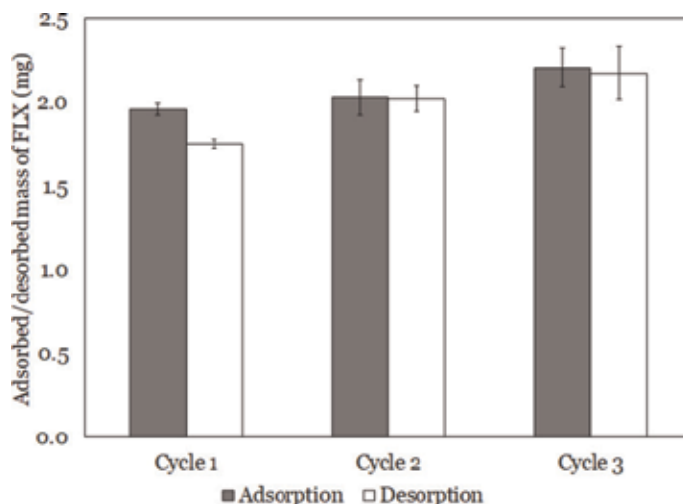


**Figure 5.**  
*Adsorption/desorption cycles for FLX using 60°C 1 M NaCl solution.*

membranes produced could be incorporated in dynamic systems in wastewater treatment plants or even at the source in hospitals or medical centre effluents. In this way, most of the potentially harmful pharmaceutical residues would be removed and would not enter aquatic ecosystems.

Meanwhile, our research is also investigating the use of nanofibres for the collection and analysis of illicit drugs such as cocaine or methamphetamine. Results obtained from this study will be the object of a future study. However, encouraging results with more than 90% of retention was obtained for both drugs (unpublished results). Moreover, desorption is also efficient. In this way, illicit drugs in complex matrices could be transferred to a simpler matrix for direct analysis in liquid chromatography during forensic investigation.

As of now, the efficiency of the nanofibres was proven for alkaline pharmaceutical contaminants. However, its efficiency is rather poor for contaminants that are neutral or acidic such as CAR or IBU. Therefore, an interesting avenue would be the coupling or sequential use of AL:PVA nanofibres and another biosorbent such as chitosan. In fact, works from our research group showed that chitosan nanofibres are efficient for adsorption of IBU in aqueous medium [32]. Therefore, it would be interesting to test a nanofibrous structure composed of AL and chitosan or a sandwich-like structure made of both types of fibres on mixtures of contaminants. In addition, surface chemical modifications are considered in the near future.

#### 4. Conclusions

Novel alkali lignin and poly (vinyl alcohol) (AL:PVA) nanofibrous membranes were tested for adsorption of pharmaceutical contaminants. Its efficiency to adsorb was first studied on a model contaminant, fluoxetine. An adsorption capacity of 78 mg/g was obtained which corresponds to the adsorption of 78% of fluoxetine present in the water. With further adsorption cycles, the membranes can adsorb up to 90% of contaminants. Compared to commercially available adsorbents (ion-exchange resins, zeolites and silica), the results are similar to costly ion-exchange resins (75–80 mg/g). Using kinetic and isotherm models, it is possible to conclude that nanofibres follow a pseudo-first order kinetic model and Sips' isotherm model

which indicate that the adsorbent is of the physical type with adsorption of the contaminants on multiple sites at the same time in a multi- or monolayer pattern (depending on the concentration). Looking at thermodynamics, adsorption on AL: PVA nanofibres is a favourable, spontaneous and exothermic reaction. This information could be used for the design of a desorption method in which the fluoxetine can be retrieved safely, and the membrane reused for at least two more cycles. The adsorption of multiple pharmaceutical contaminants (fluoxetine, venlafaxine, carbamazepine and ibuprofen) showed that nanofibres have more affinity for alkaline compounds, which adsorb more given the right amount of possible intermolecular forces occurring. Hence, for remediation applications, it would become necessary to combine this adsorbent with another one for maximum retention efficiency.

## **Acknowledgements**

The authors would like to thank the UQTR Foundation, the Innovations Institute for Ecomaterials, Eco-products and Ecoenergies Biomass Based, the EcotoQ Research Group and the Forensic Research Group for their financial support during this study. Special thanks are addressed to Agnes Lejeune for her assistance during the collection of SEM images. All technicians at the UQTR are also acknowledged for their technical support.

## **Conflict of interest**

No conflict of interest to declare.



## Author details

Alexandre Camiré<sup>1</sup>, Bruno Chabot<sup>2</sup> and André Lajeunesse<sup>1,3,4\*</sup>

1 Department of Chemistry, Biochemistry and Physics, Université du Québec à Trois-Rivières, Trois-Rivières, Quebec, Canada

2 Innovations Institute in Ecomaterials, Eco-products, and Ecoenergies Biomass Based (I2E3), Université du Québec à Trois-Rivières, Trois-Rivières, Quebec, Canada

3 Forensic Research Group, Université du Québec à Trois-Rivières, Trois-Rivières, Quebec, Canada

4 EcotoQ Research Group, Institut National de la Recherche Scientifique, Quebec, Canada

\*Address all correspondence to: [andre.lajeunesse@uqtr.ca](mailto:andre.lajeunesse@uqtr.ca)

## IntechOpen

---

© 2019 The Author(s). Licensee IntechOpen. This chapter is distributed under the terms of the Creative Commons Attribution License (<http://creativecommons.org/licenses/by/3.0/>), which permits unrestricted use, distribution, and reproduction in any medium, provided the original work is properly cited. 

## References

- [1] Sousa JCG, Ribeiro AR, Barbosa MO, Pereira MFR, Silva AMT. A review on environmental monitoring of water organic pollutants identified by EU guidelines. *Journal of Hazardous Materials*. 2018;**344**:146-162
- [2] Gavrilescu M, Demnerova K, Aamand J, Agathos S, Fava F. Emerging pollutants in the environment: Present and future challenges in biomonitoring, ecological risks and bioremediation. *New Biotechnology*. 2015;**32**(1):147-156
- [3] Schwarzenbach RP, Egli T, Hofstetter TB, von Gunten U, Wehrli B. Global water pollution and human health. *Annual Review of Environment and Resources*. 2010;**35**(1):109-136
- [4] Oulton RL, Kohn T, Cwiertny DM. Pharmaceuticals and personal care products in effluent matrices: A survey of transformation and removal during wastewater treatment and implications for wastewater management. *Journal of Environmental Monitoring*. 2010;**12**(11):1956-1978
- [5] Cai Z, Dwivedi AD, Lee W-N, Zhao X, Liu W, Sillanpää M, et al. Application of nanotechnologies for removing pharmaceutically active compounds from water: Development and future trends. *Environmental Science: Nano*. 2017;**5**(1):27-47
- [6] Lajeunesse A, Blais M, Barbeau B, Sauvé S, Gagnon C. Ozone oxidation of antidepressants in wastewater-treatment evaluation and characterization of new by-products by LC-QToFMS. *Chemistry Central Journal*. 2013;**7**:15
- [7] Capodaglio AG, Bojanowska-Czajka A, Trojanowicz M. Comparison of different advanced degradation processes for the removal of the pharmaceutical compounds diclofenac and carbamazepine from liquid solutions. *Environmental Science and Pollution Research International*. 2018;**25**(28):27704-27723
- [8] Yin L, Wang B, Yuan H, Deng S, Huang J, Wang Y, et al. Pay special attention to the transformation products of PPCPs in environment. *Emerging Contaminants*. 2017;**3**(2):69-75
- [9] Calisto V, Ferreira CI, Oliveira JA, Otero M, Esteves VI. Adsorptive removal of pharmaceuticals from water by commercial and waste-based carbons. *Journal of Environmental Management*. 2015;**152**:83-90
- [10] Mansour F, Al-Hindi M, Yahfoufi R, Ayoub GM, Ahmad MN. The use of activated carbon for the removal of pharmaceuticals from aqueous solutions: A review. *Reviews in Environmental Science and Bio/Technology*. 2017;**17**(1):109-145
- [11] Sarma H, Lee W-Y. Bacteria enhanced lignocellulosic activated carbon for biofiltration of bisphenols in water. *Environmental Science and Pollution Research*. 2018;**25**(18):17227-17239
- [12] Wertz J-L, Richel A, Gérin P. Molecules derived from valorization of lignin. Contract No.: March. 2015
- [13] Norgren M, Edlund H. Lignin: Recent advances and emerging applications. *Current Opinion in Colloid and Interface Science*. 2014;**19**(5):409-416
- [14] Yang Q, Pan X. Correlation between lignin physicochemical properties and inhibition to enzymatic hydrolysis of cellulose. *Biotechnology and Bioengineering*. 2016;**113**(6):1213-1224
- [15] Zhu W, Theliander H. Precipitation of lignin from softwood black liquor: An investigation of the equilibrium and

- molecular properties of lignin. *BioResources*. 2015;**10**(1):1696-1714
- [16] Wysokowski M, Klapiszewski L, Moszynski D, Bartczak P, Szatkowski T, Majchrzak I, et al. Modification of chitin with Kraft lignin and development of new biosorbents for removal of cadmium(II) and nickel(II) ions. *Marine Drugs*. 2014;**12**(4):2245-2268
- [17] Berrima B, Maatar W, Mortha G, Boufi S, El Aloui L, Belgacem M. Adsorption of heavy metals on charcoal from lignin. *Cellulose Chemistry and Technology*. 2016;**50**:701-709
- [18] Šćiban MB, Klašnja MT, Antov MG. Study of the biosorption of different heavy metal ions onto Kraft lignin. *Ecological Engineering*. 2011;**37**(12):2092-2095
- [19] Nair V, Panigrahy A, Vinu R. Development of novel chitosan–lignin composites for adsorption of dyes and metal ions from wastewater. *Chemical Engineering Journal*. 2014;**254**:491-502
- [20] Ortiz JE, Chabot B. Electrospun nanofibers for the removal of heavy metals from aqueous solutions. *Mitacs Globalink Internship Report*. Monterrey, Mexico: Monterrey Institute of Technology and Higher Education; July 2016
- [21] Chang C-Y, Chang F-C. Development of electrospun lignin-based fibrous materials for filtration applications. *BioResources*. 2016;**11**(1):2202-2213
- [22] Aslanzadeh S, Zhu Z, Luo Q, Ahvazi B, Boluk Y, Ayranci C. Electrospinning of colloidal lignin in poly(ethylene oxide)<sub>N,N</sub>-dimethylformamide solutions. *Macromolecular Materials and Engineering*. 2016;**301**(4):401-413
- [23] Fang W, Yang S, Yuan T-Q, Charlton A, Sun R-C. Effects of various surfactants on alkali lignin electrospinning ability and spun fibers. *Industrial and Engineering Chemistry Research*. 2017;**56**(34):9551-9559
- [24] Beck RJ, Zhao Y, Fong H, Menkhaus TJ. Electrospun lignin carbon nanofiber membranes with large pores for highly efficient adsorptive water treatment applications. *Journal of Water Process Engineering*. 2017;**16**:240-248
- [25] Fang W, Yang S, Wang X-L, Yuan T-Q, Sun R-C. Manufacture and application of lignin-based carbon fibers (LCFs) and lignin-based carbon nanofibers (LCNFs). *Green Chemistry*. 2017;**19**(8):1794-1827
- [26] Camire A, Espinasse J, Chabot B, Lajeunesse A. Development of electrospun lignin nanofibers for the adsorption of pharmaceutical contaminants in wastewater. *Environmental Science and Pollution Research International*. 2018:1-14
- [27] Worch E. *Adsorption Technology in Water Treatment: Fundamentals, Processes, and Modeling*. Berlin: De Gruyter; 2012
- [28] Tan KL, Hameed BH. Insight into the adsorption kinetics models for the removal of contaminants from aqueous solutions. *Journal of the Taiwan Institute of Chemical Engineers*. 2017;**74**:25-48
- [29] Largitte L, Pasquier R. A review of the kinetics adsorption models and their application to the adsorption of lead by an activated carbon. *Chemical Engineering Research and Design*. 2016;**109**:495-504
- [30] Foo KY, Hameed BH. Insights into the modeling of adsorption isotherm systems. *Chemical Engineering Journal*. 2010;**156**(1):2-10
- [31] Anastopoulos I, Kyzas GZ. Are the thermodynamic parameters correctly

estimated in liquid-phase adsorption phenomena? *Journal of Molecular Liquids*. 2016;**218**:174-185

[32] Paradis-Tanguay L, Camiré A, Renaud M, Chabot B, Lajeunesse A. Sorption capacities of chitosan/polyethylene oxide (PEO) electrospun nanofibers used to remove ibuprofen in water. *Journal of Polymer Engineering*. 2019;**39**(3):207-215

[33] Dragan ES, Dinu M, Shankar G. Recent developments in composite biosorbents and their applications for wastewater treatment. *Research Journal of Chemistry and Environment*. 2015;**19**(11):42-58

[34] Riley KE, Ford CL, Demouchet K. Comparison of hydrogen bonds, halogen bonds, C H... $\pi$  interactions, and C X... $\pi$  interactions using high-level ab initio methods. *Chemical Physics Letters*. 2015;**621**:165-170

[35] Wendler K, Thar J, Zahn S, Kirchner B. Estimating the hydrogen bond energy. *The Journal of Physical Chemistry A*. 2010;**114**(35):9529-9536

# Processes and Factors Affecting Phosphorus Sorption in Soils

*Samuel Kwesi Asomaning*

## Abstract

The subject of this chapter is soil chemistry. The chapter is entitled Processes and Factors Affecting Phosphorus (P) Adsorption in Soils. The chapter aims to give an overview of the major mechanisms responsible for phosphate sorption (i.e., adsorption and absorption of phosphate) in soils, particularly of acid soils. According to studies conducted by some soil scientists, the major soil factors affecting P sorption are time, soil pH, soil organic matter, and iron and aluminium oxides of soils. Studies conducted indicated that adsorption of the P increases as the P ages in the soil. Soil pH affects phosphate adsorption but the effect is limited for adsorption by soils in the pH range of 4–8. Organic matter may affect P adsorption in two ways: indirectly by inhibiting iron oxide crystallisation and directly by competing for adsorption sites. On per mole basis, oxalate extractable aluminium oxides adsorb nearly twice as much P as oxalate extractable iron oxides due to poorer crystallinity (higher specific area) of the aluminium oxides compared to the iron oxides and also to a higher charge of the former. The chapter also highlights the pedotransfer functions (PTFs) of Borggaard, which can be used to calculate for the P adsorption in highly weathered acid soils.

**Keywords:** sorption, adsorption, adsorbent, adsorbate, specific adsorption, amorphous oxides, pedotransfer functions

## 1. Introduction

With increasing demand of agricultural production and as the peak in global production will occur in the next decades, phosphorus (P) is receiving more attention as a non-renewable resource [1, 2]. One unique characteristic of P is its low availability due to slow diffusion and high fixation in soils. Few unfertilized soils release P fast enough to support the high growth rates of crop plant species. In many agricultural systems in which the application of P to the soil is necessary to ensure plant productivity, the recovery of applied P by crop plants in a growing season is very low, because in the soil more than 80% of the P becomes immobile and unavailable for plant uptake because of adsorption, precipitation, or conversion to the organic form [3]. All of this means, that P can be a major limiting factor for plant growth.

Phosphate in soils tends to react with soil components to form relatively insoluble compounds, many of which have limited availability to plants [4]. Major factors which influence these reactions include: phosphorus concentration in solution, amount of free oxides of iron and aluminium, type and amount of clay, soil pH, and organic matter [5].

Aluminium oxides, iron oxides and clay silicates are well known phosphate adsorbents in soils [6]. According to Borggaard et al. [7], aluminium and iron oxides are the main phosphate adsorbents in sandy soils. Close correlations have been found between a soil's capacity to adsorb phosphate and the content of aluminium and iron oxides, in the soil suggesting these oxides to be the main phosphate adsorbents in soils [8].

In acidic soils, P can be dominantly adsorbed by Al/Fe oxides and hydroxides, such as gibbsite, haematite, and goethite [9]. P can be first adsorbed on the surface of clay minerals and Fe/Al oxides by forming various complexes. The nonprotonated and protonated bidentate surface complexes may coexist at pH 4–9, while protonated bidentate inner-sphere complex is predominant under acidic soil conditions [10]. Clay minerals and Fe/Al oxides have large specific surface areas, which provide large number of adsorption sites. The adsorption of soil P can be enhanced with increasing ionic strength.

Phosphate is strongly adsorbed by the number of adsorption sites, which vary greatly among soils [11]. With further reactions, P may be occluded in nanopores that frequently occur in Fe/Al oxides, and thereby become unavailable to plants [10].

Therefore, the availability of soil phosphate as well as the soil solution concentration of phosphate will depend on the degree of phosphate saturation, rather than on the total phosphate content [12]. Phosphate saturation is the proportion of adsorption sites occupied by phosphate, which is normally taken as the ratio between adsorbed phosphate and the phosphate adsorption capacity (PAC) of the soil [13].

## **2. Mechanism of phosphorus adsorption in soils**

### **2.1 Specific adsorption of phosphorus by aluminium and iron oxides**

Phosphate sorption is a term used to describe all the processes resulting in the removal of phosphate from soil solution, mainly by surface adsorption and precipitation [14]. Important soil factors that determine its capacity to retain phosphorus (P) are the presence of amorphous aluminium and Iron oxides compounds [15]. The process of adsorption of the phosphate by these compounds (i.e. aluminium and Iron oxides) which are also known as adsorbents is known as specific adsorption. The phosphate molecule or ion which is adsorbed is then known as adsorbate. Specific adsorption of ions can occur onto uncharged adsorbents and sometimes even onto surfaces bearing charge of the same sign as the adsorbent. Thus phosphate can be adsorbed onto surfaces of variable-charge minerals such as aluminium and iron oxides even at alkaline pH, where these adsorbents are negatively charged. Specific adsorption is characterised by formation of inner-sphere complexes, where no water molecules are interposed between the adsorbent and the adsorbate. The most important variable-charge minerals in the soil that adsorb P include aluminium oxides and iron oxides. The poorly ordered (“amorphous”) iron and aluminium hydroxides possess very large specific surface area (SSA) which can be as high as  $800 \text{ m}^2 \text{ g}^{-1}$ , and 10 times larger than the SSA of corresponding crystalline forms. Additionally, these sesquioxides have high singly coordinated surface hydroxyl density [16]. The reactive sites of these amphoteric AlOH and FeOH minerals are the hydroxyl groups exposed on the mineral surfaces. The kind of hydroxyl (OH) groups in which the oxygen of the OH is coordinated to one structural Iron (111) ( $\text{Fe}^{3+}$ ) ion (single – coordinated), are found to protonate and deprotonate in response to solution pH.

The single-coordinated OH groups are those surface hydroxyl groups onto which specifically adsorbable anions are adsorbed [7]. The single-coordinated hydroxyl groups can be quantitatively replaced or exchanged by the phosphate anions. This results in the formation of a binuclear or surface complex for the phosphate iron oxide system, where one phosphate ion occupies two surface sites. This is accompanied by a release of hydroxyl ( $\text{OH}^-$ ) and  $\text{H}_2\text{O}$  groups (**Figure 1**).

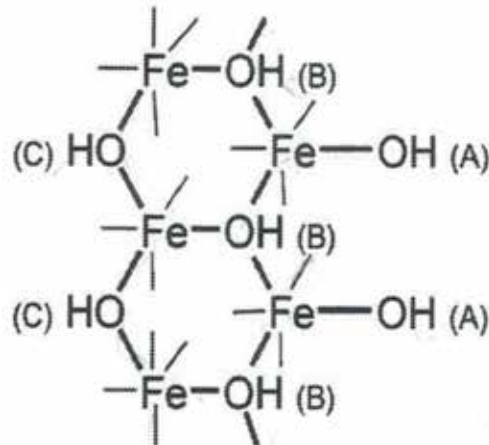


**Figure 1.** The three kinds of hydroxyl groups occurring on the goethite surface denoted (A) single-coordinated, (B) triple-coordinated and (C) double-coordinated. Source: Borggaard and Elberling [6].

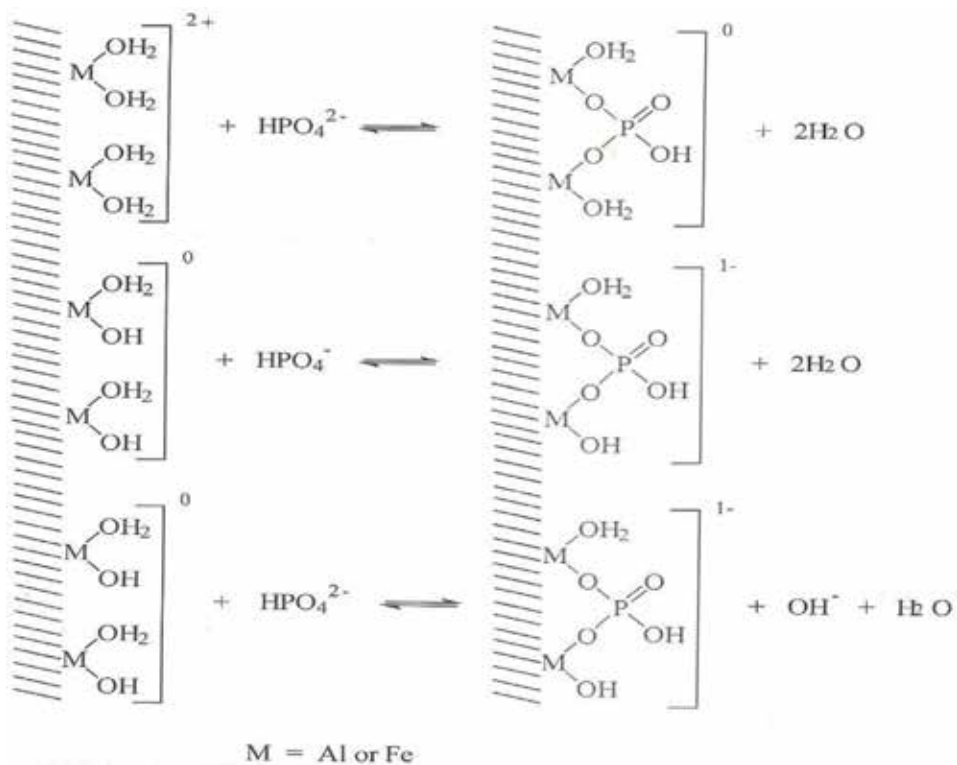


**Figure 2.** Examples of phosphate adsorption mechanisms. Source: Syers and Cornforth [17].

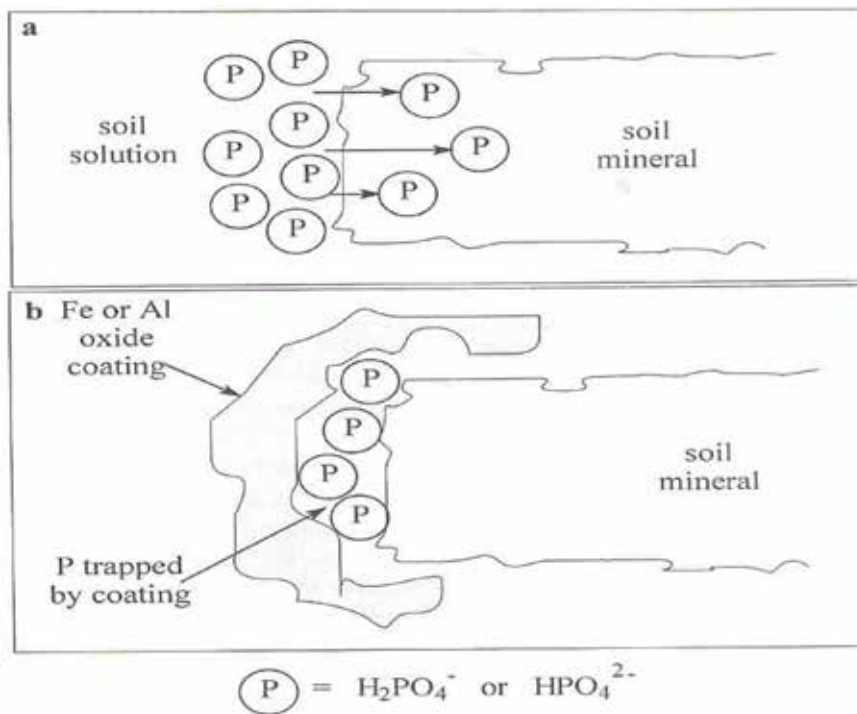


**Figure 3.**

*The inner sphere formation of P in soil minerals (a) and the subsequent occlusion of adsorbed P (b). Source: Syers and Cornforth [17].*

The precise nature of these reactions depends on pH which influences the proportions of hydroxyl ( $\text{OH}^-$ ) and  $\text{OH}_2^+$  groups on the solid surface and hence its surface charge.

If the adsorbed phosphate ions then diffuse into the solid, then they are “absorbed”. Sorption covers the combined processes. Adsorbed phosphate may become trapped on the surface of soil minerals if any Fe or Al oxide coating is precipitated on the mineral. The trapped phosphate is then described as occluded (Figures 2 and 3).

### 3. Factors affecting phosphate adsorption in soils

#### 3.1 Time

Adsorption of phosphate by soils increases with increasing reaction time, first rapidly and then slowly, but without reaching a true equilibrium [18]. Increasing phosphate concentration increases with the equilibrium time.

The slow reaction of phosphate with oxides has been attributed to formation of iron phosphate, with a surface coating on the oxides [19]. The porous structure often observed in goethite may similarly not only account for slow phosphate adsorption but also for slow desorption and thus irreversibility [20]. Accordingly, adsorption of phosphate by well crystallised goethite having few pores was complete after 3 days and remained constant up to 260 days [21]. According to Schwertmann [22], aluminium substituted goethite crystals are generally smaller and less porous than non-substituted goethite crystals therefore the former should adsorb phosphate faster and reach equilibrium faster than the latter. Furthermore,



self-aggregation (clustering) and porosity seem to be important factors in controlling adsorption/desorption (irreversibility) of phosphate by iron oxides and thus by soils. Formation of iron phosphate coatings has, however, been rejected by others [9], who considered migration (diffusion) of phosphate into aggregated iron oxides, particularly ferrihydrite, to cause the slow reaction.

### **3.2 Soil pH**

Several investigations have shown the effect of pH on phosphate adsorption by soil and synthetic iron oxides [6, 23]. The pH effect on soil iron oxide adsorption seems to be less pronounced than on pure iron oxide adsorption. According to Borggaard [24], pH affects phosphate adsorption but the effect is limited for adsorption by soils in the pH range 4–8 in contrast to adsorption by pure iron oxides. For soils, increasing pH has been shown to either increase or decrease and to have no effect on phosphate adsorption [25]. Nwoke et al. [26] found that sorption of P decreased with increasing soil pH and this was attributed to increased negative charge on variable-charge colloids which cause electrostatic repulsion of the ionic P species from the surface. In contrast, Agbenin and Mokwunye [27, 28] reported an increase in sorption with increasing pH for some savannah soils. Agbenin [27] attributed this trend to the chemistry and retention of  $\text{Ca}^{2+}$ , the predominant cation in savannah soils. Nevertheless, the pH effect on phosphate adsorption should not be exaggerated, since this effect is fairly small, particularly, over the pH range covering most soils, and ancillary effects may therefore appear relatively important [29].

### **3.3 Organic matter**

Organic matter may affect phosphate adsorption in two ways: Indirectly by inhibiting iron oxide crystallisation and directly by competing for adsorption sites [24]. Dissolved organic matter (fulvic and humic acids) has been shown to decrease phosphate adsorption by iron oxides and by soils, particularly at acid pH, indicating that dissolved organic matter can compete with phosphate for adsorption sites [30]. In the study by Sibanda [30], organic matter which was isolated from soils as humic and fulvic acids, was added in solution, and the background electrolyte was sodium chloride. Of seven naturally occurring organic compounds tested, only phytic acid reduced soil phosphate adsorption significantly [31].

In contrast, the results of the study of influence of organic matter on phosphate adsorption by aluminium and iron oxides in sandy soils clearly showed that organic matter has no direct influence on adsorption of phosphate by these soils [24]. According to these workers, the phosphate adsorption capacity changes with the amount of extractable aluminium and iron, irrespective of the organic matter content; even removal of the organic matter does not alter phosphate adsorption. In the study mentioned, there was no addition of organic matter, and calcium acetate was used as background electrolyte. Calcium flocculates organic matter, while sodium tends to disperse it. The interpretation of the results, therefore, could be that to act as a competitor, organic matter must be in solution; otherwise it has no direct effect on phosphate adsorption. In limed soils and in many cultivated soils the concentration of dissolved organic matter is considered to be very low. Interactions are known to occur between organic matter and the aluminium and iron oxides inhibiting their crystallisation, and thereby increasing their phosphate adsorption capacity [22, 32]. Soil organic matter, can indirectly affect soil phosphate adsorption capacity (PAC) by retarding crystal growth of poorly crystalline aluminium and iron oxides, which because of high specific surface areas have very high PACs [33, 34].

Iron oxides and probably also aluminium adsorb phosphate and other anions of weak acids, including organic matter, by ligand exchange. Factors which affect the development of aluminium and iron oxides crystals (crystallisation) may influence adsorption, due to a change in the specific surface area of the adsorbent. In soils, organic matter acts as a factor [32], although its effects are complicated and it appears to affect aluminium and iron differently.

The formation of crystalline iron oxides may be inhibited in the presence of certain organic acids, and the ratio of poorly crystalline to well-crystallised forms (or  $Fe_{ox}:Fe_{dcb}$ ) increases as the soil organic matter content increases [22]. However, the interaction between organic matter and iron seems weak. Borggaard [24] found that although most  $Fe_{ox}:Fe_{dcb}$  ratios were rather high in some Danish sandy soils, the correlation between  $Fe_{ox}:Fe_{dcb}$  and organic matter was not significant which suggests that there is no inhibition of adsorption sites for phosphate. Also they found that the crystallinity of the aluminium oxides seems very poor, in as much as extractable  $Al_{ox}$  was similar to  $Al_{dcb}$  probably because of strong interaction between aluminium and organic matter. Hydrogen peroxide – treated soil, to remove organic matter, did not change amounts of phosphate adsorbed which strongly suggests that, organic matter affects phosphate adsorption indirectly by decreasing aluminium oxide crystallinity, but not directly by competing for adsorption sites.

Aluminium oxides are found to be more effective adsorbents of phosphate than are the iron oxides [24]. On per mole basis oxalate extractable aluminium oxides ( $Al_{ox}$ ) adsorb nearly twice as much phosphate as oxalate-extractable iron oxides. This may be due to poorer crystallinity (higher specific surface area) of the aluminium oxides compared to the iron oxides and also to, a higher charge on the former [35]. For synthetic oxides, the amounts of phosphate adsorbed per  $m^2$  seem to be higher for aluminium oxides than for iron oxides, although the trend is weak [35]. This suggests that differences in crystallinity are the main reason for the observed differences in adsorption capacity [24]. This may explain, at least partly, the observed positive correlations between phosphate adsorption capacity and organic matter content.

### **3.4 Phosphate sorption as a function of the iron and aluminium oxides of soils**

The reactivity of Al and Fe oxides is determined by the conditions under which the soil is formed. Thus, under cold, humid and nutrient-poor conditions, which result in organic matter accumulation, poorly crystalline oxides of small particle size are favoured, while under well-aerated tropical conditions larger, more well developed crystals are formed [7, 36]. Since the reactivity depends on the specific surface areas the poorly crystalline Al and Fe oxides with smallest particle size will be the most reactive.

On the basis of laboratory measurements of P sorption, Borggaard [24] found that the P sorption capacity of some Danish Spodosol or Spodosol-like samples was a function of amorphous Al and Fe and crystalline iron. For 43 samples from Canadian Spodosols, the P sorption capacity was, however, found to be a linear function of the sum of amorphous Al and Fe but independent of the crystalline Fe oxides [37]. A similar relationship was found for some German soils [11]. According to these workers, the total P sorption measured was predominantly related to amounts of amorphous Fe and Al. Similarly, Van der Zee [38] reported that P sorption in different acid soils from Netherlands was linearly related to the sum of oxalate-extractable Fe and Al of the soils. For some tropical and subtropical soils, Loganathan [39] found that P sorption was positively correlated with the contents of amorphous Fe and Al. In Ghana, a study of P sorption in relation to Al and Fe oxides of Oxisols by Owusu-Benoah et al. [40] indicated that the P sorption capacity

( $P_{max}$ ) of the soils significantly correlated with oxalate extractable Fe and Al but not with crystalline Fe and Al.

On the contrary, Pena and Torrent [41] described P sorption in Mediterranean soils as being strongly affected by crystalline Fe. Crystalline Fe oxides were also reported to be the most important P sorption compounds in some Spanish clay samples [18] and of great importance for the P sorption in some strongly weathered, tropical soil samples from Australia [42]. However,  $P_{max}$  of 97 soil samples of some South-Western Australian soils was closely related to crystalline Al while amorphous and crystalline extractable Fe gave low or no relationship [43].

#### 4. Adsorption isotherms

When an adsorbent (a soil sample or a soil component) is shaken with a solution containing an adsorbate, the amount of adsorbate adsorbed by the adsorbent depends on the experimental conditions including adsorbate concentration, adsorbate:adsorbent ratio, pH, shaking time and temperature. At fixed adsorbate:adsorbent ratio, pH, shaking time and temperature, the amount adsorbed adsorbate,  $q$ , increases at increasing adsorbate concentration,  $C_{eq}$  following a curve (isotherm) like that in **Figure 4**.  $C_{eq}$  denote the equilibrium concentration of the adsorbate, i.e. the initial concentration less adsorbed adsorbate.

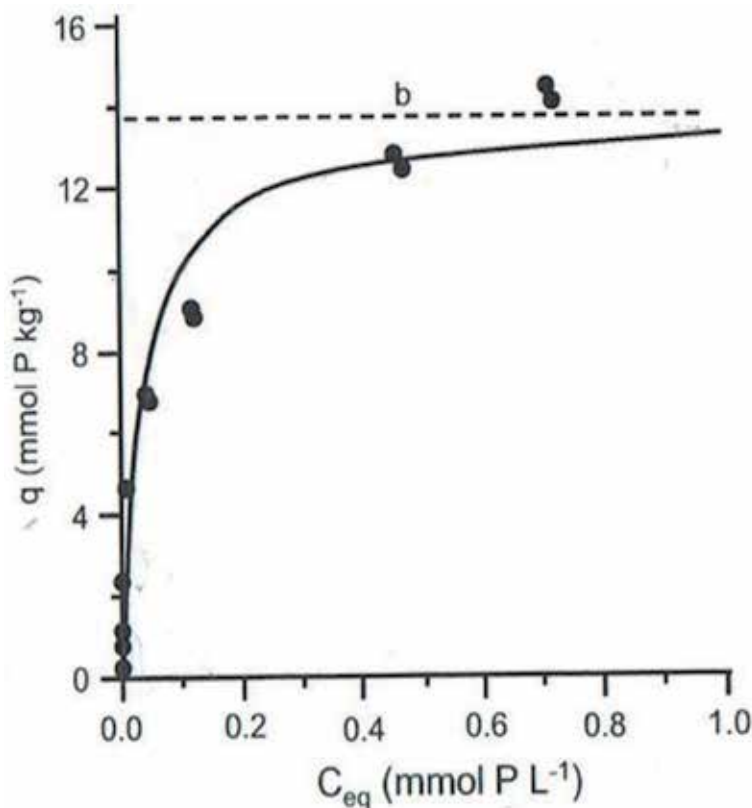


**Figure 4.** A plot of adsorbed phosphate,  $q$ , against the equilibrium phosphate concentration,  $C_{eq}$ . The adsorbent is a sample from the A horizon of an Oxisol (Typic Hapludalf) from Ghana. The curve is fitted to the experimental points (dots) by the Langmuir equation (Eq. 1) the dashed line (b) indicates the adsorption maximum (modified) from Owusu-Bennoah et al. [40].

An isotherm like that shown in **Figure 4**, which is a L-curve isotherm because it can be fitted by the Langmuir equation (see subsequent Eq. 1), is often seen, particularly when soil is the adsorbent. In some cases an extreme version of the L-curve isotherm is seen; the H-curve isotherm, where  $q$  increases sharply for a small increase in  $C_{eq}$  until  $q$  achieves an upper value, where upon  $q$  is virtually independent of  $C_{eq}$ . The initial very high slope of the H-curve isotherm indicates a very high affinity (hence the designation H for high) between adsorbate adsorbent. On the other hand, if  $q$  is proportional to  $C_{eq}$ , a straight-line isotherm is obtained. It can be noticed that a straight line or almost straight line relation between  $q$  and  $C_{eq}$  can also be obtained if only an initial small part of the curve in **Figure 1** is included in the plot, e.g. the part of the curve where  $C_{eq} < 0.05$  mM. Adsorption of organic compounds such as most pesticides by soil organic matter-containing soil often follows a straight line. For straight line adsorption, the adsorbate-adsorbent affinity is independent of the amount adsorbed, in contrast to the initially very high and then decreasing affinity for adsorptions following the L- and H-curves.

#### 4.1 Phosphorus sorption isotherms and equations

The relationship between the amounts of P sorbed per unit weight of soil ( $q$ ) and the equilibrium P concentration in solution ( $C$ ) bathing the soil at a constant temperature has been described by several sorption isotherms. The main motivations for describing curves were to (1) identify the soil constituents involved in the sorption [39], (2) predict the amount of fertiliser needs of soils to meet the demand of plant uptake for optimum yield and (3) study the nature of the sorption process to learn more about the mechanism of the process [25].

The Langmuir, Freundlich and Temkin equations are common models for describing P sorption when input data are limited [44].

##### 4.1.1 Langmuir equation

Langmuir equation may be written as:

$$q = \frac{b K C_{eq}}{1 + K C_{eq}} \quad (1)$$

where  $b$  and  $K$  are fitting parameters. The parameter  $b$  represents the value of  $q$  that is approached asymptotically as  $C_{eq}$  becomes arbitrarily large. Accordingly  $b$  has been taken as a measure of maximum adsorption, the upper limit of adsorbate that can be adsorbed by the adsorbent. The  $b$  parameter is, therefore, commonly used in comparison of soils and soil components.  $K$  determines the initial slope of the isotherm and has sometimes been considered a measure of the affinity of the adsorbate and the adsorbent; a binding constant. By rearrangement, Eq. (1) can be expressed in linear forms such as:

$$\frac{C_{eq}}{q} = \frac{C_{eq}}{b} + \frac{1}{bK} \quad (2)$$

Eq. (2) which is the linearized form of Eq. (1) is often used to estimate the adsorption ( $b$ ), affinity index ( $k$ ) and buffer capacity of soils. The straight line resulting from plotting  $C_{eq}/q$  against  $C_{eq}$  will have slope equal to  $1/b$  and an intercept equal to  $1/(bk)$ .

#### 4.1.2 Freundlich equation

Freundlich equation has the form:

$$q = aC_{eq}^b \quad (3)$$

where a and b are fitting parameters. The linearized form of the equation is

$$\log q = \log a + b \log C_{eq}$$

A plot of  $\log q$  against  $\log C_{eq}$  result in a straight line with slope equal to b and an intercept equal to  $\log a$ .

#### 4.1.3 Temkin equation

Temkin equation is in the form:

$$\frac{x}{b} = \frac{RT}{B} \ln AC_{eq} \quad (4)$$

where x is the amount of P adsorbed, and A and B are the Temkin isotherm constants. A represents the equilibrium binding constant ( $\text{dm}^3 \text{g}^{-1}$ ). R is the universal gas constant.

The linearized form of the equation is

$$x = a + b \ln C_{eq} \quad (5)$$

where a and b are constants obtained from the intercept (a) and the slope (b). Eq. (5) indicates that a plot of x against  $\ln C$  should yield a straight line but such plots for soils in many cases yielded curves rather than straight lines. The b value of Temkin equation is taken as the P buffering capacity (retention capacity of adsorbed P) of soils ( $\text{ug P g}^{-1}$ ).

## 4.2 Pedotransfer functions (PTFs) for estimation of phosphate adsorption capacity

Apart from the solution concentration, the amount of phosphate to be adsorbed depends on phosphate loading (content) and the content and reactivity of phosphate adsorbents, such as aluminium and iron oxides in sandy soils [24]. The maximum phosphate adsorption capacity ( $P_{max}$ ), corresponding to adsorption at high (infinite) phosphate concentrations, can be calculated by applying the Langmuir adsorption equation to the measured data. The limitation of the Langmuir equation is indicated by the deviation of points corresponding to the highest equilibrium of P concentration. Langmuir equation is restricted to a limited concentration range [45, 46].

Again, due to the discrepancies of phosphate adsorption in relation to aluminium and iron oxides in different soils, various models have been proposed for predicting P sorption [18, 24].

Aluminium and iron oxides are the main phosphate adsorbent in soils, especially in Spodosols and other sandy soils [15, 47]. Accordingly, close relationships have been found between amounts of adsorbed phosphate of some forms of soil aluminium and iron, which have resulted in creation of pedotransfer functions for predicting adsorbed phosphate from aluminium and iron oxide contents quantified

by selective extractions. Thus, for a range of soils, which have received high amounts of fertiliser P, phosphate adsorption (in  $\text{mmol kg}^{-1}$ ) was found to be well predicted by the simple pedotransfer function of Van der Zee and Riemsdijk [48]:

$$P_{\text{adsorbed}} = \alpha \times (\text{Al}_{\text{ox}} + \text{Fe}_{\text{ox}}) \quad (6)$$

Where  $\text{Al}_{\text{ox}}$  and  $\text{Fe}_{\text{ox}}$  are the soil contents of aluminium and iron ( $\text{mmol kg}^{-1}$ ) that can be extracted by means of the oxalate method [49]. The fitting constant was found to be between 0.14 and 0.48, depending on phosphate concentration and equilibrium time in the adsorption experiments [50]. With  $\alpha = 0.5$ , this pedotransfer function is commonly used for estimating phosphate adsorption capacity in phosphate pollution assessment.

For strongly weathered soils enriched in Al and Fe oxides with different degree of ordering, a model that is able to account for different oxide fractions such as that of [24] will be a logical choice. This model was based on studies of Danish sandy soils (Spodosols and podzolised Entisols) low in adsorbed phosphate. Therefore, the phosphate adsorption maximum may be calculated from the content of poorly crystalline aluminium and iron oxides ( $\text{Al}_{\text{OX}}$ ,  $\text{Fe}_{\text{OX}}$ ) and well crystallised iron oxides ( $\text{Fe}_{\text{CBD}} - \text{Fe}_{\text{OX}}$ ) according to the equation [24]:

$$P_{\text{calc}} = (0.22 \pm 0.02) \times \text{Al}_{\text{OX}} + (0.12 \pm 0.02) \times \text{Fe}_{\text{OX}} + (0.04 \pm 0.03) (\text{Fe}_{\text{CBD}} - \text{Fe}_{\text{OX}}) + (0.3 \pm 0.5) \quad (7)$$

Where  $\text{Al}_{\text{OX}}$  and  $\text{Fe}_{\text{OX}}$  denote oxalate extractable aluminium and iron and  $\text{Fe}_{\text{CBD}}$  is citrate-bicarbonate-dithionite extractable iron. Phosphate adsorption maximum calculated using the pedotransfer model of [24] ( $P_{\text{calc}}$ ),  $\text{Al}_{\text{OX}}$ ,  $\text{Fe}_{\text{OX}}$ , and  $\text{Fe}_{\text{CBD}}$  are in  $\text{mmol kg}^{-1}$ . According to the function, 0.22 mmol P is adsorbed by 1 mmol  $\text{Al}_{\text{OX}}$   $\text{kg}^{-1}$ , 0.12 mmol P is adsorbed by 1 mmol  $\text{Fe}_{\text{OX}}$   $\text{kg}^{-1}$  and 0.04 mmol P is adsorbed by 1 mmol ( $\text{Fe}_{\text{CBD}} - \text{Fe}_{\text{OX}}$ )  $\text{kg}^{-1}$ . On a per mole basis the aluminium oxides ( $\text{Al}_{\text{OX}}$ ) adsorb nearly twice as much phosphate as the oxalate-extractable iron oxides. This may be caused by poorer crystallinity (higher specific surface area) of the aluminium oxides compared to the iron oxides, but it could also be attributed to a higher charge on the former [24].

Apart from other coefficients to  $\text{Al}_{\text{OX}}$ , and  $\text{Fe}_{\text{OX}}$ , the main difference between the two pedotransfer functions is that the function of [24] accounts for crystalline ( $\text{Fe}_{\text{CBD}} - \text{Fe}_{\text{OX}}$ ) as well as amorphous iron ( $\text{Fe}_{\text{OX}}$ ) and aluminium ( $\text{Al}_{\text{OX}}$ ), while only amorphous oxides are considered by Van der Zee [38]. According to Szilas et al. [51], amorphous aluminium and iron oxides are undoubtedly the dominating phosphate adsorbents, especially on heavily fertilised non-calcareous soils and sandy soils of humid temperate regions such as parts of Canada and Western Europe. However, crystalline iron oxides corresponding to ( $\text{Fe}_{\text{CBD}} - \text{Fe}_{\text{OX}}$ ) can be important phosphate adsorbents in more tropical upland soils and some clayey soils of drier climates [24]. Therefore, application of the pedotransfer function of [38] should be restricted to temperate, non-calcareous soils as pointed out by [11], while the pedotransfer function of [24] is expected to have a wider application range.

The pedotransfer function of [24] was, however, found to overestimate PAC of Ghanaian and Tanzanian soils (mainly Oxisols and Ultisols) enriched in well-crystallised iron oxides corresponding to ( $\text{Fe}_{\text{CBD}} - \text{Fe}_{\text{OX}}$ ) [47]. This is because the coefficient (0.04) to the term ( $\text{Fe}_{\text{CBD}} - \text{Fe}_{\text{OX}}$ ) was found to be too high. In fact, this coefficient is very uncertain and insignificant as is the intercept, whereas the  $\text{Al}_{\text{OX}}$ , and  $\text{Fe}_{\text{OX}}$  coefficients were highly significant [24].

In order to widen its applicability, the following linear expression was used with data from a wide range of soils including Danish Entisols, Inceptisols, and Spodosols [24]

together with strongly developed Ghanaian and Tanzanian Alfisols, Inceptisols, Oxisols, and Ultisols [7]:

$$P_{\text{calc}} = x \text{Al}_{\text{OX}} + \beta x \text{Fe}_{\text{OX}} + \gamma x (\text{Fe}_{\text{CBD}} - \text{Fe}_{\text{OX}}) \quad (8)$$

The regression analysis resulted in the following pedotransfer function with  $P_{\text{calc}}$ ,  $\text{Al}_{\text{OX}}$ ,  $\text{Fe}_{\text{OX}}$ , and  $\text{Fe}_{\text{CBD}}$  in  $\text{mmol kg}^{-1}$ :

Where  $x$   $\beta$   $\gamma$  are the coefficient of  $\text{Al}_{\text{OX}}$ ,  $\text{Fe}_{\text{OX}}$  and  $\text{Fe}_{\text{CBD}} - \text{Fe}_{\text{OX}}$  respectively.

$$P_{\text{calc}} = (0.22 \pm 0.03) x \text{Al}_{\text{OX}} + (0.12 \pm 0.03) x \text{Fe}_{\text{OX}} + (0.02 \pm 0.01) (\text{Fe}_{\text{CBD}} - \text{Fe}_{\text{OX}}) \quad (9)$$

The three parameters were found to be significant at 0.1% level [47]. The calculated PAC was plotted against experimentally determined values of the phosphate adsorption isotherms based on phosphate adsorption data. The linear regression line for this plot has  $R^2 = 0.87$ , indicating that 87% of the variation in PAC of the soils is accounted for by oxalate-extractable aluminium and iron together with dithionite-citrate-bicarbonate-extractable iron. Furthermore, the slope of the regression line is indistinguishable from 1, and the intercept is 0 [47].

#### 4.2.1 Predictability of the PTF of Borggaard et al.

The PTF of Borggaard [24] has been tested on a wide range of soils. Soil samples were from Denmark, Canada, Ghana and Tanzania representing non calcareous Alfisols, Entisols, Histosols, Inceptisols, Mollisols, Oxisols, Spodosols and Ultisols. While the Danish soils covered several soil groups, the Ghanaian and Tanzanian soils were restricted to strongly weathered soils, mainly Acrisols and Ferralsols and the Canadian soils were Podzols. Despite the great variability of the soil samples, the investigation clearly demonstrated the very close relationship between phosphate adsorption capacity (PAC) and contents of Al and Fe oxides, and hence the fairly good predictability of PAC by means of Al and Fe oxide-based PTF [47]. This was in general agreement with results of previous studies carried out, however, on fewer and considerably less different soil samples [11, 24].

In Ghana, Owusu-Benoah et al. [40] evaluated P sorption characteristics of the ploughed layer of six natural Ghanaian Oxisols. Except for one soil in which phosphate adsorption capacity calculated ( $P_{\text{calc}}$ ) using the PTF was more than twice that for phosphate adsorption capacity ( $P_{\text{max}}$ ) determined from the Langmuir's adsorption isotherm, measured ( $P_{\text{max}}$ ) and modelled ( $P_{\text{calc}}$ ) P sorption capacities were in fair agreement.

Further testing of this PTF was performed by data from two Tanzanian Andisols. The results demonstrated, however, that PAC of these soils is substantially overestimated by the function. The poor predictability of PAC of soils developed on volcanic materials compared to that of the other soils is probably due to differences of the main phosphate adsorbents. While poorly crystalline aluminium silicates (allophane and imogolite) with very high specific surface area, and hence, PAC can dominate phosphate adsorbents in Andisols, the other soils adsorb most phosphate onto more or less crystallised aluminium and iron oxides [7, 8]. Consequently, the pedotransfer function  $P_{\text{calc}} = 0.22 x \text{Al}_{\text{OX}} + 0.12 x \text{Fe}_{\text{OX}} + 0.02 x (\text{Fe}_{\text{CBD}} - \text{Fe}_{\text{OX}})$  is not recommended to be used for PAC estimation of Andisols. Hopefully, future testing will more precisely delineate the kinds of soils in which the suggested PTF can be used as well as those in which it would give unacceptable PAC estimates.

## **5. Conclusion**

Phosphorus adsorption in soils account for the low P availability for plant uptake.

The Langmuir, Freundlich and Temkin equations are common models for describing P sorption when input data are limited.

The review indicated that, in acid soils amorphous Al and Fe oxides compounds are the important factors that determine the soils' capacity to retain P.

For strongly weathered soils enriched in Fe and Al oxides, with different degree of ordering, a model that is able to account for the different oxide fractions and which can be used to predict the adsorption P capacity of these soils is the pedotransfer model of Borggard et al. [7].

However in alkaline soils, calcium carbonate may determine the amount of P sorbed by the soils.

### **Author details**

Samuel Kwesi Asomaning

School of Agriculture and Technology, University of Energy and Natural Resources, Sunyani, Ghana

\*Address all correspondence to: [samuel.asomaning@uenr.edu.gh](mailto:samuel.asomaning@uenr.edu.gh)

### **IntechOpen**

---

© 2020 The Author(s). Licensee IntechOpen. This chapter is distributed under the terms of the Creative Commons Attribution License (<http://creativecommons.org/licenses/by/3.0>), which permits unrestricted use, distribution, and reproduction in any medium, provided the original work is properly cited. 



## References

- [1] Cordell D, Drangert JO, White S. The story of phosphorus: Global food security and food for thought. *Global Environmental Change*. 2009;**19**: 292-305
- [2] Gilbert N. Environment: The disappearing nutrient. *Nature*. 2009; **461**:716-718
- [3] Holford ICR. Soil phosphorus: Its measurement, and its uptake by plants. *Australian Journal of Soil Research*. 1997;**35**:227-239
- [4] White RE. Retention and release of phosphate by soils and soil constituents. In: Tinker PB editor. *Soils and Agriculture*. New York: Halsted Press, John Wiley and Sons; 1981. pp. 71-114
- [5] Juo ASR, Fox RL. Phosphate sorption characteristics of some benchmark soils of West Africa. *Soil Science*. 1977;**114**: 370-376
- [6] Borggaard OK, Elberling BO. Pedological Biogeochemistry. Part 2 Paritas Grafik a/S Brøndbytoften; 2004. 396
- [7] Borggaard OK, Szilas C, Gimsing AL, Rasmussen LH. Estimation of soil phosphate adsorption capacity by means of a pedotransfer function. *Geoderma*. 2004;**118**:55-61
- [8] Borggaard OK, Jørgensen SS, Moberg JP, Raben-Lange B. Influence of organic matter on phosphate adsorption by aluminium and iron oxides in sandy soils. *Journal of Soil Science*. 1990;**41**: 443-449
- [9] Pena F, Torrent J. Predicting phosphate sorption in soils of mediterranean regions. *Fertilizer Research*. 1990;**32**:17-19
- [10] Arai Y, Sparks DL. Phosphate reaction dynamics in soils and soil minerals: A multiscale approach. *Advances in Agronomy*. 2007;**94**: 135-179
- [11] Freese D, van der Zee SEATM, Van Riemsdijk WH. Comparison of different models for phosphate sorption as a function of the iron and aluminium oxides of soils. *Journal of Soil Science*. 1992;**43**:729-738
- [12] Kleinman PJA, Bryant RB, Reid WS. Development of pedotransfer functions to quantify phosphorus saturation of agricultural soils. *Journal of Environmental Quality*. 1999;**28**: 2026-2030
- [13] Hooda PS, Rendell AR, Edwards AC, Withers PJA, Aitken MN, Truesdale VW. Relating soil phosphorus indices to potential phosphorus release to water. *Journal of Environmental Quality*. 2000; **29**:1166-1171
- [14] Del Campillo MC, van der Zee SEATM, Torrent J. Modelling long-term phosphorus leaching and changes in phosphorus fertility in excessively fertilized acid sandy soils. *European Journal of Soil Science*. 1999;**50**:391-399
- [15] Borggaard OK. Dissolution and adsorption properties of soil iron oxides [D.Sc thesis]. Copenhagen Denmark: Royal Veterinary and Agricultural University; 1990
- [16] Schwertmann U, Kodama H, Fischer WR. Mutual interactions between organics iron oxides. In: Huang PM, Schnitzer M, editors. *Interactions of Soil Minerals with Natural Organics and Microbes*. Soil Science Society of America, Madison, WI. 1986. pp. 223-250
- [17] Syers JK, Cornforth IS. Chemistry of soil fertility. In: *New Zealand Institute of Chemistry Annual Conference*, Hamilton; 1983

- [18] Toreu BN, Thomas FG, Gillman GP. Phosphate-sorption characteristics of soils of the north Queensland coastal region. *Australian Journal of Soil Research*. 1988;**26**:465-477
- [19] Jonasson RG, Martin RR, Giuliacci ME, Tazaki K. Surface reactions of goethite with phosphate. *Journal of the Chemical Society, Faraday Transactions 1*. 1988;**84**:2311-2315
- [20] Cornell RM, Giovanoli R. Factors that govern the formation of multi-domainic goethites. *Clays and Clay Minerals*. 1986;**34**:557-564
- [21] Willett IR, Chartres CJ, Nguyen TT. Migration of phosphate into aggregated particles of ferrihydrite. *Journal of Soil Science*. 1988;**39**:275-282
- [22] Schwertmann U. Aluminium substitution in pedogenen Eisen-oxiden—eine Übersicht. *Zeitschrift für Pflanzenernährung und Bodenkunde*. 1984;**147**:385-399
- [23] Barrow NJ. *Reactions with Variable-Charge Soils*. Dordrecht, Netherlands: Martinus Nijhoff Publishers; 1985
- [24] Borggaard OK. Iron oxides in relation to phosphate adsorption by soils. *Acta Agriculturae Scandinavica*. 1986;**36**:107-118
- [25] Barrow NJ, Bowden JW. A comparison of models for describing the adsorption of anions on a variable charge mineral surface. *Journal of Colloid and Interface Science*. 1987;**119**: 236-250
- [26] Nwoke OC, Vanlauwe B, Diels J, Sanginga N, Osonubi O, Merckx R. Assessment of labile phosphorus fractions and adsorption characteristics in relation to soil properties of west African savanna soils. *Agriculture, Ecosystems and Environment*. 2003; **100**:285-294
- [27] Agbenin JO. Phosphorus sorption by three savanna alfisols as influenced by pH. *Fertilizer Research*. 1996;**44**:107-112
- [28] Mokwunye U. The influence of pH on the adsorption of phosphate by soils from Guinea and Sudan savannah zones of Nigeria. *Soil Science Society of America Proceedings*. 1975;**39**: 1100-1102
- [29] Bolt GH, Van Riemsdijk WH. Surface chemical processes in soil. In: Stumm W, editor. *Aquatic Surface Chemistry*. New York: John Wiley and Sons; 1987. pp. 127-164
- [30] Sibanda HM, Young SD. Competitive adsorption of humus acids and phosphate on goethite, gibbsite, and two tropical soils. *Journal of Soil Science*. 1986;**37**:197-204
- [31] Evans A Jr. The adsorption of inorganic phosphate by a sandy soil as influenced by dissolved organic compounds. *Soil Science*. 1985;**140**: 251-255
- [32] Huang PM, Schnitzer M. Interactions of Soil Minerals with Natural Organics and Microbs. *SSSA Spec. Publ. 17*. Soil Sci. Soc. Amer., Madison, WI, USA; 1986
- [33] Huang PM, Wang MK. Formation chemistry and selected surface properties of iron oxides. In: Auerswald K, Stanjek H, Bigham JM, editors. *Soil and Environment – Soil Processes from Mineral to Landscape Scale*. *Advances in GeoEcology 30*. Reiskircheri, Germany: Caten Verlag; 1997. pp. 241-270
- [34] Huang PM, Violante A. Influence of organic acids on crystallization and surface properties of precipitation products of aluminium. In: Huang PM, Schnitzer M, editors. *Interactions of Soil Minerals with Natural Organics and Microbes*. Soil Science Society of America, Madison, WI. 1986. pp. 159-221

- [35] Bolan NS, Barrow NJ, Posner AM. Describing the effect of time on sorption of phosphate by iron and aluminum hydroxides. *Journal of Soil Science*. 1985;**36**:187
- [36] Hsu PH. Aluminum hydroxides and oxihydroxides. In: *Minerals in Soil Environments*. 2nd ed. Soil Science Society of America, Madison, WI; 1989
- [37] Yuan G, Lavkulich LM. Phosphate sorption in relation to extractable iron and aluminum in Spodosols. *Soil Science Society of America Journal*. 1994;**58**:343-346
- [38] Van Der Zee SEATM, Van Riemsdijk WH. Model for long-term phosphate reaction kinetics in soil. *Journal of Environmental Quality*. 1988; **17**:35-41
- [39] Loganathan P, Isirimah NO, Nwachuku DA. Phosphorus sorption by ultisols and inceptisols of the Niger delta in southern Nigeria. *Soil Science*. 1987; **144**:330-338
- [40] Owusu-Benoah E, Szilas C, Hansen HCB, Borggaard OK. Phosphate sorption in relation to aluminum and iron oxides of oxisols from Ghana. *Communications in Soil Science and Plant Analysis*. 1997;**28**:685-697
- [41] Parfitt RL. Phosphate reactions with natural allophane, ferrihydrite and goethite. *Journal of Soil Science*. 1989; **40**:359-369
- [42] Torrent J. Rapid and slow phosphate sorption by Mediterranean soils. Effect of iron oxides. *Soil Science Society of America Journal*. 1987;**51**:78-82
- [43] Singh B, Gilkes RI. Phosphorus sorption in relation to soil properties for the major soil types of South-Western Australia. *Australian Journal of Soil Research*. 1991;**29**:603-618
- [44] Sanyal SK, De Datta SK, Chan PY. Phosphate sorption-desorption behavior of some acidic soils of south and Southeast Asia. *Soil Science Society of America Journal*. 1993;**57**:937-945
- [45] Osodeke VE, Asawalam DOK, Kamalu OJ, Ugwa IK. Phosphorus sorption characteristics of some soils of the rubber belt of Nigeria. *Communications in Soil Science and Plant Analysis*. 1993;**24**:1733-1743
- [46] Owusu-Benoah E, Acquaye DK. Phosphate sorption characteristics of selected major Ghanaian soils. *Soil Science*. 1989;**148**:114-123
- [47] Borggaard OK. *Soil Chemistry in a Pedological Context*. 6th ed. Frederiksberg, Denmark: DSR Forlag; 2002
- [48] Van der Zee SEATM, van Riemsdijk WH. Sorption kinetics and transport of phosphate in sandy soil. *Geoderma*. 1986;**38**:293-309
- [49] Schwertmann U. Differenzierung der Eisenoxide des Bodens durch Extraktion mit Ammoniumoxalat-lösung. *Zeitschrift für Pflanzenernährung und Bodenkunde*. 1964;**105**:194-202
- [50] Reddy KR, O'Connor GA, Gale PM. Phosphorus sorption capacities of wetland soils and stream sediments impacted by dairy effluent. *Journal of Environmental Quality*. 1998;**27**: 438-447
- [51] Szilas CP, Borggaard OK, Hansen HCB, Rauter J. Potential iron and phosphate mobilization during flooding of soil material. *Water, Air, and Soil Pollution*. 1998;**106**:97-109



# Microwave Radiated Sorption-Hazardous Emission Control by Popped Borax and Salted Pumice for Coal Combustion in Thermal Power Plants

*Yıldırım İsmail Tosun*

## Abstract

Considerable research on emission control of coal combustion with popped borax and salted pumice has been conducted in this study. However, the packed bed column adsorption results are widely dispersed because of the complex chemistry of coal. Time-related hazardous emission, stack gas coal-mixing with slurries washing in microwave-heated packed bed column sorption units and cycling sorption modeling assumed basically first-order kinetic equations, or less sensitive for microwave heating rate. The other reactivity distributed on activation model was dependent on the microwave heating rate. The more advanced models for microwave radiation progressed sorption need three and four constants, respectively, which basically depend on the coal properties but also cover, to some extent, the effect of porosity and gas to salt mass transfer phenomena. That was the reactivity reason for the different conditions of sorbents values on the activation energy and pre-exponential factor. The same situation exists in the other sorbent case of coal-lead and CS, COS gas. The sorption reaction rate of popped borax and bed effected of the salt reaction of pumice and the specific surface area of pumice, which changed the sorption reaction cycle with the development of internal pores type.

**Keywords:** microwave activation, stack gas control, pollution control, postcombustion desulfurization, toxic emissions, char reactivity

## 1. Introduction

Marble wastes, fine limestone, or hydrated lime is used as sorbent in fluidized bed combustion as desulfurizing sorbent in postcombustion. Popped borax and Tatvan pumice waste and char waste are yielded in two different size forms over sand size and – 20 micron. The forest wood wastes is in lump size conventionally evaluated in char carbon industry and other may be evaluated as filling materials in fine size lower than 20 microns. The waste carbon may be evaluated as sorbent in fluidized combustion of coal in composite forms following solid-liquid separation thickeners. In this study, Şırnak asphaltite char and clayish char as sorbent coal waste or char in finer size lower than 10 mm pyrolyzed may avoid heat decrease and

without deteriorate nature and environment near thermal power plants. The waste fine of marble processing plants may be very effective in neutralizing acidic industrial waste waters and avoiding water contamination in streams. The utility of coal char and clayish char waste in toxic gas emission control during fluidized bed combustion can efficiently be made possible. However, fluidized combustion is carried out below 8 mm solid fuel combustion with addition of sorbent at weight rate of 20–25%. In order to avoid this high amount of sorbent consumption, the clayish char or coal waste could be sufficient in homogenous disturbing flow manner of that waste material, clayish coal waste and Şırnak asphaltite char or biomass waste char pellets following pyrolyzed manure and local wood waste were used in laboratory type combustion chamber at 20% weight rate.

About 40, 60, and 80% manure char containing Şırnak asphaltite pellets were used in our combustion experiments as 1–2 mm sized pellets. The popped borax and pumice waste pellets provided an 88% sulfur dioxide emission and also wood char and soot pellets provided 45% emission reduction in fluidized bed combustion. Microwave activity in wet pellet columns was found to be effective in desulphurization of flue gas and char occurrence.

In the Thermal Coal Power station in Silopi, Şırnak, Park Elektrik Co., 405 MW electricity was produced using fluidized bed combustion in three boilers by burning 232 kg coal per MW [1]. Şırnak asphaltite contained 6.7% pyrite and 3.8% organic sulfur and combusted with local limestone as 92% calcium carbonate and 4% magnesium carbonate at 10% weight rate in the fluidized bed for desulfurizing sorbent [2]. Processing technologies using animal manure and combustible municipal waste should be under contribution to the fuel side for energy production in European countries (**Figure 1**) [3]. About 49% of the total municipal waste in Sweden was converted to energy in 2014 and this rate was 39, 7, and 22% for the Netherlands, the USA, and the EU27, respectively.

Regarding advanced technological developments in energy production, the low-quality municipal wastes needed the most economical technologies. In order to make it possible to produce waste-derived fuel products as Char and even coal waste diverted source in China [4–9]. Combustible municipal waste rate reached

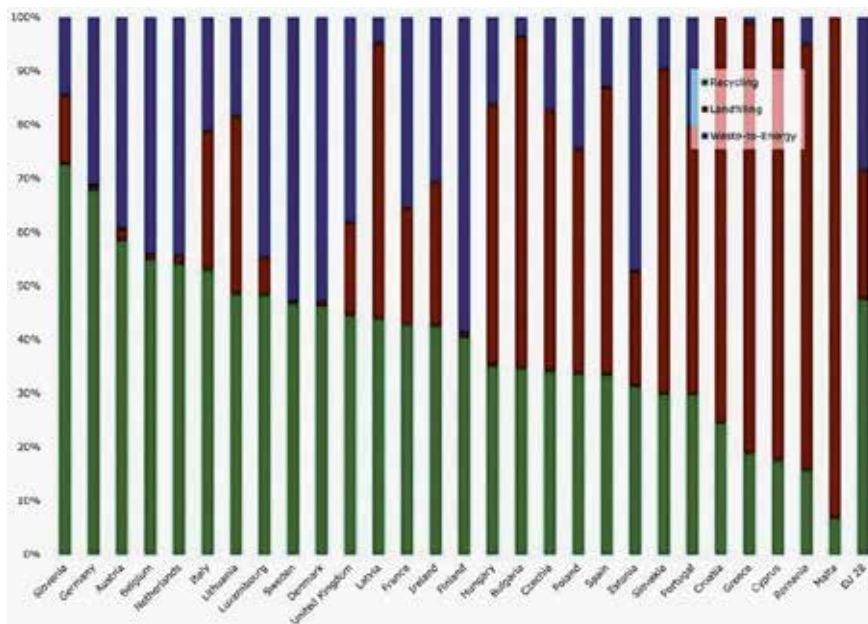


**Figure 1.** Waste-to-energy production and distribution of countries according to the European waste [3].

27.0% as paper and cardboards, and additionally, dried food waste was 14.6% and the yard waste was 13.5% after suitable segregation of the total collected waste in China in 2015 as seen in **Figure 2**.

On the way of washing and processing characteristics of the lignite as considered environment are distinctly separated in utilization and classification. In the view of producing high-value cleaned products, pyrolysis municipal waste or lignite char are being processed for their final products, managed on this active carbon purpose. Carbonized char waste and amount could also be evaluated in sorption and energy need in this study.

### 1.1 Carbonization to char

Effective carbonization processes depend on numerous factors including coal rank in carbonization and the volatile gaseous matter of coal such as the presence of hydrogen, carbonyl gas, and carbonization rate [11]. For stabilizing the desorption, the settings of optimal diffusion conditions including structure defects (nitrogen, phosphorus, sulfur, etc.), temperature, and oxygen content of coal and the optimizing carbon dioxide concentration ratios [12] added to the adsorption-desorption balance, the residence time, and the spatial distribution of molecules in coal pores among other factors that determine the efficiency of carbonization. Guerrero et al. [13] also included the carbon reactivity and the adsorption characteristics as factors affecting the rate and extent of carbonization that is dependent on the site activation, its gas desorption properties, and its porosity [14]. Carbonization is a prerequisite step for oil generation and soot formation from tire waste, biomass wastes, and coal. TGA results of waste materials showing sufficient carbon conversion are shown in **Figure 3** [15].

#### 1.1.1 Coal particle size

A major reason is that the retention time in fixed film processes is longer than that in solid-gas processes. This allows more time for carbonization by cracking the

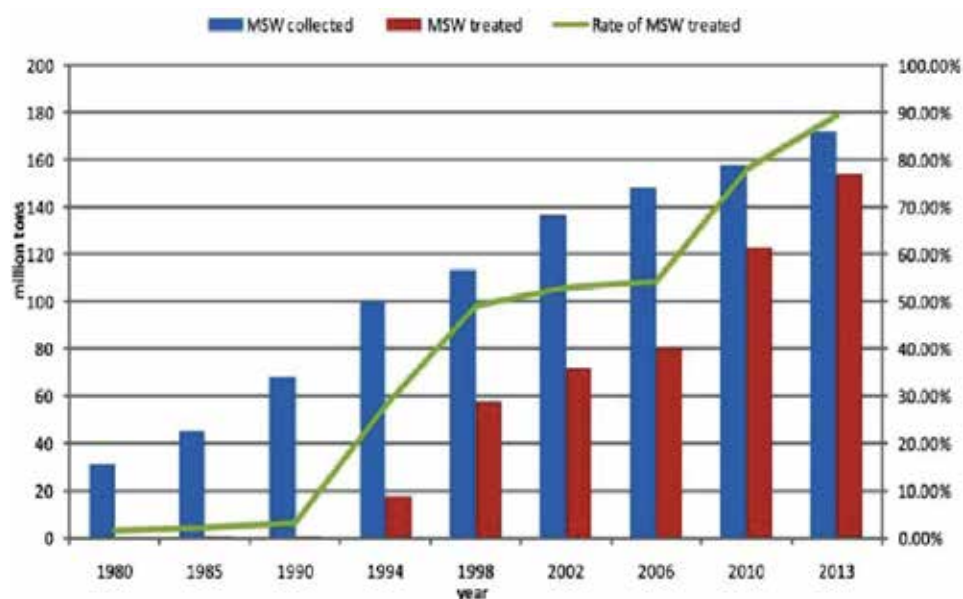


**Figure 2.** Municipal solid waste (MSW) management in China from 1980 to 2013 [10].

desorbed persistent compounds. Furthermore, high-rank coals allow sufficient intimate contact between surface pores and gas atmosphere in the furnace due to more gas desorption [16, 17].

### 1.1.2 Coal porosity

The porous structure of activated carbon is a factor that determines to a great extent both the rate and degree of carbonization [18]. Sharma et al. [19] found that a mesoporous coal carbonized more efficiently than a microporous coal.

Phenol molecules that may undergo an oxidative coupling reaction may be irreversibly adsorbed on coal, which in column back flow may result in low carbonization efficiency. Phenol radicals formed by the removal of a hydrogen atom from each phenol molecule can participate in direct coupling with other phenol-type radicals at even room temperature, with the coal surface serving as a catalyst. The types of catalysts are given in **Table 1**.

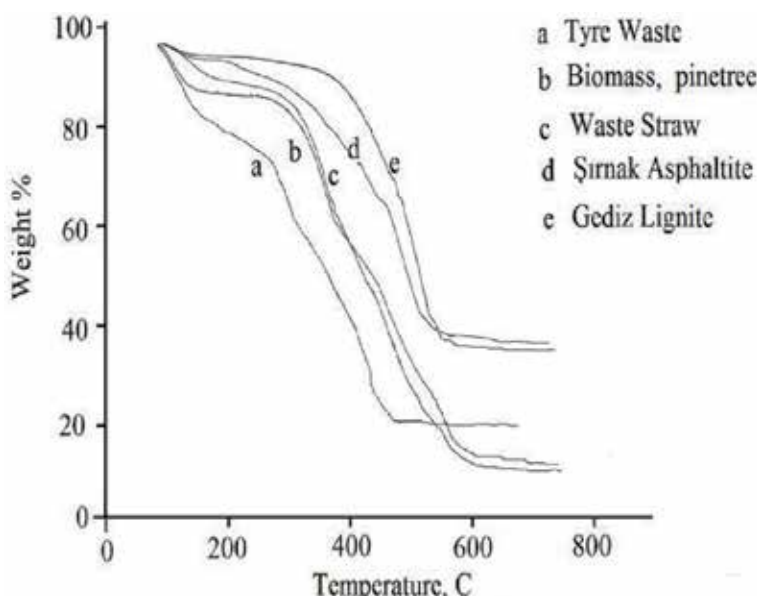


**Figure 3.** TGA analysis showing carbon conversion of different waste materials used for carbon production.

Type	Surface area m <sup>2</sup> /gr	Weight rate, %	Reaction performance	Contamination	Reference
Hematite over clay	43	34	45	Strong	
Ferrite over fly ash	20	56	33	Strong	[20]
Titanium oxide over ZEOLITE	120	12	55	Strong	
Vanadium oxide over alumina	78	23	57	Weak	
Cobalt oxide over alumina	54	12	45	Weak	
Nickel/Pt	2	77	33	Strong	

**Table 1.** The types of catalysts and substrates and properties used in gas conversion syngas production.



Carbonization efficiencies exceeding the total desorption abilities during increased fast pyrolysis on coal and wood were also reported by Tosun [21].

### 1.1.3 Surface properties of coal reactivity

The specific surface area measured as BET N<sub>2</sub> sorption, total surface activity, oxygen functional groups, total surface impurities, metal concentrations, dielectric value, free radical concentration, and reactivity of coal were related to the carbonization activity. However, in some investigations, the pore size distribution of coal is also greatly to reduce pyrolysis kinetics [15].

Although molecular gas diffusion is described to be the primary mass transport process in the combustion chamber, complex convective gas emissions proliferated the alkali clusters below 1–2 mm size and exothermic combustion reactions increased toxic substances in the gas form, and a relatively porous structure of expanded clay interstitial spaces and cracks reduced over 5 mm size. The combustion gas substances toward the expanded clay surface through this surface alkali are primarily accomplished by molecular diffusion across the microcracks and alkali clusters. In the combustion experiments, the experimental condition is calculated on the basis of the ash composition in the ambient state. So neither the contained water vapor nor the condensing hydrocarbons are taken into account. Expanded clay and limestone sorbent use in asphaltite combustion provided sufficient hold-up gas as shown in **Figure 4**.

### 1.2 Pyrolysis to char of waste coal, tire, wood, and biomass

Soot matter removal during BC treatments results from the combined effect of adsorption and degradation. The efficiency of the combined combustion of waste

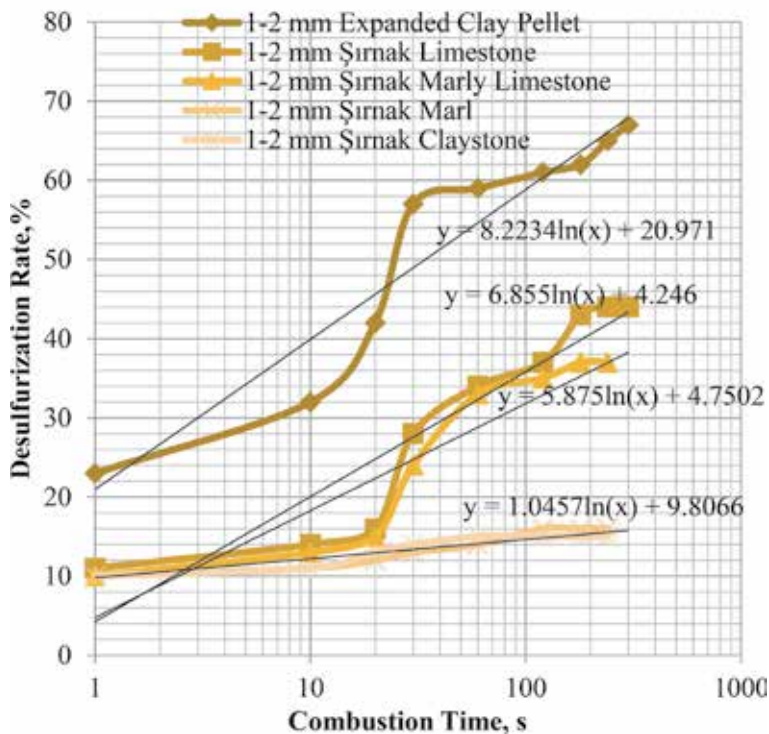


**Figure 4.** The sulfur sorption effect of expanded clay and limestone in combustion of Şırnak asphaltite [18].

for soot formation needs lack of oxygen combustion method. The process is higher than expected for either soot formation or carbon without oil alone. The carbon surface for pollutants protects them from shock loadings of toxic and inhibitory materials, such as carbon. High inert gas processes using catalyst carbon as carrier for iron film attachment are efficient to remove soot from ethylene. However, in catalytic systems, the gas attachment to surface is less efficient than that in iron film or in fluidized bed reactors using CO<sub>2</sub> and pellets as iron film carrier [22].

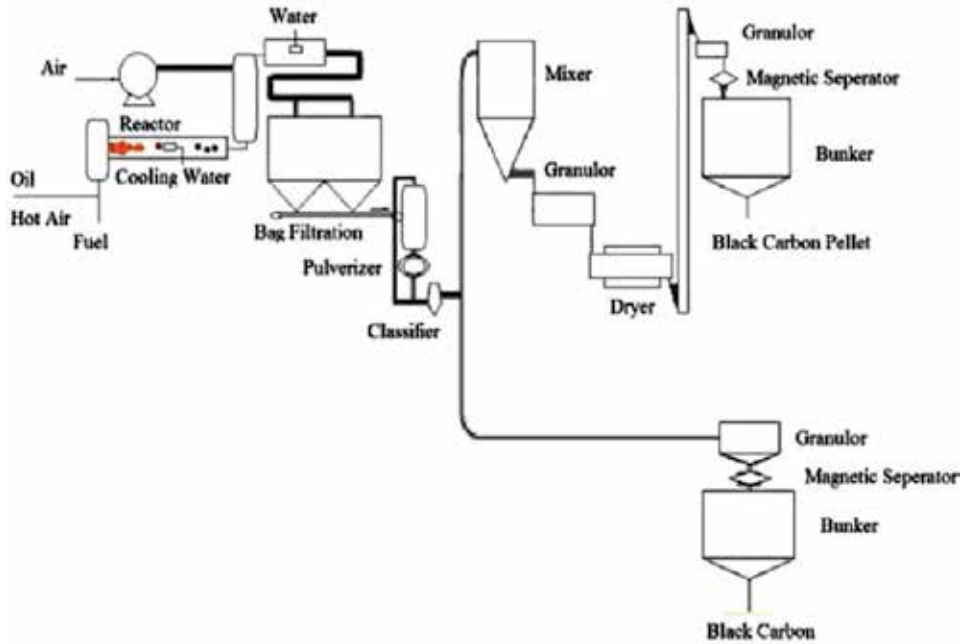


**Figure 5.** Black carbon production system, purposed plant flowsheet from waste oil and pyrolysis oil and natural gas [17].

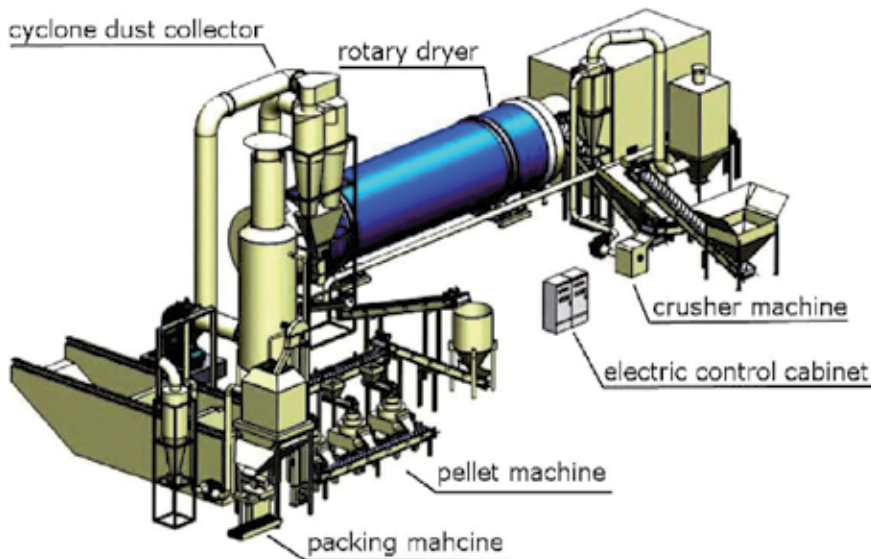


**Figure 6.** Waste carbon production system proposed for waste pyrolysis purposed furnace unit.

This is because, in the latter, then retention time of solids is generally much higher than in black carbon processes, allowing more time for gas attachment to BC.

**Figure 5** shows the flowsheet used in BC production from pyrolysis oil, waste oil, and natural gas and sometimes oil mixtures [20]. Waste char was proposed to produce from local waste sources in terms of agricultural and forest biomass waste in waste char carbon production system in waste pyrolysis purposed furnace unit for Şırnak as illustrated in **Figure 6** [20].

Carbonization of oil waste, asphalt or bitumen for active carbon production in slurries could evaluate efficiently sorption Au in pulp was commonly gold extraction systems, they use AC in fine size and as slurries gold cyanide solutions passed through. Fine activated carbon or char is more advantageous than granule AC. Additionally, powder AC provided uniform carbon site distribution on solids and agitation slurries without contamination or active site blocking. Additionally, less energy is required for milling of carbon considering the oily structure. It is a fact that pyrolysis of oil could become at low temperature carbonization blocking the active carbon sites even contaminated carbon pores when the condensate is removed from the liquid phase through furnace. The oil gradient should be determined for a suitable char production used as sorbent.

## 2. Solid sorbent use in emission control

Alkali salts such as burned lime and hydrated lime, fluorite and calcium borates, limestone, and fly ash could be used in desulfurization in coal combustion. Marble wastes, coal, and wood char produced in two different forms in size may be also evaluated as sorbent in postcombustion. One type of sorbent, carbonized wood char is in lump size and can easily be evaluated in carbon industry and other fine size may be evaluated as filling materials in paint, rubber, and plastic as fire barrier mixed at fine size under 5 microns, which are collected following solid-liquid separation and milling. Char as carbonized from coal and coal waste in finer size may deteriorate nearby environment and may be used in water treatment and avoid contamination in industrial waste streams. Beneficiating from char waste in toxic gas emission control during combustion can efficiently be made possible. However, fluidized combustion is carried out below 7 mm solid fuel combustion. Fine matters below 100 microns may deteriorate flow manner, so to avoid this disturbing flow manner of that fine char waste material, clayish char pellets were used in combustion chamber. Fine char wastes may also be evaluated with lime as sorbent raw material. The coal fly ash and Şırnak asphaltite fine could manage remediation of soil as sorbent utility without carbonation and neutralizing humate material as waste [23]. The black carbon used in industrial sectors such as rubber, paper, and animal food production may evaluate as much as 40% marble waste fine coal char and fly ash. The fly ash of Silopi Power Plant combusting Şırnak asphaltite fine containing Ca ferrite and alkali ferrite pellets could be used as sorbent in postcombustion. In this study, TGA experiments with 1–2 mm sized ash ferrite pellets of Silopi Power Plant were evaluated and compared with char.

Microwave activity and chemical activity in postcombustion were found to be effective in desulfurization of flue gas and soot occurrence. Microwave activation of fly ash with Ca ferrite and metallic slag was much efficient in humidified exhaust gas reactions. Fine chemical washing during microwave absorption columns and heating may also be evaluated as active site formation at raw material without destroying chemical form for industrial sectors such as active chemical reactivity.

### 3. Theory of adsorption on sorbent

According to the Clapeyron Equation, there is a direct proportionality between the concentration  $c$  adsorbent gas mixture and  $p$  partial pressure:

$$p = cRT \quad (1)$$

$$c = \frac{-P}{RTL\ln K} \quad (2)$$

For sorbents that have microporous mesoporous structure, Dubinin Equation for first-order isotherm

$$(w_{Ads})^n = \frac{v_{pore}}{V} e^{\left[-B\frac{T^2}{\beta^2}(\log \frac{p}{P})^2\right]} \quad (3)$$

For meso- and nanoporous sorbents,

$$\log p_2^x = \log p_2 - B\frac{T^2}{\beta^2} \log \frac{p_2}{P} \quad (4)$$

For second-order isotherm in which dynamic rate of adsorption by Shilov Equation

$$t = KH - t \quad (5)$$

$$t = \frac{a}{vc} \left[ H - \frac{T^2}{\beta^2} \left( \log \frac{p_2}{P} - 1 \right) \right] \quad (6)$$

For third-order heterogeneous adsorption, where  $K = B/v = a/vc$ , thermal power generation causes gas pollution by nitrogen oxide sulfur oxide and heavy toxic cyanide and lead emissions due to fuel contamination in Austria (**Figure 7**) [24] and coal firing power plant data for Turkey is given in **Table 2** [24].

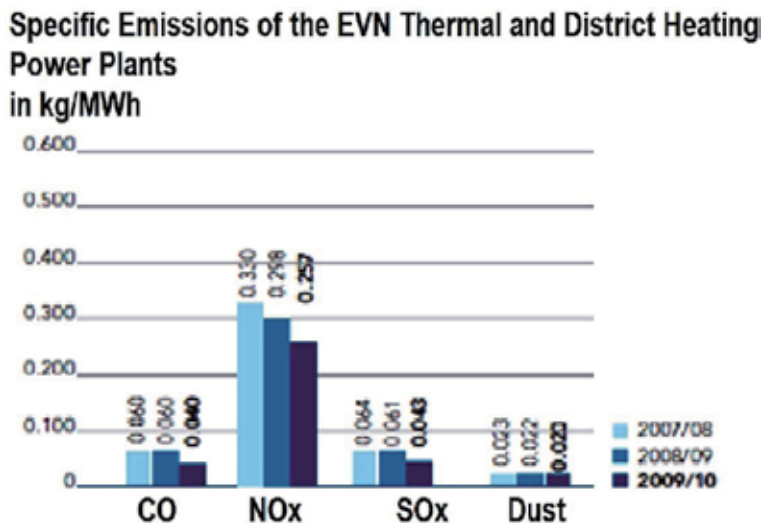


**Figure 7.** Emission of thermal power plants in Austria.

Pollution	Emission kg/MWh	Emission %/MWh
CO <sub>2</sub>	1.650	13
Particle	0.174	0.3
SO <sub>2</sub>	0.011	0.01
NO <sub>x</sub>	0.046	0.02

**Table 2.**  
*Polluting gas emission of thermal power plants in Turkey.*

### 3.1 Adsorption of SO<sub>x</sub> at combustion

The sulfur oxide emissions greatly concerned the thermal boilers and energy sector, and caused more efficient new methods for postcombustion SO<sub>2</sub> capture from the stack gas. Among procombustion and postcombustion systems, wet flue gas washing was carried out in higher and wider shower stacks, and lime slurry sorption one, which was used for a gas cleaning separation for many years. The characteristic features of adsorption column provide long life of the sorbents used, low energy consumption, and less effect on the environment. However, sorption column by lime slurries at postcombustion application required distinct preparation of the stack gas fed into the washing tower of SO<sub>2</sub> separation so that the flue gas temperature is as low as possible and with a lack of steam in it.

#### 3.1.1 Langmuir model

The gaseous matter reacts with adsorbent and then adsorbs the sorbent in certain amount that is equal to the amount of previous adsorbent that was partially degraded on the surface of the expanded clay, removing aliphatic hydrocarbons and phenols/chlorinated phenols and carbonyl toxins, along with organic matter-related odor substances.

The Langmuir model [25, 26] is the common one sorption explanation for well-known reacting column packed explaining sequential diffused and concentrated adsorbed matter and kinetics. Although the linear concentration sequentially followed, sequential adsorption packed bed column was usually experimented by various researchers for the sorption diffusion process of fuel carbon materials, and it can also be used for the sorption over leafy composites. The carbon material is soaked in fluid in an ethanol extraction vessel, and after some time, the solute is diffused from the leafy composite substrate matrix and gets adsorbed on the active surface sites, which further mass transfers to the separator vessel in the solvent. The Langmuir extraction model is presented in the following form:

$$Y = Y_f \cdot t / (K_L + t) \quad (7)$$

where Y is % extraction yield (w/w) and Y<sub>f</sub> and K<sub>L</sub> are constants (Y<sub>f</sub> is the yield at infinite time).

The temperature dependence of the adsorption coefficient is governed by an Arrhenius equation as follows [27]:

$$K_L = K_{0L} \exp(-ERT) \quad (8)$$

where E is the activation energy (kJ/mol), K<sub>0L</sub> is the pre-exponential coefficient, and R is the universal gas constant.

### 3.2 Microwave activation of wet char

This type of microwave treatment may be advantageous in internal selective heating and activating coal grains and provides selective surface oxidation of pyrite in coal desulfurization.

Microwave energy with frequency nonionizing electromagnetic radiation in the range of 300 MHz to 300 GHz stopped. The radiation includes tri-band microwave frequency (UHF: 300 MHz to 3 GHz), super high frequency (SHF: 3 GHz and 30 GHz), and extremely high frequency (EHF 30 GHz to 300 GHz) [28]. The microwaves penetrate the depth of the sample in the form of electromagnetic energy, which increases the temperature of the sample volume, unlike conventional heating [29].

Mineral leaching in slurries under microwave thermal effect, melting of the microwave wet roasting of sulfide concentrates, wet oxidation of refractory gold concentrates, and activated carbon regeneration can be accomplished in wet solutions [30, 31]. There will be wet solutions of ferrite affected by microwave heating as sorbent effect of fly ash of Şırnak asphaltite same as that of limestone rock [20, 21, 32].

Microwave heating technology provides oxidation heating and the interaction was determined to be applicable successfully [28]. Microwave interaction parameters of rocks, microwave penetration, expansion of different mineral grains, and grain boundary cracking properties were examined. The temperature varies according to the thermal effects of microwave on mineral species [33]. **Table 3** showed microwave radiation, the higher penetration of mineral grains of pyrite as given and has lead 1019°C like a temperature change.

Pore structure of the coal side rock, shale texture, contained pyrite at grain size in microns and determined the resistance at intergranular interaction with microwave. The wet heat sorption of the coal's texture of side rocks and coal was determined with TGA standard test.

Mineral	Maximum temperature, °C	Time, min
Albite	69	7
Chromite	155	7
Chalcopyrite	920	1
Zinabar	144	8.5
Gehlenite	956	7
Hematite	1082	7
Magnetite	1258	2.75
Marble	74	4.25
Molybdenite	192	7
Orthoclase	67	7
Pyrite	1019	6.75
Pvrotine	586	1.75
Quartz	79	7
Sphalerite	88	7
Zircon	52	7

**Table 3.**  
*Mineral microwave thermal interaction values [33].*

## 4. Materials and method

The biochar and char waste with clay produced from different combustion temperatures at 700–900°C were tested in three column series for adsorption of SO<sub>2</sub> as seen in **Figure 5**. Test results were determined as weight change in TGA.

The experimentation studied weight adsorbed matter presenting decrease or increase at TGA analyzer and simulated numerical calculations of the carbon porous counted system for letting sequential passage of the flue gas fed as the wet SO<sub>2</sub> sorption, by primarily under vacuum pressure swing sorption separation unit, containing the absorption chiller (AC). Steam matter in flue gas affected resulted numerical concept, Mainly it is assumed that gas flowing as the wet flue gas which occurred in comparison upper and lower heat source for AC; the flue gas, which is larger heat carrier so that required by the AC, heat exchangers must be practiced.

### 4.1 Microwave acted hollow fiber membranes use for gas sorption

The SEPURAN® hollow membrane was effective in gas separation and cleaning. The gas cleaning unit compromised various membrane systems for different applications. SEPURAN® Green is tailored exactly to the specific application, which was ideally clean biogas due to its high CO<sub>2</sub>/CH<sub>4</sub> selectivity.

### 4.2 The reactivity for gas sorption

Gas sorption sequential columns and composite sorbent membranes provided adsorption work according to the principle of selective gas permeation through the char and composite membrane surface. The reactivity and active site pore improve permeation and the inner site mass rate of each gas depend on its solubility on the char surface and active composite membrane material and on the diffusion rate of the gas.

The active char could improve reactivity and high mobility of molecules that pass through the composite membrane. The larger gas molecules take more time to permeate the membrane. The experiments showed that different type of composite polymer membrane materials could work heavier gas separately. The mainly selective gas passage through the membrane in order to clean the flue gases was achieved by means of a partial pressure gradient.

### 4.3 Active char production from municipal waste

Municipal solid waste (MSW) yielded worthless litter as disposed matter and recycled or covered by land in certain areas, and in many states, it may evaluate as a renewable energy source by incineration. Totally, about 130 million tons of MSW are incinerated annually in waste-to-energy facilities that produce electricity and steam for district heating and even metal contents may be recovered in recycling plants. A large amount of paper is recycled in China, evaluating a significant amount of paper sludge and residue during the paper production process. The incineration plants [34] can use that sludge and provide waste elimination. Currently, two incineration methods, distinguished as either direct incineration of partially dewatered sludge (generally 80% water content) or dried sludge incineration (dried to about 40% water content), are available. Research on comparison of fixed cost, operating cost, and pollutant emissions between the two systems is presented. Fixed cost and steam consumption increase for the dried sludge

incineration system though this method possesses many advantages; these include the decrease in consumption of auxiliary coal, service power, and flue gas purification.

#### 4.4 Adsorption of SO<sub>x</sub> at combustion

The distinct character of adsorption column sorption in packed bed layer was mainly long life use of the sorbents, consuming low energy. The alkali and lime slurries used for washing protect the environment from acid rains and acidic gas emissions such as chlorides and sulfates. Higher column units are used sequentially and in cycling manner provide much efficient capture of the toxic gases in the flue gas fed into the postcombustion system with SO<sub>2</sub>, even lead and cyanide gases

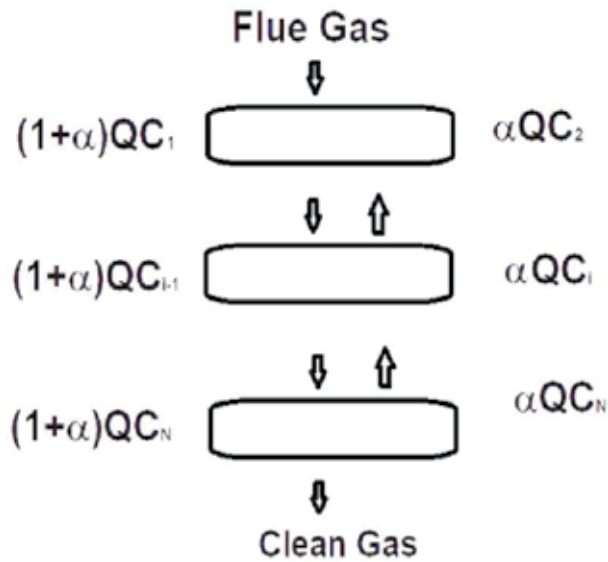


**Figure 8.** Adsorption amount sequent at back mixing model for column sorption [23].

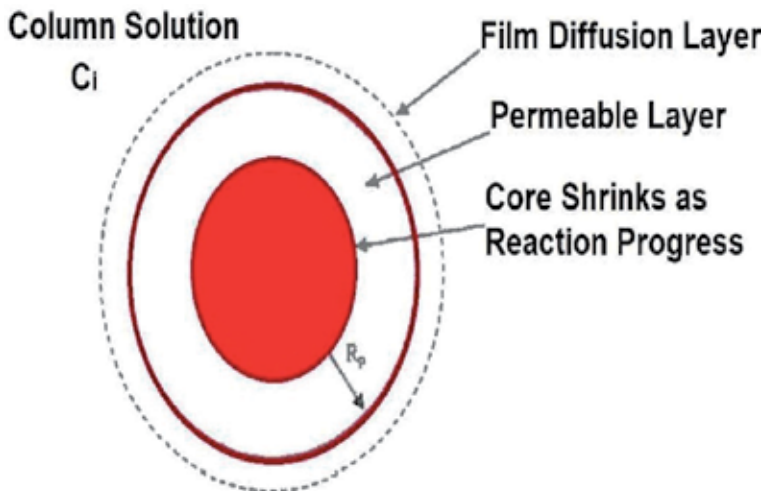


**Figure 9.** Proposed adsorption model, sequential column series in fluidized bed combustion of Şirnak asphaltite.



separated on char and composite waste char clay composites so that the flue gas temperature is as low as possible, and there is no water content in it.

Microwave heating of wet coal char samples containing pyrite of minerals may provide the inner thermal stress and interfacial cracks. In this work, following microwave sorption and pellets to a size of minus 1–2 mm from 200  $\mu\text{m}$  and especially, the effect of microwave radiation on char sorption of those char and ferrite fly ash samples was investigated. Limestone and lime mixed pellets were also tested by TGA with microwave wet sorption in columns on combusted Şırnak asphaltite; marl from Şırnak Coal Mine and shale taken from coal mine waste dumps were also tested. In the experiment, microwave power of 900 W microwave radiation were practiced at 20 min cycling sorption bed in Bosch-type microwave laboratory equipment, as shown in **Figure 8** [35–37].

Hydrodynamic parameters investigated pressurized column (**Figure 9**), and simulation results of the output of concentrations (step curve  $F(t/\tau)$ , where  $\tau$  is the mean residence time of fluid in the column) are shown in **Figure 10**. According to

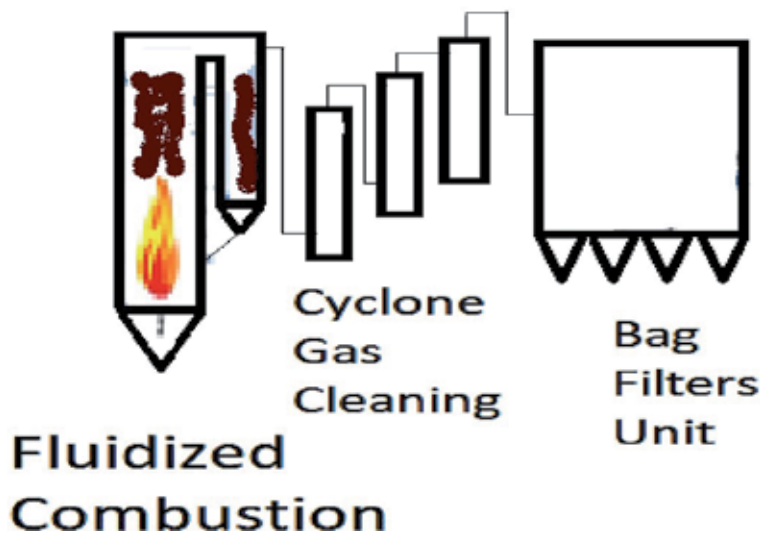


**Figure 10.** Microwave radiation carried out in wet steam of stack gas flow in pressurized packed counter current flow matter.

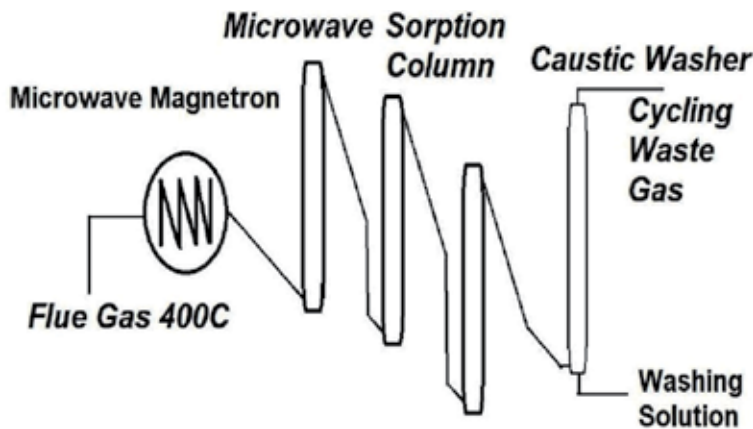


**Figure 11.** Spherical core shrinking sorption reaction model [23].

the shape of the curves in column adsorption shown in **Figure 11**, the response of the stage-wise back mixing model changes from a mixed flow condition managed at low pressure.

## 5. Results and discussions

The popped borax-char column temperature produced from different combustion flue gas exit level or long duration of cooling of exhaust system (**Figures 12 and 13**). The temperatures at 50–200°C were tested in three column series for adsorption of SO<sub>2</sub> as seen in **Figure 14**. Test results were determined as weight in TGA.

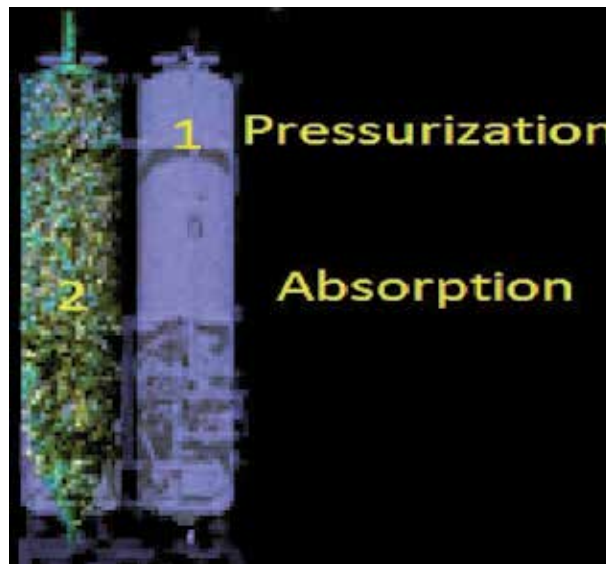


**Figure 12.**  
Adsorption column used in postcombustion with packed popped borax-char carbon tubes.

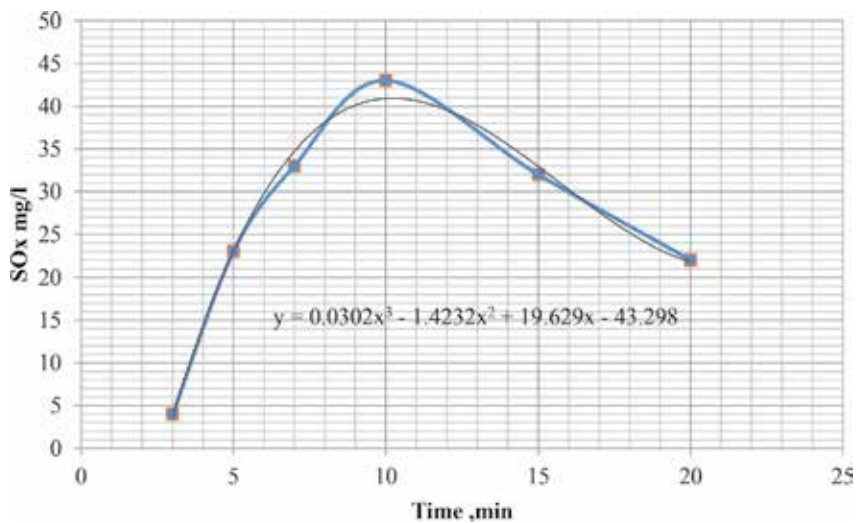


**Figure 13.**  
SO<sub>x</sub> output concentrations packed bed residence time of waste gas in the column unit.

The popped borax-char column humidity produced from different combustion fuel and combustion temperature exit or fuel moisture content in the exhaust system. The steam amount in flue gas at exhaust chamber that varied at 5–20% was tested in three column series for adsorption of SO<sub>2</sub> as seen in **Figure 15**. Test results were determined as weight in TGA.

Advanced materials and technologies should be used to prevent pollution of exhaust gas; the material used in this study is finally concluded as efficient and high cut with ecological environmental protection (**Figure 16**).

The representative popped borax composite samples at 1–3 mm sized pellet fractions of combustion Şirnak asphaltite, shale and coal waste raised SO<sub>2</sub> sorption weight by the microwave radiation increased to 23, 21, and 12% at decreasing pressure., respectively, and all those valuse with char raised to 46, 24, and 14% at decreasing pressure. Microwave wet heating of porous coal did not change. The optimum sorption with char and ferrite using column was effective far more than waste coal and limestone as was discussed in microwave heating ability and heat conduction in the wet column designed in laboratory TGA.

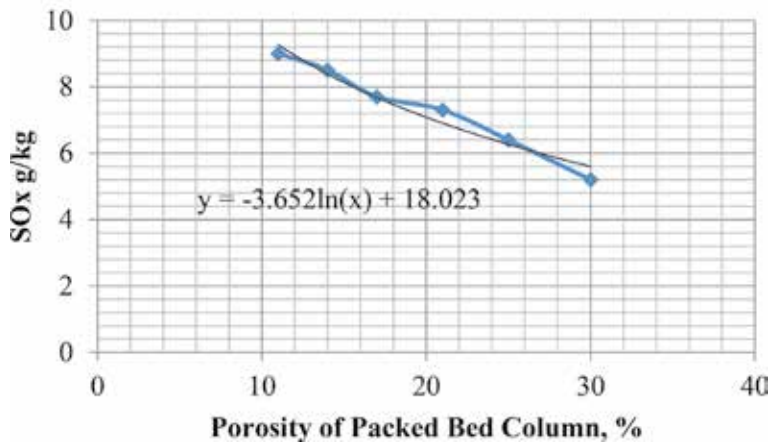


**Figure 14.**  
The effect of adsorption pressure effect on sorbent pore change as %.

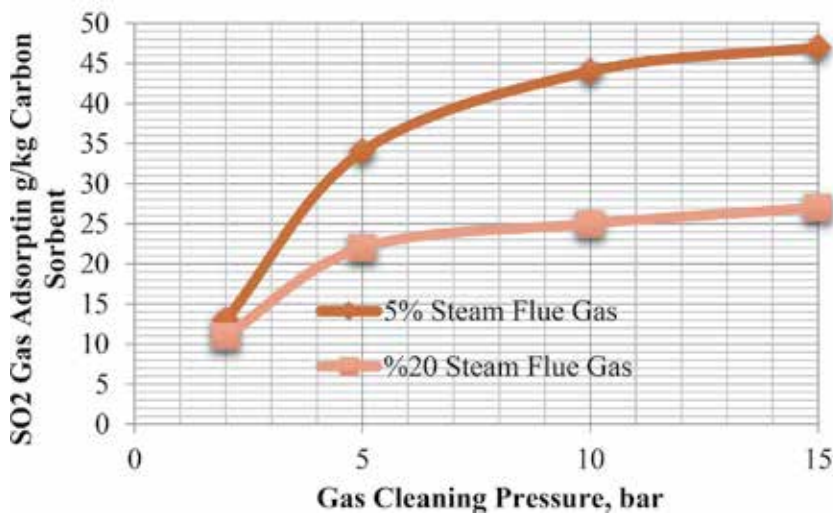


**Figure 15.**  
The effect of adsorption pressure effect on sorbent weight change as %.

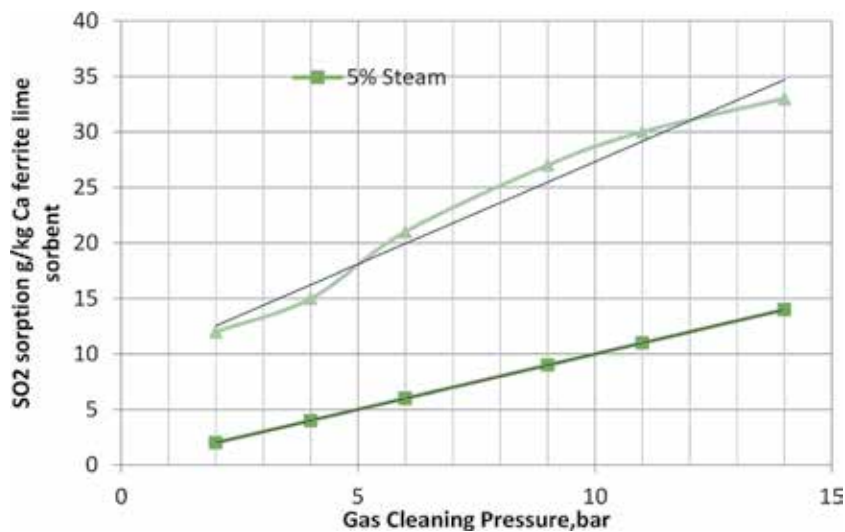


**Figure 16.**

*The effect of adsorption pressure effect on pumice popped borax compost sorbent weight change as %.*

## 6. Conclusion

Fine marble waste and char composite may also be evaluated as lime raw material for sorbent material in power sectors and industrial furnaces such as rubber, paper, and wood plants.

The popped borax and char waste pellets managed at 10 minutes in packed bed with a porosity of 21 and 88% sulfur dioxide emission hold up and soot reduced 45% emission reduction in fluidized bed combustion.

The results showed expansion of the operational envelope for gas having much steam carryover and improved performance of the modified column. For low pressures, the modified column can remove all the toxic emissions from the gas stream, resulting in low steam carryover (separation efficiency = 70%). The study of emission control at sustainable development from many aspects in power generation was compulsory, and then advanced materials and technologies should be used to prevent pollution of exhaust gas. The material used in this study is finally concluded as efficient and high cut with ecological environmental protection.

## Abbreviations

AC	activated carbon
C	constant defined in Eq.(1)(g/kg)
D <sub>p</sub>	mean pore diameter of adsorbent (nm)
PD	intraparticle diffusion
k <sub>p</sub>	rate constant (mg/(g min <sup>1/2</sup> ))
V	surface of adsorbate (cm <sup>2</sup> g <sup>-1</sup> )
r	volume of adsorbate (mL)
D	distance in radial direction of adsorbent; 0 < r < R (cm)
ε	adsorbent dose (g L <sup>-1</sup> )
ρ <sub>P</sub>	void fraction in the adsorbent
d	particle density of adsorbent (g cm <sup>-3</sup> )

m	weight of adsorbent (g)
E <sub>a</sub>	activation energy (J mol <sup>-1</sup> )
R	gas constant (8.314 J mol <sup>-1</sup> K <sup>-1</sup> ) or Radius of the particle of adsorbent in the Crank model (cm)
T	temperature (K)
S <sub>ext</sub>	specific area of the adsorbent due to external surface(m <sup>2</sup> /g)
S <sub>PBET</sub>	specific surface area of the adsorbent (m <sup>2</sup> /g)
t <sub>ref</sub>	the longest time in adsorption process (min)
V <sub>micro</sub>	micropore volume of the adsorbent (cm <sup>3</sup> /g)
V <sub>pore</sub>	total pore volume of the adsorbent (cm <sup>3</sup> /g)
D <sub>effA</sub> =1-YAYB/DAB +YC/DAC+YD/DAD	Diffusivity
(k <sub>a</sub> )	adsorption and
(k <sub>b</sub> )	desorption rate constants
k <sub>i</sub>	is the IPD rate constant [mg/(g·min <sup>0.5</sup> )], and
B	is the initial adsorption (mg/g)

## Author details

Yıldırım İsmail Tosun

Department of Mining Engineering, Şırnak University, Şırnak, Turkey

\*Address all correspondence to: [yildirimtosun@sirnak.edu.tr](mailto:yildirimtosun@sirnak.edu.tr)

## IntechOpen

© 2019 The Author(s). Licensee IntechOpen. This chapter is distributed under the terms of the Creative Commons Attribution License (<http://creativecommons.org/licenses/by/3.0>), which permits unrestricted use, distribution, and reproduction in any medium, provided the original work is properly cited. 

## References

- [1] TKI, 2013. The Turkish Ministry of Energy, Energy, Dept., Lignite Coal Report
- [2] Global EIA Report, 2013, Silopi Thermal Power Plant Proposal Sheet
- [3] EEA, 2015, EEA Coal Institute, Coal Report. EU29 Report
- [4] Anonymous, 2015b. Yakma Kazanları, Available from: <http://www.alfakazan.com.tr>, Alfa Kazan ve Makine AŞ, Ankara
- [5] Anonymous, 2015c. Kalina Cycle. İmparator Enerji, GeoPower, İstanbul. Available from: <http://www.imparatorenerji.com.tr>
- [6] Anonymous, 2015d. Akışkan Yataklı Yakma Kazanı, Mimsan A.Ş., İstanbul. Available from: <http://www.mimsan.com.tr>
- [7] Anonymous, 2015e. Available from: <http://www.atlasinc.dk/>
- [8] Anonymous, 2015f. Available from: <http://www.santes.com.tr/>
- [9] Anonymous, 2015g. Available from: [http://www.ottusa.com/mobile\\_systems/mobile\\_systems.htm](http://www.ottusa.com/mobile_systems/mobile_systems.htm)
- [10] Chinese Environmental Ministry. Statistical Document over Municipal Waste Report. Beijing: China Source; 2015
- [11] Mendiara T, Alzueta MU, Millera A, Bilbao R. Oxidation of acetylene soot: Influence of oxygen concentration. *Energy Fuels*. 2007;**21**(6):3208-3215
- [12] Amal C, Esarte C, Abián M, Millera A, Bilbao R, Alzueta MU. Characterization and reactivity of soots obtained under different combustion conditions. *Chemical Engineering Transactions*. 2010;**22**:251-256
- [13] Guerrero M, Ruiz MP, Millera A, Alzueta MU, Bilbao R. Characterization of biomass chars formed under different devolatilization conditions: differences between rice husk and eucalyptus. *Energy Fuels*. 2008;**22**(2):1275-1284
- [14] Bell DA, Towler BF, Fan M. *Coal Gasification and Applications*. Oxford: Elsevier Inc.; 2011. ISBN: 978-0-8155-2049-8
- [15] Tosun YI. Benefaction and pyrolysis of Şirnak asphaltite and lignite. *IJCCE International Journal of Clean Coal and Energy*. 2014a;**3**(2):13-18. DOI: 10.4236/ijcce.2014.32002
- [16] Kajitani S, Suzuki N, Ashizawa M, et al. CO<sub>2</sub> gasification rate analysis of coal char in entrained flow coal gasifier. *Fuel*. 2006;**85**:163-169
- [17] Tosun Yİ. Partial fast pyrolysis of Turkish coals. In: IMPS 2014, Kuşadası, Turkey. 2014b
- [18] Shadle LJ, Monazam ER, Swanson ML. Coal gasification in a transport reactor. *Industrial and Engineering Chemistry Research*. 2001;**40**:2782-2792
- [19] Sharma A, Saito I, Takanohashi T. Catalytic steam gasification reactivity of hypercoals produced from different rank of coals at 600-775°C. *Energy & Fuels*. 2008;**22**:3561-3565
- [20] Tosun Yİ. Black carbon production from şirnak asphaltite coal and wood. In: BMPC 2015, XVI. Balkan Mineral Processing Symposium, 17–19 Haziran, Belgrad. 2015a
- [21] Tosun YI. Ferrite nano fill catalyst clay pellet production. In: 15th International Multidisciplinary Scientific GeoConference SGEM 2015, SGEM2015 Conference Proceedings, Albena Resort, Bulgaria. ISBN 978-619-7105-42-1/ISSN 1314-2704. 2015b. DOI: 10.5593/SGEM2015/B61/S24.009

- [22] Jess A, Andresen A-K. Influence of mass transfer on thermogravimetric analysis of combustion and gasification reactivity of coke. *Fuel*. 2009;**89**(7). DOI: 10.1016/j.fuel.2009.09.002
- [23] Tosun Yi. Microwave pyrolysis of coal slime and wood straw by pyrite for active carbon product. *EJONS International Journal on Mathematic, Engineering and Natural Sciences*. 2018; **2**:116-123
- [24] Tosun YI. Semi-fused salt-caustic mixture leaching of Turkish lignites–Sorel cement use for desulfurization. In: *Proceedings of 13th International Mineral Processing Symposium, Bodrum, Turkey*. 2012
- [25] Manohar B, Kadimi US. Extraction modelling and characterization of bioactive components from *Psoralea corylifolia* L. obtained by supercritical carbon dioxide. *Journal of Food Processing & Technology*. 2012;**3**:144
- [26] Murthy TPK, Manohar B. Mathematical modeling of supercritical carbon dioxide extraction kinetics of bioactive compounds from mango ginger (*Curcuma amada* Roxb). *Open Journal of Organic Chemistry*. 2014;**2**: 36-40
- [27] Al-Jabari M. Modeling analytical tests of supercritical fluid extraction from solids with Langmuir kinetics. *Chemical Engineering Communications*. 2003;**190**:1620-1640
- [28] Walkiewicz JW, Clark AE, McGill SL. Microwave assisted grinding. *IEEE Transactions on Industry Applications*. 1991;**27**(2):s.239-s.243
- [29] Gabriel C, Gabriel S, Grant EH, Halstead BSJ, Mingos DMP. Dielectric parameters relevant to microwave dielectric heating. *Chemical Society Reviews*. 1998;**27**:s.213-s.223
- [30] Kelly RM, Rowson NA. Microwave reduction of oxidised ilmenite concentrates. *Minerals Engineering*. 1995;**8**(11):s.1427-s.1438
- [31] VanWyk EJ, Bradshaw SM, Swardt JB. The dependence of microwave regeneration of activated carbon on time and temperature. *Journal of Microwave Power and Electromagnetic Energy*. 1998;**33**(3):151-157
- [32] Tosun Yi. Elimination of toxic gas emissions by MgO soaked expanded clay in waste combustion chambers. In: *GCGW 2015, XV. Global Conference on Global Warming Symposium, 24-27 Mayıs, Athen*. 2015c
- [33] Walkiewicz JW, Kazonich G, McGill SL. Microwave heating characteristics of selected minerals and compounds. *Minerals and Metallurgical Processing*. 1988;**5**(1):39-42
- [34] IEA. 2012. *World Energy Outlook*
- [35] Jacob J, Chia LHL, Boey FYC. Review—thermal and non-thermal interaction of microwave radiation with materials. *Journal of Materials Science*. 1995;**30**(21):s.5321-s.5327
- [36] TKI. 2009. *The Turkish Ministry of Energy, Energy, Dept., Lignite Coal Report*
- [37] TTK. 2009. *The Turkish Ministry of Energy, Energy, Dept., Hard Coal Report*





# Treatment of Agro-Food Wastewaters and Valuable Compounds Recovery by Column Sorption Runs

*Jacques Romain Njimou, Fridolin Kouatchie Njeutcha, Emmanuel Njungab, André Talla and Nkeng George Elambo*

## Abstract

Olive oil extraction generates a large quantity of wastewater which is a strong pollutant due to its high organic load and phytotoxic. However, its content in antibacterial phenolic substances displays to be resistant to biological degradation. The discharge of olive mill wastewater (OMWW) is not allowed through the municipal sewage system and/or in a natural effluent. Unfortunately, the current technologies for the treatment of OMWW are expensive and complicated to be operated in a mill factory where the objective of this study. We have designed and implemented a process that permitted both the treatment of agro-food processing water and the recovering of compounds of market interest. The process was applied in the effluents of olive oil mill factories to recover polyphenols with a possible significant reduction of organic waste. The nanofiltration fraction obtained from a sequential treatment involved coagulation, photocatalysis, ultrafiltration and nanofiltration was performed to separate the most valuable compounds using column adsorption runs. Competitive adsorption and the selectivity were obtained for phenol and hydroxytyrosol onto macro-reticular aromatic polymer (FPX66) and macroporous polystyrene cross-linked with divinylbenzene (MN202), respectively. The investigations were followed by a single component of phenol or tyrosol, binary phenol and tyrosol and ternary components in NF concentrate of OMWW for valuable compounds recovery conducted in a fixed-bed adsorber of resins. During the intermediate stage of the column operation, adsorbed tyrosol molecules were replaced by the incoming phenol molecules due to the lower tyrosol affinity for FPX66 resin and the tyrosol concentration was higher than its feed concentration.

**Keywords:** OMWW, ultrafiltration, nanofiltration, fixed-bed column, polyphenols recovery, polymeric resins

## 1. Introduction

Phenol and phenolic species are chemicals commonly found in various industrial waste in general and in a particular in olive mill wastewater. Phenol is also known as

carbolic acid. It's a white crystalline toxic solid with a sweet tarry odor commonly referred to as a "hospital smell"; with a pKa of 9.98 and solubility of 8% (wt.) in the water at 25°C. In fact, the US Environmental Protection Agency (EPA) and the European Union (EU) directive number 80/778/EC consider phenol as a priority pollutant [1]. The concentration of phenol in wastes varies in a wide range from several ppm to 2–3% and phenols degradability are limited. Several techniques are available currently for the treatment of phenolic effluents.

Adsorption processes have been intensively used in wastewater treatment for phenol and other organic compounds. Phenols in olive mill wastewaters (OMWW) have very complex compositions and the treatment feasibility has to be separately made through experimental approaches [2–6]. Conventional fixed bed processes involve a saturation, adsorption or loading step, followed by desorption, elution or regeneration steps [7]. The use of granular activated carbon (GAC) for removing toxic organic chemicals including phenol from wastewater is one of the best commercially proven methods. Although activated carbons exhibit an excellent adsorption capacity for the removal of phenol from wastewater, this method exhibited the difficulty to its regeneration and quite expensive to dispose of [7–12].

Therefore, the necessity of the alternative adsorbents which are equally effective and easier to regenerate and recently, a new kind of hypercrosslinked polymeric adsorbent was found to be very effective for removing aromatic compounds from aqueous solutions [5, 7, 13, 14]. Macroreticular resins are the most promising in the separation processes due to its easier regeneration and it is well used in industrial practices. The wide variations in functionality, surface area, and porosity available for macroreticular resins present the possibility of its selective separation of the effective components. Furthermore, the regeneration of the resins can easily be accomplished with a solvent and hence, the adsorption of phenol can be realized by macroreticular resins. Numerous studies on the removal of metals and organic pollutants by these adsorbents in discontinuous systems have been reported [10, 11, 15]. However, the application in continuous systems i.e. in a fixed-bed column is often preferred, since it is simple to operate, given to high yields and can be scaled-up in the laboratory process. In order to design and operate fixed-bed adsorption process successfully, both equilibrium and dynamic adsorptions in specified systems must be known. The indicators are the breakthrough curves under specified operating conditions must be predictable. The shape of this curve is determined by the shape of the isotherm equilibrium and it is influenced by the individual transport processes in the column of adsorbent [10, 11, 15].

In this chapter, the experimental results on adsorption tests performed by resins were presented. The polyphenols are extracted from a nanofiltration concentrate stream produced during the purification of olive vegetation wastewater from a 3 phase process. This wastewater contains many polyphenols, mostly hydroxytyrosol, which may have a market.

The high organic content of olive wastewater exhibits to its impossible direct recovering of polyphenols content. The high suspended solids in the raw stream will quickly block the adsorption column, making the recovery process difficult. Moreover, many other interfering and undesired pollutants would interfere with the recovery process. For this reason, the recovery of polyphenols will be accomplished on a pretreated stream that is the concentrate of nanofiltration which is produced after the treatment of the raw wastewater by flocculation, photocatalysis and ultrafiltration. The concentrate of nanofiltration is rich enough of polyphenols to permit a suitable recovery from a technical and economical point of view.

## 2. Materials and methods

### 2.1 Packaging of wastewaters from olive mills

The samples of water were placed in 30 L bottles and were transported to the laboratory. The samples of OMWW were kept at  $-20^{\circ}\text{C}$  for the later use. The research process developed in the laboratory for processing OMWWs is comprised of the steps described below.

### 2.2 Protocol processing of OMWW in laboratory pilot

The processes applied during the treatment of agro-food wastewaters (OMWW) and valuable compounds recovery are the following:

#### 2.2.1 Sieving of OMWW

The OMWW were separated from solid particles by using a 300-micron sieve.

#### 2.2.2 Clarification by coagulation-flocculation for removing particles

The coagulation helps to destabilize the suspended particles and facilitate their agglomeration. This method is characterized by injecting and dispersing chemicals. The flocculation aims to promote contact between the destabilized particles through slow mixing. These particles combine to form a flock which is removed by decantation. The water flocculation was performed by nitric acid at the temperature of  $50^{\circ}\text{C}$  and the initial pH of 5.2 was reduced to 3.0; followed the photocatalysis.

#### 2.2.3 Photocatalysis

The heterogeneous photocatalysis is based on the interaction of the light and nanoparticles. Photocatalysis has been an innovative and promising technique for the purification of wastewater. The titanium dioxide ( $\text{TiO}_2$ ) is the most of the common catalyst used nowadays due to its high performance, low cost, high photoactivity, low toxicity, chemical stability, insolubility and the resistance to photo-corrosion. The photocatalysis of clarified water stirred by a stirrer type Heidolph RZR 2014 was carried out by [16, 17]; on magnetic nanoparticle size of 79 nm coated with titanium oxide. The device is irradiated by a UV lamp VL-315 BLB 3x15W-385 nm Tube Power 90 W made in France for 4 h followed by the membrane treatment.

#### 2.2.4 Ultrafiltration

The clarified OMWW was ultra-filtered on GM membranes, GK, GH and GE Type (TFM) tubular listed in **Table 1** with the cutoff between 100 and 200 kDa, and the recovering of the permeate. The ultrafiltration method is followed by nanofiltration.

#### 2.2.5 Nanofiltration step

The permeate obtained by ultrafiltration is nano-filtered on DK and DL; spiral and tubular membranes type (TFM) listed in **Table 1** with the cutoff between 150

ID	Type of operation	Material	P <sub>max</sub>	T <sub>max</sub>	Pore size
JX	MF (microfiltration)	PVDF	12	T <sub>max</sub>	300.00nm
JW	UF (ultrafiltration)	PVDF	12	50°C	n.d
GM	UF	TFM	16	50°C	2.00 nm
GK	UF	TFM	16	50°C	1.63 nm
GH	UF	TFM	16	50°C	0.90 nm
GE	UF	TFM	16	50°C	0.63nm
DL	NF(nanofiltration)	TFM	32	50°C	0.65 nm
DK	NF	TFM	32	50°C	0.50 nm
AK	RO (reverse osmosis)	TFPS	70	50°C	< 0.1 nm
SG	RO	TFPP	70	50°C	< 0.1 nm
SC	RO	TFPP	70	50°C	< 0.1 nm

PVDF: difluorure de polyvinyl, TFC or TFM: thin-film composite membranes, TFPP: talc filled polypropylene co-polymer, TFPS: thin-film polymer on silicon.

**Table 1.**  
Characteristics of membrane modules used.

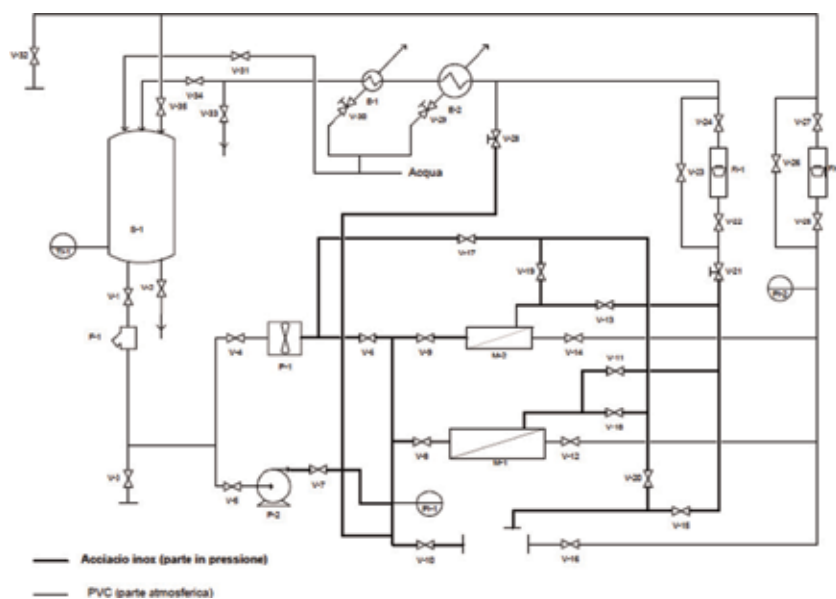


**Figure 1.**  
Schematic of the pilot plant used.

and 400 Da, and at the maximum pressure of 16 Bar. Following this operation is obtained the rich fraction in polyphenols called nanofiltration concentrate. This concentrate is used in the adsorption/desorption tank for the separation of toxic compounds and the recovery of polyphenols of interest. If the operation is pursued we have the reverse osmosis which leads to the production of pure water. The membrane characteristics of this operation are recorded in **Table 1** and both **Figures 1** and **2** present the installation of the pilot plant used in the membrane treatment.



**Figure 2.**  
*Photography of the pilot plant used (Ecosystem S. L Technologies).*

### 2.3 Schematic description of the pilot plant

The pilot plant used is Ecosystem S. L Technologies and described as the following [18–21]:

S<sub>01</sub>: Feed tank with the capacity: min 10 liters, max 100 liters where is introduced the water to be treated.

F<sub>01</sub>: Cartridge filters of 50  $\mu\text{m}$  to remove power remaining solids.

P<sub>01</sub>: Volumetric pump.

P<sub>02</sub>: Centrifuge pump.

M<sub>01</sub>: Housing for medium size membrane modules, mod. 2540, area 2.51  $\text{m}^2$ .

M<sub>02</sub>: Housing for small size membrane modules, mod. 1812, area 0.52  $\text{m}^2$ .

FI<sub>01</sub>: Flow-meter concentrate stream.

FI<sub>02</sub>: Flow-meter permeate stream.

E<sub>01</sub>: concentrate heat exchanger (big).

E<sub>02</sub>: concentrate heat exchanger (small).

V<sub>xx</sub>: valves ( $x = 1, 2, 3, \dots, 35$ ).

OMMW pre-treated feedstock was stored in a feed tank (FT1) of 100 L. The centrifugal (P1) and volumetric (P2) pumps to drive the wastewater stream over the spiral-wound membrane supplied by osmotic fitted in the housing M1, at a flow rate of 600 L/h. The active membrane area of each module was 2.51  $\text{m}^2$  [18–21].

The maximum one for the used membranes in this work that can be obtained constantly on this system, for the ultrafiltration (“UF”), the nanofiltration (“NF”) and the reverse osmosis (“RO”) type is reported in **Table 2**. The membranes are characterized when new by their pure water permeability value  $m_w$ , the average of the pore size  $D_p$  and the maximum operating pressure  $P_{\text{max}}$ . The membrane modules were used under the flux threshold conditions at least of 1000 operating hours. Each module exhibited reduced pure water permeability values compared to new ones. By acting on the regulation valves  $V_1$  and  $V_2$ , it was possible to set a desired operating pressure  $P_{\text{EXT}}$  over the membrane by maintaining a feed constant flow rate with an accuracy of 0.5 bar. The permeate and concentrate streams were cooled down to the feedstock temperature, mixed together and the feedstock composition was maintained constant during each experimental batch run. The temperature was

set at  $20 \pm 1^\circ\text{C}$  for all experiments [18, 19, 22]. The pretreatment processes aim to reduce TSS and organic matter by measuring the COD. The results obtained by the authors [18, 19, 22] are shown in **Table 2** and are reported as a percentage of the reduction ( $\Delta\%$ ). The adsorption step on polymeric resins is applied after the membrane treatment and obtaining the fraction of nanofiltration.

#### 2.4 Characteristic and activation of FPX66 and MN202 resins

FPX66 and MN202 resins were provided courtesy of Rohm & Haas aromatic and Puroilite Ltd., respectively. The physicochemical characteristics of these resins are summarized in **Table 3**. FPX66 and MN202 resins were activated by using sodium

Type	Characteristic of membrane modules [18, 19, 22]				
	Id	$m_w$ [L/hm <sup>2</sup> bar]	$m_w$ [L/hm <sup>2</sup> bar]	$D_p$ [nm]	$P_{max}$ [bar]
UF	Osmonics model GM	16.3	4.8	2.0	16
NF	Osmonics model DK	7.9	5.2	0.5	32
RO	Osmonics model SC	2.7	2.6	< 0.1	65
Stream	Pretreatment of OMWW raw materials [18, 19, 22]				
	COD		TSS		pH
	[g/L]	$\Delta\%$	[g/L]	$\Delta\%$	—
Raww OMWW	32.4	—	33.0	—	5.2
After flocculation	22.2	31.5	10.9	66.9	3.1
After centrifugation	19.2	13.5	8.4	22.9	—
After photocatalysis	16.5	14.1	5.2	38.1	—

**Table 2.**  
Characteristics of the membrane and the pretreatment of OMWW.

Properties	FPX66	MN202
Physical form	White spherical beads	White spherical beads
Matrix	Macro-reticular aromatic polymer	Macroporous polystyrene cross-linked with divinylbenzene
Moisture holding capacity	60–80%	50–60%
Shipping weight	680 g/L	655–685 g/L
Specific gravity	1.015–1.025	1.04
Surface area <sup>(2)</sup>	$\geq 700$ m <sup>2</sup> /g	825 m <sup>2</sup> /g
Porosity <sup>(2)</sup>	$\geq 1.4$ cc/g	1–1.1 mL/g
Mean diameter	Harmonic mean size 0.600–0.750 mm	535 $\pm$ 85 $\mu\text{m}$
Particle size	$\leq 2.0$	d50, meso and macropores: 600–900
• Uniformity coefficient <sup>(1)</sup>	<0.300 mm:3.0% max >1.180 mm:5.0% max	D50, micropores: 15
• Fine content <sup>(1)</sup>		
• Coarse beads <sup>(1)</sup>		

**Table 3.**  
Physicochemical characteristics of the resins FPX 66 and MN202.

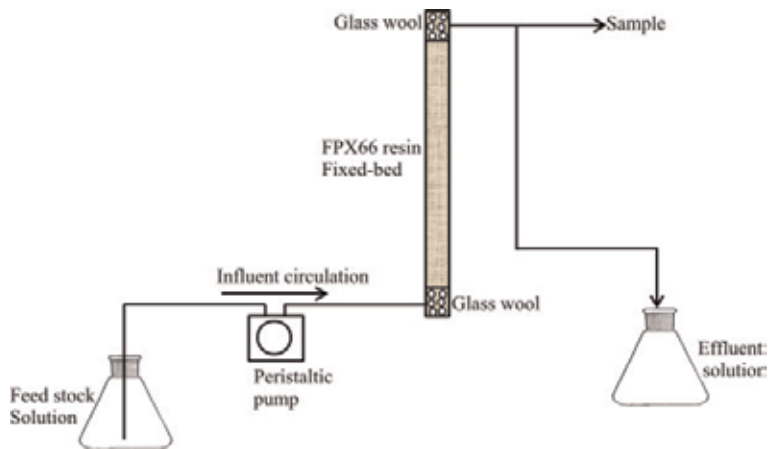


**Figure 3.**  
*Schematic of the experimental setup in upward mode.*

chlorite and washing with distilled water and then filtrating with a Buchner filter connected to a vacuum pump system. The filtrated resins were put into the beakers that already contained distilled water and the resulting solution was then left at constant stirring (70 rpm) for an hour. At the end of this procedure, the quantities of dissolved salts were evaluated through a digital conductivity meter. Since the results were not satisfactory, the new filtrations were made and the stirs were repeated, again for 60 minutes.

The solutions were again measured at the end and the decreases in salt concentrations were revealed. Finally, the treated resins were put into others beaker containing 96% ethylic alcohol, and then the contents of the beakers were stirred (120 rpm) for an hour. After this procedure, the resins were filtrated and conserved in a distilled water environment ready for use.

## 2.5 Column adsorption and desorption experiments

Lab-scale packed bed column experiments were carried out to evaluate the performance of the resin for the adsorption of phenolic compounds. In a typical procedure, the fixed-bed columns were made of Pyrex glass tubes of 1 or 2 cm inner diameter with 9.5 and 19.5 cm height respectively. The model column was packed with the adsorbent between glass wool and supported by inert glass beads as shown in **Figure 3**.

The column performance adsorption onto resin was studied at different phenol concentrations of 200, 400 and 600 mg/L, bed height 9.5 and 19.5 cm and flow rate between 0.8–4.0 mL/min. The bed diameters and depths took were 10.0 and 19.5 cm (resin mass of 5.07 g), 2.0 and 19.5 cm (resin mass of 41.6 g), respectively. The influent of phenol solution was pumped in an upward mode with a peristaltic pump in order to avoid channeling inside the column.

### 2.5.1 Performance indicators in a fixed-bed column

The breakthrough curves showed the loading behaviour of phenol, tyrosol and hydroxytyrosol to be removed in a fixed bed. It is expressed in normalized concentration defined as the ratio of effluent solute concentration to inlet (feed) solute concentration ( $C_{out}/C_{in}$ ), as a function of time or volume of effluent for a given bed height [23].

Effluent volume ( $V_{\text{eff}}$ ) can be calculated by the following relationship:

$$V_{\text{eff}} = Q t_{\text{total}} \quad (1)$$

where  $Q$  and  $t_{\text{total}}$  are the volumetric flow rate (mL/min) and the total flow time (min). The adsorption performance for a given bed mass is directly related to the number of bed volumes (BV) processed before the breakthrough point is reached [24]. The number of bed volumes treated before a breakthrough can be calculated as follows:

$$\text{BV} = \frac{\text{Volume of water treated at breakthrough point (L)}}{\text{Volume of adsorbent (L)}} \quad (2)$$

The rate for saturating the adsorbent during adsorption run was used to determine the regularity at which the adsorbent was replaced or regenerated. The adsorption exhaustion rate (AER), where low AER values imply the good performance of the bed was given by [23, 25] Eq. (3):

$$\text{AER} = \frac{\text{mass of adsorbent (m, (g))}}{\text{Volume of water treated (L)}} \quad (3)$$

The area under the breakthrough curve ( $A$ ) calculated by integrating the plot of adsorbed concentration ( $C_{\text{ad}}$ ; mg/L) versus  $t$  (min) and used to find the total adsorbed phenol or tyrosol quantity (maximum column capacity). The total adsorbed phenol or tyrosol quantity ( $q_{\text{total}}$ ; mg) in the column for a given feed concentration and the flow rate was calculated as the following:

$$q_{\text{total}} = \frac{QA}{1000} = \frac{Q}{1000} \int_{t=0}^{t=t_{\text{total}}} c_{\text{ad}} dt \quad (4)$$

The total amount of phenol or tyrosol in feed sent to column ( $m_{\text{total}}$ ; mg) is calculated by:

$$m_{\text{total}} = \frac{C_{\text{in}} Q \cdot t_{\text{total}}}{1000} \quad (5)$$

Equilibrium phenol/tyrosol uptake ( $q_{\text{eq}}$ ; mg/g) (or the maximum capacity of the column) in the column is defined as the total of solute adsorbed ( $q_{\text{total}}$ ) per g of adsorbent ( $X$ ; g) at the end of total flow time, that is:

$$q_{\text{eq}} = \frac{q_{\text{total}}}{X} \quad (6)$$

The column performance (Total removal percentage of solute) can be defined as the ratio of the total adsorbed quantity of phenol/tyrosol ( $q_{\text{total}}$ ) to the total amount sent to the column as follows:

$$\text{Column performance (\%)} = \frac{q_{\text{total}}}{m_{\text{total}}} \times 100 \quad (7)$$

Unadsorbed phenol/tyrosol concentration at equilibrium in the column ( $C_{\text{eq}}$ ; mg/L) can be defined by the following relationship:

$$C_{\text{eq}} = \frac{m_{\text{total}} - q_{\text{total}}}{V_{\text{eff}}} \times 1000 \quad (8)$$



In respect to the breakthrough separation of phenol, tyrosol and HO-tyrosol in binary and in OMWW NF concentrate:

A. Tyrosol solution with 100% purity is represented by Time (h) in which the outlet contains the only tyrosol since its breakpoint (B.T = Breakthrough time) as:

$$\Delta V_{100}(\text{mL}) = Q[\text{Time}_{(100\%)} - \text{Time}_{(\text{B.T})}] \quad (9)$$

B. Tyrosol solution with 90% purity is represented by Time (h) in which the outlet contains the only tyrosol at 90% and phenol at 10% since its breakpoint (B.T = Breakthrough time) as:

$$\Delta V_{90}(\text{mL}) = Q[\text{Time}_{(90\%)} - \text{Time}_{(\text{B.T})}] \quad (10)$$

C. In multi-component system OMWW NF concentrate, polyphenol solution with 100% purity (tyrosol and hydroxytyrosol) is represented by latest time (h) at which the outlet stream contains the target polyphenols of this study, that is tyrosol and hydroxytyrosol, at 100% purity towards phenol since their breakpoint (B.T = Breakthrough time) as:

$$\Delta V_{100}^*(\text{mL}) = Q[\text{Time}_{(100\%)} - \text{Time}_{(\text{B.T})}] \quad (11)$$

D. Tyrosol+ Hydroxytyrosol solution with 90% purity is represented by Time (h) in which the outlet contains only tyrosol+ hydroxytyrosol at 90% and phenol at 10% since its breakpoint (B.T = Breakthrough time) as:

$$\Delta V_{90}^*(\text{mL}) = Q[\text{Time}_{(90\%)} - \text{Time}_{(\text{B.T})}] \quad (12)$$

## 2.5.2 Breakthrough model studies

### 2.5.2.1 Thomas model

The Thomas model is widely used in column performance modeling. Its derivation assumes Langmuir kinetics of adsorption-desorption and no axial dispersion. The expression for the Thomas model for adsorption column is given by [26]:

$$C^* = \frac{C_{\text{out}}}{C_{\text{in}}} = \frac{1}{1 + \exp\left[\left(\frac{k_{\text{Th}}q_e X}{Q}\right) - k_{\text{Th}}C_{\text{in}}t\right]} \quad (13)$$

where  $k_{\text{Th}}$  (mL/min/mg) a Thomas constant,  $q_e$  (mg/g) the predicted adsorption capacity,  $m$  mass of adsorbent (g),  $Q$  influent flow rate (mL/min),  $C_{\text{in}}$  the initial concentration (mg/L), and  $C_{\text{out}}$  effluent concentration (mg/L). The linearization of the Thomas model was expressed in Eq. (14):

$$\text{TM} = \ln(C^* - 1) = \frac{k_{\text{Th}}q_e X}{Q} - k_{\text{Th}}C_{\text{in}}t \quad (14)$$

### 2.5.2.2 Yoon-Nelson (YN) model

Yoon-Nelson model as other models did not require data about the characteristics of the system such as well as the type of adsorbent and physical properties of adsorption bed.

The YN was expressed as follows [27]:

$$\frac{C_{out}}{C_{in} - C_{out}} = \exp(k_{YN}t - \tau k_{YN}) \quad (15)$$

where  $k_{YN}$  (L/min) the rate constant and  $\tau$  (min) the time required for 50% of adsorbate breakthrough. The linear form of YN model was expressed as follows:

$$YN = \ln \frac{C_{out}}{C_{in} - C_{out}} = k_{YN}t - \tau k_{YN} \quad (16)$$

### 2.5.2.3 Adams-Bohart (AB) model

Adams-Bohart model was based on the assumption that the rate of adsorption was proportional to the concentration of adsorbed species and the residual capacity of adsorbent. The AB model was used to describe the initial part of the breakthrough curve and expressed as [24]:

$$C^* = \frac{C_{out}}{C_{in}} = \exp\left(k_{AB}C_{in}t - k_{AB}N_0 \frac{z}{U_0}\right) \quad (17)$$

Where  $k_{AB}$  (l/min.mg) is rate constant of Adams-Bohart model,  $z$  (cm) is the bed depth,  $N_0$  (mg/L) is maximum ion adsorption capacity per unit volume of the adsorbent column, and  $U_0$  (cm/min) is the linear velocity of influent solution. The linear form of Adams-Bohart model is expressed as follows:

$$ABM = \ln C^* = k_{AB}C_{in}t - k_{AB}N_0 \frac{z}{U_0} \quad (18)$$

## 2.6 Characterization techniques

### 2.6.1 Porosity and microporosity resins

#### 2.6.1.1 Mercury porosimetry

Penetration of a liquid in a capillary is related to the shape and dimensions of the capillary, and the surface tension of mercury and the pressure that is exerted on the latter. The relationship between the pressure and the pore radius in the case of a cylindrical pore is given by the following equation:

$$p.r = 2\gamma \cos \theta \quad (19)$$

where  $r$ : is the pore radius.

$\gamma$ : mercury surface tension and equals to 480 mN.m<sup>-2</sup>. (Data Carlo Erba).

$\theta$ : contact angle equal to 141.3 degrees (data Carlo Erba).

The measuring instrument used is the automatic mercury porosimetry 2000 Carlo Erba, it gives a distribution based pore volume and the cumulative volume per cent.

#### 2.6.1.2 Measurement of micropores by *t*-plot method (thickness plot)

This method is used to estimate the volume and the surface of the micropores, or to characterize the material from the point of view of their porosity. The data

provided is the surface area of meso and macropores, and the volume of micropores. It enables the determination of the specific surface area of the micropores when coupled with the BET method. The accepted parameters for characterizing materials according to the diameter (d in nm) pores are: micropores (d < 2 nm); mesopores (2 < d < 50) macropores (50 < d < 7500) and megapores (7500 nm < d).

The calculation method is based on the layout of the volume of gas adsorbed as a function of the thickness of the monomolecular film of the same gas. This diagram called thickness is subsequently used to evaluate quantitatively and qualitatively the porosity of the adsorbent. The film thickness is calculated by either equation Halsey Eq. (20) that of Harkins and Jura Eq. (21) [28].

$$t = \left( \frac{13.99}{\log \frac{P_a}{P_c} + 0.034} \right)^{1/2} \quad (20)$$

$$t = 3.54 \left( \frac{5}{2.303 * \log \frac{P_a}{P_c} + 0.034} \right)^{1/3} \quad (21)$$

By plotting the adsorbed volume according to the calculated thickness of the film, the intercept (Y) of this curve (t-plot) is converted to the volume of gas to liquid volume to provide micropores. The slope  $\alpha$  of the linear section of the graph used to calculate the surface area of the mesopores and macropores. The corresponding formulas are given the following:

$$\text{Micropores Volume} = (0.001547) * Y \quad (22)$$

$$\text{Mesopores specific area} = 1547 * \alpha \quad (23)$$

The calculations also used to obtain the surface area A of the micropores as follows:

$$A = \text{BET specific area} - \text{Specific area of mesopores} \quad (24)$$

The shapes of the curves and hysteresis provide information on the porosity of the material studied according to the classification proposed by isothermal [29] and modified by International Union of Pure and Applied Chemistry (IUPAC) [30].

### 2.6.2 Determination of point of zero charge (PZC)

The points of zero charge of FPX66 and MN202 resins were determined [31]. In different flasks, 50 mL of NaNO<sub>3</sub> 0.1 mol/L was introduced and the pH of the solution was adjusted by using 1 mol/L NaOH or HCl to obtain a denoted pH<sub>i</sub> value between 2 and 12. One gram of activated resin was then introduced in each flasks, covered and allowed to rest for 48 hours during which they were manually stirred. At the end of the operation, the pH of the solution (pH<sub>f</sub>) was recorded. pH<sub>pzc</sub> were derived from the curve  $\Delta\text{pH} = \text{pH}_i - \text{pH}_f = f(\text{pH}_i)$  as the intercept of the abscissa for resins.

### 2.6.3 The specific surface area by the BET method

The determination of the recovery capacity by a mono-molecular layer of adsorbate (V<sub>m</sub>) allows for the calculation of the specific surface. The number (V<sub>m</sub>)

was calculated from the adsorption isotherm, mainly by the BET method depends on the surface, temperature and pressure (STP) and the form of the following linear transform:

$$A = \frac{P_e}{V_a(P_o - P_e)} = \frac{C - 1}{V_m C} \frac{P_e}{P_o} + \frac{1}{V_m C} \quad (25)$$

where  $V_m$  was the volume of a monolayer,

$V_a$  = volume adsorbed at a relative pressure  $P_e/P_o$ ;

$P_e$  = sample equilibrium pressure,

$P_o$  = saturation vapor pressure of the gas to the temperature of the experiment,

$C$  = relative constant to the enthalpy of adsorption.

The route of  $A = f(P_e/P_o)$  is a line of a slope  $(C - 1)/V_m C$ , and intercepts origin at  $1/V_m C$ . In practice, this line was checked only in a limited area of relative pressure ( $0.05 < P_e/P_o < 0.2$ ) and in many cases, it is always  $C > > 1$ . The BET specific surface area ( $m^2/g$ ) was then determined from the following expression:

$$S_{BET} = \frac{V_m \cdot N \cdot A_m}{M_v} = V_m \cdot A_m \cdot N \cdot 10^{-20} \text{ (m}^2/\text{g)} \quad (26)$$

where  $N$  = is Avogadro constant ( $6.02 \times 10^{23}$ ),

$M_v$  = Molecular volume per gram ( $22,414 \text{ cm}^3$ ),

$A_m$  = area occupied by each molecule of adsorbate ( $0.162 \text{ nm}^2$  for  $N_2$ ).

#### 2.6.4 Analysis of phenolic compounds by HPLC

High-pressure liquid chromatography (HPLC) is a technique to identify compounds within a sample by measuring the retention time through a separation column transported by a proper bulk stream. The use of high pressure permits to fasten the separation and obtain the results quicker. The measurement is done by a mass spectrometer at the exit of the separation column and is capable to measure a peak in terms of mAU, strictly connected to the concentration of the compound.

In this work, a C18 column was used. The bulk stream is composed of an aqueous solution of 1% of acetic acid. At the start of each experimental run and afterwards at regular time intervals, samples were withdrawn every 15 min, filtered through a cellulose acetate membrane filter (0.20 mm, Schleicher & Schuell) and analyzed. 25  $\mu$ L of the sample was injected into the HPLC system. The temperature of the column was 20°C and the flow-rate was 1 mL/min. The mobile phase: 0.5% acetic acid volume ("A") and acetic nitrile ("B"). Elution was performed under conditions:

- At the start of 2 min of the run with 100% of A.
- From 2 to 60 min 40% of A and 60% of B.

Polyphenols were detected by a UV detector (280 nm). Beforehand, the retention times of the polyphenolic compounds of interest were measured using single phenol, tyrosol and OH-tyrosol standard solutions ranging from a concentration of 100–600 mg/L. The chromatographic parameters, described in the following in **Table 4** [32, 33].

The quantification was based on the size of the chromatogram peaks and achieving a standard range is developed for each of the standards polyphenols.

Parameters	Details
Mediterranea sea column Serial number: NF-21905	C18, thickness: 5µm, length 25 cm Diameter: 0.46 mm
Pressure	150 bars
Temperature	20°C
Flow rate	1.0 mL/min
Eluant	Acetonitrile + acetic acid 0.5%
Injection volume	20 µL
Wavelength	280 nm

**Table 4.**  
*HPLC parameters for the determination of polyphenols.*

### 3. Fixed bed studies

#### 3.1 Effect of initial phenol concentration

The sorption breakthrough curves obtained at inlet phenol concentrations of 200, 400 and 600 mg/L at 0.106 L/h flow rate are given in **Figure 4**.

A decreasing inlet concentration gave a later breakthrough curve as displayed in **Figure 4**. The treated volume was greatest at the lowest inlet concentration due to a lower concentration gradient caused a slower transport and the decreasing in diffusion coefficient or decreasing in mass transfer coefficient. The breakpoint time decreased with increasing inlet phenol concentration as the binding sites became more quickly saturated in the system. The breakthrough concentration ( $C_t/C_o = 0.03$ ) occurred after 30 hours (3000 mL of effluent) i.e. 200 mg/L phenol inlet concentration. It appeared after 17 hours and 15,5 hours corresponding to 1700 mL and 1550 mL of inlet concentration of phenol 400 and 600 mg/L, respectively.

#### 3.2 Effect of the flow rate

The effect on flow rate for the adsorption of phenol at flow rates 0.8; 2.0 and 4.0 mL/min at an influent concentration of 600 mg/L and bed height 19.5 cm displayed in **Figure 5**. It was clearly observed that a rapid uptake was noticed in the initial stages of adsorption and decreases thereafter and finally reaches saturation. The increase in flow rate, the breakthrough curves become steeper and reach the breakpoint quickly. This probe displayed a well-defined of the residence time of the solute in the column, which was not long enough for adsorption equilibrium to be reached at a high flow rate. So at the high flow rate, the phenol solution left the column before equilibrium occurs. Furthermore, a fixed saturation capacity of bed based on the same driving force gave rise to a shorter time for saturation at a higher flow rate [8, 34, 35].

#### 3.3 Effect of bed height

The breakthrough curves for the adsorption of phenol on macro-aromatic resin FPX66 at various bed heights by fixing the influent concentration at 600 mg/L and flow rate at 2 mL/min are given in **Figure 5**. The results indicated that the throughput volume of phenol solution increased with increasing bed height, due to the

availability of more sorption sites due to the increase in the total surface for adsorption [34]. The equilibrium capacity decreases with the increase of the bed height. In a fixed bed method the probability of contact between the adsorbate and the adsorbent is less when compared to the batch mode, which results in lesser equilibrium sorption capacity in column mode.

### 3.4 Dynamic adsorption models

#### 3.4.1 Thomas model

The adsorption data were applied to the Thomas model and the results are presented in **Table 5**.

**Table 5** shows that the Thomas constant ( $k_{Th}$ ) as the equilibrium capacity  $q_{0(Th)}$  increases with the increase of the phenol concentration, the bed height increases with the decrease of the flow rate. A negligible difference was observed between experimental and calculated values of the bed capacity  $q_{0(Th)}$  obtained at all inlet phenol concentrations studied although the deviations of experimental data from predicted values were evident at 2.0 and 4.0 mL/min flow rates. Thomas model gives a good correlation with the experimental data at flow rates, bed heights for all

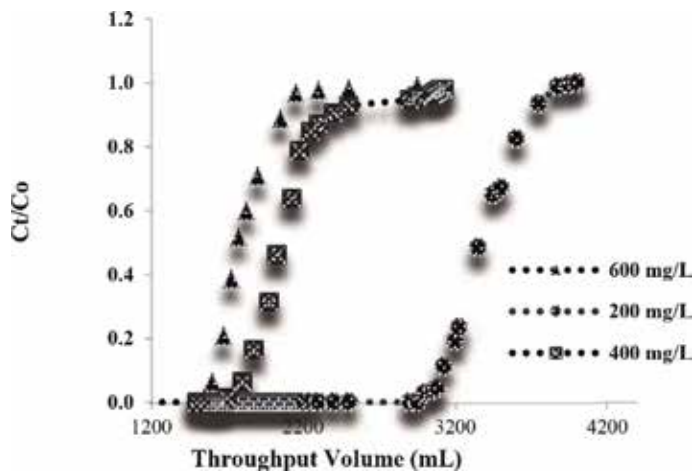


**Figure 4.** Throughput volume and breakthrough for phenol at inlet concentrations.

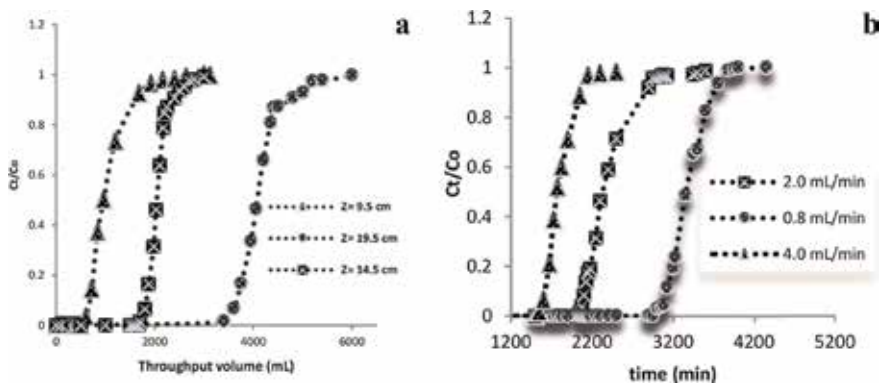


**Figure 5.** Effect of bed height (a) and flow rate (b) for the removal of phenol on FPX66 column.

Parameters	Experimental conditions					
Feed stock $C_0$ (mg/L)	200	400	600	400	400	400
Flow rate $Q$ (mL/min)	2.0	2.0	2.0	4.0	2.0	2.0
Bed height $Z$ (cm)	19.5	19.5	19.5	19.5	9.5	14.5
Mass of sorbent $X$ (g)	41.6	41.6	41.6	41.6	20.8	30.9
Mass sorbate $X$ (mg)	1372.84	1740.50	2204	1603.90	814.23	1336.92
$q_0$ (exp) (mg/g)	31.40	41.84	52.98	48.55	39.15	40.26
<b>Thomas parameters at different conditions using linear regression analysis</b>						
$k_T$ (mL/min/mg) $\times 10^{-5}$	2.08	2.13	3.21	3.12	2.7	2.43
$q_0$ (Th) (mg/g)	32.48	42.44	51.34	48.35	40.16	43.14
$R^2$	0.984	0.910	0.961	0.915	0.914	0.918
Sd	0.18	0.10	0.27	0.03	0.16	0.48
<b>Yoon-Nelson parameters at different conditions using linear regression analysis</b>						
$q_0$ (YN) (mg/g)	29.64	36.15	41.26	48.30	48.61	37.64
$K$ (YN) (L/min) $\times 10^{-2}$	1.12	1.14	1.93	1.25	1.07	0.85
$\tau$ (min)	3082	1879	1430	1256	1264	1454
$R^2$	0.959	0.918	0.961	0.15	0.914	0.966
Sd	0.29	0.94	1.95	0.04	1.57	0.43

**Table 5.**  
 Thomas and Yoon-Nelson kinetic model for phenol onto FPX66 in a fixed bed.

inlet phenol concentrations. Thomas model is suitable for adsorption processes where the external and internal diffusions will not be the limiting step [34, 36].

### 3.4.2 Yoon-Nelson model

**Table 5** showed the rate of constant  $k_{YN}$  of Yoon-Nelson increased with increasing phenol concentration. This was due to the fact that the increase in initial phenol from 200 to 600 mg/L. This displayed an increase in the competition between phenol molecules for the adsorption sites, which ultimately results in increased uptake rate. The rate constant increased with increasing the flow rate and decreased with an increase in bed height. At high flow rate, the number of phenol molecules passing through an adsorbent was more which increased the rate. The time required for 50% breakthrough  $\tau$  decreases with increasing as the phenol concentration, flow rate and bed height.

The adsorption capacities calculated based on Thomas and Yoon-Nelson models are in good agreement with the observed value with high  $R^2$  values and very low error analysis ( $0.03 \leq Sd \leq 1.95$ ). Both models describe the behaviour of phenol onto FPX66 resin column. The obtained results are in agreement with other authors [34, 36, 37].

### 3.4.3 Adsorption of OMWW NF concentrate by FPX66 resin

In order to determine the adsorption effectiveness in a more complex and realistic scenario, the FPX66 resin in fixed mode was exposed to an OMWW NF concentrated containing all polyphenols from the membrane of nanofiltration plant selected for this work [21, 22, 38]. The influent flow rate was kept at a constant flow

rate of 2 mL/min whereas the bed height, the diameter of the column and resin particle size were  $Z = 3.8$  cm,  $D = 4$  cm,  $0.600 \leq d \leq 0.750$  mm) at ambient temperature, respectively.

A considerable reduction in breakthrough time was observed for tyrosol i.e. 12; 11.5 and 6.5 hours respectively in single, binary and multiple component systems. Although the increase of breakthrough time was observed for the phenol during 17; 18 and 22.5 hours respectively proved that the selectivity was observed for phenol than other polyphenols by the FPX66 resin.

This could be attributed to competition between adsorbates for the same sites and adsorbates include benzoic acids and its derivatives (genticic, vanillic, gallic, syringic acids), cinnamic acids and derivatives such as caffeic, ferulic, sinapic acids, and phenolic alcohols, secoiridoides aglycones (oleuropein, ligstroside), flavonols, flavones and fignans etc. coexisting frequently in OMWW (**Figure 6**) and more in NF concentrate [18, 39, 40]. The macro-reticular aromatic resin pore adsorption sites could be blocked by the polyphenol molecules.

The overall outlet capacities estimated for the tyrosol and the hydroxytyrosol were only slightly enhanced plausibly indicating a combination of pore blockage and unique interactions with the FPX66 surface. Phenol ( $pK_a = 9.95$ ) has a net neutral charge, so that means binding onto FPX66 is probably to be attributed to several types of molecular interactions, including hydrophobic interaction, hydrogen bonding, ionic attraction and complex formation [41]. Azonova and Hradil [42] found that hydrophobic interaction was the binding mechanism for adsorption by the hypercrosslinked Amberlite XAD-4. In addition, Maity et al. [43] showed that the degrees of adsorption for phenols, alcohols and aromatic amines increased with the strength of the hydrogen bond between the organic chemicals and the resin. Juang and Shiau [44] found that adsorption of phenol and chlorophenol by the macroporous Amberlite XAD resins was affected by the resin's hydrophobicity, the number of active sites and pore size distribution. By comparing the adsorption of five organic chemicals, Weber and Van Vliet [45] concluded that hydrophobic interaction played a key role in the adsorption of macroporous Amberlite XAD resins. In addition, the swelling of resin-like, in this case, increases the volume of the polymer phase and, thus, the absorption capacities of organic chemicals and it is

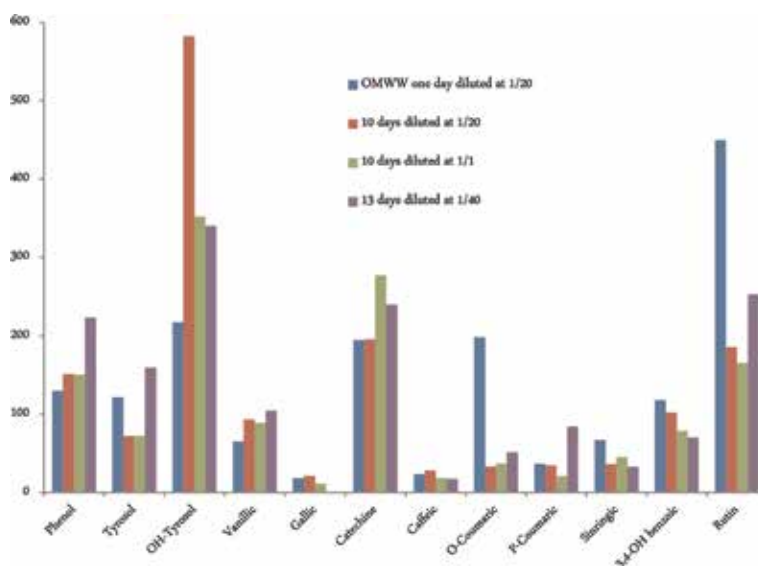


**Figure 6.** Profile of the phenolic compounds identified in nanofiltration fraction of OMWW.



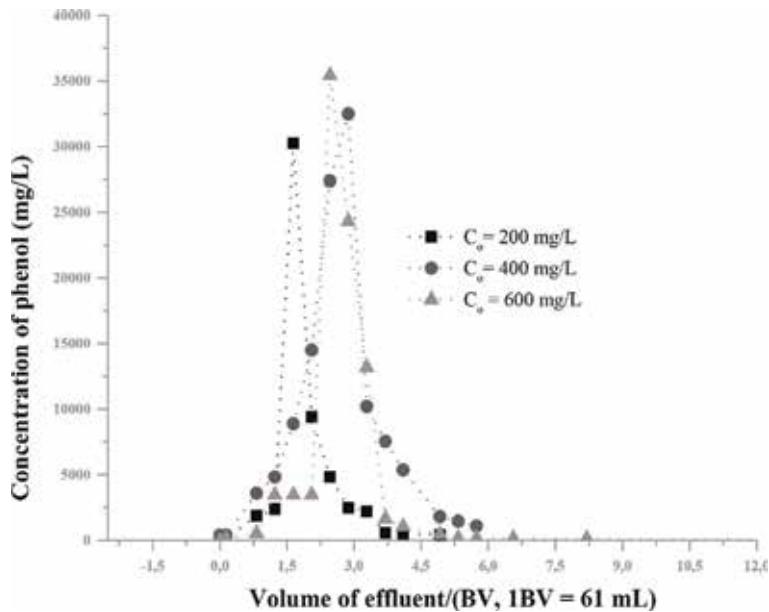


**Figure 7.**  
*Dynamic desorption curves of phenol concentrations on FPX66 resin.*

probably affected by hydrogen bonding of polar organic chemicals and the macroporous resins, such as Amberlite XAD-8 [43].

### 3.5 Dynamic adsorption/desorption

After the dynamic adsorption experiments, a 50% (v/v) EtOH solution at a flow rate of 0.1 L/h was used to purge the resin column. Desorption results are displayed in **Figure 7** for different inlet phenol concentrations of 200, 400 and 600 mg/L. About 3.0; 5.0 and 6.0-bed volumes of 50% (v/v) EtOH aqueous solution were used to regenerate the FPX66 resin column, for initial phenol concentrations of 200, 400 and 600 mg/L respectively. The desorption capacities of phenol from FPX66 resin were calculated to be 31.86, 37.06 and 48.00 mg/g at initial phenol concentrations of 200, 400 and 600 mg/L, respectively, which agrees well with the dynamic adsorption capacities of phenol with three inlet columns. This is also in agreement with the results obtained by Li *et al.* [46].

## 4. Conclusions

The study, we can conclude that FPX66 resin is an effective adsorbent for phenol removal from aqueous solutions.

From batch investigations, the effect of contact time for phenol removal by the FPX66 resin showed rapid adsorption of phenol in the first 30 min. The equilibrium data were fitted by Langmuir, Freundlich, Temkin and Dubinin-Radushkevich isotherms with good correlation coefficient  $R^2$ . The adsorption kinetics followed the pseudo-second-order model with a maximum capacity of 28.44 mg/g and obeyed the intra-particle diffusion with high  $R^2$  (>0.999). Higher desorption efficiency was obtained after 20 min of shaking time and the percentage of desorption decreased with the increase in the initial concentration of phenol.

From the fixed bed investigations, as the flow rate increased, the breakthrough curve became steeper. The breakpoint time was obtained earlier at a high flow rate and effluent phenol concentration ratio increased more rapidly. For lower bed height, the effluent phenol concentration ratio increased more rapidly than for higher bed height. For larger initial phenol concentration, steeper breakthrough curves were obtained and breakpoint time was achieved sooner. The column experimental data were fitted well to the Thomas and Yoon-Nelson models. Coming to the end, we can draw a conclusion that, the use of resin column could be completely regenerated by a 50% (v/v) ethanol aqueous solution.

## Acknowledgements

The authors express the sincere thanks to the European Commission for the Fellowship ‘Erasmus Mundus ACP’ offered and the Department of Chemical Materials Environmental Engineering of the University of Rome “La Sapienza” for their hospitality and access to scientific instrumentation.

## Conflict of interest

The authors declare that there is no conflict of interests.

## Acronyms and abbreviations

OMWW	olive mill wastewater
FPX66	macro-reticular aromatic polymer
MN202	macroporous polystyrene cross-linked with divinylbenzene
EPA	Environmental Protection Agency
EU	European Union
GAC	granular activated carbon
MF	microfiltration
UF	ultrafiltration
NF	nanofiltration
RO	reverse osmosis
PVDF	difluorure de polyvinyl
TFC or TFM	thin-film composite membranes
TFPP	talc filled polypropylene co-polymer
TFPS	thin film polymer on silicon
BV	bed volumes
BT	breakthrough
AER	adsorption exhaustion rate
IUPAC	International Union of Pure and Applied Chemistry
PZC	point of zero charge
STP	surface, temperature and pressure
HPLC	high pressure liquid chromatography

## Nomenclature

A	area under the breakthrough curve obtained by integrating ( $C_{ad}$ ) versus $t$ (mg min/L)
AER	adsorption exhaustion rate (–)

BV	bed volumes (mL)
$C^*$	normalized concentration (–)
C	constant that gives an idea about the thickness of the boundary layer (mg/g)
$C_{ad}$ ( $C_{ad} = C_o - C_t$ )	adsorbed phenol concentration (mg/L)
$C_d$	concentration in the desorption solution (mg/L)
$C_e$	equilibrium concentration of phenol (mg/L)
$C_{max}$	highest initial concentration in solution (mg/L)
$C_o$	initial concentration (mg/L)
$C_t$	effluent concentration (mg/L)
D	desorption ratio of the resin (%)
$k_{Th}$	Thomas rate constant (L/min/mg)
$k_{YN}$	Yoon-Nelson rate constant (1/min)
m	initial mass of resin in batch mode (g)
$m_{total}$	total amount of phenol in the feeding sent to the column (mg)
Q	volumetric flow rate (mL/min)
$q_{o(Th)}$	maximum Thomas adsorption capacity (mg/g)
$q_{o(cal)}$	adsorption capacity calculated using three models (mg/g)
$q_t, q_e$	amounts of adsorbed at time t and at equilibrium (mg/g)
R	gas constant (J/mol/K)
$R^2$	determination coefficient associated with data fitting (–)
t, $t_{total}$	time and total flow time (min)
T	temperature (K)
V	volume of solution (L)
$V_d$	volume of desorption solution (L)
$V_{eff}$	effluent volume (mL)
X	amount of adsorbent in the column (g)
Z	bed height column or upward vertical axial distance inside the fixed bed (cm)
$\epsilon$	void fraction in the bed (–)
$\rho_a$	density of the adsorbent material (g/L)
$\tau$	time required for 50% of adsorbate breakthrough (min)

## **Author details**

Jacques Romain Njimou<sup>1,2\*</sup>, Fridolin Kouatchie Njeutchi<sup>3</sup>, Emmanuel Njungab<sup>4,5</sup>, André Talla<sup>3,4</sup> and Nkeng George Elambo<sup>3</sup>

1 Laboratory of Analytical Chemistry, Faculty of Sciences, University of Yaoundé I, Yaoundé, Cameroon

2 School of Chemical Engineering and Mineral Industries, University of Ngaoundere, Ngaoundere, Cameroon

3 Research Center, National Advanced School of Public Works, Yaounde, Cameroon


4 Energy, Water and Environment Laboratory, National Advanced School of Engineering, University of Yaounde, Yaounde, Cameroon

5 Institut Universitaire des Sciences des Technologies et de l'éthique de Mendong, Yaounde, Cameroon

\*Address all correspondence to: njimoujacques@gmail.com

## **IntechOpen**

---

© 2019 The Author(s). Licensee IntechOpen. This chapter is distributed under the terms of the Creative Commons Attribution License (<http://creativecommons.org/licenses/by/3.0>), which permits unrestricted use, distribution, and reproduction in any medium, provided the original work is properly cited. 

## References

- [1] Hill GA, Robinson CW. Substrate inhibition kinetics: Phenol degradation by *Pseudomonas putida*. *Biotechnology and Bioengineering*. 1975;1599-1615
- [2] Adhoum N, Monser L. Decolourization and removal of phenolic compounds from olive mill wastewater by electrocoagulation. *Chemical Engineering and Processing Process Intensification*. 2004;**43**(10): 1281-1287. DOI: 10.1016/j.cep.2003.12.001
- [3] Balice V, Cera O. Acidic phenolic fraction of the juice of olives determined by gas chromatographic method. *Grasas y Aceites*. 1984:178-180
- [4] Lafka T-I, Lazou AE, Sinanoglou VJ, Lazos ES. Phenolic and antioxidant potential of olive oil mill wastes. *Food Chemistry*. 2011;**125**(1):92-98. DOI: 10.1016/j.foodchem.2010.08.041
- [5] Li A, Zhang Q, Zhang G, Chen J, Fei Z, Liu F. Adsorption of phenolic compounds from aqueous solutions by a water-compatible hypercrosslinked polymeric adsorbent. *Chemosphere*. 2002;**47**(9):981-989. DOI: 10.1016/S0045-6535(01)00222-3
- [6] De Marco E, Savarese M, Paduano A, Sacchi R. Characterization and fractionation of phenolic compounds extracted from olive oil mill wastewaters. *Food Chemistry*. 2007; **104**(2):858-867. DOI: 10.1016/j.foodchem.2006.10.005
- [7] Busca G, Berardinelli S, Resini C, Arrighi L. Technologies for the removal of phenol from fluid streams: A short review of recent developments. *Journal of Hazardous Materials*. 2008;**160**(2-3): 265-288. DOI: 10.1016/j.jhazmat.2008.03.045
- [8] Abdelkreem M. Adsorption of phenol from industrial wastewater using olive mill waste. In: 4th International Conference on Environmental Science and Development (ICESD 2013). Vol. 5. 2013. pp. 349-357. DOI: 10.1016/j.apcbee.2013.05.060
- [9] Ahmaruzzaman M, Sharma DK. Adsorption of phenols from wastewater. *Journal of Colloid and Interface Science*. 2005;**287**(1):14-24. DOI: 10.1016/j.jcis.2005.01.075
- [10] Anisuzzaman SM, Bono A, Krishnaiah D, Tan YZ. A study on dynamic simulation of phenol adsorption in activated carbon packed bed column. *Journal of King Saud University-Engineering Sciences*. DOI: 10.1016/j.jksues.2014.01.001
- [11] Lin S-H, Juang R-S. Adsorption of phenol and its derivatives from water using synthetic resins and low-cost natural adsorbents: A review. *Journal of Environmental Management*. 2009; **90**(3):1336-1349. DOI: 10.1016/j.jenvman.2008.09.003
- [12] Richard D, Delgado Núñez M, Schweich D. Adsorption of complex phenolic compounds on active charcoal: Breakthrough curves. *Chemical Engineering Journal*. 2010; **158**(2):213-219. DOI: 10.1016/j.cej.2009.12.044
- [13] Huang J, Wu X, Zha H, Yuan B, Deng SA. Hypercrosslinked poly(styrene-co-divinylbenzene) PS resin as a specific polymeric adsorbent for adsorption of 2-naphthol from aqueous solutions. *Chemical Engineering Journal*. 2013;**218**(0):267-275. DOI: 10.1016/j.cej.2012.12.032
- [14] Li H, Xu M, Shi Z, He B. Isotherm analysis of phenol adsorption on polymeric adsorbents from nonaqueous solution. *Journal of Colloid and Interface Science*. 2004;**271**(1):47-54. DOI: 10.1016/j.jcis.2003.10.026

- [15] Vázquez G, Alonso R, Freire S, González-Álvarez J, Antorrena G. Uptake of phenol from aqueous solutions by adsorption in a *Pinus pinaster* bark packed bed. *Journal of Hazardous Materials*. 2006;**133**(1–3): 61-67. DOI: 10.1016/j.jhazmat.2004.12.041
- [16] Ruzmanova Y, Ustundas M, Stoller M, Chianese A. Photocatalytic treatment of olive mill wastewater by N-doped titanium dioxide nanoparticles under visible light. *Chemical Engineering Transactions*. 2013: 2233-2238
- [17] Vaiano V, Sacco O, Stoller M, Chianese A, Ciambelli P, Sannino D. Influence of the photoreactor configuration and of different light sources in the photocatalytic treatment of highly polluted wastewater. *International Journal of Chemical Reactor Engineering*. 2014
- [18] Cicci A, Stoller M, Bravi M. Microalgal biomass production by using ultra- and nanofiltration membrane fractions of olive mill wastewater. *Water Research*. 2013;**47**(13): 4710-4718. DOI: 10.1016/j.watres.2013.05.030
- [19] Stoller M, Bravi M. Critical flux analyses on differently pretreated olive vegetation waste water streams: Some case studies. *Desalination*. 2010;**250**(2): 578-582. DOI: 10.1016/j.desal.2009.09.027
- [20] Stoller M, De Caprariis B, Cicci A, Verdone N, Bravi M, Chianese A. About proper membrane process design affected by fouling by means of the analysis of measured threshold flux data. *Separation and Purification Technology*. 2013;**114**(0):83-89. DOI: 10.1016/j.seppur.2013.04.041
- [21] Stoller M, Bravi M, Chianese A. Threshold flux measurements of a nanofiltration membrane module by critical flux data conversion. *Desalination*. 2013;**315**:142-148. DOI: 10.1016/j.desal.2012.11.013
- [22] Stoller M. On the effect of flocculation as pretreatment process and particle size distribution for membrane fouling reduction. *Desalination*. 2009; **240**(1–3):209-217. DOI: 10.1016/j.desal.2007.12.042
- [23] Bhaumik M, Setshedi K, Maity A, Onyango MS. Chromium(VI) removal from water using fixed bed column of polypyrrole/Fe<sub>3</sub>O<sub>4</sub> nanocomposite. *Separation and Purification Technology*. 2013;**110**:11-19. DOI: 10.1016/j.seppur.2013.02.037.
- [24] Zahra S, Reyhane S, Reza F. Fixed-bed adsorption dynamic of Pb(II) adsorption from aqueous solution using nanostructured  $\gamma$ -alumina. *Journal of Nanostructure in Chemistry*. 2013:1-8
- [25] Setshedi KZ, Bhaumik M, Onyango MS, Maity A. Breakthrough studies for Cr(VI) sorption from aqueous solution using exfoliated polypyrrole-organically modified montmorillonite clay nanocomposite. *Journal of Industrial and Engineering Chemistry*. 2014;**20**(4):2208-2216. DOI: 10.1016/j.jiec.2013.09.052
- [26] Thomas H. Heterogeneous ion exchange in a flowing system. *Journal of the American Chemical Society*. 1944: 1466-1664
- [27] Yoon Y, Nelson J. Application of gas adsorption kinetics. I. a theoretical model for respirator cartridge service time. *American Industrial Hygiene Association Journal*. 1984:509-516
- [28] Tonle KI. Capteurs Électrochimiques à Base d'argiles Smectitiques Camerounaises Fonctionnalisées Par Les Groupements Thiol et Amine: Élaboration, Caractérisation et Application Au Piégeage Des Métaux Lourds à Effet

Polluant [These]. Yaoundé, Cameroun: Université de Yaoundé 1; 2004

[29] Brunauer S, Deming LS, Deming WE, Teller E. On a theory of the Van Der Waals adsorption of gases. *Journal of the American Chemical Society*. 1940;1723

[30] Sing KSW, Everett DH, Haul RAW. Reporting physisorption data for gas/solid systems with special reference to the determination of surface area and porosity. *Pure and Applied Chemistry*. 1985;603

[31] Ofomaja AE, Ho Y-S. Effect of temperatures and PH on methyl violet biosorption by *Mansonia* wood sawdust. *Bioresource Technology*. 2008;99(13):5411-5417. DOI: 10.1016/j.biortech.2007.11.018

[32] Liang Q-Q, Li Y-S. A rapid and accurate method for determining protein content in dairy products based on asynchronous-injection alternating merging zone flow-injection spectrophotometry. *Food Chemistry*. 2013;141(3):2479-2485. DOI: 10.1016/j.foodchem.2013.05.075

[33] Wang J, Zhang Q-H, Wang Z-H, Lih H-M. Determination of major bovine milk proteins by reversed-phase high-performance liquid chromatography. *Chinese Journal of Analytical Chemistry*. 2009:1667-1670

[34] Aksu Z, Gönen F. Biosorption of phenol by immobilized activated sludge in a continuous packed bed: Prediction of breakthrough curves. *Process Biochemistry*. 2004;39(5):599-613. DOI: 10.1016/S0032-9592(03)00132-8

[35] Calero M, Hernainz F, Blazquez G, Tenorio G, Martín-Lara MA. Study of Cr (III) biosorption in a fixed-bed column. *Journal of Hazardous Materials*. 2009:886-893

[36] Yahaya N, Khan EM, Abustan I, Muhamad Faizal Pakir ML, Olugbenga SB, Mohd AA. Fixed-bed column study for Cu (II) removal from aqueous solutions using rice husk based activated carbon. *International Journal of Engineering and Technology*. 2011:186-190

[37] Sivakumar P, Palanisamy PN. Packed bed column studies for the removal of acid blue 92 and basic red 29 using non-conventional adsorbent. *Indian Journal of Chemical Technology*. 2009:301-307

[38] Ochando-Pulido JM, Stoller M, Bravi M, Martínez-Ferez A, Chianese A. Batch membrane treatment of olive vegetation wastewater from two-phase olive oil production process by threshold flux based methods. *Separation and Purification Technology*. 2012;101(0):34-41. DOI: 10.1016/j.seppur.2012.09.015

[39] Bendini A, Cerretani L, Carrasco-Pancorbo A, María Gómez-Caravaca A, Segura-Carretero A, Fernández-Gutiérrez A, et al. Phenolic molecules in virgin olive oils: A survey of their sensory properties, health effects, antioxidant activity and analytical methods. *Molecules*. 2007;12(12):1679-1719

[40] Soto ML, Moure A, Domínguez H, Parajó JC. Recovery, concentration and purification of phenolic compounds by adsorption: A review. *Journal of Food Engineering*. 2011;105(1):1-27. DOI: 10.1016/j.jfoodeng.2011.02.010

[41] Streat M, Sweetland LA. Removal of pesticides from water using hypercrosslinked polymer phases: Part 1-physical and chemical characterization of adsorbents. *Transactions of the Institution of Chemical Engineers*. 1998;B76:115-126

[42] Azonova VV, Hradil J. Sorption properties of macroporous and

Hypercrosslinked copolymers. *Reactive and Functional Polymers*. 1999:163-175

[43] Maity N, Payne GF, Chipchosky JL. Adsorptive separations based on the differences in solute-sorbent hydrogen-bonding strengths. *Industrial and Engineering Chemistry Research*. 1991: 2456-2463

[44] Juang RS, Shiau JY. Effect of temperature on equilibrium adsorption of phenols onto nonionic polymeric resins. *Separation Science and Technology*. 1999:1819-1831

[45] Weber WJ Jr, Van Vliet BM. Synthetic adsorbents and activated carbons for water treatment: Overview and experimental comparisons. *Journal of the American Chemical Society*. 1981: 420-426

[46] Li C, Xu M, Sun X, Han S, Wu X, Liu Y-N, et al. Chemical modification of amberlite XAD-4 by carbonyl groups for phenol adsorption from wastewater. *Chemical Engineering Journal*. 2013; 229:20-26. DOI: 10.1016/j.cej.2013.05.090



# Glyphosate Resistance of *Chloris virgata* Weed in Australia and Glyphosate Mobility Are Connected Problems

Aman D. Sharma

## Abstract

The purpose of this review paper is to address two major aspects of glyphosate application on farmers' fields. The first aspect is the development of glyphosate resistance in weeds like *Chloris virgata*, and the second aspect is glyphosate mobility, which is directly controlled by soil sorption processes and indirectly by molecule degradation processes. This is a global problem, as excessive glyphosate residues in groundwater, drinking water, and urine of subsistence farmers from intensive agricultural localities have been reported, which can pose a risk to human health. Approaches like biochar as a possible strategy to control glyphosate leaching and crop competition as a cultural method to control glyphosate-resistant weed like *Chloris virgata* can be the potential solutions of the glyphosate resistance and glyphosate mobility.

**Keywords:** resistance, glyphosate, mobility, biochar, crop competition

## 1. Introduction

### 1.1 Chemistry of glyphosate

Glyphosate (N-(phosphonomethyl) glycine) is a non-selective post-emergence herbicide widely used in field crops, vegetable crops, and orchards. Glyphosate is absorbed by plants via leaves and shoots and is transported throughout the whole plant. Its usual formulation is salt of a deprotonated acid of glyphosate and a cation, e.g. isopropylamine or trimethylsulfonium. Its chemical structure has three groups (amine, carboxylate, and phosphonate) that form strong coordination bonds with metal ions to form bidentate and tridentate complexes (**Figure 1**). Hence it is a strong chelating herbicide [1].

Chemically, glyphosate is a phosphonate. It is mainly the phosphonate group via which glyphosate is bonded to iron and aluminum oxides by ligand exchange with the formation of mononuclear, monodentate, and/or binuclear, bidentate surface complexes [2].

### 1.2 Glyphosate degradation

Among the microorganisms, bacteria represent the majority of the glyphosate-degrading organisms [3]. Bacteria degrade glyphosate by cleaving the C-N bond and

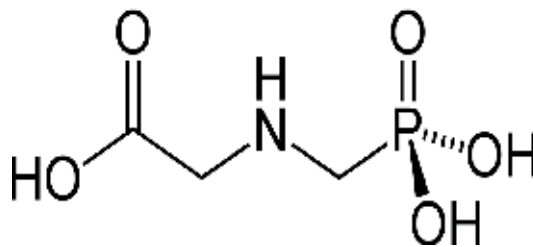


**Figure 1.**  
Chemical structure of glyphosate [1].

converting glyphosate to AMPA (amino-methyl phosphonic acid) which is further decomposed and finally excreted to the environment. Glyphosate degradation can also occur via C-P lyase pathway to sarcosine, rather than AMPA. A bacterial strain *Bacillus subtilis* Bs-15 degraded 18% (12 h) to 67% (96 h) of glyphosate in sterile soil and 19% (12 h) to 72% (96 h) in unsterilized soil. It indicates that Bs-15 can significantly enhance glyphosate degradation.

### 1.3 Mobility of glyphosate

The binding mechanisms of clay minerals and organic colloids result in non-occurrence of free glyphosate, but leaching of glyphosate complexes via preferential flow paths through the soil and transfer to waterways can occur, which could be a concern from the environmental pollution point of view [4]. In another study related to the desorption rate of glyphosate from goethite mineral surfaces, the rate of glyphosate desorption is mainly controlled by the breaking of the Fe-glyphosate bond through a dissociative or a dissociative interchange mechanism [5]. Soil redox condition is also an important factor controlling the mobility of glyphosate. Microbial degradation and mineralization of glyphosate were slow in anoxic environments compared with oxic environments [6].

In US soils, glyphosate and AMPA have been detected together and found widely in the environment. The occurrence was more frequent in soils and sediments, ditches and drains, and rivers and streams and less in lakes, ponds, wetlands, soil water, and groundwater [7]. In western Switzerland, the surface runoff has been suggested as the major reason for the occurrence of glyphosate and AMPA in surface waters [8]; however, in a study related to Danish soils, limited leaching of glyphosate was reported in non-structured sandy soils, while subsurface leaching to drainage systems was observed in a structured soil when high rainfall followed glyphosate application [9].

In a study related to  $^{14}\text{C}$  glyphosate transport in undisturbed topsoil columns, the amounts of glyphosate leached from the macroporous sandy loam were 50–150 times larger than that from the sandy soil [10].

### 1.4 Glyphosate residues

Glyphosate and its decomposition product AMPA have been reported in stream water samples in areas of Zurich, Switzerland, with median concentrations of 0.11 and 0.20  $\mu\text{g/l}$ ; however, these compounds were not detected in groundwater [11].

In a Canadian study, glyphosate residues were observed in both upland and wetland settings; however, the concentrations were well below the Canadian guidelines for drinking water quality. Many other studies have reported glyphosate residues in streams and groundwater systems [8].

An enzyme-linked immunosorbent assay (ELISA) was used to determine glyphosate presence levels in Hungarian water samples. Few samples showed exceedingly high concentration levels of glyphosate with this method [12]. Liquid chromatography is another method that can be used for the detection of glyphosate residues in cereal, oilseed, and pulse crops [13].

### 1.5 Soil properties and glyphosate mobility

Data from sorption studies indicated that sorption coefficients are the most sensitive parameters for environmental risk assessment and soil properties like pH and clay content govern the glyphosate adsorption in Argentinian soils. In a related study in Argentina, high glyphosate sorption with low desorption in mollisols and ultisols indicated a low risk of groundwater contamination [14].

In another study on glyphosate mineralization in different agricultural soils, exchangeable acidity ( $H^+$  and  $Al^{3+}$ ), exchangeable  $Ca^{2+}$  ions, and ammonium lactate extractable K were the key soil parameters governing mineralization [15]. In a study related to glyphosate sorption with high soil phosphate levels, glyphosate sorption distribution constant  $K_d$  in soils ranged from 173 to 939  $l\ Kg^{-1}$  under very strong to strongly acidic conditions, but the  $K_d$  was always  $<100\ l\ Kg^{-1}$  under moderately acidic to slightly alkaline conditions suggesting that glyphosate may become mobile by water in soils with high phosphate levels [16]. This is important concerning the application of phosphatic fertilizers, as the phosphate ion would desorb glyphosate from adsorption sites resulting in the mobility of glyphosate towards aquatic environments [17].

Generally, iron and aluminum oxides adsorb a greater amount of glyphosate and phosphates in comparison to layer silicates [18] supporting the role of soil mineralogy concerning glyphosate sorption. As high phosphorus application can desorb glyphosate from sorption sites, application of char can be effective in these scenarios concerning sorption of glyphosate. The rapid degradation of glyphosate in surface waters and its practically irreversible sorption indicated a low potential environmental risk [19].

An investigation on adsorption of the herbicide glyphosate and its main metabolite AMPA found that  $pH_{(CaCl_2)}$  values, available phosphate, and amorphous iron and aluminum contents were the major parameters to predict the adsorption constants for these molecules [20]. In a similar study, while examining the effect of humic acid (HA) on the adsorption/desorption behaviour of glyphosate on goethite minerals, the herbicide was desorbed by two parallel processes: (i) a direct detachment from the surface, which is first order in adsorbed glyphosate, and (ii) a ligand exchange with HA molecules, which is first order in adsorbed glyphosate and first order in dissolved humic acid [21]. Glyphosate is adsorbed by humic acids via hydrogen bonding [22].

A laboratory study related to the fate of glyphosate and degradation in cover crop residues and underlying soil indicated that the differences in sorption and degradation levels were due to differences in the composition of the crop residues and availability to microorganisms [23]. In a related study of adsorption and mobility of glyphosate in different soils under no-till and conventional tillage, adsorption of glyphosate was influenced by the soil clay content and cation exchange capacity (CEC) and negatively related to pH and phosphorus. High Freundlich parameter ( $K_F$ ) values obtained in isotherm studies were the dominant factor influencing glyphosate mobility.  $K_F$  values indicate the adsorption capacity of the soil [24].

### 1.6 Methods to understand glyphosate mobility

Sorption coefficients provide accurate information needed for reliable risk assessments of groundwater contaminants by pesticides [25]. In a study related to sorption

and leaching of  $^{14}\text{C}$ -glyphosate in agricultural soils, non-extractable glyphosate residues become available eventually and take part in biodegradation and leaching. Empirical constants ( $K_F$ ) of Freundlich sorption isotherm were 16.6 for the clay loam, 33.6 for the silty clay loam, and 34.5 for the sandy clay loam indicating that it is the soil structure which dictates the glyphosate sorption behaviour [26]. Leaching of glyphosate was dependent on hydrodynamic and biodegradation properties of soils [26]. Application of char can be used as a strategy to increase the sorption of glyphosate [27].

Movement of pesticides and their bioavailability and biotransformation are controlled by adsorption/desorption mechanisms operating at the interface between organic and inorganic soil colloids. High-resolution magic angle spinning and nuclear magnetic resonance techniques can distinguish mobile and immobile phases of pesticides like glyphosate [28]. Another study on glyphosate transport parameters suggested that glyphosate sorption is a kinetic process that depends on pore-water velocities and residence time of soil solution [29].

### 1.7 Why is glyphosate application on field sites a concern?

The International Agency for Research on Cancer (IARC) has reclassified that glyphosate is “probably carcinogenic to humans” [30]; however, the United States Environment Protection Agency (US EPA) concluded that there is no convincing evidence that “glyphosate induces mutations” [31]. The US EPA relied mostly on unpublished regulatory studies, 99% of which were negative, while IARC relied mostly on peer-reviewed studies, 70% of which were positive [31]. Glyphosate-based herbicides often contaminate drinking water sources, air, and precipitation in agricultural regions [30]. As the usage of glyphosate-based herbicides continues to increase, investment in epidemiological studies, biomonitoring, and toxicology studies based on the principles of endocrinology should be done [30]. Apart from cancer, glyphosate has been found to be a potential factor causing chronic kidney disease due to drinking water faced by Sri Lankan farmers [32]. The role of drinking water has also been reported in another study which caused ill health in Indian farmers [33].

### 1.8 Biochar’s potential role as a sorbent for organic pollutants like glyphosate

Biochar can be defined as “the porous carbonaceous solid produced by the thermochemical conversion of organic materials in an oxygen-depleted atmosphere that has physicochemical properties suitable for safe and long-term storage of carbon in the environment” [34]. Biochar and activated charcoal are similar concerning production via pyrolysis, with medium to high surface areas [35]; however, biochar is not activated or treated like activated charcoal [35, 36]. Crop residues are pyrolyzed at high temperature ( $>500^\circ\text{C}$ ) in the absence of oxygen, followed by various activation processes to form activated charcoal [35]. In comparison to activated charcoal, biochar has a non-carbonized fraction that interacts with soil contaminants like glyphosate. Soil minerals can increase the surface area and pore size of biochar, which in turn increase the adsorption capacity of biochars for organic pollutants like glyphosate [37]. Biochar application can reduce the bioavailability and leachability of organic pollutants in soils through adsorption and other physicochemical reactions [38]. An increase in the surface area of biochars has been observed to increase the biochar’s ability to adsorb organic contaminants [39, 40]. The addition of phosphorus fertilizer to biochar-amended soils can, however, remobilize glyphosate and damage non-target plants; therefore, improved understanding of this risk is important (**Figure 2**) [41].

The soil environment is a three-dimensional structure of water-filled pores, gas-filled pores, and soil particulates (organic matter, sand, silt, and clay) [42]. Biochar can be used as a sorbent for organic pollutants due to its highly aromatic

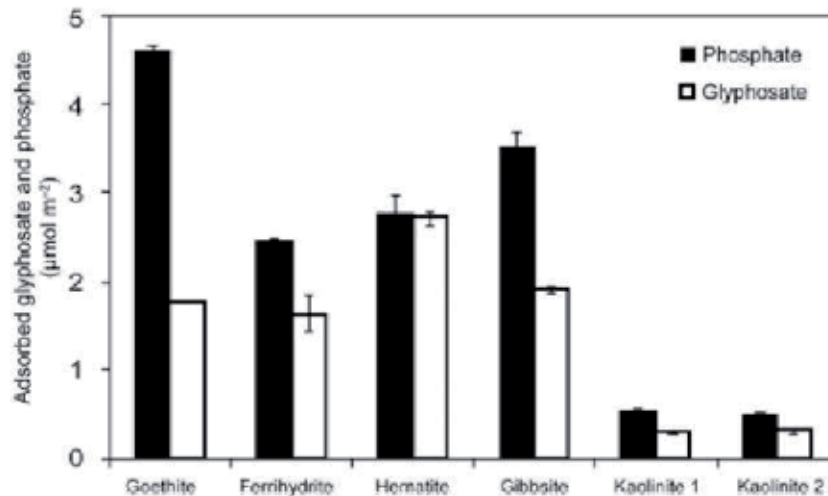


**Figure 2.**  
*Phosphate and glyphosate adsorption by minerals [5].*

nature, high surface area, micropore volume, and abundance of polar functional groups [43]. Factors affecting biochar's performance for adsorption include pyrolysis temperature and surface area. Pyrolysis temperature is one of the factors directly affecting biochar's performance. An increase in pyrolysis temperature of biochar generally increases the degree of carbonization and consequently surface area.

Even with the increase in surface area of biochars, sorption sites can be blocked by organic matter, and this is the likely cause for the diminished capability of aged biochars to adsorb organic contaminants [44]. The behaviour of biochar changes with time after its application to soil, and this process is known as "aging". Aging can alter the behaviour of biochar. To increase the remediation efficiency of biochar concerning herbicides, more detailed research to explore the aspect of aging is warranted.

### 1.9 Behaviour of herbicides in a soil-biochar system

In a study related to herbicide terbuthylazine-biochar-soil interaction, there was higher adsorption of herbicide in soil with low organic matter than in soil with the high organic matter. The reason for this result was attributed to a high concentration of organic molecules competing with herbicide for sorption sites in the soil having a high amount of organic matter [40]. Availability of herbicides can be greatly reduced with the application of biochar [45]. Even a low application rate (0.1%) of biochar in the soil can appreciably reduce the availability of herbicides like diuron [44].

In a comparative study [46], 42 times higher hexachlorobenzene sorption by biochar than that by control soil was observed, resulting in the reduction of volatilization and earthworm (*Eisenia foetida*) uptake of hexachlorobenzene from the soil. The extent of sorption of pesticides generally depends on the aromaticity of soil organic carbon. Properties that make biochars effective against herbicides are a high specific surface area, high microporosity, and high aromatic carbon.

### 1.10 The behaviour of glyphosate in a soil-biochar system

Plant uptake of pesticides decreases markedly with increasing biochar content of the soil despite the greater persistence of the pesticide residues in biochar-amended soils [47]. In a similar study related to the effects of biochar, wood vinegar, and plants on glyphosate leaching and degradation, the addition of biochar to the soil

decreased the leaching of glyphosate irrespective of plants. Hence, it was concluded that biochar can be used as an effective strategy to reduce the potential environmental risk to aquatic environments caused by glyphosate [27].

In a study related to the effects of wood-based biochar on the leaching of pesticides chlorpyrifos, diuron, and glyphosate, it was concluded that biochar can be used as an adsorptive layer directly on or close to the soil surface to prevent losses of pesticides [48]. In another study, biochar was found to limit glyphosate transport in soil systems; however, the addition of phosphatic fertilizer remobilized the glyphosate from biochar-amended soils. This phosphate-induced glyphosate desorption phenomenon is important to consider in soils having biochar amendment [41]. The type of biochar also plays an important role, as hardwood biochars were ineffective sorbents of glyphosate in high-phosphate soils [41]. Biochars produced at high temperature were effective sorbents of glyphosate [41]. Reduced glyphosate sorption on biochars was observed with the increase in pH from 6 to 9 [41, 49, 50].

## 2. Glyphosate-resistant weeds

The second major aspect in this review paper is the evolution of glyphosate resistance in weeds due to heavy reliance on glyphosate. Glyphosate toxicity and glyphosate resistance are not different but connected problems, as glyphosate is applied to control weeds and its application results in movement of glyphosate to water bodies via soil systems affecting human health. When glyphosate-contaminated drinking water is used for human consumption, it may potentially result in diseases like cancer or chronic kidney disease; however, frequent application of glyphosate not only results in its downward movement via soil systems but also results in the development of glyphosate resistance in weeds. Hence these problems are interconnected.

While assessing the weeds at risk of evolving glyphosate resistance in Australian subtropical glyphosate-resistant cotton systems, species with the highest risk to glyphosate resistance were *Brachiaria eruciformis*, *Conyza bonariensis*, *Urochloa panicoides*, *Chloris virgata*, *Sonchus oleraceus*, and *Echinochloa colona* [51]. Thirty-eight weeds in total distributed over 37 countries have shown resistance to glyphosate [52]. These weeds represent the greatest threat to sustainable weed control practices [52]. Weed surveys in the cotton-growing areas of New South Wales (NSW) and Queensland, Australia, indicated the dominance of *Conyza bonariensis*, *Echinochloa colona*, and *Chloris virgata* [53].

*Chloris virgata* is a high-risk species to glyphosate resistance in summer fallow [51]. Glyphosate resistance in *Chloris virgata* populations in Australia has emerged due to transformation in Australian cropping systems, particularly unirrigated cotton systems, from regular tillage and use of residual herbicides to minimum or no-tillage systems with a heavy reliance on glyphosate [54]. This lack of tillage is the major reason for the emergence of weeds like *Chloris virgata* that are small-seeded and emerge at or close to the surface [54]. A weed management system depending on only one tactic, for example, application of glyphosate, is the main driver for this species shift. With repeated use of glyphosate, *Chloris virgata* populations have become less susceptible to glyphosate formulations, especially after the early tillering stage [54].

Mechanisms involved in providing resistance to glyphosate in weeds include (i) target-site alterations (target site mutation, target site gene amplification) [55, 56] and (ii) non-target site mechanisms involving reduced glyphosate uptake and/or reduced translocation of glyphosate [57–59]. The alterations inhibit glyphosate binding or increase the effective dose needed for enzyme inhibition. Target site EPSPS mutations are the primary mechanism conferring glyphosate resistance in populations of *Chloris virgata* [55].

## 2.1 *Chloris virgata* (feathertop Rhodes grass)

*Chloris virgata* as a glyphosate-resistant weed [51] has also been identified as a host for barley yellow dwarf and cereal yellow dwarf viruses [60]. As *Chloris virgata* can tolerate high-salinity and high-alkalinity soil environments, *Chloris virgata* can form a dominant community in these environments [61, 62]. *Chloris virgata* is tolerant to drought stress [63]. Many studies on *Chloris virgata* seed biology have been completed in China, India, Qatar, and Honduras [63], while very few studies have been conducted in Australia [64, 65].

*Chloris virgata* grass seed biology includes the study on dormancy, germination conditions, seed bank dynamics, growth, and development [66]. Dormancy mechanisms enable the seed to sense the optimum environmental conditions for the establishment of seedlings and hence play a pivotal role in control strategies for weedy grasses [67]. There are two types of seed dormancy mechanisms, those based in the tissues surrounding the embryo (seed coat based) or those found within the embryo [67]. The role of smoke in breaking the dormancy of plump windmill grass (*Chloris ventricosa*), a related species to *Chloris virgata* grass [68], has been reported; but no study related to dormancy breakdown of *Chloris virgata* grass by smoke has been reported. The seeds of *Chloris virgata* are triangular in shape and light in weight and hence shed easily from the heads making them good wind (anemochory) and water (hydrochory) dispersers [64].

Seed germination is a key event in the growth of annual plants like *Chloris virgata* grass which is regulated by several environmental factors such as temperature and water potential [69–71]. High rainfall has been associated with *Chloris virgata* population outbreaks [72], suggesting that water plays an important role in the germination process. *Chloris virgata* grass possesses the C<sub>4</sub> photosynthesis mechanism and has better water use efficiency than grasses having the C<sub>3</sub> photosynthesis mechanism. Among all the potential factors for *Chloris virgata* germination; light, salinity, and osmotic potential are the most critical factors [64]. A light requirement for germination has been observed among many small-seeded species and warm-season grasses [67, 73]. In a study related to germination responses of *Chloris virgata* to temperature and reduced water potential, maximum germination percentages of *Chloris virgata* seeds were found at 15–25°C [74]. Germination of *Chloris virgata* seeds is affected by several factors; however, temperature and light play a significant role in the germination of *Chloris virgata* seeds. More studies on factors affecting *Chloris virgata* growth are needed due to the paucity of information.

In a study related to growth, development, and seed biology of *Chloris virgata* in South Australia, *Chloris virgata* seedlings emerging after summer rainfall events under field conditions needed 1200 growing degree days from emergence to mature seed production [65]. Harvested seeds of *Chloris virgata* were dormant for a period of about 2 months and took 5 months of after-ripening to reach 50% germination [75]. Seedling emergence of *Chloris virgata* was highest (76%) for seeds present on the soil surface and seedling emergence was significantly reduced by burial at 1 (57%), 2 (49%), and 5 cm (9%) soil depth. Furthermore, *Chloris virgata* seeds buried in the soil persisted longer than those left on the soil surface [75].

The thermal time to panicle emergence of *Chloris virgata* is similar to shattercane (*Sorghum bicolor*) [76]. A related species of *Chloris virgata*, windmill grass (*Chloris truncata*) under irrigated field requires 21–23, 43–45, and 74–75 days from seedling emergence to reach tillering, panicle emergence, and mature seed stage [75]. Maximum plant density and biomass in case of windmill grass have been found to be 4.2–28.2 plants m<sup>-2</sup> and 8.3–146.1 g dry biomass m<sup>-2</sup> depending on location [77].

Water stress due to extremely low rainfall over the summer months was the reason for the delayed growth of *Chloris virgata* under rained conditions when

compared to irrigated conditions [75]. Under irrigated conditions, 619 to 730 g of dry biomass  $\text{m}^{-2}$  of *Chloris virgata* (89 days after sowing) was observed; however, this value was much higher than one of its related species, windmill grass (*Chloris truncata*) (146 g  $\text{m}^{-2}$ ) [75].

*Chloris virgata* has several characteristics like rapid germination and low base temperature (2.1 to 3.0°C) for seed germination enabling it to survive rainfall events in spring, summer, and autumn in South Australia [75].

## 2.2 Evolution of glyphosate resistance in *Chloris virgata*

On national ranking basis in Australia, *Chloris virgata*, as an herbicide-resistant weed, ranks ninth, resulting in herbicide-resistant weed cost of \$2.6 million [78]. In the northern region of Australia, it is the top fourth herbicide-resistant weed after ryegrass (*Lolium rigidum*), wild turnip (*Brassica rapa*), and barnyard grass (*Echinochloa crus-galli*) [78].

Minimum tillage due to its benefits like reduced soil erosion and improvement in moisture conservation has resulted in the reduction of soil disturbance in grain cropping fields. The factors that aided the adoption of minimum tillage systems in Australian cropping systems include machinery modifications that allow greater flexibility in the cropping systems, precision agriculture and refinement of controlled traffic farming, improved crop resistance or tolerance to plant diseases associated with stubble retention, availability of more crop options and rotations, development of a broader spectrum of effective herbicides, and the use of genetic modification technologies to breed herbicide-resistant crops [79].

Minimum tillage has increased the use of herbicides and consequently increased the rapid appearance of herbicide resistance in weeds [75]. Another reason for evolution is the introduction of glyphosate-resistant crops in the mid-1990s that has resulted in a sharp increase in the populations of *Chloris virgata* [80].

Glyphosate resistance was first reported in broadleaf *Conyza* (horseweed) species. The mechanism suggested for resistance was an altered subcellular distribution resulting in sequestration of the glyphosate molecule away from the enzyme target site in the chloroplast [81]. Weeds receiving repeated exposure to a single mode of action of herbicide are the most likely candidates to develop resistance [82].

From the evolution point of view, minimum tillage along with reliance on glyphosate has contributed the most towards glyphosate resistance in *Chloris virgata*. The evolution of the glyphosate resistance in *Chloris virgata* highlights the need for diversity in weed management strategies for successful control of *Chloris virgata* and other *Chloris* species [82].

## 2.3 Crop competition as a strategy to control *Chloris virgata*

Crop competition can be used as an effective strategy against *Chloris virgata*, especially when herbicides like glyphosate fail or underperform [83]. Crop competition to control weeds has proven to be one of the most effective cultural strategies in Australian cropping systems, aiming at suppression of weed biomass and fecundity resulting in crop yield gains [84]. Three major weed variables that affect crop-weed competition are:

- Time of emergence of the weed relative to the crop and weeds that emerge later than the crop are much less competitive than the weeds that emerge before the crop.



- Weed seedling density is the second most important factor influencing weed-crop competition.
- Differences in the competitive ability of weeds due to rapid leaf area development, high-density root systems, and plant heights [85].

Crop and weed plants compete for limited resources like water, nutrients, and light. Competition for nutrient uptake is dependent on intrinsic nutrient requirements and uptake efficiencies. Uptake efficiencies are further dependent on root length densities and nutrient membrane transporters. Species with a low nutrient requirement, extensive root systems, and effective membrane transporters will have a competitive advantage in a nutrient-limited system [85].

Crop and weed plants compete for water, as water is required for plant growth. In the absence of water, a reduction in photosynthesis, wilting, and nutrient deficiencies can occur. The length, magnitude, and timing of the drought periods as well as soil attributes (water holding capacity, texture, structure, and hydraulic conductivity), plant traits (root structure and density, drought tolerance, and water use efficiency) are the major factors that influence the competition for water availability between crop and weed plants [85].

Light as a third major factor affects the growth of crop and weed plants [86]. Different phenophases of both crop and weed plants are affected by light. Morphological changes in both crop and weed plants due to competition for light include an increase in stem elongation and reduction in stem diameter, the rate of leaf appearance, and root and shoot biomass [87, 88].

Crop competition studies under field conditions are mainly influenced by the environment, soil type, plant density, spatial arrangement, the proportion of each species, and design of experiment [89]. The design of the crop competition experiment depends on the objective, as different objectives require different techniques [90].

Crop species may outcompete weed species depending on factors such as crop density, crop planting pattern, crop vigor, and weed vigor. Crop density or the number of plants per unit of area is important for competition studies considering the relationship among plant yield and the number of individuals and resources present in the area [91]. The competitiveness of a crop can be enhanced using competitive cultivars, higher plant densities, narrow row spacings, and different row orientation [92].

Weed growth can be substantially reduced by shading weeds in the inter-row space by physical orientation of the crop rows [92]. Competitive ability of the crops can also be increased by increasing plant density [84]. The significant interaction between sorghum cultivars and planting densities in suppressing weed biomass has been observed [93]. A high-density crop can limit water and nutrients available to weeds more effectively than a low-density crop, and high-density crops can result in the reduction of light available to weeds [92].

### 3. Summary

In summary, the review paper covered two major problems associated with single reliance on glyphosate application for controlling weeds. The first one is glyphosate mobility via soil systems, a potential risk for aquatic environments, and there is no information on the fate of glyphosate on Australian soils from the last 22 years apart from a single study in Western Australia. This research gap prompted an investigation into glyphosate sorption behaviour in Australian soils of the different mineral composition due to increased usage of glyphosate as a single strategy to

control weeds. The second major problem is the evolution of glyphosate-resistant weeds like *Chloris virgata* in New South Wales and Queensland, Australia, a major threat to sustainable weed control strategies, and due to paucity of information on the management of *Chloris virgata*, we hypothesized that cultural methods like crop competition can be used as a strategy to control glyphosate-resistant *Chloris virgata*.


## Author details

Aman D. Sharma  
Faculty of Science, School of Life and Environmental Sciences, Australian  
Technology Park, The University of Sydney, Australia

\*Address all correspondence to: aman.sharma@sydney.edu.au;  
aman.saluki@gmail.com

## IntechOpen

---

© 2019 The Author(s). Licensee IntechOpen. This chapter is distributed under the terms of the Creative Commons Attribution License (<http://creativecommons.org/licenses/by/3.0>), which permits unrestricted use, distribution, and reproduction in any medium, provided the original work is properly cited. 

## References

- [1] Subramaniam V, Hoggard PE. Metal complexes of glyphosate. *Journal of Agricultural and Food Chemistry*. 1988;**36**(6):1326-1329
- [2] McBride MB. Electron-spin-resonance study of copper-ion complexation by glyphosate and related ligands. *Soil Science Society of America Journal*. 1991;**55**(4):979-985
- [3] Sundaram A, Sundaram KMS. Solubility products of six metal-glyphosate complexes in water and forestry soils, and their influence on glyphosate toxicity to plants. *Journal of Environmental Science and Health, Part B. Pesticides, Food Contaminants, and Agricultural Wastes*. 1997;**32**(4):583-598
- [4] Borggaard OK, Gimsing AL. Fate of glyphosate in soil and the possibility of leaching to ground and surface waters: A review. *Pest Management Science*. 2008;**64**(4):441-456
- [5] Gimsing AL, Borggaard OK. Phosphate and glyphosate adsorption by hematite and ferrihydrite and comparison with other variable-charge minerals. *Clays and Clay Minerals*. 2007;**55**(1):108-114
- [6] Zhan H, Feng YM, Fan XH, Chen SH. Recent advances in glyphosate biodegradation. *Applied Microbiology and Biotechnology*. 2018;**102**(12):5033-5043
- [7] Sviridov AV, Shushkova TV, Zelenkova NF, Vinokurova NG, Morgunov IG, Ermakova IT, et al. Distribution of glyphosate and methylphosphonate catabolism systems in soil bacteria *Ochrobactrum anthropi* and *Achromobacter* sp. *Applied Microbiology and Biotechnology*. 2012;**93**(2):787-796
- [8] Yu XM, Yu T, Yin GH, Dong QL, An M, Wang HR, et al. Glyphosate biodegradation and potential soil bioremediation by *Bacillus subtilis* strain Bs-15. *Genetics and Molecular Research*. 2015;**14**(4):14717-14730
- [9] Gros P, Ahmed A, Kuhn O, Leinweber P. Glyphosate binding in soil as revealed by sorption experiments and quantum-chemical modeling. *Science of the Total Environment*. 2017;**586**:527-535
- [10] Arroyave JM, Waiman CC, Zanini GP, Tan WF, Avena MJ. Desorption rate of glyphosate from goethite as affected by different entering ligands: Hints on the desorption mechanism. *Environment and Chemistry*. 2017;**14**(5):288-294
- [11] Kanissery RG, Welsh A, Sims GK. Effect of soil aeration and phosphate addition on the microbial bioavailability of carbon-14 glyphosate. *Journal of Environmental Quality*. 2015;**44**(1):137-144
- [12] Battaglin WA, Meyer MT, Kuivila KM, Dietze JE. Glyphosate and its degradation product AMPA occur frequently and widely in US soils, surface water, groundwater, and precipitation (1). *Journal of the American Water Resources Association*. 2014;**50**(2):275-290
- [13] Daouk S, De Alencastro LF, Pfeifer HR. The herbicide glyphosate and its metabolite AMPA in the Lavaux vineyard area, western Switzerland: Proof of widespread export to surface waters. Part II: The role of infiltration and surface runoff. *Journal of Environmental Science and Health, Part B. Pesticides, Food Contaminants, and Agricultural Wastes*. 2013;**48**(9):725-736
- [14] Ortiz AMG, Okada E, Bedmar F, Costa JL. Sorption and desorption of glyphosate in mollisols and ultisols soils

- of Argentina. *Environmental Toxicology and Chemistry*. 2017;**36**(10):2587-2592
- [15] Nguyen NK, Dorfler U, Welzl G, Munch JC, Schroll R, Suhadolc M. Large variation in glyphosate mineralization in 21 different agricultural soils explained by soil properties. *Science of the Total Environment*. 2018;**627**:544-552
- [16] Munira S, Farenhorst A, Flaten D, Grant C. Phosphate fertilizer impacts on glyphosate sorption by soil. *Chemosphere*. 2016;**153**:471-477
- [17] de Jonge H, de Jonge LW, Jacobsen OH, Yamaguchi T, Moldrup P. Glyphosate sorption in soils of different pH and phosphorus content. *Soil Science*. 2001;**166**(4):230-238
- [18] Gimsing AL, Borggaard OK, Bang M. Influence of soil composition on adsorption of glyphosate and phosphate by contrasting Danish surface soils. *European Journal of Soil Science*. 2004;**55**(1):183-191
- [19] Maqueda C, Undabeytia T, Villaverde J, Morillo E. Behaviour of glyphosate in a reservoir and the surrounding agricultural soils. *Science of the Total Environment*. 2017;**593**:787-795
- [20] Sidoli P, Baran N, Angulo-Jaramillo R. Glyphosate and AMPA adsorption in soils: Laboratory experiments and pedotransfer rules. *Environmental Science and Pollution Research*. 2016;**23**(6):5733-5742
- [21] Arroyave JM, Waiman CC, Zanini GP, Avena MJ. Effect of humic acid on the adsorption/desorption behavior of glyphosate on goethite. Isotherms and kinetics. *Chemosphere*. 2016;**145**:34-41
- [22] Piccolo A, Gatta L, Campanella L. Interactions of glyphosate herbicide with a humic-acid and its iron complex. *Annali di Chimica*. 1995;**85**(1-2):31-40
- [23] Cassigneul A, Benoit P, Bergheaud V, Dumény V, Etievant V, Goubard Y, et al. Fate of glyphosate and degradates in cover crop residues and underlying soil: A laboratory study. *Science of the Total Environment*. 2016;**545**:582-590
- [24] Okada E, Costa JL, Bedmar F. Adsorption and mobility of glyphosate in different soils under no-till and conventional tillage. *Geoderma*. 2016;**263**:78-85
- [25] Paradelo M, Norgaard T, Moldrup P, Ferre TPA, Kumari K, Arthur E, et al. Prediction of the glyphosate sorption coefficient across two loamy agricultural fields. *Geoderma*. 2015;**259**:224-232
- [26] Al-Rajab AJ, Amellal S, Schiavon M. Sorption and leaching of (14)C-glyphosate in agricultural soils. *Agronomy for Sustainable Development*. 2008;**28**(3):419-428
- [27] Hagner M, Hallman S, Jauhiainen L, Kemppainen R, Ramo S, Tiilikka K, et al. Birch (*Betula* spp.) wood biochar is a potential soil amendment to reduce glyphosate leaching in agricultural soils. *Journal of Environmental Management*. 2015;**164**:46-52
- [28] Chamignon C, Haroune N, Forano C, Delort AM, Besse-Hoggan P, Combourieu B. Mobility of organic pollutants in soil components. What role can magic angle spinning NMR play? *European Journal of Soil Science*. 2008;**59**(3):572-583
- [29] Candela L, Alvarez-Benedi J, de Melo MTC, Rao PSC. Laboratory studies on glyphosate transport in soils of the Maresme area near Barcelona, Spain: Transport model parameter estimation. *Geoderma*. 2007;**140**(1-2):8-16
- [30] Myers JP, Antoniou MN, Blumberg B, Carroll L, Colborn T, Everett LG, et al. Concerns over use of glyphosate-based herbicides and risks

associated with exposures: A consensus statement. *Environmental Health*. 2016;**15**:13

[31] Benbrook C. How did the US EPA and IARC reach diametrically opposed conclusions on the genotoxicity of glyphosate-based herbicides? *Environmental Sciences Europe*. 2019;**31**:16

[32] Jayasumana C, Gunatilake S, Senanayake P. Glyphosate, hard water and nephrotoxic metals: Are they the culprits behind the epidemic of chronic kidney disease of unknown etiology in Sri Lanka? *International Journal of Environmental Research and Public Health*. 2014;**11**(2):2125-2147

[33] Reddy DV, Gunasekar A. Chronic kidney disease in two coastal districts of Andhra Pradesh, India: Role of drinking water. *Environmental Geochemistry and Health*. 2013;**35**(4):439-454

[34] Shackley S, Carter S, Knowles T, Middellink E, Haefele S, Haszeldine S. Sustainable gasification-biochar systems? A case-study of rice-husk gasification in Cambodia, part II: Field trial results, carbon abatement, economic assessment and conclusions. *Energy Policy*. 2014;**71**:199-199

[35] Cao XD, Harris W. Properties of dairy-manure-derived biochar pertinent to its potential use in remediation. *Bioresource Technology*. 2010;**101**(14):5222-5228

[36] Ahmad M, Lee SS, Dou XM, Mohan D, Sung JK, Yang JE, et al. Effects of pyrolysis temperature on soybean Stover- and peanut shell-derived biochar properties and TCE adsorption in water. *Bioresource Technology*. 2012;**118**:536-544

[37] Zhao ZD, Zhou WJ. Insight into interaction between biochar and soil minerals in changing biochar properties and adsorption capacities

for sulfamethoxazol. *Environmental Pollution*. 2019;**245**:208-217

[38] Zhang XK, Wang HL, He LZ, Lu KP, Sarmah A, Li JW, et al. Using biochar for remediation of soils contaminated with heavy metals and organic pollutants. *Environmental Science and Pollution Research*. 2013;**20**(12):8472-8483

[39] Yu XY, Ying GG, Kookana RS. Sorption and desorption behaviors of diuron in soils amended with charcoal. *Journal of Agricultural and Food Chemistry*. 2006;**54**(22):8545-8550

[40] Wang HL, Lin KD, Hou ZN, Richardson B, Gan J. Sorption of the herbicide terbuthylazine in two New Zealand forest soils amended with biosolids and biochars. *Journal of Soils and Sediments*. 2010;**10**(2):283-289

[41] Hall KE, Spokas KA, Gamiz B, Cox L, Papiernik SK, Koskinen WC. Glyphosate sorption/desorption on biochars—Interactions of physical and chemical processes. *Pest Management Science*. 2018;**74**(5):1206-1212

[42] Dimitrov S, Nedelcheva D, Dimitrova N, Mekenyan O. Development of a biodegradation model for the prediction of metabolites in soil. *Science of the Total Environment*. 2010;**408**(18):3811-3816

[43] Kupryianchyk D, Hale S, Zimmerman AR, Harvey O, Rutherford D, Abiven S, et al. Sorption of hydrophobic organic compounds to a diverse suite of carbonaceous materials with emphasis on biochar. *Chemosphere*. 2016;**144**:879-887

[44] Yang YN, Sheng GY. Enhanced pesticide sorption by soils containing particulate matter from crop residue burns. *Environmental Science & Technology*. 2003;**37**(16):3635-3639

[45] Hildebrandt A, Lacorte S, Barcelo D. Occurrence and fate of

- organochlorinated pesticides and PAH in agricultural soils from the Ebro river basin. *Archives of Environmental Contamination and Toxicology*. 2009;**57**(2):247-255
- [46] Song WP, Guo MX. Quality variations of poultry litter biochar generated at different pyrolysis temperatures. *Journal of Analytical and Applied Pyrolysis*. 2012;**94**:138-145
- [47] Yu XY, Ying GG, Kookana RS. Reduced plant uptake of pesticides with biochar additions to soil. *Chemosphere*. 2009;**76**(5):665-671
- [48] Cederlund H, Borjesson E, Stenstrom J. Effects of a wood-based biochar on the leaching of pesticides chlorpyrifos, diuron, glyphosate and MCPA. *Journal of Environmental Management*. 2017;**191**:28-34
- [49] Herath I, Kumarathilaka P, Al-Wabel MI, Abduljabbar A, Ahmad M, Usman ARA, et al. Mechanistic modeling of glyphosate interaction with rice husk derived engineered biochar. *Microporous and Mesoporous Materials*. 2016;**225**:280-288
- [50] Mayakaduwa SS, Kumarathilaka P, Herath I, Ahmad M, Al-Wabel M, Ok YS, et al. Equilibrium and kinetic mechanisms of woody biochar on aqueous glyphosate removal. *Chemosphere*. 2016;**144**:2516-2521
- [51] Werth J, Thornby D, Walker S. Assessing weeds at risk of evolving glyphosate resistance in Australian sub-tropical glyphosate-resistant cotton systems. *Crop & Pasture Science*. 2011;**62**(11):1002-1009
- [52] Heap I, Duke SO. Overview of glyphosate-resistant weeds worldwide. *Pest Management Science*. 2018;**74**(5):1040-1049
- [53] Manalil S, Werth J, Jackson R, Chauhan BS, Preston C. An assessment of weed flora 14 years after the introduction of glyphosate-tolerant cotton in Australia. *Crop & Pasture Science*. 2017;**68**(8):773-780
- [54] Werth J, Boucher L, Thornby D, Walker S, Charles G. Changes in weed species since the introduction of glyphosate-resistant cotton. *Crop & Pasture Science*. 2013;**64**(8):791-798
- [55] Baerson SR, Rodriguez DJ, Tran M, Feng YM, Biest NA, Dill GM. Glyphosate-resistant goosegrass. Identification of a mutation in the target enzyme 5-enolpyruvylshikimate-3-phosphate synthase. *Plant Physiology*. 2002;**129**(3):1265-1275
- [56] Malone JM, Morran S, Shirley N, Boutsalis P, Preston C. EPSPS gene amplification in glyphosate-resistant *Bromus diandrus*. *Pest Management Science*. 2016;**72**(1):81-88
- [57] Lorraine-Colwill DF, Powles SB, Hawkes TR, Hollinshead PH, Warner SAJ, Preston C. Investigations into the mechanism of glyphosate resistance in *Lolium rigidum*. *Pesticide Biochemistry and Physiology*. 2002;**74**(2):62-72
- [58] Bostamam Y, Malone JM, Dolman FC, Boutsalis P, Preston C. Rigid ryegrass (*Lolium rigidum*) populations containing a target site mutation in EPSPS and reduced glyphosate trans location are more resistant to glyphosate. *Weed Science*. 2012;**60**(3):474-479
- [59] Ghanizadeh H, Harrington KC, James TK, Woolley DJ, Ellison NW. Mechanisms of glyphosate resistance in two perennial ryegrass (*Lolium perenne*) populations. *Pest Management Science*. 2015;**71**(12):1617-1622

- [60] Hawkes JR, Jones RAC. Incidence and distribution of barley yellow dwarf virus and cereal yellow dwarf virus in over-summering grasses in a Mediterranean-type environment. *Australian Journal of Agricultural Research*. 2005;**56**(3):257-270
- [61] Li CY, Fang B, Yang CW, Shi DC, Wang DL. Effects of various salt-alkaline mixed stresses on the state of mineral elements in nutrient solutions and the growth of alkali resistant halophyte *Chloris virgata*. *Journal of Plant Nutrition*. 2009;**32**(7):1137-1147
- [62] Yang CW, Zhang ML, Liu J, Shi DC, Wang DL. Effects of buffer capacity on growth, photosynthesis, and solute accumulation of a glycophyte (wheat) and a halophyte (*Chloris virgata*). *Photosynthetica*. 2009;**47**(1):55-60
- [63] Li X, Li XL, Jiang DM, Liu ZM. Germination strategies and patterns of annual species in the temperate semiarid region of China. *Arid Land Research and Management*. 2006;**20**(3):195-207
- [64] Fernando N, Humphries T, Florentine SK, Chauhan BS. Factors affecting seed germination of feather fingergrass (*Chloris virgata*). *Weed Science*. 2016;**64**(4):605-612
- [65] Ngo TD, Boutsalis P, Christopher P, Gill G. Growth, development, and seed biology of feather Fingergrass (*Chloris virgata*) in Southern Australia. *Weed Science*. 2017;**65**(3):413-425
- [66] Mennan H, Ngouajio M. Seasonal cycles in germination and seedling emergence of summer and winter populations of catchweed bedstraw (*Galium aparine*) and wild mustard (*Brassica kaber*). *Weed Science*. 2006;**54**(1):114-120
- [67] Adkins SW, Bellairs SM, Loch DS. Seed dormancy mechanisms in warm season grass species. *Euphytica*. 2002;**126**(1):13-20
- [68] Read TR, Bellairs SM. Smoke affects the germination of native grasses of New South Wales. *Australian Journal of Botany*. 1999;**47**(4):563-576
- [69] Chachalis D, Reddy KN. Factors affecting *Campsis radicans* seed germination and seedling emergence. *Weed Science*. 2000;**48**(2):212-216
- [70] Alvarado V, Bradford KJ. A hydrothermal time model explains the cardinal temperatures for seed germination. *Plant Cell and Environment*. 2002;**25**(8):1061-1069
- [71] Koger CH, Reddy KN, Poston DH. Factors affecting seed germination, seedling emergence, and survival of texasweed (*Caperonia palustris*). *Weed Science*. 2004;**52**(6):989-995
- [72] Pezzani F, Montana C. Inter- and intraspecific variation in the germination response to light quality and scarification in grasses growing in two-phase mosaics of the Chihuahuan Desert. *Annals of Botany*. 2006;**97**(6):1063-1071
- [73] Grime JP, Mason G, Curtis AV, Rodman J, Band SR, Mowforth MAG, et al. A comparative-study of germination characteristics in a local flora. *Journal of Ecology*. 1981;**69**(3):1017-1059
- [74] Lin J, Shao S, Wang Y, Qi M, Lin L, Wang Y, et al. Germination responses of the halophyte *Chloris virgata* to temperature and reduced water potential caused by salinity, alkalinity and drought stress. *Grass and Forage Science*. 2016;**71**(3):507-514
- [75] Ngo TD, Boutsalis P, Preston C, Gill G. Plant development and seed biology of windmillgrass (*Chloris truncata*) in Southern Australia. *Weed Science*. 2017;**65**(3):395-405

- [76] Donatelli M, Hammer GL, Vanderlip RL. Genotype and water limitation effects on phenology, growth, and transpiration efficiency in grain sorghum. *Crop Science*. 1992;**32**(3):781-786
- [77] Borger CPD, Riethmuller GP, Hashem A. Emergence, survival, biomass production, and seed production of *Chloris truncata* (windmill grass) in the Western Australian wheatbelt. *Crop & Pasture Science*. 2011;**62**(8):678-685
- [78] Impact of weeds on Australian grain production: the cost of weeds to Australian grain growers and the adoption of weed management and tillage practices. Available from: [https://grdc.com.au/\\_\\_data/assets/pdf\\_file/0027/75843/grdc\\_weeds\\_review\\_r8.pdf](https://grdc.com.au/__data/assets/pdf_file/0027/75843/grdc_weeds_review_r8.pdf)
- [79] Thomas GA, Titmarsh GW, Freebairn DM, Radford BJ. No-tillage and conservation farming practices in grain growing areas of Queensland—A review of 40 years of development. *Australian Journal of Experimental Agriculture*. 2007;**47**(8):887-898
- [80] Powles SB. Evolved glyphosate-resistant weeds around the world: Lessons to be learnt. *Pest Management Science*. 2008;**64**(4):360-365
- [81] Kleinman Z, Rubin B. Non-target-site glyphosate resistance in *Conyza bonariensis* is based on modified subcellular distribution of the herbicide. *Pest Management Science*. 2017;**73**(1):246-253
- [82] Heap I. Global perspective of herbicide-resistant weeds. *Pest Management Science*. 2014;**70**(9):1306-1315
- [83] Wu H, Walker SR, Osten VA, Robinson G. Competition of sorghum cultivars and densities with Japanese millet (*Echinochloa esculenta*). *Weed Biology and Management*. 2010;**10**(3):185-193
- [84] Lemerle D, Lockett DJ, Lockley P, Koetz E, Wu HW. Competitive ability of Australian canola (*Brassica napus*) genotypes for weed management. *Crop & Pasture Science*. 2014;**65**(12):1300-1310
- [85] Swanton CJ, Nkoa R, Blackshaw RE. Experimental methods for crop-weed competition studies. *Weed Science*. 2015;**63**:2-11
- [86] Odonovan JT, Destremy EA, Osullivan PA, Dew DA, Sharma AK. Influence of the relative-time of emergence of wild oat (*Avena-fatua*) on yield loss of barley (*Hordeum vulgare*) and wheat (*Triticum aestivum*). *Weed Science*. 1985;**33**(4):498-503
- [87] Rajcan I, Swanton CJ. Understanding maize-weed competition: Resource competition, light quality and the whole plant. *Field Crops Research*. 2001;**71**(2):139-150
- [88] Page ER, Tollenaar M, Lee EA, Lukens L, Swanton CJ. Shade avoidance: An integral component of crop-weed competition. *Weed Research*. 2010;**50**(4):281-288
- [89] Vila M, Williamson M, Lonsdale M. Competition experiments on alien weeds with crops: Lessons for measuring plant invasion impact? *Biological Invasions*. 2004;**6**(1):59-69
- [90] Cousens R. Aspects of the design and interpretation of competition (interference) experiments. *Weed Technology*. 1991;**5**(3):664-673
- [91] Radosevich SR. Methods to study interactions among crops and weeds. *Weed Technology*. 1987;**1**(3):190-198
- [92] Borger CPD, Hashem A, Powles SB. Manipulating crop row



orientation and crop density to suppress  
*Lolium rigidum*. Weed Research.  
2016;**56**(1):22-30

[93] Al-Bedairy NR, Alsaadawi IS,  
Shati RK. Combining effect of  
allelopathic *Sorghum bicolor* L.  
(Moench) cultivars with planting  
densities on companion weeds.  
Archives of Agronomy and Soil Science.  
2013;**59**(7):955-961



# Hybrid Two-step Preparation of Nanosized MgAl Layered Double Hydroxides for CO<sub>2</sub> Adsorption

*Xiani Huang, Xiaogang Yang, Guang Li, Collins I. Ezeh, Chenggong Sun and Collins Snape*

## Abstract

Hybrid Two-step synthesis method for preparation of MgAl LDHs materials for CO<sub>2</sub> adsorption has been employed because of the features of fast micromixing and enhanced mass transfer by using a 'T-mixer' reactor. MgAl LDHs with different morphologies were successfully obtained by three different synthesis routes: ultrasonication-intensified in 'T-mixer' (TU-LDHs), conventional co-precipitation (CC-LDHs) and ultrasonic-intensified in 'T-mixer' pretreatment followed by conventional co-precipitation (TUC-LDHs). The synthesized samples characterized by the XRD showed that LDHs formed a typical layered double hydroxide structure and no other impurities were identified in the compound. The SEM and TEM analyses also confirmed that the size distribution of TUC-LDHs was relatively uniform (with an average size of approximate 100 nm) and layered structure was clearly visible. The BET characterization indicated that such LDHs had a large surface area (235 m<sup>2</sup> g<sup>-1</sup>), which makes it a promising adsorbent material for CO<sub>2</sub> capture in practical application. It can be found that the CO<sub>2</sub> adsorption capacities of TU-LDHs, CC-LDHs and TUC-LDHs at 80°C were 0.30, 0.22 and 0.28 mmol g<sup>-1</sup>, respectively. The CO<sub>2</sub> adsorption capacities of TU-LDHs, CC-LDHs and TUC-LDHs at 200°C were 0.33, 0.25 and 0.36 mmol g<sup>-1</sup>, respectively. The order of CO<sub>2</sub> adsorption capacity to reach equilibrium at 80°C seen in Avrami model is: TU-LDHs > TUC-LDHs > CC-LDHs. The CO<sub>2</sub> adsorption/desorption cycling test reveals that TU-LDHs and TUC-LDHs have good adsorption stability than CC-LDHs.

**Keywords:** MgAl LDHs, ultrasonic, co-precipitation, T-mixer, CO<sub>2</sub> adsorption capacity, Avrami model

## 1. Introduction

The removal of CO<sub>2</sub> emission from fossil fuel combustion, especially from coal-fired power stations, has attracted much attention in recent years because of its potential negative impact on global warming and on human beings. It was reported that CO<sub>2</sub> concentration in atmosphere now is close to 400 ppm, which is significantly higher than the reported industrial level of 300 ppm [1]. CO<sub>2</sub> capture and storage (CCS) technology is considered to be an effective means to cope with the global demand of CO<sub>2</sub> reduction in the long run. Among many technologies existing for CO<sub>2</sub> capture, the use of amine-based solutions is still the main practical

technology on a large scale capture operation which could produce a series of bad effects such as toxicity, degradability, high regeneration energy requirements and corrosivity [2]. Hence, developing efficient and environmental friendly CO<sub>2</sub> adsorbents will be crucial to CO<sub>2</sub> capture. Layered double hydroxides (LDHs) are considered as good candidates for CO<sub>2</sub> adsorption because of their fast sorption/desorption kinetics and simple regenerability [3, 4]. LDHs are a class of ionic lamellar compounds made up of positively charged brucite-like layers with an interlayer region containing charge compensating anions and solvation molecules. The typical structure of LDHs consists of positively charged brucite-like layers, containing anions and water molecules in the interlayer spaces. Metal cations occupy the centre of octahedral structures and hydroxides occupy the vertices. The general formula of LDHs can be expressed as  $[M^{2+}_{1-x}M^{3+}_x(OH)_2][A^{n-}]_{x/n}zH_2O$ , where M<sup>2+</sup> are divalent cations, such as Mg<sup>2+</sup>, Zn<sup>2+</sup>, Ni<sup>2+</sup>, etc., and M<sup>3+</sup> are trivalent cations, such as Al<sup>3+</sup>, Ga<sup>3+</sup>, Fe<sup>3+</sup>, Mn<sup>3+</sup>, etc. A<sup>n-</sup> is a non-framework charge compensating anion, such as CO<sub>3</sub><sup>2-</sup>, Cl<sup>-</sup>, SO<sub>4</sub><sup>2-</sup>, etc., and the value of x is between 0.10 and 0.33 [5].

The performance of LDHs and derived CO<sub>2</sub> adsorbents have been investigated for several years, and most of the studies are focused on the effects of divalent cations [6, 7], trivalent cations [8], charge compensating anions [9, 10], Mg-Al ratio [6, 11, 12], alkaline metal cations (e.g. K<sup>+</sup>, Cs<sup>+</sup>, Na<sup>+</sup>, etc.) [13–16], synthetic method [17], the presence of SO<sub>2</sub> and H<sub>2</sub>O [18, 19], particle size [3, 20] and calcination temperature or adsorption temperature [21, 22]. Yong and Rodrigues compared several commercial hydrotalcite-like compounds that can have the average CO<sub>2</sub> adsorption capacity (0.2–0.5 mmol g<sup>-1</sup>) at 300°C and 1 bar of CO<sub>2</sub> [6]. Wang et al. found that similar CO<sub>2</sub> capture capacities (0.41–0.46 mmol g<sup>-1</sup>) can be obtained when using Mg<sub>3</sub>Al<sub>1</sub>, Mg<sub>3</sub>Ga<sub>1</sub> and Mg<sub>3</sub>Fe<sub>1</sub> at different calcination temperatures [8]. Except for changing the composition of LDHs, controlling its particle size is also believed to be an effective way for improvement of the CO<sub>2</sub> capture capacity. Significant amount of efforts have been made on developing new methods to control its particle size. Hanif et al. investigated the effect of synthetic routes (co-precipitation, ultrasonication and microwave irradiation) on improving the CO<sub>2</sub> adsorption capacity of hydrotalcite-based sorbents in the temperature range 300–400°C [17]. They have reported that the CO<sub>2</sub> adsorption capacity of LDHs prepared by ultrasound-assisted route and microwaving are better than that of co-precipitation method.

Adoption of confined impinging T-jet mixer (CITJ) is a simple component that contains two inlet tubes and let two streams flow out from the tube. The local micromixing effect could be intensified during the CITJ reactor, which is beneficial for a fast homogenization of reactors. The mass transfer rate and chemical reaction rate can also be enhanced during the preparation process. This has been confirmed by the studies on the preparation of FePO<sub>4</sub> nanoprecursor particles of LiFePO<sub>4</sub> cathode material where the high specific areas can be obtained [23, 24]. Co-precipitation method is the conventional procedure used for synthesis of hydrotalcites. Ultrasonication and microwave irradiation of the synthesis gel during hydrotalcite precipitation leads to disruption in the layer stacking which in turn increases surface area [17]. To the best of our knowledge, the effect of the synthesis for the preparation of LDHs by applying jointly co-precipitation and ultrasonication in a T-jet mixer on the CO<sub>2</sub> adsorption capacity of LDHs has not yet been reported in the literature.

In the present study, we will present a hybrid two-step method approach for preparation of MgAl layered double hydroxide (MgAl LDHs). The novel two-step preparation route utilising the MgAl LDHs synthesized from confined impinging T-jet mixer (CITJ) as seeds for future preparation. The synthesized samples were

characterized using X-ray diffraction (XRD), scanning electron microscopy (SEM), transmission electron microscopy (TEM) and BET analysis. Their performance of CO<sub>2</sub> adsorption was evaluated using thermogravimetric analysis (TGA). The effect of the rate of addition of Mg(NO<sub>3</sub>)<sub>2</sub> and Al(NO<sub>3</sub>)<sub>3</sub> on improvement of the CO<sub>2</sub> capture capacity of MgAl LDHs and initial NH<sub>3</sub>H<sub>2</sub>O is also investigated.

## 2. Experimental

### 2.1 Materials preparation

#### 2.1.1 LDH synthesized in T-Mixer with ultrasonic process

Salt solution A (100 mL) containing a mixture of 0.03 mol L<sup>-1</sup> Mg(NO<sub>3</sub>)<sub>2</sub> and 0.01 mol L<sup>-1</sup> Al(NO<sub>3</sub>)<sub>3</sub> and solution B-NH<sub>3</sub>H<sub>2</sub>O (100 mL) with certain concentration was simultaneously transported into a 'T-type' impinging-stream reactor by means of metering pumps at the rate of 100 r min<sup>-1</sup> to produce MgAl LDHs. Ultrasonic processing was also applied during this process and the frequency of ultrasonic processing kept to be 20 kHz. The pH of the whole solution was always kept to be 10 ± 0.2 though regulating the concentration of NH<sub>3</sub>H<sub>2</sub>O. The resulting mixture washed with water for several times until pH = 7 and then dried at 100°C in an oven. The resulting material was denoted as **TU-LDHs**.

#### 2.1.2 LDH synthesized by conventional co-precipitation method

For the synthesis of traditional LDHs, LDHs was prepared by co-precipitation method. The salt solution with a fixed concentration of 0.03 mol L<sup>-1</sup> Mg(NO<sub>3</sub>)<sub>2</sub> and 0.01 mol L<sup>-1</sup> Al(NO<sub>3</sub>)<sub>3</sub>-A (200 mL) with a certain rate of addition and 1 mol L<sup>-1</sup> of NH<sub>3</sub>H<sub>2</sub>O were simultaneously added to the mixture at the second step, where the pH of the whole solution was always kept to be 10 ± 0.2 and continuous stirring rate is 400 r min<sup>-1</sup>. The mixture was then aged for further 4 h with stirring maintained. The final obtained materials were filtered and washed with distilled water until pH = 7, followed by drying at 100°C in an oven. The obtained material was denoted as **CC-LDHs**.

#### 2.1.3 LDH synthesized by hybrid two-step method

MgAl layered double hydroxides (MgAl LDHs) were prepared using a hybrid two-step preparation approach. The hybrid two-step preparation consists of the mother solution prepared in 'T-mixer' accompanying with ultrasonic processing (first step) and the following step of co-precipitation (second step) process. The mother solution was synthesized according to the preparation method of the above section. About 50 mL of mother solution from the above solution was put into a beaker for continuous stirring with a rate of 400 r min<sup>-1</sup>. Then, 150 mL of salt solution with a fixed concentration of 0.03 mol L<sup>-1</sup> Mg(NO<sub>3</sub>)<sub>2</sub> and 0.01 mol L<sup>-1</sup> Al(NO<sub>3</sub>)<sub>3</sub> and 1 mol L<sup>-1</sup> of NH<sub>3</sub>H<sub>2</sub>O were simultaneously added to the mixture at the second step. The addition rate of salt solution was controlled by regulating the speed of peristaltic pump, where the pH of the whole solution was always kept to be 10 ± 0.2. The whole preparation process of MgAl LDHs by two steps were illustrated in **Figure 1**. The final obtained materials were filtered and washed with distilled water until pH = 7, followed by drying at 100°C in an oven. The obtained material was denoted as **TUC-LDHs**.



**Figure 1.** Schematic illustrating the preparation process of MgAl LDHs by hybrid two steps.

## 2.2 Materials characterization

The structures of MgAl LDHs were characterized using a combination of methods including BET-specific surface areas, X-ray diffraction (XRD), scanning electron microscopy (SEM), energy dispersive X-ray spectroscopy (EDX) analysis and transmission electron microscope (TEM).

### 2.2.1 BET

Nitrogen adsorption/desorption isotherms were carried out on a Micromeritics ASAP2020 surface area and pore size analyser at 77 K. Before conducting each measurement, the prepared LDHs were first degassed at 110°C overnight.

### 2.2.2 XRD

The structure of the prepared samples were analysed by XRD through conducting in a Bruke-AXS D8 advance powder diffractometer using Cu-K $\alpha$  radiation ( $\lambda = 1.5418 \text{ \AA}$ ) and a power of 40 kv\*20 Ma, where the diffraction patterns were recorded in the range  $2\theta = 5\text{--}80^\circ$  with a step size of  $0.01^\circ$ .

### 2.2.3 SEM and EDXS

The morphologies of synthesized LDHs were observed using SEM produced from ZEISS ZIGMA 174C CZ. The element analysis was conducted by use of an Oxford Instrument INCAx-act PentaFET® Precision EDXs.

### 2.2.4 TEM

High-resolution TEM images were obtained using JEM-2100 electron microscope operating at 200 kV, whereby a drop of solution was placed onto a Cu grid and dried in infrared lamp for several minutes.

### 2.3 Carbon dioxide adsorption measurements

The CO<sub>2</sub> adsorption test and regenerability of the synthesized adsorbents were measured by Netzsch TG 209 F1 thermogravimetric analyser (TGA) at atmosphere pressure under dry conditions. Pure CO<sub>2</sub> gas was used to carry out the whole adsorption/desorption measurement. Before adsorption test, all the samples were calcined at 500°C for 5 h in an Ar atmosphere. About 10 mg of sample loaded into an alumina crucible was heated from 25 to 105°C at 10°C min<sup>-1</sup> under N<sub>2</sub> atmosphere for 60 min and then switched to desired temperature (80, 150 and 200°C) at the rate of 10°C min<sup>-1</sup>. During the isothermal stage, the gas input changed from N<sub>2</sub> to CO<sub>2</sub> and held for 90 min. The CO<sub>2</sub> adsorption capacity of the sample- $q_t$  (mmol g<sup>-1</sup>) was calculated according to the weight gain of the sample and expressed as the mole of CO<sub>2</sub> absorbed per gram of adsorbent:

$$q_t = \frac{m_t - m_o}{m \times M} \times 1000 \quad (1)$$

where  $m_o$  and  $m_t$  (mg) are the initial mass of adsorbent for CO<sub>2</sub> adsorption and mass of adsorbent for CO<sub>2</sub> adsorption at time  $t$ , respectively.  $m$  is the total mass of sorbent (mg) and  $M$  is molar mass of CO<sub>2</sub> (44 mol g<sup>-1</sup>).

In the absorption/desorption cycle, about 10 mg of the above calcined samples was heated from 25 to 105°C at 10°C min<sup>-1</sup> under N<sub>2</sub> atmosphere (40 mL min<sup>-1</sup>) for 60 min and then switched to 80°C at a cooling rate of 10°C min<sup>-1</sup>. After adsorption, the desorption process was carried out as the gas input was switched from CO<sub>2</sub> to N<sub>2</sub> at 105°C. The adsorption/desorption process was repeated in six cycles.

### 2.4 Error analysis

To determine the validity of isotherm and kinetics models, two different error functions, i.e. chi-square ( $X^2$ ) and normalized standard deviation  $\Delta q$  (%), and correlation coefficient equation  $R^2$  were evaluated between experimental and calculated data, which are given by

$$\text{Chi - square : } X^2 = \sum_{i=1}^n \frac{(q_t - q_e)^2}{q_e} \quad (2)$$

$$\text{Normalized standard deviation : } \Delta q(\%) = \sqrt{\frac{\sum_{i=1}^n [(q_t - q_e)/q_e]^2}{n - 1}} \times 100 \quad (3)$$

$$\text{Correlation coefficient equation : } R^2 = 1 - \left( \frac{\sum_{j=1}^N (q_t - q_e)^2}{\sum_{j=1}^N (q_t - \bar{q}_e)^2} \right) \times \left( \frac{N - 1}{N - p} \right) \quad (4)$$

where  $q_t$  and  $q_e$  are CO<sub>2</sub> uptake determined by experiment and computed by model, respectively.  $q_e$  is the mean experimental data,  $p$  is the number of model parameters and  $N$  is total number of experimental points. The most suitable model to describe the CO<sub>2</sub> adsorption process is the one with highest  $R^2$  value.

### 3. Results and discussion

#### 3.1 Synthesis and characterization of LDHs prepared by different ways

Co-precipitation method is a common method used in preparation of MgAl LDHs materials in the previous studies. The main requirement for improving the CO<sub>2</sub> adsorption capacity of MgAl LDHs is to develop it with high surface area and pore volume. It is well known that the formation process of MgAl LDHs includes both nucleation and growth process. Controlling the process of nucleation properly may have an effect on the whole size of MgAl LDHs, thus increasing its surface area. Here, we reported the first synthesis of MgAl LDHs using a hybrid two-step method. At first step, the salt solution and initial concentration of NH<sub>3</sub>H<sub>2</sub>O solution were transported into 'T-type' impinging-stream reactor. Two solutions interact on each other on the 'T-type' impinging-stream reactor and ultrasonic wave were also applied in the interaction process. At second step, the conventional co-precipitation method was used. This means that a certain rate of salt solution and NH<sub>3</sub>H<sub>2</sub>O were simultaneously added to the mixture to produce the MgAl LDHs. The chemical and physical effects of ultrasonic irradiation originated from acoustic cavitation lead to rapid reaction rate and change the selectivity performance of the reaction [25], thus improving the nucleation of MgAl LDHs.

The XRD patterns of MgAl LDHs prepared using three different methods are shown in **Figure 2**. For all the samples, the characteristic reflections based on the structure of (PDF #35-0965) were clearly observed, which can be indexed to (i) (00 $l$ ) peaks of (003) and (006) with corresponding to the basal spacing and higher order reflections; (ii) (0 $kl$ ) peaks of (012), (015) and (018) with broad reflections; (iii) sharp ( $hk0$ ) and ( $hkl$ ) peaks of (110) and (113). It can be seen that LDHs samples synthesized under different conditions have similar structures. The lattice parameter  $a$  and  $c$  are calculated according to the parameters of (110) and (003) plane assuming a 3R stacking of layer structure, where the value  $a$  ( $a = 2d_{110}$ ) represents average distance between two metal ions and  $c$  is three times of the brucite-like layer and interlayer distance ( $d_{003}$ ). The lattice parameter  $a$  is almost independent of the synthesis method, which can be explained that it was affected

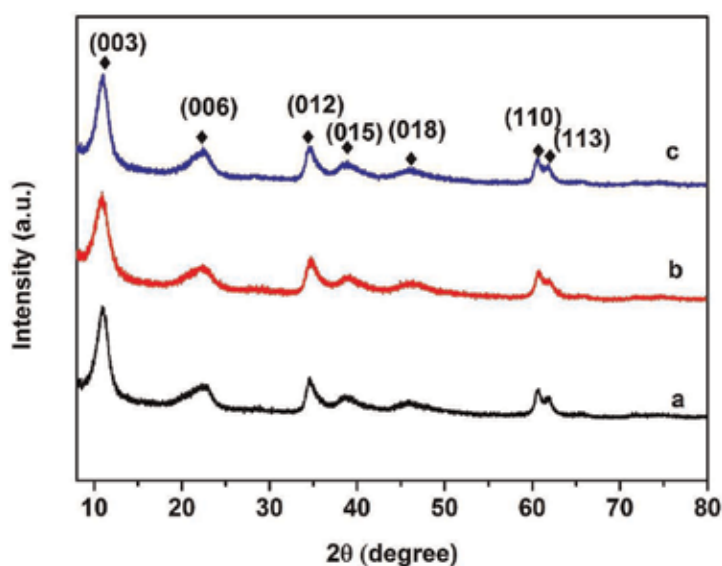


**Figure 2.** XRD patterns for MgAl LDHs prepared using (a) TU method, (b) CC method and (c) TUC method.



by the type of metal cation (Mg<sup>2+</sup> and Al<sup>3+</sup>). Although LDHs are prepared by three different ways, the metal cation of Mg<sup>2+</sup> and Al<sup>3+</sup> still keep the same without any change. Similar observations can be found in the research of Wang et al. for the formation of LDHs by co-precipitation and IEP method [20]. Concerning the lattice parameter *c*, it was affected by three main factors: the average charge of the metal cations, the nature of the interlayer anion and the water content. TU-LDHs have lowest lattice parameter *c* compared to other two LDHs. All the samples use the same anion and metal cations so that the slight difference between samples may be related to a slow water content in the layer.

The crystalline size of particles was calculated using the *Debye-Scherrer's formula*

$$D = \frac{0.89\lambda}{\beta \cos \theta} \quad (5)$$

where *D* is the grain size (nm),  $\lambda$  is the wavelength of the X-ray radiation,  $\beta$  is the full width at half maximum and  $\lambda$ ,  $\theta$  is the angle of diffraction. The crystallite size along the *c* direction was calculated according to (003) and (006) diffraction peaks. The values given in **Table 1** showed that the crystallite size in the *c* direction by TU-LDHs and TUC-LDHs were a slightly higher than the crystallite size of CC-LDHs. There is no obvious reduction of crystallite size in the *c* direction of materials prepared by three different methods.

N<sub>2</sub> adsorption-desorption isotherm of MgAl LDHs is given in **Figure 3**. All the adsorbents show a Type IV isotherm according to the IUPAC classification, which is associated with mesoporous materials [26]. TUC-LDHs and CC-LDHs show a H3 type hysteresis loop, suggesting that the pores are produced by 'slit-shaped' of plate-like particles [27]. This type of isotherm is commonly observed in the mesoporous stacking structure of sheet-like 2D crystallites [28]. In the case of TU-LDHs, it shows a H2 type hysteresis loop corresponding to a complex and interconnected pore structure, indicating that the pores are produced by rapid nucleation process. This difference could be related to the different synthetic route applied in this work. The surface area (*S*<sub>BET</sub>) of the samples were determined using BET (Brunauer, Emmett and Teller) model. The total volumes (*V*<sub>Total</sub>) were calculated according to the amount of nitrogen (N<sub>2</sub>) absorbed at a relative pressure (*P*/*P*<sub>O</sub>) of 0.99. The pore volumes were calculated from the desorption branch of the isotherms using the Barrett-Joyner-Halenda (BJH) method, for the pores between 1.7 and 300.0 nm. **Table 2** lists the textural parameters of MgAl LDHs obtained from N<sub>2</sub> adsorption-desorption isotherms. It can be seen clearly that the *S*<sub>BET</sub> of TUC-LDHs is the highest of 235.3 m<sup>2</sup> g<sup>-1</sup> compared to 198.7 m<sup>2</sup> g<sup>-1</sup> for TU-LDHs and 148.1 m<sup>2</sup> g<sup>-1</sup> for CC-LDHs as well as the pore sizes (90.83 Å) and highest pore

Property	TU-LDHs	CC-LDHs	TUC-LDHs
<i>d</i> <sub>003</sub> (nm)	0.7977	0.8058	0.8011
<i>d</i> <sub>110</sub> (nm)	0.1518	0.1516	0.1519
<i>a</i> <sup>a</sup> (nm)	0.3036	0.3032	0.3038
<i>c</i> <sup>b</sup> (nm)	2.3931	2.4174	2.4033
Crystallite size in <i>c</i> direction (nm) <sup>c</sup>	8.65	7.35	8.63

<sup>a</sup>*a* = 2*d*<sub>110</sub>

<sup>b</sup>*c* = 3*d*<sub>003</sub>

<sup>c</sup>Value calculated from (003) and (006), according to Debye-Scherrer's formula.

**Table 1.**  
 Lattice parameters of LDHs prepared by different methods.

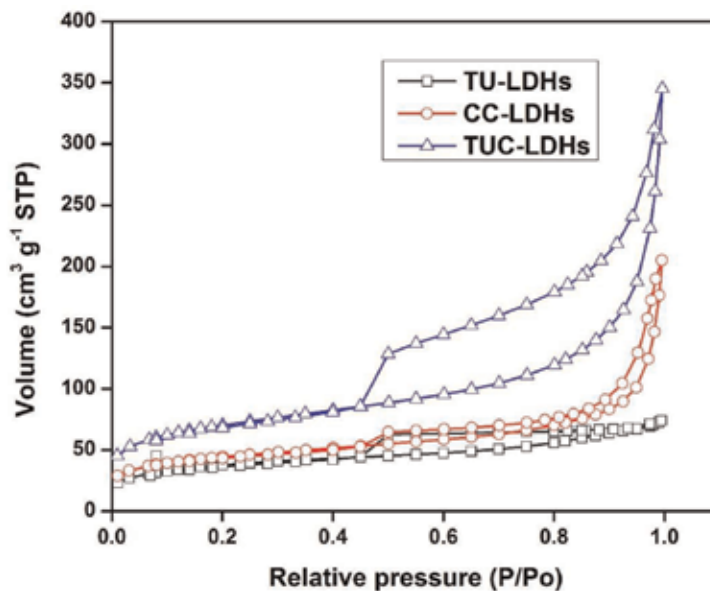


**Figure 3.** Nitrogen adsorption-desorption isotherm for TU-LDHs, CC-LDHs and TUC-LDHs.

Sample name	BET surface area ( $\text{m}^2 \text{g}^{-1}$ )	Average pore diameter ( $\text{\AA}$ )	Pore volume ( $\text{cm}^3 \text{g}^{-1}$ )
TU-LDHs	198.7	24.4	0.08
CC-LDHs	148.1	85.61	0.28
TUC-LDHs	235.3	90.83	0.48

**Table 2.** Textural parameters of MgAl LDHs obtained from  $\text{N}_2$  adsorption-desorption isotherms.

volume ( $0.48 \text{ cm}^3 \text{ g}^{-1}$ ). Both of TUC-LDHs and CC-LDHs facilitate the macro-structure of pores. Although TU-LDHs has the second largest  $S_{\text{BET}}$ , its pore sizes ( $24.4 \text{ \AA}$ ) and pore volume ( $0.08 \text{ cm}^3 \text{ g}^{-1}$ ) are the lowest in comparison with other two materials. This indicates that the TU method contributes to the formation of mesoporous structure. The increase in surface area of TU-LDHs is very likely caused by the enhanced micromixing in the ‘T-mixer’, where the use of ultrasonication can intensify the turbulent eddies and those microbubble bursting that erode the surface area of hydroxalicates of layered structure through removal of the interlayer anions [17]. This effect may be more evident as TUC-LDHs compared with CC-LDHs possess smaller size so that the erosion can be taking place for TUC-LDHs. This explanation seems to be supported by SEM and TEM observation of TUC-LDHs.

The size, morphologies and structure of MgAl LDHs prepared by different methods are characterized using FESEM. It can be clearly seen from **Figure 4(a)** that the morphology and structure of TU-LDHs looks like a house-of-cards-type stacking structure, which is similar to that from ‘exfoliation-self-assembly’ method. However, no significant differences can be observed between CC-LDHs and TUC-LDHs, as shown in **Figure 4(b)** and **(c)**. Both of them show rose-like morphology, while morphology of TUC-LDHs looks quite loose compared with CC-LDHs. In order to further explore the morphology and structure of the prepared LDHs, CC-LDHs and TUC-LDHs were also characterized using TEM analysis. The TEM image in **Figure 4(f)** shows that the TUC-LDHs has an average size of 100 nm and

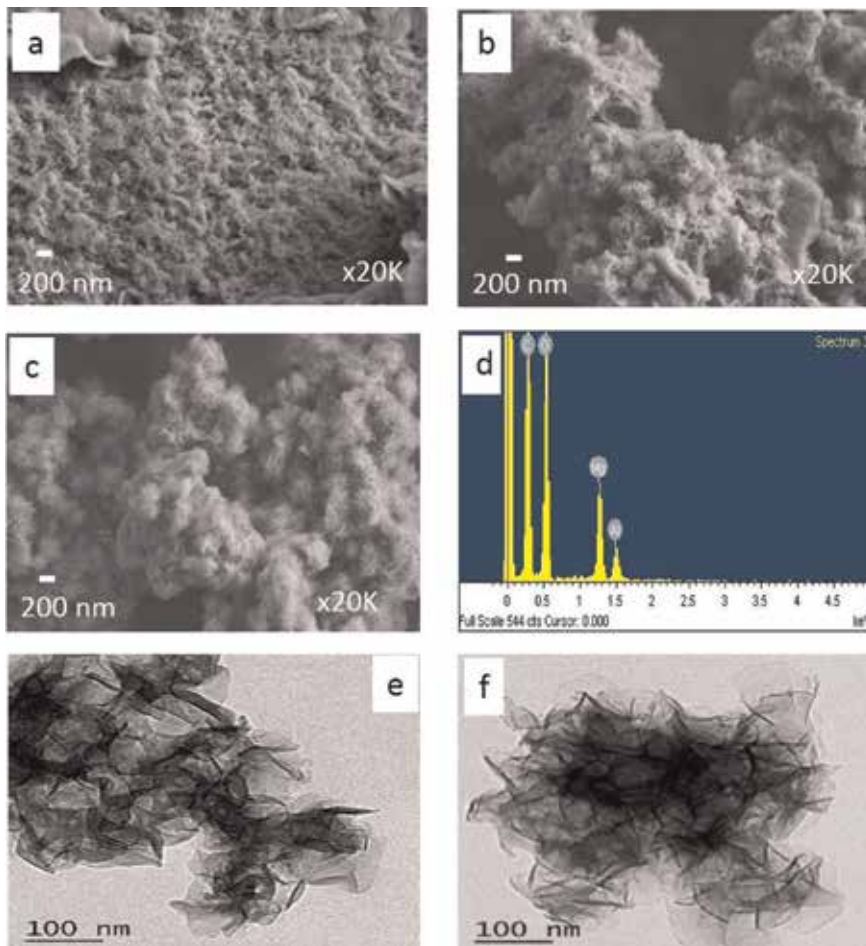


**Figure 4.** SEM images of MgAl LDHs for (a) TU-LDHs, (b) CC-LDHs and (c) TUC-LDHs; EDS of (d) TUC-LDHs; TEM of (e) CC-LDHs and (f) TUC-LDHs.

thickness of 10–20 nm. However, the average size and thickness of CC-LDHs (shown in **Figure 4(e)**) are significantly larger than in the case of TUC-LDHs. In addition, EDX analysis of TUC-LDHs (shown in **Figure 4(d)**) is given as a rough molar ratio of  $M_{\text{Mg}/\text{Al}} \approx 3$ , which is consistent with chemical composition of raw materials.

From the above XRD, BET, SEM and TEM results, further analyses are as follows. Mixing is very slow, relying on the molecular diffusion process due to the absence of turbulence in a low Reynold number. However, the mixing can be enhanced by changing the geometry of mixing channel from conventional agitated vessel to ‘T-mixer’. Ultrasonic wave, an external energy force, can generate additional force to interfere with the flow field in the ‘T-mixer’ channel so that a high level of supersaturation is generated and micromixing process of chemical reaction can be enhanced in extremely short time ( $\sim 10^{-7}$  s) [23, 24]. Thus, the high level of supersaturation contributes to form large amounts of nuclei in a short time, resulting in a small average particle size accumulating together, which is consistent with the BET results in **Table 2**. Finally, the layered structure of TU-LDHs seems to stack together tightly. For TUC-LDHs, the presence of TU-LDHs during the growth of TUC-LDH may introduce defects into LDH structure, through modified nucleation conditions or induced curvature [29]. The final particles exhibit fluffy shapes

and the flake-like structures are formed. Another important reason may be related to the isoelectric point (IEP) of MgAl LDHs. The IEP of MgAl LDHs is around 10, so it can be positively ( $\text{pH} > \text{IEP}$ ), neutrally ( $\text{pH} = \text{IEP}$ ), or negatively ( $\text{pH} < \text{IEP}$ ) charged depending on the relationship between the IEP and the pH. Because it is electronic neutrally on its surface, its growth is inhibited due to the repulsive force between negatively charged TUC-LDH primary particles and  $\text{Al}(\text{OH})_4^-$ ,  $\text{CO}_3^{2-}$ ,  $\text{OH}^-$  anions. Hence, the formation rate of LDHs is so fast that the growth in all directions under such basic conditions. It is well known that the formation process of TUC-LDH includes both nucleation and growth process. In our experiment, the growing of TUC-LDH is based on the mixture solution, which suggests that it supplies a nucleation environment for TUC-LDH growth, then the directions of LDHs growth could be determined. As reported in literature, the deposition of a colloidal suspension of TUC-LDH on substrates, such as glass or silicon, generally leads to the TUC-LDH nanoplatelets having preferred orientation with their c-axis perpendicular to the substrate. The fact that the MgAl- $\text{CO}_3$  LDH nanoplatelets are perpendicularly attached to the surface via their edges suggests they are grown onto the substrate via a strong chemical interaction. Wang et al. reported the first synthesis of nanosized spherical MgAl LDHs using IEP method [20].

### 3.2 TGA analysis

Calcination is a very important step for activating the MgAl LDHs, because the fresh LDHs do not contain much basic sites so that the  $\text{CO}_2$  uptake capacity is quite low. **Figure 5** shows the TGA spectrum of the three different types of synthesized LDHs. The curves for the LDHs prepared by three methods are all fairly similar in shape. The TGA spectra of TU-LDHs show a weight loss of 13% between 50 and 207°C due to the loss of the physisorbed water. In the second weight loss, 33.2% occurred between 207 and 600°C, which is mainly caused by dehydroxylates and decarbonates of LDHs to a large extent, finally leading to the formation of a mixed oxide with a three-dimensional network [8]. For CC-LDHs, the first weight loss

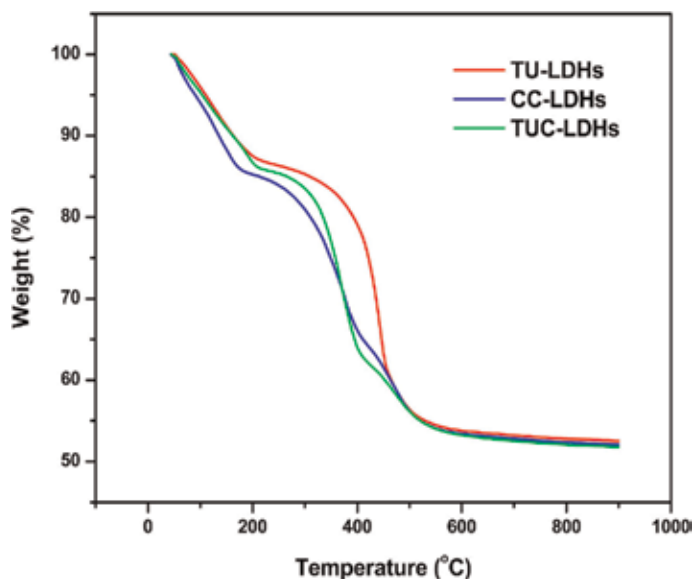


**Figure 5.**  
TGA spectrum of the three different types of synthesized LDHs.

(14%) was found to occur between 50 and 170°C. In the temperature range of 50 and 214°C, TUC-LDHs observed a weight loss of 14%. There are no much differences during the second weight loss process among three samples.

### 3.3 CO<sub>2</sub> adsorption capacity

The CO<sub>2</sub> capture capacity of the above-mentioned three types of LDHs, including TU-LDHs, TUC-LDHs and CC-LDHs, were evaluated using isothermal CO<sub>2</sub> adsorption tests. In the present work, we are particularly interested in whether the modified methods would influence the final CO<sub>2</sub> adsorption capacity or not. The CO<sub>2</sub> adsorption capacities of the different types of LDHs are given in **Figure 6**. All the samples were first calcined at 500°C before each CO<sub>2</sub> adsorption test. Then, the thermogravimetric adsorptions of CO<sub>2</sub> on the samples were measured at 80, 150 and 200°C using a TGA analyser. It can be found that the CO<sub>2</sub> adsorption capacities of TU-LDHs, CC-LDHs and TUC-LDHs at 80°C are 0.30, 0.22 and 0.28 mmol g<sup>-1</sup>, respectively. While for the sample at 200°C, the CO<sub>2</sub> adsorption capacities of TU-LDHs, CC-LDHs and TUC-LDHs are 0.33, 0.25 and 0.36 mmol g<sup>-1</sup>, respectively. The CO<sub>2</sub> adsorption capacity of LDHs at 200°C was higher than that of 80 and 150°C. The main reason maybe that a surface phenomenon and chemical interactions are restricted at 80°C due to the higher activation energy [19]. We can see that TUC-LDHs had better adsorption capacity than other two TU-LDHs and CC-LDHs independent of adsorption temperature. The removal of water during calcination process leads to the formation of channels and pores. As the BET surface area of TUC-LDHs is higher than TU-LDHs and CC-LDHs, it could increase more basic sites for CO<sub>2</sub> adsorption [7].

### 3.4 Kinetic studies of CO<sub>2</sub> capture performance

In order to get a good adsorbent, fast adsorption kinetics is considered as one of the most important parameters to evaluate the adsorbent in a dynamic process. Hence, the ability of withstanding large adsorbate flows are connected with the rate of adsorption. Here, we mainly study the PFO model and Avrami model on the function of CO<sub>2</sub> adsorption on our LDHs [30]. The general sorption rate equations are expressed as:

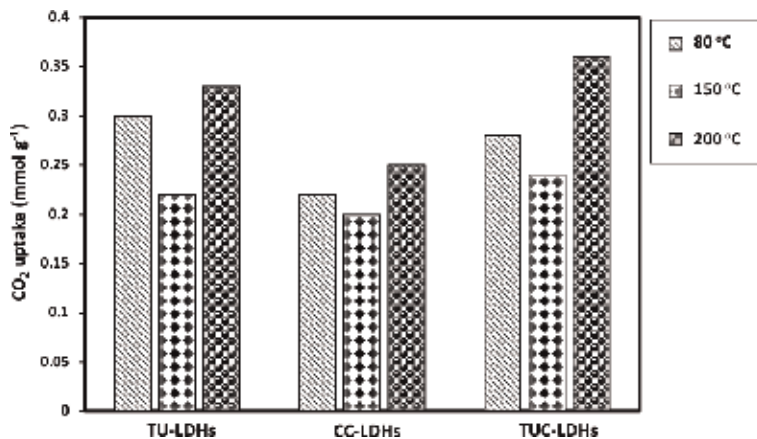


**Figure 6.** CO<sub>2</sub> adsorption capacities of the different types of LDHs at different temperatures.

Pseudo-first-order (PFO) model:

$$q_t = q_e(1 - \exp(-k_f t)) \quad (6)$$

Avrami model:

$$q_t = q_e(1 - \exp(-(k_A t)^{n_A})) \quad (7)$$

where  $q_e$  is the adsorption capacity at equilibrium and at time  $t$ , respectively,  $k_f$  is the kinetic parameter of pseudo first order model,  $k_A$  is the kinetic parameter of Avrami model, the Avrami exponent and  $n_A$  is a factionary number, which reflects the adsorption mechanism.

To investigate the CO<sub>2</sub> adsorption kinetics of LDHs, **Figure 7** shows that the CO<sub>2</sub> uptake vs. time of TU-LDHs, CC-LDHs and TUC-LDHs at 80, 150 and 200°C and the corresponding profiles as predicted by pseudo-first-order and Avrami kinetic models. From the figure, it could be seen that the adsorption curves of LDHs

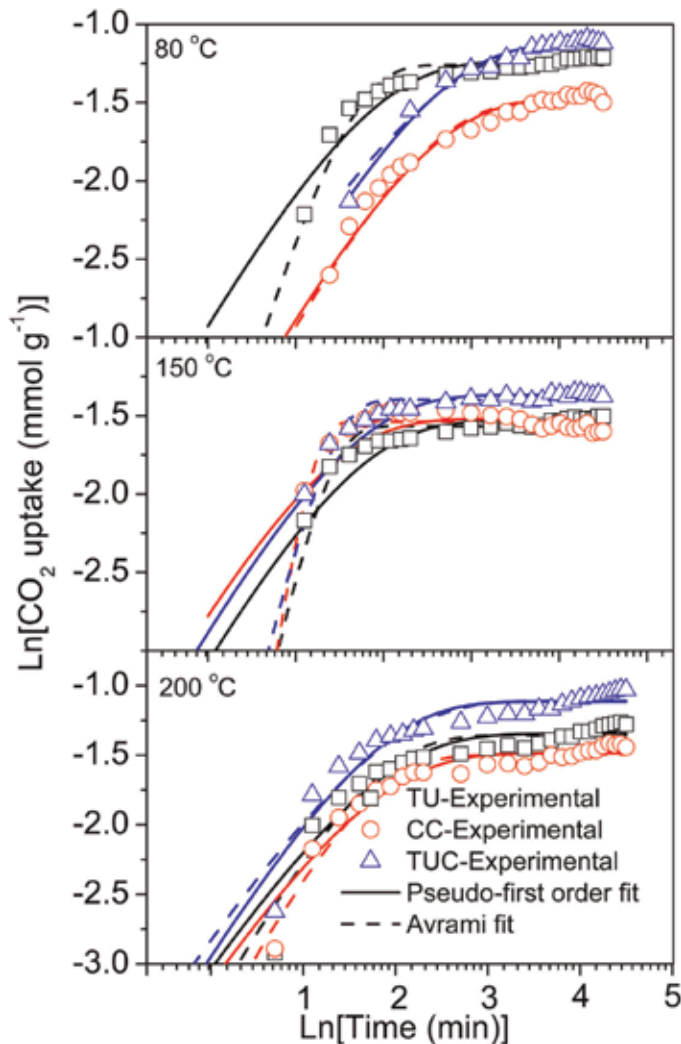


**Figure 7.** Experimental CO<sub>2</sub> uptake on different LDHs at different temperatures and corresponding fit to kinetic models: (□) TU-LDHs, (○) CC-LDHs, (△) TUC-LDHs, (—) Pseudo-first order fit and (---) Avrami fit.

showed obvious two-stage adsorption process under different adsorption conditions. That means, adsorption process of CO<sub>2</sub> sorption by LDHs consists of a fast reaction stage and a much slower second stage controlled by CO<sub>2</sub> diffusion. Clearly, both of the models predict CO<sub>2</sub> adsorption process well. But, Avrami kinetic model offers a better description of the adsorption of CO<sub>2</sub>, since the R<sup>2</sup> value was higher and X<sup>2</sup> and Δq yielded low values in comparison of pseudo-first order model. Therefore, Avrami kinetic model is more suitable to predict the CO<sub>2</sub> adsorption process of LDHs in our experiment. **Table 3** shows the values of kinetic constants and the characteristic parameters from the kinetic model, along with the X<sup>2</sup>, Δq, R<sup>2</sup> as calculated using Eqs. (1)–(3). This is because pseudo-first order kinetic model is suitable for explaining the low surface coverage adsorption, and hence describes the early stages of adsorption [30, 31]. In the process of CO<sub>2</sub> adsorption by LDHs, it is not a simple physical adsorption process. LDHs consists of positively charged Mg-Al-OH brucite type network in an octahedral network. After calcination, the LDHs gradually loses its interlayer water and form a mixed oxide with sufficient basic sites which are favourable for CO<sub>2</sub> sorption. It is a complex reaction in combination of physical and chemical process during CO<sub>2</sub> uptake [19, 32]. Avrami kinetic model is logical to attribute the fitting of CO<sub>2</sub> uptake process in our experiment.

The pseudo-first order model and Avrami model kinetic parameters  $k_f$  and  $k_A$  are the time scales for measuring the process to reach equilibrium. The higher  $k_f$  and  $k_A$ , the quicker speed for the process to reach equilibrium. It can be observed from **Table 3** that  $k_f$  and  $k_A$  of CC-LDHs and TUC-LDHs increase with temperature overall. When the temperature increases, the molecule's speed (kinetic energy) also increases. So, the CO<sub>2</sub> molecules will migrate faster inside the pores, which in turn will result in an increase in the rate of diffusion. Hence, it is reflected in the form of CO<sub>2</sub> uptake curves with much steeper ones (shown in **Figure 7**). For TU-LDHs,  $k_f$  and  $k_A$  do not change much as the temperature increases. This might be caused by the fact that the pores of TU-LDHs are easy to saturate or block during the CO<sub>2</sub> adsorption even at high temperature due to its small pore size and volume. This phenomenon usually occurs in the microporous material such as porous MgO [33], zeolites [34] and active carbons [35]. The order of CO<sub>2</sub> adsorption capacity to reach equilibrium ( $k_A$ ) at 80°C seen in Avrami model is: TU-LDHs > TUC-LDHs > CC-LDHs. The order of CO<sub>2</sub> adsorption capacity to reach equilibrium at 150°C seen in Avrami model is: CC-LDHs > TU-LDHs = TUC-LDHs. When the CO<sub>2</sub> adsorption temperature is 200°C, the time of reaching equilibrium by three materials is almost the same. This indicates that TU-LDHs and TUC-LDHs show the potential application of reaching equilibrium to absorb the CO<sub>2</sub> gas at low temperature (<100°C). The Avrami exponent  $n_A$  reflects the extent of driving force on adsorption apparatus. The data of  $n_A$  in the range of 1–4 suggest that CO<sub>2</sub> adsorption occurs more than one-reaction pathway from adsorption sites [36].

Here, the schematic CO<sub>2</sub> adsorption mechanism on LDHs is shown in **Figure 8**. During the CO<sub>2</sub> adsorption process in MgAl porous material, it is known that CO<sub>2</sub> molecule diffuses through the gas film to pore structure among the agglomerate particles and the crystalline grains; or the CO<sub>2</sub> molecule interacts with the adsorbent (surface reaction). Generally, the surface reaction process is quite rapid, and the resistance associated with the surface adsorption can be assumed to be negligible [33]. The whole process of CO<sub>2</sub> adsorption can be simplified that CO<sub>2</sub> permeates in a tube with tubular structure. As mentioned above, TUC-LDHs has the largest BET surface area as well as pore size and volume. The effective absorbed area is larger and it is easy to absorb the CO<sub>2</sub> in the tubular tube with less resistance. This trend is obvious when the adsorption is operated at a high temperature. For the TU-LDHs, although it shows a second largest surface area, its pore size and volume are limited. The pores of LDHs are easy to block when the CO<sub>2</sub> concentration in the tubular tube

Material	Temperature (°C)	Parameters for Simulation										
		Pseudo-first order model					Avrami model					
		$K_f$ (s <sup>-1</sup> )	$q_e$ (mmol g <sup>-1</sup> )	$X^2$	$\Delta q$ (%)	$R^2$	$K_f$ (s <sup>-1</sup> )	$q_e$ (mmol g <sup>-1</sup> )	$n_a$	$X^2$	$\Delta q$ (%)	$R^2$
TU-LDHs	80	0.20	0.29	0.021	7.05	0.9131	0.22	0.28	1.82	0.019	5.78	0.9544
	150	0.24	0.22	0.015	5.74	0.9149	0.27	0.21	2.64	0.019	6.68	0.9463
	200	0.20	0.26	0.024	6.93	0.9420	0.21	0.26	1.22	0.042	11.06	0.9434
CC-LDHs	80	0.10	0.23	0.017	11.18	0.9717	0.11	0.23	1.06	0.017	10.33	0.9708
	150	0.33	0.22	0.034	8.02	0.7791	0.32	0.21	3.9	0.013	5.14	0.9640
	200	0.21	0.23	0.16	21.42	0.9337	0.22	0.22	1.28	0.023	8.32	0.9399
TUC-LDHs	80	0.11	0.33	0.015	8.37	0.9774	0.12	0.32	1.1	0.016	7.35	0.9775
	150	0.25	0.25	0.013	5.04	0.9222	0.27	0.25	2.41	0.015	5.63	0.9727
	200	0.20	0.33	0.024	6.93	0.9447	0.20	0.33	1.09	0.043	11.06	0.9430

**Table 3.**  
Values of the kinetic model parameters for CO<sub>2</sub> adsorption on LDHs.



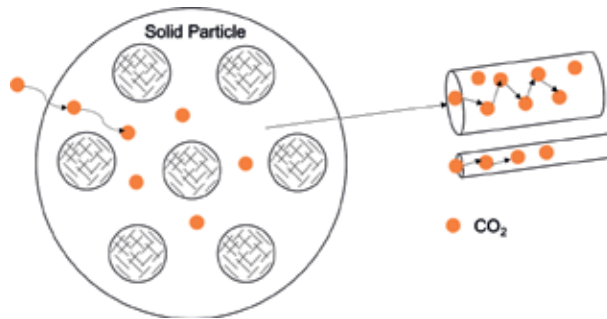


**Figure 8.**  
Schematic CO<sub>2</sub> adsorption mechanism on LDHs.

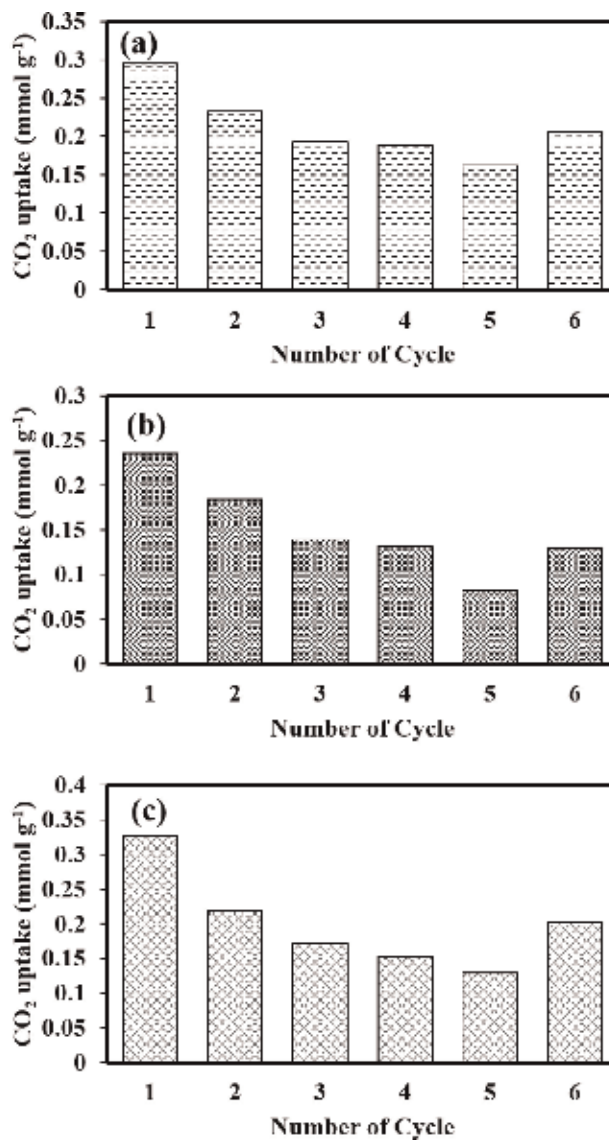


**Figure 9.**  
CO<sub>2</sub> uptake using temperature during six cycles at 80°C (a) TU-LDHs, (b) CC-LDHs and (c) TUC-LDHs.

increases; finally, the CO<sub>2</sub> diffusion rate will slow down. As for CC-LDHs, it has the lowest effective surface area, which finally influences its CO<sub>2</sub> adsorption ability.

### 3.5 CO<sub>2</sub> adsorption/desorption cycling test

For practical applications, the stability of adsorbents during the adsorption-desorption process should be considered. Hence, it is badly needed to test its cycle operation. **Figure 9** shows six successive runs of adsorption-desorption isotherms of LDHs at 80°C. TUC-LDHs shows an initial cyclic adsorption capacity (0.33 mmol g<sup>-1</sup>). However, it decreased to CO<sub>2</sub> adsorption capacity of 0.21 mmol g<sup>-1</sup> at second cycle, which is 67% of the original capacity. At six cycles of adsorption, the adsorption capacity is still 0.2 mmol g<sup>-1</sup> with 60.6% of the original capacity although CO<sub>2</sub> adsorption is fluctuated during the middle process. The decrease of adsorption capacity over several cycles has also been reported by several research groups. The main reason for the decrease of CO<sub>2</sub> adsorption is possible that some chemical sorption sites are blocked during the subsequent adsorption/desorption cycles. TU-LDHs and CC-LDHs show an initial CO<sub>2</sub> adsorption capacity of 0.30 and 0.24 mmol g<sup>-1</sup>, in which the retentions could achieve as high as 69.8 and 54.7%, respectively. These results indicate that the TU process played a role not only in increasing CO<sub>2</sub> sorption capacity, but also in improving the cyclic performance. The experimental results show that stability of hydrotalcites synthesized by both TUC and TU method are higher than the conventional prepared LDHs, which seems promising adsorbents for CO<sub>2</sub> adsorption.

## 4. Conclusions

The present studies have demonstrated that the MgAl LDHs as a CO<sub>2</sub> adsorbent can be synthesized successfully through an ultrasonic assisted ‘T-mixer’ (TU-LDHs), hybrid two-step preparation method (TUC-LDHs) and conventional co-preparation (CC-LDHs) method. The conclusions reached as the results of the current study are as follows:

1. It was found that the prepared TUC-LDHs had a clear layered structure and the average size was approximately 100 nm with the largest surface area, which makes it a promising adsorbent material for CO<sub>2</sub> capture in practical application.
2. Increasing the adsorption temperature is benefit to improve the CO<sub>2</sub> adsorption capacity of LDHs. The highest capture capacity was got when the CO<sub>2</sub> adsorption took place at 200°C by TUC-LDHs.
3. The CO<sub>2</sub> adsorption stability of TU-LDHs and TUC-LDHs is higher than the CC-LDHs after six adsorption/desorption cycles.

## Acknowledgements

This work was financially supported by National Natural Science Foundation of China (NSFC) (Grant No. 21576141) and Zhejiang Provincial Natural Science Foundation (Grant No. LY15B060001). This work was carried out at the International Doctoral Innovation Centre (IDIC). Xiani Huang would also like to

acknowledge the support through the Ph.D. scholarship of the International Doctoral Innovation Centre (IDIC) of University of Nottingham Ningbo China.

## Abbreviations

TU-LDHs	MgAl LDHs prepared by ultrasonication-intensified in ‘T-mixer’
CC-LDHs	MgAl LDHs prepared by conventional co-precipitation
TUC-LDHs	MgAl LDHs prepared by ultrasonic-intensified in ‘T-mixer’ pretreatment followed by conventional co-precipitation

## Author details


Xiani Huang<sup>1</sup>, Xiaogang Yang<sup>1\*</sup>, Guang Li<sup>1</sup>, Collins I. Ezeh<sup>1</sup>, Chenggong Sun<sup>2</sup> and Collins Snape<sup>2</sup>

<sup>1</sup> Department of Mechanical, Materials and Manufacturing Engineering, University of Nottingham Ningbo China, Ningbo, P.R. China

<sup>2</sup> Department of Chemical and Environmental Engineering, University of Nottingham, University Park, Nottingham, UK

\*Address all correspondence to: [xiaogang.yang@nottingham.edu.cn](mailto:xiaogang.yang@nottingham.edu.cn)

## IntechOpen

© 2019 The Author(s). Licensee IntechOpen. This chapter is distributed under the terms of the Creative Commons Attribution License (<http://creativecommons.org/licenses/by/3.0>), which permits unrestricted use, distribution, and reproduction in any medium, provided the original work is properly cited. 

## References

- [1] Yu C-H, Huang C-H, Tan C-S. Mint: A review of CO<sub>2</sub> capture by absorption and adsorption. *Aerosol and Air Quality Research*. 2012;**12**:745-769. DOI: 10.4209/aaqr.2012.05.0132
- [2] Stevens L, Williams K, Han WY, Drage T, Snape C, Wood J, et al. Mint: Preparation and CO<sub>2</sub> adsorption of diamine modified montmorillonite via exfoliation grafting route. *Chemical Engineering Journal*. 2013;**215–216**: 699-708. DOI: 10.1016/j.cej.2012.11.058
- [3] Manohara GV. Mint: Exfoliation of layered double hydroxides (LDHs): A new route to mineralize atmospheric CO<sub>2</sub>. *RSC Advances*. 2014;**4**: 46126-46132. DOI: 10.1039/C4RA08865D
- [4] Kou X, Guo H, Ayele EG, Li S, Zhao Y, Wang S, et al. Mint: Adsorption of CO<sub>2</sub> on MgAl-CO<sub>3</sub> LDHs-derived sorbents with 3D nanoflower-like structure. *Energy and Fuels*. 2018;**32**: 5313-5320. DOI: 10.1021/acs.energyfuels.8b00024
- [5] Wang J, Stevens LA, Drage TC, Wood J. Mint: Preparation and CO<sub>2</sub> adsorption of amine modified Mg–Al LDH via exfoliation route. *Chemical Engineering Science*. 2012;**68**:424-431. DOI: 10.1016/j.ces.2011.09.052
- [6] Yong Z, Rodrigues AE. Mint: Adsorption of carbon dioxide onto hydrotalcite-like compounds (HTlcs) at high temperatures. *Industrial and Engineering Chemistry Research*. 2001;**40**:204-209. DOI: 10.1021/ie000238w
- [7] Aschenbrenner O, McGuire P, Alsamaq S, Wang J, Supasitmongkol S, Al-Duri B, et al. Mint: Adsorption of carbon dioxide on hydrotalcite-like compounds of different compositions. *Chemical Engineering Research and Design*. 2011;**89**:1711-1721. DOI: 10.1016/j.cherd.2010.09.019
- [8] Wang Q, Tay HH, Ng DJW, Chen L, Liu Y, Chang J, et al. Mint: The effect of trivalent cations on the performance of Mg-M-CO<sub>3</sub> layered double hydroxides for high-temperature CO<sub>2</sub> capture. *ChemSusChem*. 2010;**3**:965-973. DOI: 10.1002/cssc.201000099
- [9] Hutson ND, Attwood BC. Mint: High temperature adsorption of CO<sub>2</sub> on various hydrotalcite-like compounds. *Adsorption*. 2008;**14**:781-789. DOI: 10.1007/s10450-007-9085-6
- [10] Hou XJ, Li H, He P, Sun Z, Li S. Mint: Structural and electronic analysis of Li/Al layered double hydroxides and their adsorption for CO<sub>2</sub>. *Applied Surface Science*. 2017;**416**:411-423. DOI: 10.1016/j.apsusc.2017.04.187
- [11] Kim S, Jeon SG, Lee KB. Mint: High-temperature CO<sub>2</sub> sorption on hydrotalcite having a high Mg/Al molar ratio. *ACS Applied Materials and Interfaces*. 2016;**8**:5763-5767. DOI: 10.1021/acsami.5b12598
- [12] Gao Y, Zhang Z, Wu J, Yi X, Zheng A, Umar A, et al. Mint: Comprehensive investigation of CO<sub>2</sub> adsorption on Mg-Al-CO<sub>3</sub> LDH-derived mixed metal oxides. *Journal of Materials Chemistry A*. 2013;**1**:12782-12790. DOI: 10.1039/c3ta13039h
- [13] Silva JM, Trujillano R, Rives V, Soria MA, Madeira LM. Mint: High temperature CO<sub>2</sub> sorption over modified hydrotalcites. *Chemical Engineering Journal*. 2017;**325**:25-34. DOI: 10.1016/j.cej.2017.05.032
- [14] Oliveira ELG, Grande CA, Rodrigues AE. Mint: CO<sub>2</sub> sorption on hydrotalcite and alkali-modified (K and Cs) hydrotalcites at high temperatures. *Separation and Purification Technology*. 2008;**62**:137-147. DOI: 10.1016/j.seppur.2008.01.011

- [15] Zhu X, Chen C, Wang Q, Shi Y, O'Hare D, Cai N. Mint: Roles for K<sub>2</sub>CO<sub>3</sub> doping on elevated temperature CO<sub>2</sub> adsorption of potassium promoted layered double oxides. *Chemical Engineering Journal*. 2019;**366**:181-191. DOI: 10.1016/j.cej.2019.01.192
- [16] Kim S, Lee KB. Mint: Impregnation of hydrotalcite with NaNO<sub>3</sub> for enhanced high-temperature CO<sub>2</sub> sorption uptake. *Chemical Engineering Journal*. 2019;**356**:964-972. DOI: 10.1016/j.cej.2018.08.207
- [17] Hanif A, Dasgupta S, Divekar S, Arya A, Garg MO, Nanoti A. Mint: A study on high temperature CO<sub>2</sub> capture by improved hydrotalcite sorbents. *Chemical Engineering Journal*. 2014;**236**:91-99. DOI: 10.1016/j.cej.2013.09.076
- [18] Ram Reddy MK, Xu ZP, Lu GQM, Diniz da Costa JC. Mint: Influence of water on high-temperature CO<sub>2</sub> capture using layered double hydroxide derivatives. *Industrial and Engineering Chemistry Research*. 2008;**47**: 2630-2635. DOI: 10.1021/ie0716060
- [19] Ram Reddy MK, Xu ZP, (Max) Lu GQ, Diniz da Costa JC. Mint: Layered double hydroxides for CO<sub>2</sub> capture: Structure evolution and regeneration. *Industrial & Engineering Chemistry Research*. 2006;**45**:7504-7509. DOI: 10.1021/ie060757k
- [20] Wang Q, Gao Y, Luo J, Zhong Z, Borgna A, Guo Z, et al. Mint: Synthesis of nano-sized spherical Mg<sub>3</sub>Al-CO<sub>3</sub> layered double hydroxide as a high-temperature CO<sub>2</sub> adsorbent. *RSC Advances*. 2013;**3**:3414-3420. DOI: 10.1039/c2ra22607c
- [21] Ramírez-Moreno MJ, Romero-Ibarra IC, Hernández-Pérez MA, Pfeiffer H. Mint: CO<sub>2</sub> adsorption at elevated pressure and temperature on Mg-Al layered double hydroxide. *Industrial and Engineering Chemistry Research*. 2014;**53**:8087-8094. DOI: 10.1021/ie5010515
- [22] Martunus OMR, Fernando WJN. Mint: Elevated temperature carbon dioxide capture via reinforced metal hydrotalcite. *Microporous and Mesoporous Materials*. 2011;**138**: 110-117. DOI: 10.1016/j.micromeso.2010.09.023
- [23] Dong B, Huang X, Yang X, Li G, Xia L, Chen G. Mint: Rapid preparation of high electrochemical performance LiFePO<sub>4</sub>/C composite cathode material with an ultrasonic-intensified micro-impinging jetting reactor. *Ultrasonics Sonochemistry*. 2017;**39**:816-826. DOI: 10.1016/j.ultsonch.2017.06.010
- [24] Dong B, Li G, Yang X, Chen L, Chen GZ. Mint: Controllable synthesis of (NH<sub>4</sub>)Fe<sub>2</sub>(PO<sub>4</sub>)<sub>2</sub>(OH)<sub>2</sub>H<sub>2</sub>O using two-step route: Ultrasonic-intensified impinging stream pre-treatment followed by hydrothermal treatment. *Ultrasonics Sonochemistry*. 2018;**42**: 452-463. DOI: 10.1016/j.ultsonch.2017.12.008
- [25] Mallakpour S, Dinari M, Behranvand V. Mint: Ultrasonic-assisted synthesis and characterization of layered double hydroxides intercalated with bioactive N,N'-(pyromellitoyl)-bis- $\alpha$ -amino acids. *RSC Advances*. 2013;**3**:23303-23308. DOI: 10.1039/c3ra43645d
- [26] Sing KSW, Everett DH, Haul RAW, Moscou L, Pierotti RA, Rouquerol J, et al. Mint: Reporting physisorption data for gas solid systems with special reference to the determination of surface area and porosity. *Pure and Applied Chemistry*. 1985;**57**:603-619. DOI: 10.1351/pac198557040603
- [27] Carrado KA, Csencsits R, Thiyagarajan P, Seifert S, Macha SM, Harwood J. Mint: Crystallization and textural porosity of synthetic clay minerals. *Journal of Materials*

- Chemistry. 2002;**12**:3228-3237. DOI: 10.1039/b204180b
- [28] Gunjakar JL, Kim IY, Lee JM, Lee N-S, Hwang S-J. Mint: Self-assembly of layered double hydroxide 2D nanoplates with graphene nanosheets: An effective way to improve the photocatalytic activity of 2D nanostructured materials for visible light-induced O<sub>2</sub> generation. *Energy and Environmental Science*. 2013;**6**:1008-1017. DOI: 10.1039/C3EE23989F
- [29] Wang J, Huang L, Zheng Q, Qiao Y, Wang Q. Mint: Layered double hydroxides/oxidized carbon nanotube nanocomposites for CO<sub>2</sub> capture. *Journal of Industrial and Engineering Chemistry*. 2016;**36**:255-262. DOI: 10.1016/j.jiec.2016.02.010
- [30] Serna-Guerrero R, Sayari A. Mint: Modeling adsorption of CO<sub>2</sub> on amine-functionalized mesoporous silica. 2: kinetics and breakthrough curves. *Chemical Engineering Journal*. 2010; **161**:182-190. DOI: 10.1016/j.cej.2010.04.042
- [31] Loganathan S, Tikmani M, Edubilli S, Mishra A, Ghoshal AK. Mint: CO<sub>2</sub> adsorption kinetics on mesoporous silica under wide range of pressure and temperature. *Chemical Engineering Journal*. 2014;**256**:1-8. DOI: 10.1016/j.cej.2014.06.091
- [32] Wang J, Mei X, Huang L, Zheng Q, Qiao Y, Zang K, et al. Mint: Synthesis of layered double hydroxides/graphene oxide nanocomposite as a novel high-temperature CO<sub>2</sub> adsorbent. *Journal of Energy Chemistry*. 2015;**24**:127-137. DOI: 10.1016/s2095-4956(15)60293-5
- [33] Song G, Zhu X, Chen R, Liao Q, Ding Y-D, Chen L. Mint: An investigation of CO<sub>2</sub> adsorption kinetics on porous magnesium oxide. *Chemical Engineering Journal*. 2016;**283**:175-183. DOI: 10.1016/j.cej.2015.07.055
- [34] Li P, Tezel H. Mint: Equilibrium and kinetic analysis of CO<sub>2</sub>-N<sub>2</sub> adsorption separation by concentration pulse chromatography. *Journal of Colloid and Interface Science*. 2007;**313**:12-17. DOI: 10.1016/j.jcis.2007.04.015
- [35] Saha D, Deng S. Mint: Adsorption equilibrium and kinetics of CO<sub>2</sub>, CH<sub>4</sub>, N<sub>2</sub>O, and NH<sub>3</sub> on ordered mesoporous carbon. *Journal of Colloid and Interface Science*. 2010;**345**:402-409. DOI: 10.1016/j.jcis.2010.01.076
- [36] Liu Q, Shi J, Zheng S, Tao M, He Y, Shi Y. Mint: Kinetics studies of CO<sub>2</sub> adsorption/desorption on amine-functionalized multiwalled carbon nanotubes. *Industrial and Engineering Chemistry Research*. 2014;**53**: 11677-11683. DOI: 10.1021/ie502009n

# Moisture Sorption Isotherms and Isotherm Model Performance Evaluation for Food and Agricultural Products

*Ndubisi A. Aviara*

## Abstract

Moisture sorption characteristics of agricultural and food products play important roles in such technological processes as drying, handling, packaging, storage, mixing, freeze-drying and other processes that require the prediction of food stability, shelf life, glass transition and estimation of drying time and texture and prevention of deteriorative reactions. They are useful in the computation of thermodynamic energies of moisture in the products. An understanding of moisture sorption phenomena in products, moisture sorption isotherm (MSI) determination techniques and moisture sorption isotherm model evaluation procedures would be useful in the development or selection, modeling and controlling as well as optimization of appropriate processes to make for enhanced efficiency. The phenomena addressed in this chapter are equilibrium moisture content (EMC)-water activity ( $a_w$ ) relationships and MSI types, temperature influence on isotherms and occurrence of moisture sorption hysteresis. MSI measurement techniques highlighted are the gravimetric, vapor pressure manometric (VPM), hygrometric and inverse gas chromatographic and the use of AquaLab equipment. Commonly used moisture sorption isotherm models (BET, GAB, modified GAB, Hailwood-Horrobin, modified Hailwood-Horrobin, modified Halsey, modified Henderson, modified Chung-Pfost and modified Oswin) were selected, and their evaluation procedures using moisture sorption data were outlined. Static gravimetric technique involving the use of saturated salt solution appears to be the most widely used and recommended method of determining the EMC of agricultural and food products. Most of the MSI models can be fitted to moisture sorption data thorough linearization by logarithmic transformation, while others can be solved using such expression as second-order polynomial. Model goodness of fit can be determined using standard (SE) error of estimate, coefficient of determination ( $R^2$ ), mean relative percentage deviation (P) and fraction explained variation (FEV). The acceptance of a model depends on the nature of its residual plots. A model is considered acceptable if the residual plots show uniform scatter around the horizontal value of zero showing no systemic tendency towards a clear pattern. A model is better than another model if it has lower SE, lower P, higher  $R^2$  and higher FEV. Although it appears as if a generalized MSI model is yet to exist, it is recommended that the Ngoddy-Bakker-Arkema (NBA) model should be given thorough going and extensive testing on the MSI of different categories of food as it could prove true to its generalized model posture due to the fundamental nature of its derivation.

**Keywords:** adsorption, desorption, equilibrium moisture isotherm, moisture sorption isotherm models, moisture sorption isotherm hysteresis

## 1. Introduction

A fundamental characteristic of biological materials, which influence virtually every aspect of handling, storage, manufacturing and consumption of food products [1], including every aspect of the dehydration process and storage stability of the dried products [2], is their basic hygroscopicity. By this, it is meant that when biological materials are exposed to water vapor of a definite pressure, sorption of the water vapor by the product will occur. This chapter discusses the phenomena at play, their technological applications, factors that influence the characteristics, measurement techniques, models that are commonly used to predict them and models' predictive performance evaluation procedures.

## 2. Sorption phenomena in biological materials

Biological materials at constant moisture content and temperature display characteristic vapor pressure and would tend to approach equilibrium with the temperature and vapor pressure of the surrounding gaseous atmosphere. To attain this equilibrium, the material either gains moisture from the environment or loses moisture to the environment depending on whether the vapor pressure of the surrounding is higher or lower than its vapor pressure [3]. The former process is called adsorption and the latter desorption. If the conditions of the surrounding are not changed for a sufficiently long period of time (theoretically for infinitely long time), the temperature at which the vapor pressure of the material and its surrounding is the same is established. At equilibrium, no further change in moisture content of the product occurs, and the moisture content of the material at that point is called equilibrium moisture content (EMC), while the relative humidity is known as equilibrium relative humidity. Water activity ( $a_w$ ) is another term used to denote the ERH in decimal unit. The definition of water activity is based on the concept of thermodynamics and refers to the availability of moisture in biomaterials for physical, chemical and biological changes [4, 5], and it is a property of the material.

### 2.1 Moisture sorption isotherm

When equilibrium is attained, the moisture content is termed adsorption EMC or desorption EMC depending on whether the equilibrium was reached through the adsorption or desorption process. The EMC obtained through the desorption process usually lies above the one obtained through the adsorption process in the isotherm plots and leads to formation of the hysteresis loop (MSI) when graphically expressed [6]. Brunauer et al. [7] classified moisture sorption isotherms into five general types (**Figure 1**). The type I is the Langmuir, while the type II is the sigmoid or S-shaped isotherm. The type III is known as the Flory-Huggins isotherm and is usually influence by the presence of solvent or plasticizer such as glycerol above the glass transition temperature, and type IV is due to the presence of swellable hydrophilic solid that influence the moisture sorption process until a maximum site hydration is reached, while the type V is the BET multilayer adsorption isotherm. Moisture sorption isotherms of most foods are nonlinear, generally sigmoidal in shape, and of the type II classification [1, 6].



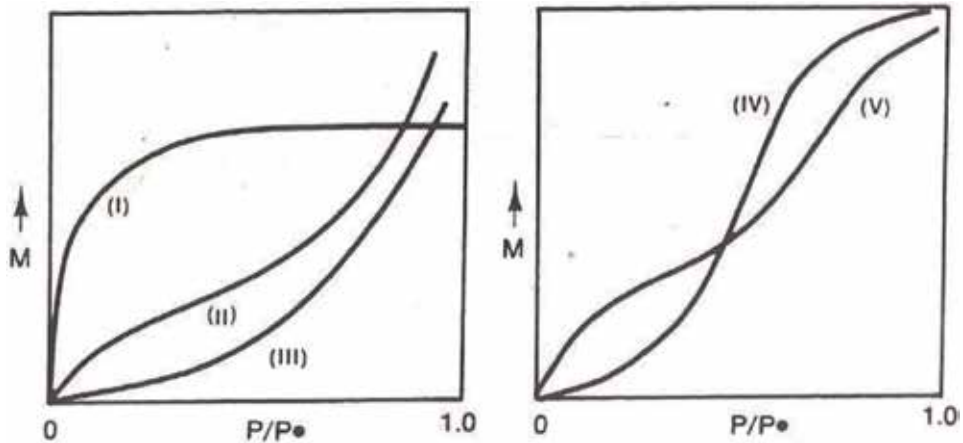


**Figure 1.**  
*Types of moisture sorption isotherm for food. Source: Rizvi [6].*

## 2.2 Applications of moisture sorption isotherm

In drying operation, it is the removal of water which is important, and hence the desorption equilibrium moisture relationship is required to determine the lowest attainable moisture content at the process temperature and relative humidity [8]. Labuza and Hyman [9] applied the changing of water activity of food ingredients and effective diffusivity to control moisture migration in multidomain foods, when temperature changes occur. The moisture sorption isotherms of food and agricultural products are therefore of special interest in the design of storage and preservation processes such as packaging, drying, mixing, freeze-drying and other processes that require the prediction of food stability, shelf life and glass transition and estimation of drying time [10], texture and deteriorative reactions in agricultural and food products. The precise determination of equilibrium moisture contents of dehydrated foods provides valuable information for the accurate computation of thermodynamic energies from existing theories [1].

## 2.3 Factors influencing moisture sorption characteristics

The adsorption and desorption characteristics of agricultural and food products are affected by numerous factors [11], and these include composition, origin, postharvest history and methodology of measurement. In general, polymers sorb more water than sugars and other soluble components at lower water activities [12]. However, the soluble components sorb more water above certain water activity. The MSIs for the same material from different sources usually differ and are comparable only with qualification. The type of treatments given to the product may change the polar and other groups that bind water, along with changes in the capillary and other configurations of the food structure [13]. Greig [14] showed that the denaturation of native cottage cheese whey had no effect on the sorption isotherm at low water activities but significantly increased sorption at high water activities. Yu et al. [15] studied the moisture sorption characteristics of freeze-dried, osmo-dried, osmo-freeze-dried and osmo-air-dried cherries and blue berries and found that the EMC of osmo-air-dried cherries was generally higher than that of the osmo-freeze-dried and freeze-dried cherries at the lower temperature of 10°C, but at higher temperatures of 25 and 40°C, the difference was not significant. Similar result was reported for blue berries. San Jose et al. [16] showed that the drying

method (freeze- and spray-drying) of lactose-hydrolyzed milk did not affect the adsorption isotherms but had profound effect on the desorption isotherms. Tsami et al. [17] investigated the effect of drying method on the sorption characteristics of model fruit powder and reported that freeze-dried gel adsorbed more vapor at 25°C than microwave-dried gel, which had a higher sorption capacity than vacuum- and conventionally dried product. Mittal and Osborne [18] determined the moisture sorption isotherms of meat emulsions and showed that their EMC was affected by the fat-protein ratio. Mazza [19] reported that at 40°C and in the monolayer region of the isotherm, the EMC of precooked dehydrated pea was higher than that of raw pea but that at water activities above 0.5, the sorption capacity of precooked pea was lower than that of raw pea. Avicara [20] noted that chemical modification (cross-linking and hydroxypropylation) of cassava, maize and sorghum starches had profound influence on their moisture adsorption and desorption characteristics. While cross-linking lowered the sorptive capacity of the starches, hydroxypropylation enhanced the ability of the starches to sorb or desorb moisture. Palou et al. [21] studied the moisture sorption characteristics of three cookies and two corn snacks whose main composition difference was in fat and total carbohydrate and found the EMC difference at 5% level of significance. Igbeka et al. [22], Ajibola and Adams [23] and Gevaudan et al. [24] studied the moisture sorption characteristics of cassava and presented data that were fitted by different moisture sorption isotherm models. The variance in EMC may be due to the source of the material, product's postharvest and sorption history and varietal differences, methodology of measurement, temperature range and limitations imposed by model selection.

### **3. Moisture sorption isotherm measurement techniques**

Several methods of determining the moisture sorption isotherm of agricultural and food products have been employed by investigators [25]. Gal [26–28] carried out a thorough review of the methods and pointed out that the basic techniques include the gravimetric, hygrometric, vapor pressure manometric and inverse gas chromatography and special method involving the use of AquaLab.

#### **3.1 Gravimetric method**

There are two common gravimetric methods of determining the EMC of agricultural and food products at different temperatures and water activities. One of these methods is the static gravimetric method which involves the placement of the product in an atmosphere with which it then comes into equilibrium (weight loss or gain stops) without mechanical agitation of the air or product. For this method, several weeks may be required for the product to come into equilibrium, and because of the long period of time, mold usually develops on high and intermediate moisture foods at water activities above 0.8. For data obtained at water activities above 0.8 to be reliable, mold growth must be prevented during equilibration. At the point of equilibration, the moisture content is then determined as the EMC. The second one is the dynamic method in which the atmosphere surrounding the product or the product itself is mechanically moved. The dynamic method is quicker but presents the problem of design and instrumentation. The static method has been used extensively and reported to be preferable for obtaining complete sorption isotherms [27]. It has also been recommended as the standard method of determining the moisture sorption isotherms of agricultural and food products [29]. It involves the placement of small sample (10–25 g) of agricultural and food material in vacuum desiccators containing different concentrations of sulfuric acid

(**Figure 2a**) to maintain the relative humidity (water activity) of the surrounding air at different values from 0 to 100% (0.00–1.00) or saturated solution (**Figure 2b**) of different salts to achieve different values of relative humidity at a specified temperature. Usually a thermostatically controlled water bath or oven

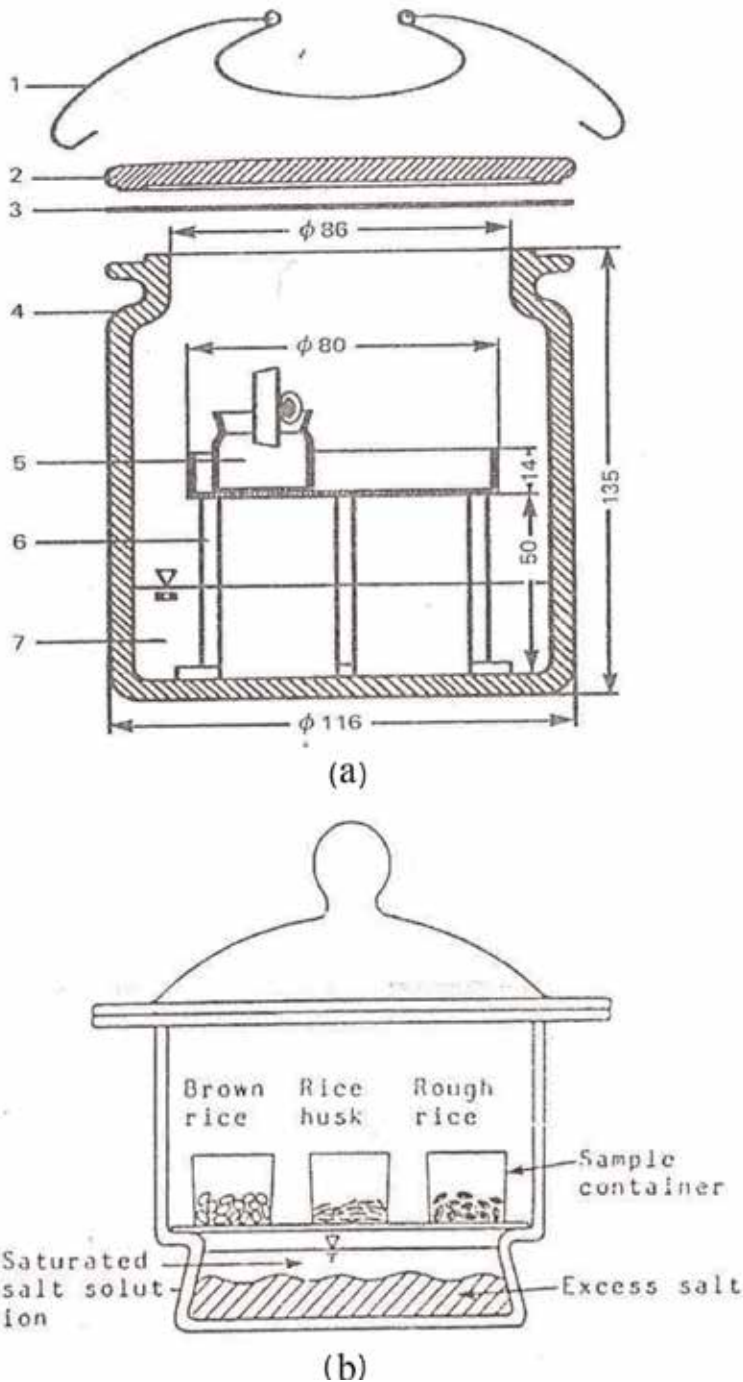


**Figure 2.**  
 (a) Desiccator containing concentrated sulfuric acid: (1) locking clamp, (2) lid, (3) rubber seal ring, (4) desiccator barrel, (5) sample basket or can, (6) sample basket mounting stand and (7) concentrated sulfuric acid. Source: Spiess and Wolf [29]. (b) Desiccator containing saturated salt solution employed by Kameoka et al. [32] in determining the EMC of brown and rough rice and hull.

(Figure 3) is used to obtain the desired temperature. The water activity of sulfuric acid at different concentrations and temperatures is presented in Table 1, and that of saturated solutions of different salts at various temperatures are presented in Table 2.

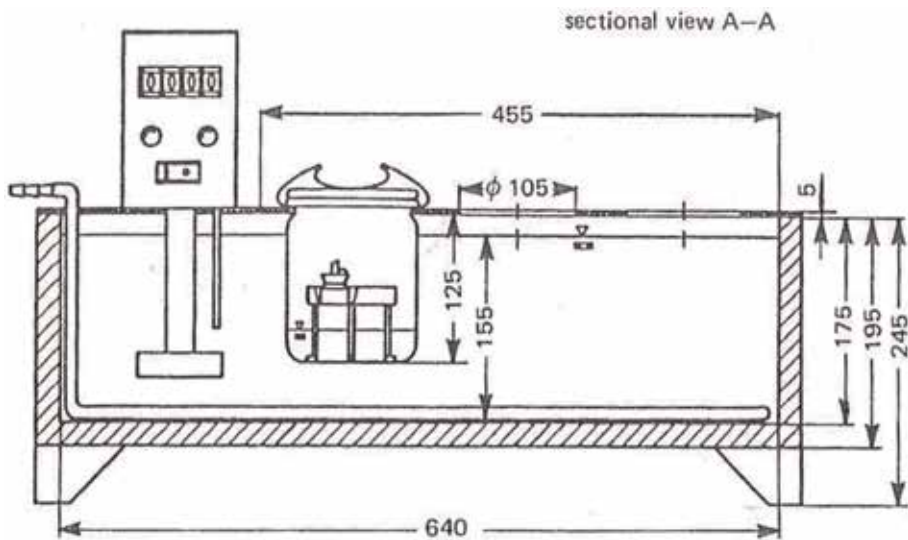


**Figure 3.** Thermostatically controlled water bath or oven for moisture sorption isotherm determination. Source: Spiess and Wolf [29].

Percent H <sub>2</sub> SO <sub>4</sub>	Density at 25°C (g/cm <sup>3</sup> )	Temperature (°C)						
		5	10	20	25	30	40	50
5.00	1.0300	0.9803	0.9804	0.9806	0.9807	0.9808	0.9811	0.9814
10.00	1.0640	0.9554	0.9554	0.9558	0.9562	0.9562	0.9565	0.9570
15.00	1.0994	0.9227	0.9230	0.9237	0.9241	0.9245	0.9253	0.9261
20.00	1.1365	0.8771	0.8779	0.8796	0.8802	0.8814	0.8831	0.8848
25.00	1.1750	0.8165	0.8183	0.8218	0.8218	0.8252	0.8285	0.8317
30.00	1.2150	0.7396	0.7429	0.7491	0.7509	0.7549	0.7604	0.7655
35.00	1.2563	0.6464	0.6514	0.6607	0.6651	0.6693	0.6773	0.6846
40.00	1.2991	0.5417	0.5480	0.5599	0.5656	0.5711	0.5816	0.5914
45.00	1.3437	0.4319	0.4389	0.4524	0.4589	0.4653	0.4775	0.4891
50.00	1.3911	0.3238	0.3307	0.3442	0.3509	0.3574	0.3702	0.3827
55.00	1.4412	0.2255	0.2317	0.2440	0.2502	0.2563	0.2685	0.2807
60.00	1.4940	0.1420	0.1471	0.1573	0.1625	0.1677	0.1781	0.1887
65.00	1.5490	0.0785	0.0821	0.0895	0.0933	0.0972	0.1052	0.1135
70.00	1.6059	0.0355	0.0377	0.0422	0.0445	0.0470	0.0521	0.0575
75.00	1.6644	0.0131	0.0142	0.0165	0.0177	0.0190	0.0218	0.0249
80.00	1.7221	0.0035	0.0039	0.0048	0.0053	0.0059	0.0071	0.0085

Source: Rizvi [6], Bell and Labuza [56].

**Table 1.** Water activity of sulfuric acid solution at different concentrations and temperatures.

Salt	Temperature (°C)								
	20	25	30	35	40	45	50	60	70
Sodium hydroxide	0.09	0.08	0.07	0.07	0.07	0.07	0.07	0.07	0.07
Lithium chloride	0.11	0.11	0.11	0.11	0.11	0.11	0.11	0.11	0.11
Potassium acetate	0.23	0.22	0.22	—	—	—	—	—	—
Calcium chloride	—	—	—	0.22	0.22	0.22	0.21	0.21	0.20
Magnesium chloride	0.33	0.33	0.32	0.32	0.32	0.32	0.31	0.31	0.30
Potassium carbonate	0.43	0.43	0.43	—	—	—	—	—	—
Magnesium nitrate	0.54	0.53	0.51	0.499	0.48	0.47	0.45	0.45	0.44
Manganese chloride	—	—	—	—	0.51	0.5	0.5	0.5	0.5
Sodium bromide	0.59	0.58	0.56	0.55	—	—	—	—	—
Sodium nitrite	—	—	—	—	0.61	0.61	0.6	0.6	0.6
Sodium chloride	0.75	0.75	0.75	0.75	0.75	0.74	0.74	0.74	0.75
Potassium chloride	0.85	0.84	0.84	0.83	0.82	0.82	0.81	0.8	0.8
Barium chloride	—	—	—	—	—	0.89	0.89	0.88	0.88
Potassium nitrate	0.95	0.93	0.92	0.91	0.89	—	—	—	—
Potassium sulfate	0.97	0.97	0.97	0.97	0.96	0.96	0.96	0.95	0.94

Source: Rizvi [6], Bell and Labuza [56].

**Table 2.**  
 Water activity of saturated salt solutions at different temperatures.

Acids are not used extensively because of the danger involved in its handling and the changes that can occur in its composition—it is susceptible to dilution or increase in concentration with time due to the release or absorption of water by the product—thereby effecting a change in the air-water activity. Acids also easily corrode and release fume that can be toxic in the food material. Saturated salts are safer to use, and constant humidity can be maintained by leaving excess salt in the solution. That way, the solution is made to remain saturated throughout the duration of the experiment in spite of the release or absorption of water by the product. The use of saturated salt solution, however, requires many salts in order to go through the relative humidity (water activity) range of 0–100% (0.00–1.00), whereas only one acid could be used for the same purpose.

The static gravimetric method involving the use of saturated salt solutions was applied successfully to the determination of MSIs of Jerusalem artichoke [30]; uncooked meat emulsions [18]; ground and short-time roasted coffee [31]; rice [32]; pigeon pea type-17 [33]; cassava [23]; plantain, winged bean seed and gari [34–36]; freeze-dried, osmo-freeze-dried and osmo-air-dried cherries and blue berries [15]; vetch seeds [37]; lupine [38]; high oleic sunflower seeds and kernels [39]; quinoa grains [40]; soya bean [41]; red chillies [42]; chickpea flour [43]; black gram nuggets [44]; sorghum malt [45]; IR-8 rice variety [46]; native and chemically modified starches [20]; and castor seeds [47]. Young [48], Oyelade et al. [49, 50], Al-Muhtaseb et al. [51], Bello [52] and Afkawa [53] applied the static gravimetric method involving the use of different concentrations of sulfuric acid in determining the MSIs of Virginia-type peanuts, maize flour, yam flour, potato, high amylopectin and high amylose starch powders, groundnut and neem seeds and shea nut and desert date kernels, respectively. Bosin and Easthouse [54] suggested the dynamic

gravimetric method, and Igbeka et al. [22], Roman et al. [25] and Rahman and Al-Belushi [55] utilized it in establishing the MSIs of cassava and potato, apple and freeze-dried garlic powder, respectively.

### 3.2 Hygrometric method

Electric hygrometers are widely used for obtaining the MSIs of agricultural and food products. There are quite a lot of commercially available and specially designed hygrometers that are in use. The instrument (**Figure 4**) consists basically of a sensor, sample chamber and potentiometer. The sensor could use a hygroscopic chemical such as lithium chloride or an ion-exchange resin such as sulfonated polysterne; the conductivity of which changes according to the water activity above the sample. The sensor could be a humidity sensor which is based on capacitance changes in a thin film capacitor. Electric hygrometers give rapid, relatively precise results and are easy to operate. The main problems involved with the use of hygrometers are:

- i. Evaluation of the equilibration time between the sample and sensor
- ii. Proper temperature control
- iii. Need for recalibration for some instrument

Crapiste and Rostein [57], Fasina and Sokhansanj [58], Tsami et al. [17] and Arslan and Togrul [59] employed the hygrometric method in studying the moisture sorption behavior of potatoes, alfalfa pellets, model fruit powders and crushed chillies, respectively.

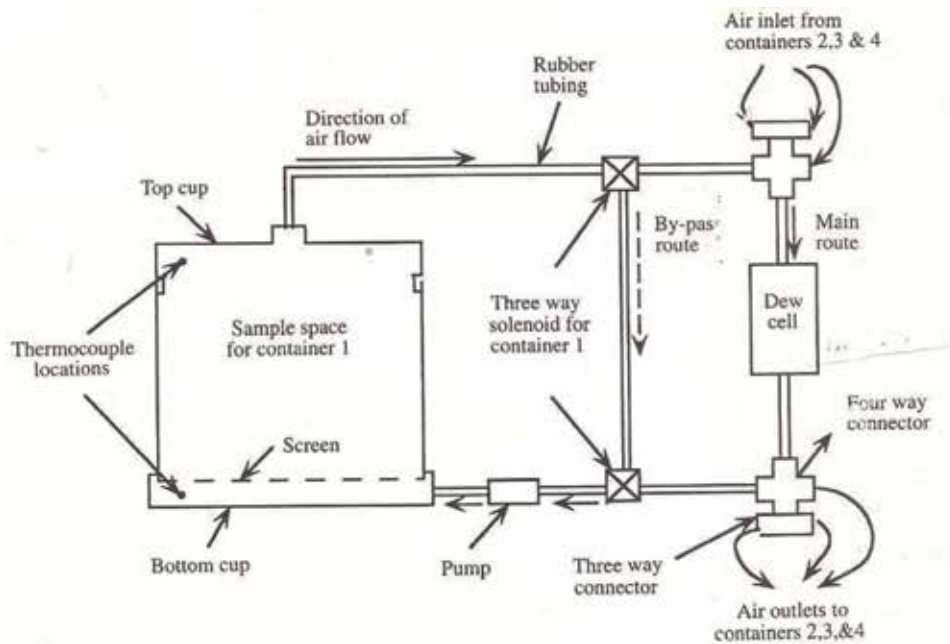


**Figure 4.** Diagram of moisture sorption isotherm apparatus utilizing the hygrometer. Source: Fasina and Sokhansanj [58].

### 3.3 Vapor pressure manometric (VPM) method

The vapor pressure manometric method involves bringing air to equilibrium with the agricultural or food product at a fixed temperature and moisture content and the relative humidity of the air measured as the equilibrium relative humidity (ERH). In this method, the vapor pressure exerted by the moisture in the product is directly measured. As a result, it is taken as one of the best methods of determining the MSI of food [60]. The equilibrium relative humidity is then obtained from the ratio of the vapor pressure in the sample to that of pure water at the same temperature. A schematic diagram of the apparatus and simplified diagram of the system set-up is shown in **Figures 5** and **6**, respectively. The procedure for determining the ERH of agricultural and food products using the method is as follows:

- i. The prepared sample and VPM system are allowed to reach the desired temperature.
- ii. About 10–50 g of sample is put in the sample flask, and an equal amount of desiccant ( $\text{CaSO}_4$ ,  $\text{CaCl}_2$ ) is placed in the desiccant flask and sealed on to the apparatus using high vacuum grease.
- iii. Keeping the sample flask isolated, the system is evacuated to less than 200  $\mu\text{mHg}$  (Rizvi, 1986). The cold strap should be filled with nitrogen prior to evacuation of the system to trap any moisture reaching the vacuum pump.
- iv. The space in the sample flask is then connected to the evacuated air space by opening the stopcock over the sample  $V_4$  (**Figure 6**), and the system is again evacuated for 1 min.

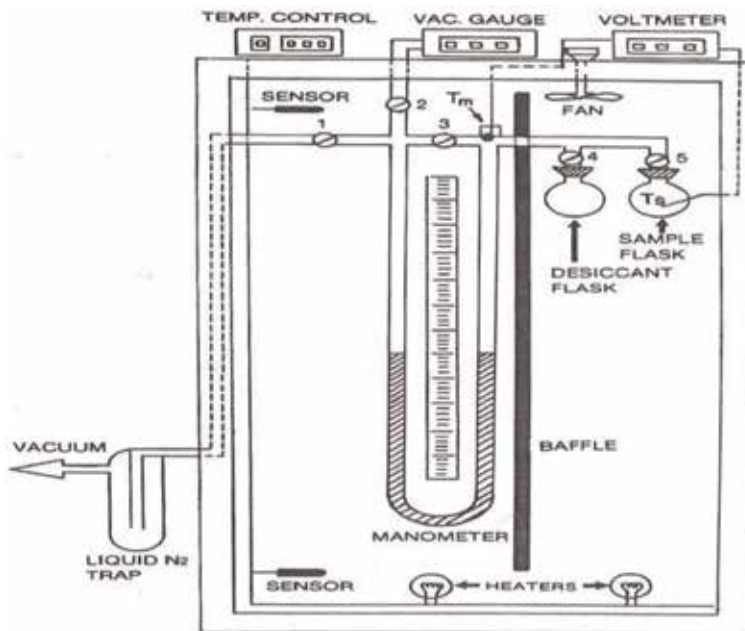


**Figure 5.** Schematic diagram of vapor pressure manometric apparatus. Source: Rizvi [6].

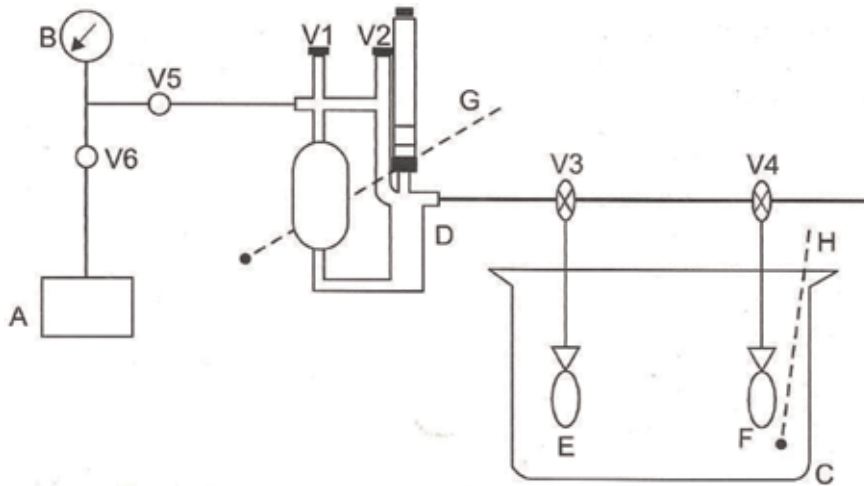


**Figure 6.** Schematic diagram of vapor pressure manometric system set-up. Source: Ajibola et al. [65].

- v. The stopcock across the manometer  $V_5$  is closed causing the oil in the micromanometer to respond to the vapor pressure exerted by the sample. When the oil level reaches a steady value, the difference is recorded as  $H_1$ .
- vi. The stopcock over the sample is then closed, and the desiccant stopcock is opened to connect the system with the desiccant, causing a change in the height of the manometric oil. After the oil reaches a constant height, the micromanometer reading is recorded as  $H_2$ .
- vii. The sample is removed from the system, and the moisture content is determined using a standard method.
- viii. With the data obtained, the equilibrium relative humidity is calculated using Eq. (1):

$$ERH = \frac{(H_1 - H_2) \left( \frac{T_s}{T_o} \right)}{P_s} \quad (1)$$

where ERH is the equilibrium relative humidity (%),  $H_1$  is the micromanometer reading with sample flask connected to the system (mm of manometric oil),  $H_2$  is the micromanometer reading with desiccant flask connected to the system (mm of manometric oil),  $T_s$  is the temperature of the environment surrounding the water bath taken as the temperature of sample (K),  $T_o$  is the temperature of the environment surrounding the micromanometer (K) and  $P_s$  is the saturated vapor pressure at sample temperature (mm of manometric oil).

The VPM method is rapid and precise but requires the use of vacuum pump, an accurate manometer and closed glass tube system. Proper temperature control is critical to this method, and volatile constituents other than water may contribute to the pressure exerted by the food.

The VPM method has been used to obtain the MSI of cereal grains and rape [61], dry milk [62], sesame seed [63], cowpea [64] and palm kernels [65].



### 3.4 Inverse gas chromatography

The inverse gas chromatography (IGC) is a rapid and effective system for studying the thermodynamic properties of a solid taken as the stationary phase in relation to a mobile gas phase containing selected solutes such as water. It is particularly suitable for the study of the lower region of water activity and for products with very low equilibrium moisture contents [66, 67]. With IGC the sorbed solute is injected into the carrier gas stream, and its linear transport is retarded owing to interaction with the product under study, which constitutes the stationary phase. Moisture sorption isotherms are then determined using the chromatographic data obtained and the following equations, which relate chromatograph operating parameters and peak data to the sorption isotherm:

$$a = \frac{m_a I_{ads}}{m I_{pic}} \quad (2)$$

and

$$p = \frac{m_a h R T}{I_{pic} W} \quad (3)$$

where  $a$  is the uptake of sorbed water (g/g stationary phase),  $m_a$  is the mass of water injected (g),  $m$  is the mass of stationary phase (g) and  $I_{ads}/I_{pic}$  is the ratio of the areas  $(A + B)/B$  calculated from the chromatogram (**Figure 7**),  $p$  is the partial pressure (atm),  $h$  is the peak height (detector units),  $R$  is the gas constant ( $82.0567 \text{ cm}^3 \text{ atm mole}^{-1} \text{ K}^{-1}$ ),  $T$  is the absolute temperature (K),  $W$  is the flow rate of carrier gas ( $\text{cm}^3/\text{min}$ ) and  $I_{pic}$  is the area  $B$  in **Figure 7**.

It has been used successfully to determine the MSIs of homogeneous solid food ingredients like sucrose, glucose and starch [68] and complex heterogeneous foods like bakery products [69], wheat flour [66] and wheat and soy flour [70].

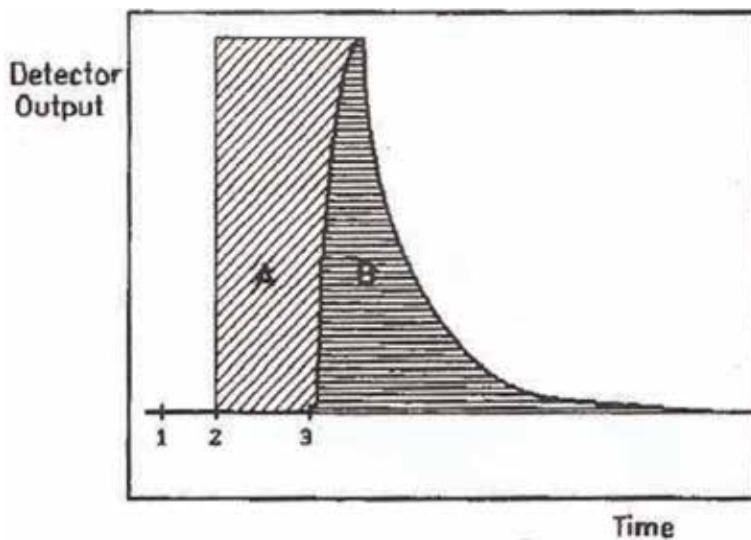


**Figure 7.** Typical gas chromatogram obtained by IGC: 1 = point of injection; 2 = point of emergence of unadsorbed peak (air); 3 = point of emergence of probe peak (water),  $I_{pic}$  = area  $B$ ; and  $I_{ads}$  = area  $A + B$ . Source: Manuel Sa and Sereno [67].



**Figure 8.** 4TE model AquaLab moisture content—water activity measuring instrument. Source: METER Group, Inc. [71].

### 3.5 AquaLab instrument

AquaLab is the fastest, most accurate and most reliable instrument available for measuring water activity, giving readings in 5 min or less [71]. It is easy to use and provides accurate and timely results. Its readings are reliable, providing  $\pm 0.003 a_w$  accuracy. The instrument is easy to clean and checking calibration is simple. The photograph of 4TE model of the equipment is shown in **Figure 8**.

## 4. Influence of temperature on moisture sorption isotherms

Temperature affects the mobility of water molecules and the dynamic equilibrium between the vapor and the adsorbed gases [13]. If water activity is kept constant, an increase in temperature causes a decrease in the amount of sorbed water [20] (**Figure 9**). This indicates that the food becomes less hygroscopic. Iglesias and Chirife [72] pointed out that increase of temperature represents a condition unfavorable to water sorption.

An exception to this rule is shown by certain sugars and other low molecular weight food constituents, which become more hygroscopic at higher temperature because they dissolve in water. Temperature shifts can have an important practical effect on the chemical and microbiological reactivity related to quality deterioration of a food in a closed container [73]. An increase of temperature at constant moisture content causes increase in water activity (**Figure 10**). This increases the rate of reactions and leads to deterioration [74–76]. Weisser [31] studied the effect of temperature on the sorption isotherms of roasted coffee and reported that the product showed consistent separation of the isotherms at different temperatures. However, not all foods exhibit such consistency. In the work reported by Saravacos et al. [12], crossing over occurred at high water activity ( $a_w = 0.78$ ) in the 20 and 30°C adsorption isotherms of sultana raisins and 5, 20 and 45°C adsorption and desorption isotherms of Chilean papaya shown in **Figure 11** [77]. Such crossing over has earlier been observed by Saravacos and Stinchfield [78] on model systems of starch-glucose, Audu et al. [79] on sugars, Weisser et al. [80] on sugar and alcohols

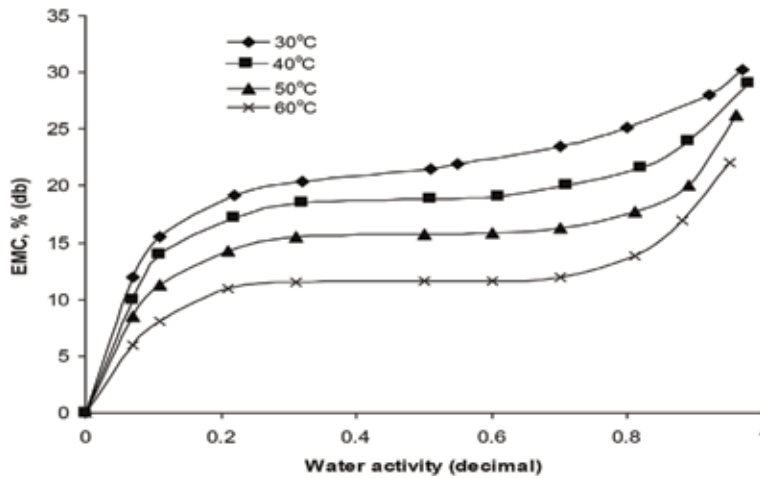


**Figure 9.** Adsorption EMC of hydroxypropylated cassava starch showing variation of MSI with temperature. Source: Aviara [20].

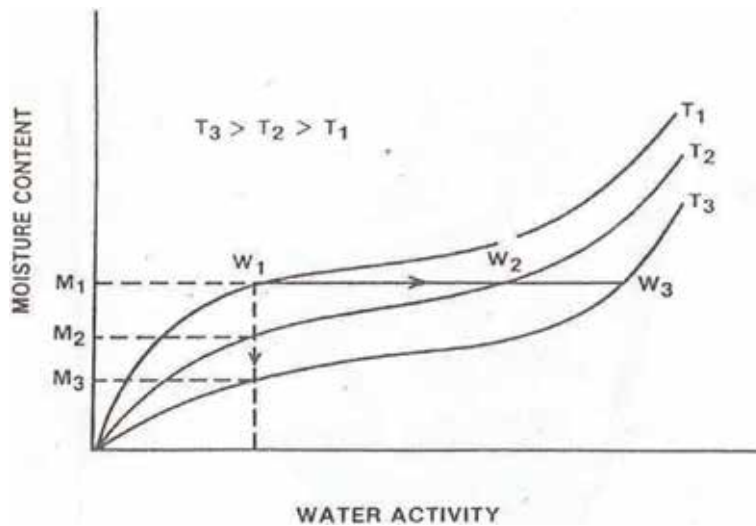


**Figure 10.** Changes in water activity at constant moisture content and in moisture content at constant water activity with changes in temperature. Source: Rizvi [6].

and Silverman et al. [81] on 20 and 37°C isotherms of precooked bacon. These substances contain large amounts of low molecular weight constituents in a mixture of high molecular weight biopolymers. At lower water activity values, the sorption of water is due mainly to the biopolymers, and an increase of temperature has the normal effect of lowering the isotherms [13]. As water activity is raised beyond the intermediate region, moisture begins to be sorbed primarily by the sugars and other low molecular constituents leading to the swinging up of the isotherm. Dissolution, which is favored by higher temperature, offsets the opposite effect of temperature on higher molecular weight constituents. The net result is an increase of moisture content (crossing over) of the isotherms. This has bearing on the sign and magnitude of the binding energy [13]. The binding energy of sultana raisin decreased as the temperature increased from 22 to 32°C in the low moisture region [12], but the effect of temperature showed a crossing over of the lines at higher moisture

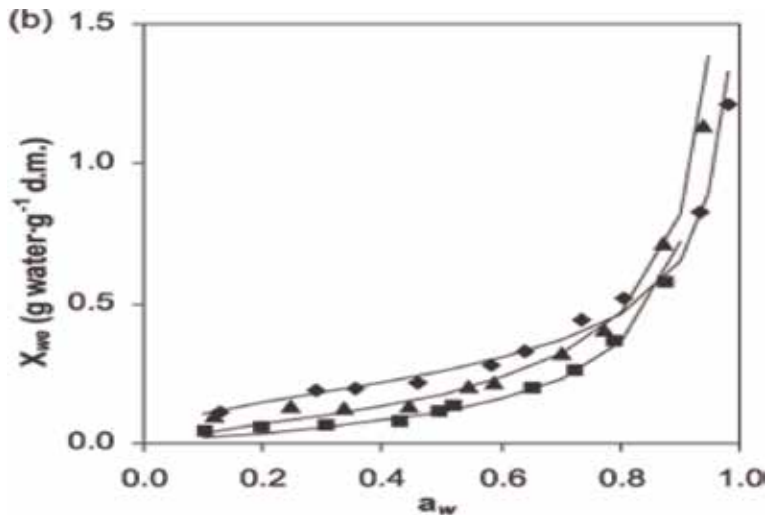


**Figure 11.**

Moisture desorption isotherms of Chilean papaya showing isotherm crossing at higher water activities with increase in temperature. Source: Vega-Gálvez et al. [84].

contents due to the endothermic dissolution of fruit sugars. Iglesias and Chirife [82] studied the equilibrium moisture contents of air-dried beef and found that the higher the drying temperature, the lower the sorption capacity of the dried beef. Similar results were reported for cookies and corn snacks [21] and apples [25]. Temperature changes also have effects on the water activity of saturated salt solutions, which are used in the determination of sorption isotherms. Labuza et al. [83] used experimental data and thermodynamic analysis to demonstrate that water activity of saturated salt solutions should decrease with increase in temperature.

## 5. Moisture sorption hysteresis

A product which attains its moisture equilibrium with the surrounding by losing moisture at a given temperature is said to have reached the desorption EMC. When the relatively dry material absorbs moisture from a high humidity environment at the same temperature, it will eventually reach the adsorption EMC. The isotherm plots may indicate a significant difference at certain water activities and temperatures between desorption and adsorption EMC values, with the desorption values being higher than the adsorption counterpart. This difference is called moisture sorption hysteresis [13, 45]. A typical hysteresis loop presented in **Figure 12** could occur within the region of monolayer moisture but could begin at a higher water activity and extend down to zero water activity, depending on its class according to Kapsalis [13] classification.

Moisture sorption hysteresis has important theoretical and practical implications in foods. These include the general aspects of the irreversibility of moisture sorption process and the question of validity of thermodynamic parameters derived from a particular arm of the isotherm. Moisture sorption hysteresis has effect on chemical and microbiological deterioration of low and intermediate moisture foods.

### 5.1 Hysteresis classification

The hysteresis phenomenon in agricultural and food products varies in magnitude, shape and extent, depending on the type of food and temperature [13]. Hysteresis size or magnitude is depicted by the area enclosed by the loop, while the

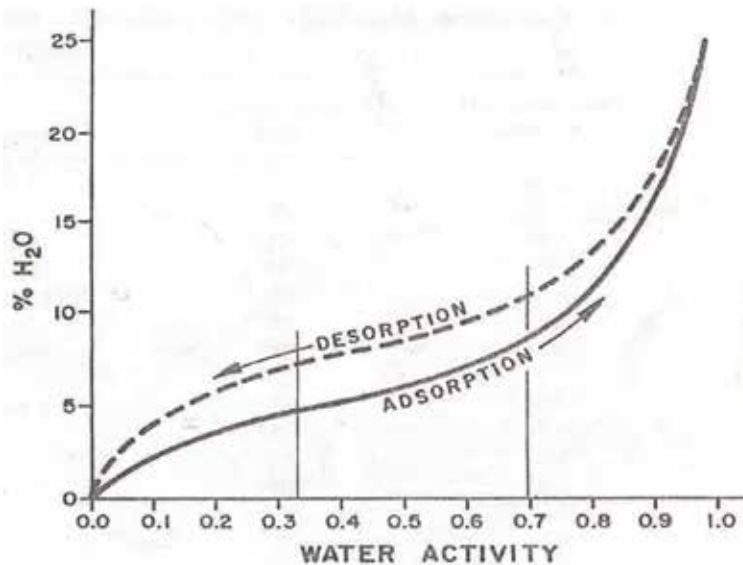


**Figure 12.**  
*Moisture sorption hysteresis loop. Source: Kapsalis [13].*

span or extent is denoted by the water activity range covered. Kapsalis [13] grouped moisture sorption hysteresis into three general types as follows:

*Type I hysteresis:* This type of hysteresis is normally pronounced mainly in the lower moisture content region, below the first inflection point of the isotherm. Although the total hysteresis may be large, no occurrence is normally observed above the 0.65 water activity or in the intermediate moisture range. The type I hysteresis is normally exhibited by high-sugar and high-pectin foods, exemplified by air-dried apple.

*Type II:* In this type, moderate hysteresis begins at high water activity, in the capillary condensation region, and extends over the rest of the isotherm to zero water activity. In both desorption and adsorption arms, the isotherm's sigmoidal shape is retained. This type of hysteresis is normally exhibited by high-protein foods exemplified by freeze-dried pork.

*Type III:* In this type, large hysteresis loop occurs with a maximum at about 0.70 water activity, which is within the capillary condensation region. This type of hysteresis normally occurs in starchy foods such as freeze-dried rice.

## 5.2 Effect of temperature on hysteresis

Increasing temperature decreases the total hysteresis and limits the span of the loop along the isotherm [84]. Iglesias and Chirife [85] studied the effect of temperature on the magnitude of moisture sorption hysteresis of foods and reported that increasing temperature decreased or eliminated hysteresis for some foods, while for others, the total hysteresis size remained constant, or even increased. In the case where the hysteresis loop decreased, it did so more appreciably at high temperatures. The effect of temperature was found to be more pronounced on the desorption isotherms than the adsorption isotherms.

## 5.3 Theories of moisture sorption hysteresis

Several theories have been proposed to explain hysteresis phenomena in agricultural and food products. The most prominent of the theories are the ink bottle

theory, the incomplete wetting theory, the open-pore theory, the shrinkage theory and the capillary condensation-swelling fatigue theory.

*Ink bottle theory:* This theory assumes that an agricultural and food product is a porous body having capillaries consisting of narrow, small-diameter necks with large bodies resembling ink bottles (**Figure 13**). It explains hysteresis on the basis of difference in the radii of the porous sorbent. During desorption, the small radii of necks control the emptying of the capillaries and result in a lowering of the relative humidity above the product; whereas during adsorption, the large area for the bodies needs to be filled, thus requiring higher relative humidity. The explanation can be better understood using the Kelvin equation which states that

$$\ln\left(\frac{P}{P_o}\right) = \frac{-2\sigma V \cos\theta}{RT r_m} \quad (4)$$

where P is the vapor pressure of liquid over the curved meniscus (Pa), P<sub>o</sub> is the saturation vapor pressure (Pa) at temperature T (K), σ is the surface tension (N/m), θ is the angle of contact (in complete wetting, θ is 0 and cosθ = 1), V is the molar volume of liquid (m<sup>3</sup>/mol) and r<sub>m</sub> is the mean radius of curvature of meniscus.

For desorption, by substituting r<sub>1</sub> in **Figure 13** for r<sub>m</sub> in Eq. (4) with cosθ = 1 (complete wetting), Eq. (4) becomes transformed into Eq. (5):

$$P_d = P_o \exp\left(\frac{-2\sigma V}{RT r_1}\right) \quad (5)$$

In adsorption with condensation first taking place in the large diameter cavity, Eq. (4) becomes

$$P_a = P_o \exp\left(\frac{-2\sigma V}{RT r_2}\right) \quad (6)$$

From the above, it follows that for a given amount of water sorbed, the pressure will be higher during adsorption than during desorption.

*Incomplete wetting theory:* This theory is also dependent on capillary condensation based on Eq. (4), but it notes that due to the presence of impurities, the contact

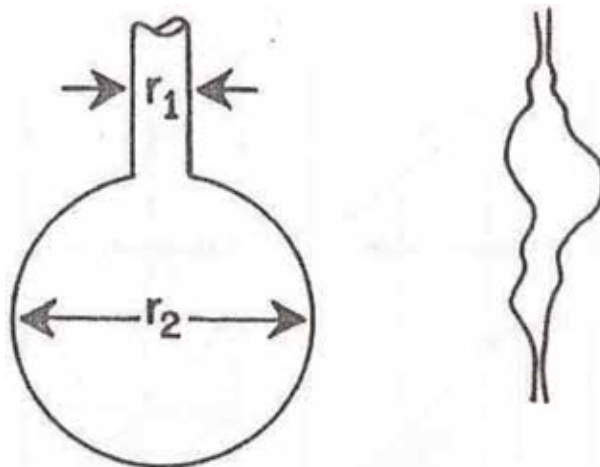


**Figure 13.** Ink bottle neck theory of moisture sorption hysteresis (left, schematic representation and, right, actual pore). Source: Kapsalis [13].

angle of the receding film upon desorption is smaller than that of the advancing film upon adsorption. Therefore, condensation along the adsorption branch of the isotherm will be at a higher vapor pressure resulting in open hysteresis as illustrated in **Figure 14**. However, in foods the most common type of hysteresis is the closed-end, retracable loop showing that this theory is limited in its application to foods.

*Open-pore theory:* this theory extends the ink bottle theory by including considerations of multilayer adsorption. It is based on the difference in vapor pressure between adsorption  $P_a$  and desorption  $P_d$  as affected by the shape of the meniscus. During adsorption, the meniscus is considered cylindrical and the Cohan equation (not presented here) applies, whereas during desorption, the shape is considered to

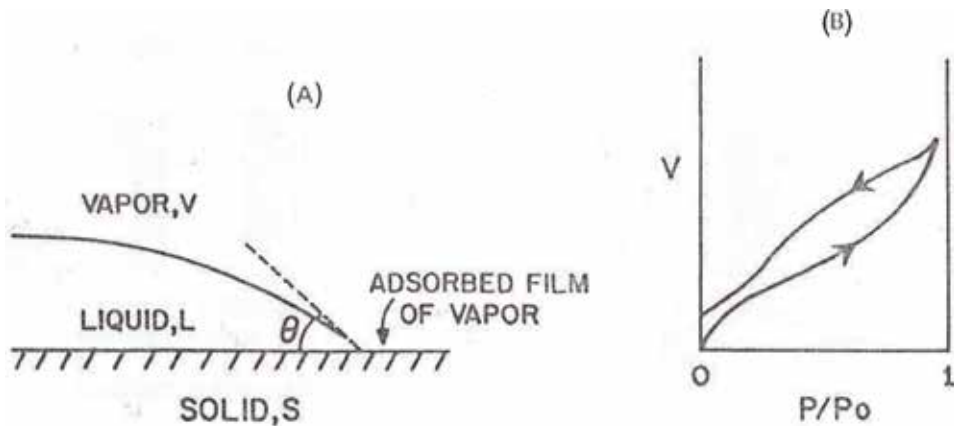


**Figure 14.** Incomplete wetting theory of hysteresis (A) contact angle and (B) open hysteresis. Source: Kapsalis [13].

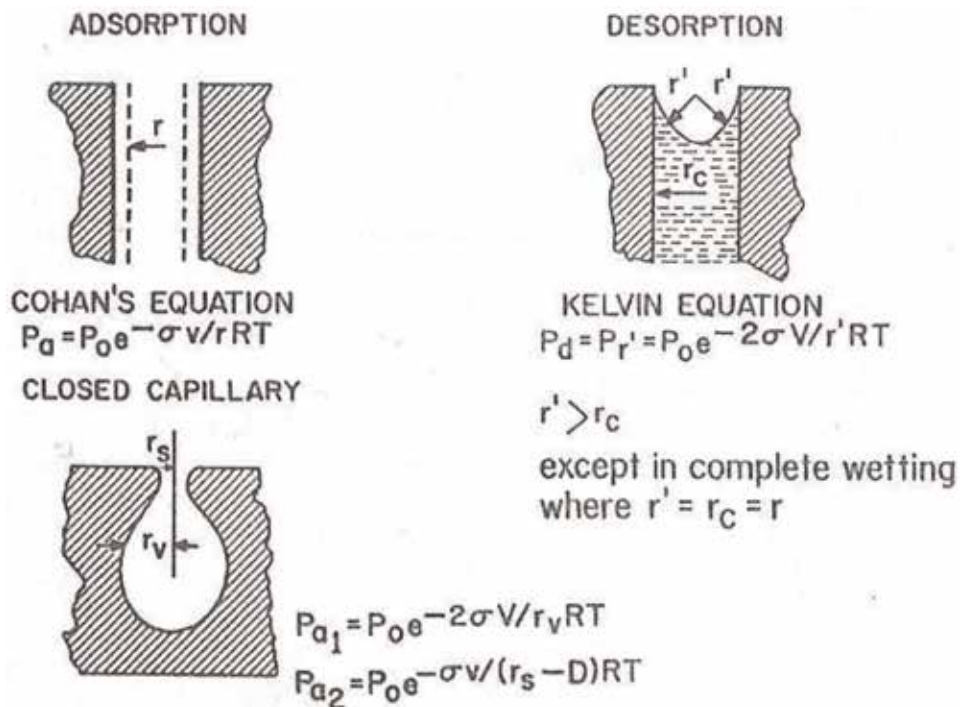


**Figure 15.** Open-pore theory of hysteresis. Source: Kapsalis [13].

be hemispherical in which the Kelvin equation is applied. The open-pore theory is illustrated in **Figure 15**.

*Shrinkage theory:* This states that while agricultural and food product is drying out, the force of attraction causes water-holding spaces to shrink (molecular shrinkage). This permanent shrinkage reduces the water-binding polar sites and water-holding capacity of the material; hence less amount of water is absorbed during the adsorption process.

*Capillary condensation and swelling fatigue theory:* In this theory proposed by Ngoddy-Bakker-Arkema [86], the sorption hysteresis is considered linked with condensation and evaporation in irregular voids (capillary condensation) and influence of adsorbed water molecules on such physical properties of agricultural and food products as strength, elasticity, rigidity, swelling and evolution of heat (swelling fatigue). The above combination was simulated by adopting the Cohan theory of capillary condensation with modifications and combining it with the ink bottle theory in the first approximation. The theory presented expressions for calculating the desorption isotherms of biomaterials from corresponding adsorption isotherm using bulk moduli determined as a function of moisture content.

## 6. Moisture sorption isotherm models

Equations for fitting the moisture sorption isotherms are of special importance in many aspects of crop and food preservation by drying. These include the prediction of the drying times, shelf life of the dried product in a packaging material and the equilibrium conditions after mixing products with varying water activities [87]. Others are the analytical determination of control for undesirable chemical and enzymatic reactions [88] and control of moisture migration in multidomain foods [9]. Moisture sorption isotherm models, therefore, not only constitute an essential part of the overall theory of drying but also provide information directly useful in the accurate and optimum design of drying equipment [1]. They are needed in the evaluation of the thermodynamic functions related to moisture sorption in biological materials [89].

Several theoretical, semi-theoretical and empirical models have been proposed and used by investigators to fit the equilibrium moisture content data of food and agricultural products. Chirife and Iglesias [87] reviewed part of the isotherm equations and presented a discussion of 23 common models, while Van den Berg and Bruin [5] presented a more comprehensive list. Ngoddy-Bakker-Arkema [1] developed a generalized moisture sorption isotherm model for biological materials based primarily on the BET and capillary condensation theories and indirectly on Polanyi's potential theory. This model appears to possess very high versatility but needs to be modified to reduce the number of parameters and incorporate the temperature term. A thorough going and extensive testing of the model on various categories of food is also necessary to confirm its versatility and prove the generalized posture. Ferro Fontan et al. [2] and Chirife et al. [90] presented a new model, which Iglesias and Chirife [91] compared with the GAB model and reported to be an alternative. Chen [92] derived a new moisture sorption isotherm model from a reaction engineering approach. The Brunauer-Emmett-Teller (BET) [87] and Guggenheim-Anderson-de Boer (GAB) [56, 91, 93] models have been used for estimating the monolayer moisture content of agricultural and food products. Boquet et al. [94] noted that the Hailwood and Horrobin model has a remarkably good ability to fit the experimental data for most food types. A test of the model on moisture sorption data of native cassava and sorghum starches [95] showed that it has good predictive



performance with  $R^2$  ranging from 0.92 to 0.99. It, however, lacked the temperature term and was modified to incorporate the term. Other commonly used models include modified Henderson, modified Chung-Pfost, modified Halsey and modified Oswin and the GAB. The modified Henderson [96] and modified Chung-Pfost [97] models have been adopted as the standard equations by the American Society of Agricultural and Biological Engineers (ASABE) for describing the EMC- $a_w$  data for cereals and oil seeds [98]. The modified Halsey [85] has been reported as the best model for predicting the EMC- $a_w$  relationships of several tropical crops [99] and alongside with the modified Oswin [100] has been shown to describe the EMC- $a_w$  data of many seed satisfactorily [101, 102]. The Guggenheim-Anderson-de Boer (GAB) model has been recognized as the most satisfactory theoretical isotherm Equation [103–106] and has been recommended as the standard model for use in food laboratories in Europe [105] (1985) and the USA [107]. The GAB does not incorporate a temperature term; therefore, the determination of the effect of temperature on isotherms using the model usually involves the evaluation of up to six constants. Jayas and Mazza [108], however, developed a modified form of the GAB, which incorporates the temperature term. The MSI models considered in this study were selected from the above list and presented as follows:

1. Brunauer-Emmett-Teller (BET) model

$$M = \frac{M_m C a_w}{(1 - a_w)[1 + (C - 1)a_w]} \quad (7)$$

2. Guggenheim-Anderson-de Boer (GAB) model

$$M = \frac{CKM_m a_w}{(1 - Ka_w)[1 - Ka_w + CKa_w]} \quad (8)$$

3. Modified GAB model

$$M = \frac{AB\left(\frac{C}{T}\right)a_w}{(1 - Ba_w)\left[1 - Ba_w + \frac{C}{T}Ba_w\right]} \quad (9)$$

4. Hailwood-Horrobin model

$$M = \left(\frac{A}{a_w} + B - Ca_w\right)^{-1} \quad (10)$$

5. Modified Hailwood-Horrobin model

$$M = \left(T\left(\frac{A}{a_w} + B\right) - \frac{C}{T^n}a_w\right)^{-1} \quad (11)$$

6. Modified Chung-Pfost model

$$M = \frac{-1}{C} \text{Ln} \left[ -\frac{(T + B)}{A} \text{Ln} a_w \right] \quad (12)$$

7. Modified Halsey model

$$M = \left[ \frac{-\text{Ln} a_w}{\exp(A + BT)} \right]^{-1/c} \quad (13)$$

### 8. Modified Henderson model

$$M = \left[ \frac{-Ln(1 - a_w)}{A(T + B)} \right]^{1/c} \quad (14)$$

### 9. Modified Oswin model

$$M = (A + BT) \left[ \frac{a_w}{1 - a_w} \right]^{1/c} \quad (15)$$

### 10. Ngoddy-Bakker-Arkema model

$$M = \frac{\rho\varepsilon}{\eta} \left\{ 3.2^\eta \left[ \left( \left( \frac{1.75}{Ln\left(\frac{P_o + P_m}{P + P_m}\right)} \right)^{\frac{1}{2}} + \frac{\sigma V}{R_g T Ln\left(\frac{P_o + P_m}{P + P_m}\right)} \right)^\eta - \left( \left( \frac{1.75}{Ln\left(\frac{P_o + P_m}{P_m}\right)} \right)^{\frac{1}{2}} + \frac{\sigma V}{R_g T Ln\left(\frac{P_o + P_m}{P_m}\right)} \right)^\eta \right] \right\} \quad (16)$$

where  $M$  is the moisture content, (db);  $M_m$  is monolayer moisture content, (db);  $a_w$  is water activity;  $T$  is absolute temperature, (K);  $A$ ,  $B$ ,  $C$  and  $k$  are constants;  $\eta$  is primary characteristic parameter of pore structure;  $\varepsilon$  is secondary characteristic parameter of pore structure;  $\sigma$  is surface tension of sorbate in bulk liquid form, (N/m);  $R_g$  is universal gas constant;  $V$  is molal volume of sorbate in its bulk liquid condition, (m<sup>3</sup>/mol);  $P_m$  is vapor pressure corresponding to monolayer, (N/m<sup>2</sup>);  $P_o$  is saturated vapor pressure, (N/m<sup>2</sup>); and  $P$  is vapor pressure at the condition under which the study is carried out, (N/m<sup>2</sup>).

## 7. Isotherm model predictive performance evaluation

Sun and Byrne [109], Sun [110] and Sun [111] evaluated the predictive performance of the moisture sorption isotherm models that have been reported for fitting the EMC and ERH data of rapeseed, rice, other grains and oilseeds and selected the models that gave the best fits.

Coefficient of terms in the moisture sorption isotherm equations is usually determined using nonlinear regression procedure, and the predictive performance of an equation on sorption data is evaluated using such goodness of fit parameters as standard error of estimate (estimate of the residual mean square), residual sum of square, coefficient of determination, mean relative percent error, fraction explained variation and residual plots. Several investigators used these parameters to evaluate the fitting ability of EMC- $a_w$  equations. For instance, Ajibola [35–37], Ajibola and Adams [34], Ajibola [112], Gevaudan et al. [24], Talib et al. [8], Pezzutti and Crapiste [113], Tsami et al. [17] and Ajibola et al. [64] used the standard error of estimate, and Young [48] and Jayas et al. [114] used the residual sum of squares to compare the fitting ability of different models. Boquet et al. [94], Chirife et al. [90], Weisser [31], Saravacos et al. [12], Pollio et al. [115], Iglesias and Chirife [91] and Khalloufi et al. [10] used the mean relative percent deviation (MRE), while Shepherd and Bhardwaj [33], Demertzis et al. [116], Diamante and Munro [117] and Sopade et al. [118] employed coefficient of determination in evaluating the fitting ability of several models. Pappas and Rao [119] used the fraction explained

variation, Chen [92] used both coefficient of determination and mean relative percent error and Sun [110] and Sun [111] employed the residual sum of squares, standard error of estimate and mean relative percent error in comparing moisture sorption isotherm models for food. Other combinations of parameters that have been used include standard error of estimate and mean relative percent error [120], coefficient of determination and residual sum of squares [18] and standard error of estimate, mean relative percent deviation and residual plots [15, 41, 65, 101, 102]. A model is considered acceptable for predictive purpose, if the residuals are uniformly scattered around the horizontal value of zero showing no systematic tendency towards a clear pattern [41, 45, 64, 65]. A model is considered better than another if it has lower standard error of estimate and mean relative percent deviation and higher fraction explained variation and coefficient of determination.

Menkov [37] reported that of five moisture sorption isotherm models fitted to the experimental data on the EMC of vetch seeds, the modified Oswin model proved the best for describing the adsorption and desorption branches. Aviara et al. [41] and Oyelade [121] reported that the modified Oswin model gave the best fit to the EMC of soya bean and lafun, respectively. Santalla and Mascheroni [39] in a similar study on the EMC of sunflower seeds and kernels reported that the GAB model gave the best fit to the experimental data. Other crops whose moisture sorption isotherms have recently been studied include quinoa grains [40], crushed chillies [59], amaranth grains [122] and black gram nuggets [44].

### 7.1 Model parameter evaluation procedures

The procedure followed in evaluating a moisture sorption isotherm model depends on the nature of the model. For the selected models (Eqs. (7)–(16)), the procedures are as follows:

- a. BET model: the BET model (Eq. (7)) can be linearized thorough algebraic manipulations to yield Eq. (17):

$$\frac{a_w}{M(1-a_w)} = \frac{1}{M_m C} + \left(\frac{C-1}{M_m C}\right)a_w \quad (17)$$

A plot of  $\frac{a_w}{M(1-a_w)}$  against  $a_w$  within the water activity range of 0.01–0.5 at each temperature yields a straight line with the slope as  $\left(\frac{C-1}{M_m C}\right)$  and intercept on the y-axis as  $\frac{1}{M_m C}$ , and from these, the values of  $M_m$  and  $C$  can be obtained and used as the starting values in nonlinear regression. The nonlinear regression analysis procedure minimizes the sum of deviation in the evaluation of a model using a series of iterative steps. The procedure could require that initial parameter estimates be chosen close to the true values.

- b. GAB model: the GAB model (Eq. (8)) can be transformed to a quadratic form by algebraic manipulation to yield Eq. (18):

$$\frac{a_w}{M} = Aa_w^2 + Ba_w + C \quad (18)$$

Eq. (18) can be solved by plotting  $\frac{a_w}{M}$  against  $a_w$  at each temperature and fitting a polynomial of the second order to the plots. This will yield the following functions from Eq. (8):

$$A = \frac{k}{M_m} \left( \frac{1}{C} - 1 \right), B = \frac{1}{M_m} \left( 1 - \frac{2}{C} \right), C = \frac{1}{M_m C k} \quad (19)$$

The values of  $M_m$ ,  $C$  and  $k$  obtained at each temperature are then used as the initial values of the parameters in the nonlinear regression procedure of Eq. (8) to evaluate the model.

- c. Modified GAB model: the modified GAB model (Eq. (9)) like the original GAB model can be transformed to a quadratic form by algebraic manipulation to yield Eq. (20):

$$\frac{a_w}{M} = X a_w^2 + Y a_w + Z \quad (20)$$

Plotting  $\frac{a_w}{M}$  against  $a_w$  and fitting a polynomial of the second order to the plot yield the following functions from Eq. (9):

$$X = \frac{B}{A} \left( \frac{T}{C} - 1 \right), Y = \frac{1}{A} \left( 1 - \frac{2T}{C} \right), Z = \frac{1}{ABC} \quad (21)$$

The average values of  $A$ ,  $B$  and  $C$  are obtained and used as initial parameter estimates in the nonlinear regression analysis to evaluate the model.

- d. Hailwood-Horrobin model: The Hailwood-Horrobin model (Eq. (10)) is mathematically similar to the GAB and can after algebraic manipulations be represented in the form

$$\frac{a_w}{M} = C a_w^2 + B a_w + A \quad (22)$$

Plotting  $\frac{a_w}{M}$  against  $a_w$  and fitting a polynomial of the second order to the plot at each temperature yield the values of  $C$ ,  $B$  and  $A$  for use as initial parameter estimates in the nonlinear regression procedure for the model evaluation.

- e. Modified Hailwood-Horrobin model: this model (Eq. (11)) also has mathematical similarity with the GAB. It can be transformed algebraically to yield Eq. (23):

$$\frac{a_w}{M} = \lambda a_w^2 + \mu a_w + \varphi \quad (23)$$

Plotting  $\frac{a_w}{M}$  against  $a_w$  and fitting a polynomial of the second order to the plot yield the following functions from Eq. (11):

$$\lambda = \frac{C}{T^m}, \mu = BT \text{ and } \varphi = TA \quad (24)$$

The average values of  $A$ ,  $B$  and  $C$  are obtained and used as initial parameter estimates in the nonlinear regression analysis to evaluate the model.

- f. Modified Chung-Pfost model: the modified Chung-Pfost model (Eq. (12)) is transformed by algebraic manipulations to yield Eq. (25):

$$a_w = \exp \left[ \left( \frac{-A}{(T+B)} \right) \exp(-CM) \right] \quad (25)$$

Linearizing Eq. (25) by logarithmic transformation is carried out as follows:

$$\ln(a_w) = \frac{-A}{(T+B)} \exp(-CM) \quad (26)$$

$$-\ln(a_w) = \frac{A}{(T+B)} \exp(-CM) \quad (27)$$

$$\ln[-\ln(a_w)] = \ln\left[\frac{A}{(T+B)}\right] - CM \quad (28)$$

A plot of  $\ln[-\ln(a_w)]$  against  $M$  at each temperature yields a straight line with slope as  $-C$  and intercept on the  $y$ -axis as  $\ln\left[\frac{A}{(T+B)}\right]$ .

With the expression for the slope, further algebraic manipulation is carried out as follows in order to solve for the temperature-related parameters of the model:

$$\exp(b) = \frac{A}{(T+B)}, \text{ implying that } T+B = \frac{A}{\exp(b)} = A \exp(-b) \quad (29)$$

From the above,  $T = A \exp(-b) - B$ .

A plot of  $T$  against  $\exp(-b)$  yields a straight line with  $A$  as slope and intercept on the  $y$ -axis as  $-B$ .

In the nonlinear regression procedure, the avC as  $C$  and  $A$  and  $B$  are used as the initial parameter estimates in the equation.

g. Modified Halsey model: the modified Halsey model (Eq. (13)) can be transformed by algebraic manipulations to yield Eq. (30):

$$a_w = \exp[-\exp(A+BT)M^{-C}] \quad (30)$$

Linearizing Eq. (30) by logarithmic transformation yields

$$\ln(a_w) = -\exp(A+BT)M^{-C} \quad (31)$$

$$-\ln(a_w) = \exp(A+BT)M^{-C} \quad (32)$$

So

$$\ln[-\ln(a_w)] = (A+BT) - CLnM \quad (33)$$

A plot of  $\ln[-\ln(a_w)]$  against  $LnM$  at each temperature yields a straight line with slope as  $-C$  and intercept on the  $y$ -axis as  $A+BT$ . Using the intercept on  $y$ -axis for different temperature plots of the above, the values of the intercepts are then plotted against temperature to yield another straight line with slope as  $B$  and intercept on  $y$ -axis as  $A$ . In the nonlinear regression analysis, the avC as  $C$  and  $A$  and  $B$  values are used as the starting values in parameter estimates for the model.

h. Modified Henderson model: the modified Henderson model (Eq. (14)) is transformed to yield Eq. (34):

$$a_w = 1 - \exp[-A(T+B)M^C] \quad (34)$$

Eq. (34) is linearized by logarithmic transformation as follows:

$$1 - a_w = \exp[-A(T + B)M^C] \quad (35)$$

$$\text{Ln}(1 - a_w) = -A(T + B)M^C \quad (36)$$

$$-\text{Ln}(1 - a_w) = A(T + B)M^C \quad (37)$$

$$\text{Ln}[-\text{Ln}(1 - a_w)] = \text{Ln}[A(B + T)] + \text{CLn}M \quad (38)$$

A plot of  $\text{Ln}[-\text{Ln}(1 - a_w)]$  against  $\text{Ln}M$  at each temperature yields a straight line with slope  $a_1 = C$  and intercept on the y-axis  $b_1 = \text{Ln}[A(B + T)]$ . To solve for the temperature-related parameters, intercept on the y-axis is used.

$$\text{Therefore, } \exp(b_1) = A(T + B) = AT + AB. \quad (39)$$

A plot of  $\exp(b_1)$  against  $T$  yields a straight line with slope  $a_2$  as  $A$  and intercept on y-axis  $b_2$  as  $AB$ . In the nonlinear regression procedure,  $\text{av}C$  and  $A$  and  $B$  are used as initial parameter estimates for the model.

- i. Modified Oswin model: the modified Oswin model (Eq. (15)) can be manipulated algebraically to yield Eq. (40):

$$a_w = \frac{1}{\left[\frac{(A+BT)}{M}\right]^C + 1} \quad (40)$$

$$\frac{1}{a_w} = \left[\frac{(A + BT)}{M}\right]^C + 1 \text{ and } \frac{1}{a_w} - 1 = \left[\frac{(A + BT)}{M}\right]^C \quad (41)$$

Linearizing Eq. (41) by logarithmic transformation yields

$$\text{CLn}(A + BT) - \text{CLn}M = \text{Ln}\left(\frac{1 - a_w}{a_w}\right) \quad (42)$$

A plot of  $\text{Ln}\left(\frac{1-a_w}{a_w}\right)$  against  $\text{Ln}M$  at each temperature yields a straight line with slope as  $-C$  and intercept on the y-axis as  $\text{CLn}(A + BT)$ .

The expression for intercept on the y-axis is solved further to evaluate the temperature-related parameters of the model and yield Eq. (43),

$$\exp(b/c) = (A + BT) \quad (43)$$

A plot of  $\exp(b/c)$  against  $T$  yields a straight line with slope as  $A$  and intercept on the y-axis as  $B$ . In the nonlinear regression procedure,  $\text{av}C$  as  $C$  and  $A$  and  $B$  are used as the initial parameter estimates in the model evaluation.

- j. Ngoddy-Bakker-Arkema model: the Ngoddy-Bakker-Arkema model, which has been postulated to be a generalized model, has the following parameters (unknowns):  $\sigma$ ,  $V$ ,  $P_m$ ,  $\rho$ ,  $\varepsilon$  and  $\eta$ .

Evaluating the model requires a lot of care. The starting values of parameters for application in the nonlinear regression procedure can be obtained as follows:

$\sigma$ ,  $V$ ,  $\rho$  and  $P_o$  can be obtained at different temperatures from the steam table  $P$  can be calculated using the expression  $P = a_w$ ,  $\varepsilon$  can be taken as having a typical value of 0.1 though its value can be less,  $P_m$  is the monolayer value of  $P$  and  $\eta$  can be assumed to lie between  $-1$  and  $+1$  in the form of  $-1 \leq \eta \leq +1$  with 0.1 as a typical starting value.

## 7.2. Moisture sorption isotherm model predictive indicators

After values of model constants have been determined using the nonlinear regression analysis, the suitability of a model for predictive purpose or its goodness of fit is determined using the following indices:

- a. Residual plots: these are plots of residuals (difference between measured and predicted values of the EMC) against the measured values.
- b. Standard error of estimate given as

$$SE = \left[ \frac{\sum (Y - Y')^2}{df} \right]^{1/2} \quad (44)$$

- c. Mean relative percent deviation given as

$$MRE = \frac{100}{N} \sum \left| \frac{Y - Y'}{Y} \right| \quad (45)$$

- d. Fraction explained variation given as

$$FEV = \frac{SSM}{SST} \quad (46)$$

- e. Residual sum of squares (RSS) given as

$$RSS = \frac{\sum (Y - Y')^2}{N} \quad (47)$$

- f. Coefficient of determination,  $R^2$ .

where  $Y$  is the measured EMC value,  $Y'$  is the EMC value predicted by the model,  $N$  is the number of data points,  $df$  is the degree of freedom,  $SSM$  is the sum of squares due to the model and  $SST$  is the total sum of squares.

## 8. Conclusions

Moisture sorption phenomena govern several technological processes (drying, storage, mixing and packaging to mention a few) involving agricultural and food products. Moisture sorption isotherms of these products are generally of the type II, sigmoidal in shape and temperature dependent. The isotherms can be determined using the static or dynamic gravimetric, vapor pressure manometric, hygrometric and inverse gas chromatographic methods. Desorption isotherm path could differ from that of adsorption leading to moisture sorption hysteresis.

Commonly used moisture sorption isotherm models include the BET, GAB, modified GAB, Hailwood-Horrobin, modified Hailwood-Horrobin, modified Chung-Pfost, modified Halsey, modified Henderson and modified Oswin models. Ngoddy-Bakker-Arkema model which was proposed as a generalized model was considered. While some of the models can be evaluated by fitting polynomial functions of the second order to them and applying nonlinear regression procedure, others can be solved thorough linearization by logarithmic transformation and nonlinear regression. For the Ngoddy-Bakker-Arkema model, the initial parameter

estimates for use in nonlinear regression have to be obtained from the steam table. A model is considered acceptable for predictive purpose, if the residuals are uniformly scattered around the horizontal value of zero showing no systematic tendency towards a clear pattern. Model goodness of fit is determined using standard error of estimate, mean relative percent deviation, fraction explained variation, coefficient of determination and residual sum of squares.

### **Conflict of interest**

This chapter has no conflict of interest.

### **Author details**

Ndubisi A. Aviara

Department of Agricultural and Environmental Resources Engineering, Faculty of Engineering, University of Maiduguri, Maiduguri, Nigeria

\*Address all correspondence to: [nddyaviara@yahoo.com](mailto:nddyaviara@yahoo.com)

### **IntechOpen**

---

© 2020 The Author(s). Licensee IntechOpen. This chapter is distributed under the terms of the Creative Commons Attribution License (<http://creativecommons.org/licenses/by/3.0>), which permits unrestricted use, distribution, and reproduction in any medium, provided the original work is properly cited. 



## References

- [1] Ngoddy PO, Bakker-Arkema FW. A generalized theory of sorption phenomena in biological materials (Part I: The isotherm equation). *Transactions of ASAE*. 1970;**13**(5):612-617
- [2] Ferro Fontan C, Chirife J, Sancho E, Iglesias HA. Analysis of a model for water sorption phenomena in foods. *Journal of Food Science*. 1982;**47**: 1590-1594
- [3] Shatadal P, Jayas DS. Moisture sorption isotherms of grains and oil seeds. *Postharvest News and Information*. 1990;**1**(6):447-451
- [4] Rockland LB, Nishi SK. Influence of water activity on food product stability. *Food Technology*. 1980;**34**(4):42
- [5] Van den Berg C, Bruin S. Water activity and its estimation in food system. Theoretical aspects. In: Rockland LB, Stewart GF, editors. *Water Activity: Influences on Food Quality*. New York: Academic Press Inc; 1981. pp. 1-61
- [6] Rizvi SSH. Thermodynamic properties of food in dehydration. In: Rao MA, Rizvi SSH, editors. *Engineering Properties of Foods*. New York: Marcel Dekker Inc; 1986. pp. 133-214
- [7] Brunauer S, Deming LS, Deming WE, Teller E. On a theory of van der Waals adsorption of gases. *American Chemical Society Journal*. 1940;**62**: 1723-1732
- [8] Talib MZM, Daud WRW, Ibrahim MH. Moisture desorption isotherms of cocoa beans. *Transactions of the ASAE*. 1995;**38**(4):1153-1155
- [9] Labuza TP, Hyman CR. *Moisture Migration and Control in Multi-Domain Foods*. St. Paul, Minnesota: Department of Food Science and Nutrition, University of Minnesota; 2001
- [10] Khalloufi S, Giasson J, Ratti C. Water activity of freeze-dried mushrooms and berries. *Canadian Agricultural Engineering*. 2000;**42**(1): 51-56
- [11] Brooker DB, Bakker-Arkema FW, Hall CW. *Drying and Storage of Grains and Oil Seeds*. New York: Van Nostrand Reinhold Inc.; 1992
- [12] Saravacos GD, Tsiourvas DA, Tsami E. Effect of temperature on the water adsorption isotherms of sultana raisins. *Journal of Food Science*. 1986;**51**: 381-383,387
- [13] Kapsalis JG. Influences of hysteresis and temperature on moisture sorption isotherms. In: Rockland LB, Beuchat LR, editors. *Water Activity: Theory and Applications to Food*. New York: Marcel Dekker Inc; 1987. pp. 173-213
- [14] Greig RIW. Sorption properties of heat denatured cheese whey protein, Part II: Unfreezable water content. *Dairy Industry International*. 1979; **June**:15
- [15] Yu L, Mazza G, Jayas DS. Moisture sorption characteristics of freeze-dried, osmo-dried and osmo-air-dried cherries, and blueberries. *Transactions of ASAE*. 1999;**42**(1):141-147
- [16] San Jose C, Asp NG, Burvall A, Dahlgvist A. Water sorption in lactose hydrolysed milk. *Journal of Dairy Science*. 1977;**60**:1539
- [17] Tsami E, Krokida MK, Drouzas AE. Effect of drying method on the sorption characteristics of model fruit powders. *Journal of Food Engineering*. 1999;**38**: 381-392

- [18] Mittal GS, Usborne WK. Moisture isotherms for uncooked meat emulsions of different composition. *Journal of Food Science*. 1985;**50**:1576-1579
- [19] Mazza G. Sorption isotherms and monolayer moisture content of raw peas and peas dehydrated after pressure cooking. *Journal of Food Technology*. 1986;**21**:503-507
- [20] Aviara NA. Drying characteristics and storage stability of chemically modified cassava (*Manihot Esculenta* Crantz), maize (*Zea Mays* Linn.) and Sorghum (*Sorghum bicolor* L. Moench) starches [PhD dissertation]. Ibadan: University of Ibadan; 2010. 285pp
- [21] Palou E, Lopez-Malo A, Argai A. Effect of temperature on the moisture sorption isotherms of some cookies and corn snacks. *Journal of Food Engineering*. 1997;**31**:85-93
- [22] Igbeka JC, Blaisdell JL, Herum FL, Hamdy MY. Equilibrium Moisture Content of Cassava and Potato. St. Joseph, Michigan: American Society of Agricultural Engineers; 1975. ASAE Paper No.: 75-6527
- [23] Ajibola OO, Adams BA. Desorption equilibrium moisture content of cassava at several temperatures. *International Agrophysics*. 1986;**2**(3):235-239
- [24] Gevaudan A, Chuzel G, Didier S, Andrieu J. Physical properties of cassava mash. *International Journal of Food Science and Technology*. 1989;**24**: 637-645
- [25] Roman GN, Urbicain MJ, Rotstein E. Moisture equilibrium in apples at several temperatures: Experimental data and theoretical considerations. *Journal of Food Science*. 1982;**47**:1484-1488, 1507
- [26] Gal S. Recent advances in techniques for the determination of sorption isotherm. In: Duckworth RB, editor. *Water Relations of Foods*. London: Academic Press; 1975. pp. 135-155
- [27] Gal S. Recent developments in techniques for obtaining complete sorption isotherms. In: Rockland LB, Stewart GF, editors. *Water Activity: Influence on Food Quality*. New York: Academic Press; 1981. p. 89
- [28] Gal S. The need for and practical applications of sorption data. In: Jowitt R, Escher F, Hallstrom B, Meffert HFT, Speiss WEL, Vos G, editors. *Physical Properties of Foods*. New York: Applied Science Publishers; 1983. pp. 13-25
- [29] Speiss WEL, Wolf W. Critical evaluation of methods to determine moisture sorption isotherms. In: Rockland LB, Beuchat LR, editors. *Water Activity: Theory and Applications to Foods*. New York: Marcel Dekker Inc; 1987. pp. 215-233
- [30] Mazza G. Sorption isotherms and drying rates of Jerusalem artichoke. *Journal of Food Science*. 1984;**49**: 384-388
- [31] Weisser H. Influence of temperature on sorption isotherms. In: Le Maguer M, Jelen P, editors. *Food Engineering and Process Application. Volume I: Transport Phenomena*. Essex: Elsevier Applied Science Publishers Ltd; 1986
- [32] Kameoka T, Jayas DS, Morishima H, Sokhansanj S. Equilibrium moisture content of rice. In: Le Maguer M, Jelen P, editors. *Food Engineering and Process Application. Volume I: Transport Phenomena*. Essex: Elsevier Applied Science Publishers Ltd; 1986
- [33] Shepherd H, Bhardwaj RK. A study of desorption isotherms of rewetted pigeon pea type – 17. *Journal of Food Science*. 1986;**51**(3):595-598

- [34] Ajibola OO. Equilibrium moisture properties of winged bean seed. Transactions of ASAE. 1986;**29**(5): 1485-1487
- [35] Ajibola OO. Desorption isotherms of plantain at several temperatures. Journal of Food Science. 1986;**51**(1):169-171
- [36] Ajibola OO. Desorption isotherms of Gari from 40 °C to 70 °C. Journal of Agricultural Engineering Research. 1986;**35**:207-210
- [37] Menkov ND. Moisture sorption isotherms of vetch seeds at four temperatures. Journal of Agricultural Engineering Research. 2000;**76**:373-380
- [38] Vazquez G, Chenlo F, Moreira R. Sorption isotherms of lupine at different temperatures. Journal of Food Engineering. 2003;**60**:449-452
- [39] Santalla EM, Mascheroni RH. Equilibrium moisture characteristics of high oleic sunflower seeds and kernels. Drying Technology. 2003;**21**:147-163
- [40] Tolaba MP, Peltzer M, Enrique N, Pollio ML. Grain sorption equilibria of quinoa grains. Journal of Food Engineering. 2004;**61**:365-371
- [41] Aviara NA, Ajibola OO, Oni SA. Sorption equilibrium and thermodynamic characteristics of soya bean. Biosystems Engineering. 2004; **87**(2):179-190
- [42] Kaleemullah S, Kailappan R. Moisture sorption isotherms of red chillies. Biosystems Engineering. 2004; **88**(1):95-105
- [43] Durakova AG, Menkov ND. Moisture sorption characteristics of chickpea flour. Journal of Food Engineering. 2005;**68**(4):535-539
- [44] Swami SB, Das SK, Maiti B. Moisture sorption isotherms of black gram nuggets (Bori) at varied temperatures. Journal of Food Engineering. 2005;**67**(4):477-482
- [45] Aviara NA, Ajibola OO, Aregbesola OA, Adedeji MA. Moisture sorption isotherms of sorghum malt at 40 and 50°C. Journal of Stored Products Research. 2006;**42**:290-301
- [46] Ajisegiri ESA, Chukwu O, Soppade PA. Moisture sorption study of locally parboiled rice. Australian Journal of Technology. 2007;**11**(2):86-90
- [47] Ojediran JO, Raji AO, Aviara NA. Moisture sorption properties of castor seeds. Agricultural Engineering Today. 2014;**38**(1):38-44
- [48] Young JH. Evaluation of models to describe sorption and desorption equilibrium moisture content isotherms of Virginia-type peanuts. Transactions of ASAE. 1976;**19**:146-150, 155
- [49] Oyelade OJ, Tunde-Akintunde TY, Igbeka JC, Oke MO, Raji OY. Modelling moisture sorption isotherms for maize flour. Journal of Stored Products Research. 2008;**44**:179-185
- [50] Oyelade OJ, Tunde-Akintunde TY, Igbeka JC. Predictive equilibrium moisture content equations for yam (*Dioscorea rotundata*, Poir) flour and hysteresis phenomena under practical storage conditions. Journal of Food Engineering. 2008;**87**:229-235
- [51] Al-Muhtaseb AH, McMinn WAM, Magee TRA. Water sorption isotherms of starch powders. Part I: Mathematical description of experimental data. Journal of Food Engineering. 2004;**61**: 297-307
- [52] Bello EA. Moisture adsorption phenomenon of groundnut (*Arachis hypogea*, L.) and neem (*Azadirachta indica*) seeds. B.Eng. Honours Project Report. Maiduguri: Department of

- Agricultural and Environmental Resources Engineering, University of Maiduguri; 2013. 48pp
- [53] Afkawa DM. Moisture adsorption phenomenon in Sheanut (*Butyrospermum paradoxum*) and Desert Date (*Balanites aegyptiaca*) kernels. B. Eng. Honours Project Report. Maiduguri: Department of Agricultural and Environmental Resources Engineering, University of Maiduguri; 2013. 55pp
- [54] Bosin WA, Easthouse HD. The rapid method for obtaining humidity equilibrium data. *Food Technology*. 1970;**24**:1155-1178
- [55] Rahman MS, al-Belushi, R. H. Dynamic isopiestic method (DIM): Measuring moisture sorption isotherm of freeze-dried garlic powder and other potential uses of DIM. *International Journal of Food Properties*. 2006;**9**(3): 421-437
- [56] Bell LN, Labuza TP. Moisture Sorption: Practical Aspects of Isotherm Measurement and Use. 2nd ed. St. Paul, Minnesota: American Association of Cereal Chemists Inc.; 2000
- [57] Crapiste GH, Rotstein E. Prediction of sorptional equilibrium data for starch containing foodstuff. *Journal of Food Science*. 1982;**47**:1501-1507
- [58] Fasina OO, Sokhansanj S. Equilibrium moisture relations and heat of sorption of alfalfa pellets. *Journal of Agricultural Engineering Research*. 1993;**56**:51-63
- [59] Arslan N, Togrul H. Moisture sorption isotherms for crushed chillies. *Biosystems Engineering*. 2005;**90**:47-61
- [60] Labuza TP, Acott K, Tatini SR, Lee RY, Flink J, McCall W. Water activity determination: A collaborative study of different methods. *Journal of Food Science*. 1976;**41**:910-917
- [61] Pichler HJ. Sorption isotherms for grain and rape. *Journal of Agricultural Engineering Research*. 1957;**2**(2):159-165
- [62] Sood VC, Heldman DR. Analysis of a vapour pressure manometer for measurement of water activity in nonfat dry milk. *Journal of Food Science*. 1974;**39**:1011-1013
- [63] Ajibola OO, Dairo UO. The relationships between equilibrium relative humidity and moisture content of sesame seed using the vapour manometric method. *Ife Journal of Science and Technology*. 1998;**8**(1): 61-67
- [64] Ajibola OO, Aviara NA, Ajetumobi OE. Sorption equilibrium and thermodynamic properties of cowpea. *Journal of Food Engineering*. 2003;**58**: 317-324
- [65] Ajibola OO, Aviara NA, Abodurin VK. Moisture sorption equilibrium and thermodynamic properties of palm kernel. *International Agrophysics*. 2005;**19**:273-283
- [66] Riganakos KA, Demertzis PG, Kontominas MG. Gas chromatographic study of water sorption by wheat flour. *Journal of Cereal Science*. 1989;**9**(3): 261-271
- [67] Manuel Sa M, Sereno AM. Effect of column material on sorption isotherms obtained by inverse gas chromatography. *Journal of Chromatography*. 1992;**600**:341-343
- [68] Smith DS, Mannheim CH, Gilbert SG. Water sorption isotherms of sucrose and glucose by inverse gas chromatography. *Food Science*. 1981;**46**(4):1051-1053
- [69] Helen HJ, Gilbert SG. Moisture sorption of dry bakery products by inverse gas chromatography. *Journal of Food Science*. 1985;**50**:454-458

- [70] Riganakos KA, Demertzis PG, Kontominas MG. Inverse gas chromatographic study of moisture sorption by wheat and sour flour and the effect of specific heat treatment on their sorption behaviour. *Developments in Food Science*. 1992;**29**:277-286
- [71] Meter Group Inc. AquaLab water activity meter. In: *Operator's Manual for Series 4*. Hopkins Court, Pullman, WA, USA: Meter Group Inc.; 2018
- [72] Iglesias HA, Chirife J. *Handbook of Food Isotherms*. New York: Academic Press; 1982
- [73] Rockland LB. Water activity and storage stability. *Food Technology*. 1969;**23**:1241-1248, 1251
- [74] Labuza TP. Properties of water as related to the keeping quality of foods. In: *Proceedings of the 3rd International Conference on Food Science and Technology*. Chicago, IL: Institute of Food Technologists; 1970
- [75] Labuza TP. Interpretation of sorption data in relation to the state of the constituent water. In: Duckworth RB, editor. *Water Relations of Foods*. New York: Academic Press; 1975
- [76] Labuza TP, Kamman JF. Reaction kinetics and accelerated tests simulations as a function of temperature. In: Saguy I, editor. *Computer Aided Techniques in Food Technology*. New York: Marcel Dekker Inc.; 1983
- [77] Vega-Galvez A, Palacios M, Lemus-Mondaca R, Passaro C. Moisture sorption isotherms and isosteric determination in Chilean papaya. *Quimica Nova*. 2008;**31**(6):1417-1442
- [78] Saravacos GD, Stinchfield RM. Effect of temperature and pressure on the sorption of water vapour by freeze dried food materials. *Journal of Food Science*. 1965;**30**:779
- [79] Audu TOK, Locin M, Weisser H. Sorption isotherms of sugars. *Lebensmittel-Wissenschaft & Technologie*. 1978;**11**:31
- [80] Weisser H, Weber J, Loncin M. Water vapour sorption isotherms of sugar substitutes in the temperature range of 25 to 80°C. *Internationale Zeitschrift Lebensmittel, Technologie und Verfahrenstechnik*. 1982;**33**:89
- [81] Silverman GJ, Munsey DT, Lee C, Ebert E. Interrelationship between water activity, temperature and 5.5% oxygen on the growth of enterotoxin—A secretion by *Staphylococcus aureus* in precooked bacon. *Journal of Food Science*. 1983;**48**:1783
- [82] Iglesias HA, Chirife J. Equilibrium moisture contents of a dried beef: Dependence on drying temperature. *Journal of Food Technology*. 1976;**11**: 565-573
- [83] Labuza TP, Kaane A, Chen JY. Effect of temperature on moisture sorption isotherms and water activity shifts of two dehydrated foods. *Journal of Food Science*. 1985;**50**(2):385-391
- [84] Wolf W, Walker JE, Kapsalis JG. Water vapour sorption hysteresis in dehydrated foods. *Journal of Agricultural and Food Chemistry*. 1972;**20**:1073
- [85] Iglesias HA, Chirife J. Prediction of the effect temperature on water sorption isotherms of food material. *Journal of Food Technology*. 1976;**11**: 109-116
- [86] Ngoddy PO, Bakker-Arkema FW. A theory of hysteresis for biological materials. *Journal of Agricultural Engineering Research*. 1975;**20**:109-121
- [87] Chirife J, Iglesias HA. Equations for fitting water sorption isotherms of food: Part 1—A review. *Journal of Food Technology*. 1978;**13**:159-174

- [88] Bone DP. Practical applications of water activity and moisture relations in foods. In: Rockland LB, Beuchat LR, editors. *Water Activity: Theory and Applications to Food*. New York: Marcel Dekker Inc; 1987. pp. 369-395
- [89] Iglesias HA, Chirife J, Viollaz P. Thermodynamics of water vapour sorption by sugar beet root. *Journal of Food Technology*. 1976;**11**: 91-101
- [90] Chirife J, Boquet R, Ferro Fontan C, Iglesias HA. A new model for describing the water sorption of food. *Journal of Food Science*. 1983;**48**:1382-1383
- [91] Iglesias HA, Chirife J. An alternative to the Guggenheim Anderson and De Boer model for mathematical description of moisture sorption isotherms of foods. *Food Research International*. 1995;**28**(3): 317-321
- [92] Chen XD. A new sorption equilibrium isotherm model. *Food Research International*. 1997;**30**(10): 755-759
- [93] Van de Berg C. Description of water activity of food for engineering purposes by means of the GAB model of sorption. In: McKenna BM, editor. *Engineering and Food, Volume 1: Engineering Sciences in the Food Industry*. London: Elsevier Applied Science Publishers; 1984
- [94] Boquet R, Chirife J, Iglesias HA. Equations for fitting water sorption isotherms of foods, Part III: Evaluation of various three-parameter models. *Journal of Food Technology*. 1979;**14**: 527-534
- [95] Aviara NA. Modification of Hailwood-Horrobin Moisture Sorption Isotherm Model. Maiduguri: Department of Agricultural and Environmental Resources Engineering Paper, Faculty of Engineering, University of Maiduguri; 2018. 25pp
- [96] Thompson HL. Temporary storage of high moisture shelled corn using continuous aeration. *Transactions of ASAE*. 1972;**15**(2):333-337
- [97] Pfoest HB, Mourer SG, Chung DS, Milliken GA. Summarising and Reporting Equilibrium Moisture Data for Grains. St. Joseph, Michigan: American Society of Agricultural Engineers; 1976. ASAE Paper No.: 76-3520
- [98] ASAE. ASAE Standards. 43rd ed. St. Joseph, Michigan: American Society of Agricultural Engineers; 2008
- [99] Ajibola OO. Adding Values to the Farmer's Harvest. Inaugural Lecture Series No. 45. Ile-Ife: Obafemi Awolowo University Press Ltd; 2000
- [100] Chen C, Morey RV. Comparison of four EMC/ERH equations. *Transactions of ASAE*. 1989;**32**(3):983-990
- [101] Mazza G, Jayas DS. Equilibrium moisture characteristics of sunflower seeds, hulls and kernels. *Transactions of ASAE*. 1991;**34**(2):534-538
- [102] Jayas DS, Mazza G. Equilibrium moisture characteristics of safflower seeds. *Transactions of ASAE*. 1991; **34**(5):2099-2103
- [103] Van den Berg C. Description of water activity of foods for engineering purposes by means of the GAB model of sorption. In: McKenna BM, editor. *Engineering and Foods*. New York: Elsevier Science Publishers; 1984. pp. 119-131
- [104] Weisser H. Influence of temperature on sorption equilibria. In: Simantos D, Multon JL, editors. *Properties of Water in Foods in Relation to Quality and Stability*. Dordrecht, The Netherlands: Martinus Nijhoff Publishers; 1985. pp. 95-118
- [105] Wolf W, Speiss WEL, Jung G. Standardization of isotherm

- measurements. (COST-Project 90 and 90 bis). In: Simantos D, Multon JL, editors. *Properties of Water in Foods in Relation to Quality and Stability*. Dordrecht, The Netherlands: Martinus Nijhoff Publishers; 1985. pp. 661-679
- [106] Multon JL. Interaction between water and the constituents of grains, seeds and by-products. In: Multon JL, editor. *Preservation and Storage of Grains, Seeds and Their By-products*. New York: Lavoisier Publishing Company; 1988. pp. 89-159
- [107] Lomauro CJ, Bakshi AS, Labuza TP. Evaluation of food moisture sorption isotherm equations, Parts I and II. *Lebensmittel-Wissenschaft & Technologie*. 1985;18:111-124
- [108] Jayas DS, Mazza G. Comparison of five three-parameter equations for the description of adsorption data of oats. *Transactions of ASAE*. 1993;36(1): 119-125
- [109] Sun DW, Byrne C. Selection of EMC/ERH isotherm equations for rapeseed. *Journal of Agricultural Engineering Research*. 1998;69:307-315
- [110] Sun DW. Comparison and selection of EMC/ERH isotherm equations for drying and storage of grain and oilseed. *Agricultural Engineering International: The CIGR e-Journal*. 1999;1(March):1-9
- [111] Sun DW. Comparison and selection of EMC/ERH isotherm equations for rice. *Journal of Stored Products Research*. 1999;35:249-264
- [112] Ajibola OO. Thin layer drying of melon seed. *Journal of Food Engineering*. 1989;9:305-320
- [113] Pezzutti A, Crapiste GH. Sorptional equilibrium and drying characteristics of garlic. *Journal of Food Engineering*. 1997;31:113-123
- [114] Jayas DS, Kukulko DA, White NDG. Equilibrium moisture-equilibrium relative humidity for Canola meal. *Transactions of ASAE*. 1988;31(5):1585-1588, 1593
- [115] Pollio ML, Resnick SL, Chirife J. Water sorption isotherms of soybean varieties grown in Argentina. *International Journal of Food Science and Technology*. 1987;22:335-338
- [116] Demertzis PG, Riganakos KA, Kontomina MG. Water sorption isotherms of crystalline raffinose by inverse chromatography. *International Journal of Food Science and Technology*. 1989;24:629-636
- [117] Diamante LM, Munro PA. Water desorption isotherms of two varieties of sweet potato. *International Journal of Food Science and Technology*. 1990;25: 140-147
- [118] Sopade PA, Ajisegiri AS, Abbas AB. Moisture sorption study of some Nigerian grains: Rice, bambara nut and tiger nut. *Proceedings of the Nigerian Society of Agricultural Engineers*. 1991; 15:158-174
- [119] Pappas G, Rao VNM. Sorption isotherms of cowpea from 25°C to 70°C. *Transactions of ASAE*. 1987;30(5): 1478-1482
- [120] Boquet R, Chirife J, Iglesias HA. Equations for fitting water sorption isotherms of foods, Part II: Evaluation of various two-parameter models. *Journal of Food Technology*. 1978;13:319-327
- [121] Oyelade OO. Equilibrium moisture content models for lafun. *International Journal of Food Engineering*. 2008;4(2):4
- [122] Pagano AM, Mascheroni RH. Sorption isotherms for amaranth grains. *Journal of Food Engineering*. 2005;67: 441-450

*Edited by George Kyzas and Nikolaos Lazaridis*

The book deliberately keeps background information to a minimum, instead it comprehensively covers adsorption of liquid solutions, the difference between equilibrium individual solute uptake and surface excess, a general discussion of adsorbate uptake mechanisms and uptake rate expression, uptake steps, performance models and their generalizations, application of performance models, and design methods based on the constant behavior assumption, and the unused bed length concept.

Published in London, UK

© 2020 IntechOpen  
© dkiidpix / iStock

**IntechOpen**

